Atmospheric Nitrate Chemistry and Response to Emissions Reductions in the Northeastern US

by

Heejeong Kim

B.S., Jeonbuk National University: Jeonju, South Korea, 2016

M.Sc., Korea University: Seoul, South Korea, 2018

M.Sc., Brown University: Providence, RI, 2022

A dissertation submitted in partial fulfillment of the requirements for the degree of Doctor of Philosophy in the Department of Earth, Environmental, and Planetary Sciences at Brown University

Providence, Rhode Island, USA

May 2025

This dissertation by Heejeong Kim is accepted in its present form by The Department of Earth, Environmental and Planetary Sciences as satisfying the dissertation requirement for the degree of Doctor of Philosophy.

Date _____ _____

Meredith G. Hastings, Ph.D., Advisor

Recommended to the Graduate Council

Date _____ _____

Victor Tsai, Ph.D., Reader

Date _____ _____

Daniel Ibarra, Ph.D., Reader

Date _____ _____

Wendell W. Walters, Ph.D., Reader

Date _____ _____

Havala O.T. Pye, Ph.D., Reader

Approved by the Graduate Council

Date _____ _____

Thomas A. Lewis

Dean of the Graduate School

Curriculum Vitae

Heejeong Kim

E-mail: heejeong_kim@brown.edu
Address: 167 Thayer st, Providence, RI, USA, 02912

Education

9/2020 - present	**Brown University** *Ph.D.* candidate in the Department of *Earth, Environmental, and Planetary Sciences* Advisor: *Prof. Meredith Hastings*
9/2020 – 5/2022	**Brown University** *Master of Science* in the Department of *Earth, Environmental, and Planetary Sciences* *Advisor: Prof. Meredith Hastings*
3/2016 - 8/2018	**Korea University** *Master of Science* in *Earth and Environmental Science* Thesis: "*Photochemical Mechanisms of High Ozone Formation in Seoul"* Advisor: *Prof. Meehye Lee*
3/2011 - 2/2016	**Jeonbuk (Chonbuk) National University** *Bachelor of Science* in *Earth and Environmental Science*

Research Experience

Brown University, 2020 – present

- Short-term atmospheric aerosol study in the northeastern US, 2024-present.
  - Investigated the impact of COVID-19 lockdown impact on air quality using an archived aerosol filter record (2019-2020)
  - Conducted stable nitrogen and oxygen isotope analysis using isotope ratio mass spectrometry (IRMS)
- Long-term atmospheric aerosol study in the northeastern US, 2020-present.
  - Investigated the impact of emission regulations on atmospheric oxidation chemistry of nitrate and sulfate using an archived aerosol filter record (2005-2018)
  - Analyzed stable nitrogen and oxygen isotopes using IRMS and major inorganic concentrations using ion chromatography.
- Atmospheric Emissions and Reactions Observed from Megacities to Marine Areas (AEROMMA) campaign, 2023.
  - Performed surface air pollutants measurement to assess atmospheric composition in urban areas influenced by marine emissions.
  - Collected reactive nitrogen species in the atmosphere samples in New Haven, CT and analyzed their nitrogen and oxygen isotopic composition.
- Michigan-Ontario Ozone Source Experiment (MOOSE) campaign, 2021.

- Performed surface air pollutants measurement to investigate the ozone formation sensitivity to VOC and NO_x emissions in the U.S. and Canada border regions.
- Collected atmospheric reactive nitrogen species in Detroit, MI and analyzed their nitrogen and oxygen isotopic composition.

Korea University, 2016 – 2018

- KORea-US Air Quality (KORUS-AQ) Campaign, 2016.
  - Performed surface measurement to identify photochemical factors controlling O_3 formation and diagnose O_3 formation sensitivity in Seoul.
  - Operated High-Performance Liquid Chromatography (HPLC) to measure Hydrogen Peroxide (H_2O_2) and Methyl Hydrogen Peroxide (MHP) at the Olympic Park in Seoul.
- Aerosol Study in Beijing, China.
  - Conducted as part of joint research with the Chinese Research Academy of Environmental Sciences (CRAES), NIER, and Korea University.
  - Operated the Potential Aerosol Mass (PAM) chamber to observe characteristics of secondary aerosol formation and to investigate atmospheric gas-to-particle conversion.at CRAES in Beijing.
  - Collected VOCs in Beijing using thermal desorption sorbent tubes and analyzed in Korea University using Gas Chromatography - Flame Ionization Detectors (GC-FID).
- O_3 and Reactive Gases in Marine Boundary Layer (MBL) over the Yellow Sea, 2017
  - Conducted shipboard measurement using the GS1 Vessel in the Yellow Sea to investigate the influence of ship emissions and transport of pollutants over the Yellow Sea in Korea.
  - Operated O_3, CO, NO_x, and SO_2 Analyzer and Low-Volume Particle Sampler to collect aerosol samples.

Publications

- **Kim, H.**, Walters, W. W., & Hastings, M. G. Tracking Atmospheric Nitrate Chemistry Change during COVID-19 Lockdown, *In preparation.*
- **Kim, H.**, Chai, J., & Hastings, M. G. Quantification of Isotopic Compositions of Atmospheric Ozone, Nitrogen Dioxide, and Nitrate at Downwind Site of NYC during AGES+ campaign in Summer 2023, *In preparation.*
- **Kim, H.**, Walters, W. W., & Hastings, M. G. Regulation Impact on Particulate Nitrate Precursor Emissions in the Northeastern US, *In preparation.*
- **Kim, H.**, Walters, W. W., Pye, H.O.T., Foley, K. M., & Hastings, M. G. Isotopes Constrain Nitrogen Oxides Chemistry Changes due to Emission Regulations in the Northeastern US, *Nature Geoscience, In review.*
- Walters, W. W., Pye, H.O.T., **Kim, H.**, & Hastings, M. G. (2024). Modeling the Oxygen Isotope Anomaly ($\Delta^{17}O$) of Reactive Nitrogen in the Community Multiscale Air Quality (CMAQ) Model: Insights into Nitrogen Oxide Chemistry in the Northeastern United States. *ACS EST Air*.

- **Kim, H.**, Walters, W. W., Kysela, L., & Hastings, M. G. (2023). Long-term trends in inorganic aerosol chemical composition and chemistry at an urban and rural site in the northeastern US. *Science of The Total Environment*, *904*, 166848.
- **Kim, H.**, Walters, W. W., Bekker, C., Murray, L. T., & Hastings, M. G. (2023). Nitrate chemistry in the northeast US–Part 2: Oxygen isotopes reveal differences in particulate and gas-phase formation. *Atmospheric Chemistry and Physics*, 23(7), 4203-4219.
- **Kim, H.,** Gil, J., Lee, M., Jung, J., Andrew, W. L., James, S., Lee, G., Kim, D.-S., Cho, S., Ahn, J., Hong, J., and Park, M-S. (2020), "Factors controlling surface ozone in the Seoul Metropolitan Area during the *KORUS-AQ campaign", Elementa: Science of the Anthropocene,* 8, 46.
- **Kim, H.,** Choi, W.-C., Rhee, H.-J., Suh, I., Lee, M., Blake, D. R., Kim, S., Jung, J., Lee, G., and Kim, D.-S. (2018), "*Meteorological and Chemical Factors Controlling Ozone Formation in Seoul during MAPS-Seoul 2015"*, *Aerosol and Air Quality Research*, 18, 2274-2286.

Teaching Experience

Teaching assistant, Brown University, Providence, RI, US, 2020 – present

- *Weather and Climate* 1/2022 – 5/2022
- *Environmental Science in a Changing World* 1/2024 – 5/2024

Teaching assistant, Korea University, Seoul, South Korea, 2016 – 2018

- *Earth and Environmental Science* for freshman 3/2016 – 6/2016
- *Earth and Environmental Science* 9/2016 – 12/2016
- *Atmospheric Chemistry* 3/2017 – 6/2017
- *Oceanography* 9/2017 – 12/2017

Award & Fellowships

- **IBES Graduate Research Training & Travel Awards,** Institute at Brown for Environment and Society, Brown University, 2021
- **University Scholarship**, Chonbuk National University, 2020
- **NASA Group Achievement Award,** The Korea-US Air Quality (KORUS-AQ) Airborne Earth Science Mission, 2017
- **Best Poster Presentation Award,** The 22nd Chinese Society for Environmental Sciences (CSES) Annual Meeting, October 2016
- **Best Student Award,** The Geological Society of Korea, February 2016
- **Honor Scholarship for Academic Excellence**, Department of Earth and Environmental Sciences, Chonbuk National University, 2014
- **Honor Scholarship for Academic Excellence,** Department of Earth and Environmental Sciences, Chonbuk National University, 2013

Service & Leadership

- Vice President, Korean Graduate Student Association, Brown University 1/2022 – 8/2024
- Korean teacher, Rhode Island Korean School 9/2024 – present

Presentations

ORAL PRESENTATION

- **Kim, H.,** Walters, W.W. and Hastings, M.G., Atmospheric Oxidation Chemistry Shifts Following the Clean Air Act. Hankuk University of Foreign Studies., Jan. 2025 *[invited]*
- **Kim, H.,** Walters, W.W. and Hastings, M.G., Feedbacks of Emission Regulation on Atmospheric Nitrate Formation Chemistry in the Northeastern U.S. Insight from Oxygen Isotopes. American Geophysical Union 2023 Fall Meeting in San Francisco. Dec. 2023
- **Kim, H.,** Lee, M., Jung, J., Cho, S., Russell, W. L., Lee, G., Kim, D.-S., Hong, J., Shin, H., and Ahn, J., "High Surface O_3 Episode in Seoul during KORUS-AQ Campaign*",* Korean Society for Atmospheric Environment 2018 Annual Meeting. Oct. 2018

POSTER PRESENTATIONS

- **Kim, H.,** Walters, W.W. and Hastings, M.G., Regulation Impact on Particulate Nitrate Precursor Emissions in the Northeastern US., American Geophysical Union 2024 Fall Meeting in Washington D.C., Dec. 2024
- **Kim, H.,** Chai, J., Horsford, M., and Hastings, M.G., Quantification of Isotopic Compositions of Atmospheric Ozone, Nitrogen Dioxide, and Nitrate at Downwind Site of NYC during AGES+ campaign in Summer 2023., American Geophysical Union 2024 Fall Meeting in Washington D.C., Dec. 2024
- **Kim, H.,** Walters, W.W. and Hastings, M.G., Long-term trends inorganic aerosol chemical composition and chemistry at an urban and rural site in the northeastern US. Gordon Research Conference-Atmospheric Chemistry in Maine, Aug. 2023
- **Kim, H.,** Walters, W.W. and Hastings, M.G., Long-term trends in aerosol chemical composition at an urban versus rural site in the northeastern US. American Geophysical Union 2022 Fall Meeting in Chicago., Dec. 2022
- **Kim, H.,** Walters, W.W. and Hastings, M.G., Diagnosing spatiotemporal variations of atmospheric nitrate sources and production in the northeastern U.S., American Geophysical Union 2021 Fall Meeting in New Orleans., Dec. 2021
- **Kim, H.,** Lee, M., Jung, J., Park, M., Lee, G., Cho, S., Shin, H., and Hong, J., "High Surface O_3 Episodes in Seoul under Different Meteorological Regimes during KORUS-AQ campaign*",* American Geophysical Union 2017 Fall Meeting in New Orleans., Dec. 2017
- **Kim, H.,** Lee, M., Jung, J., Cho, S., Lee, G., Park, M., Shin, H., and Hong, J., "Characteristics of High O_3 Episodes in Seoul during KORUS-AQ Campaign*",* Korean Society for Atmospheric Environment 2017 Annual Meeting., Nov. 2017
- **Kim, H.,** Lee, M., Jung, J., Park, M., Lee, G., Cho, S., Shin, H., and Hong, J., "Characteristics of High Surface Ozone Episodes under Different Meteorological Factors in Seoul during KORUS-AQ Campaign*",* Korean Meteorological Society 2017 Annual Meeting. Oct. 2017

- **Kim, H.,** Lee, M., Jung, J., Cho, S., Lee, G., Park, M., Shin, H., and Hong, J., "High O_3 Episodes in Seoul, Korea during early summer 2016*",* The 5th Integrated Land Ecosystem-Atmosphere Processes Study (ILEAPS) 2017 meeting in Oxford, UK, Sep. 2017
- **Kim, H.,** Lee, M., Cho, S., Jung, J., Lee, G., and Hong, J., "High O_3 episodes in Seoul, 2016: VOC or NO_x limited?*"*, KORUS-AQ Science Team Meeting in Jeju, Korea, Feb. 2017
- **Kim, H.,** Gil, J., Lee, M., Cho, S., and Jung, J., "Measurement of H_2O_2, PAN, and HONO in Seoul during summer, 2016*",* The 22nd Chinese Society for Environmental Sciences (CSES) Annual Meeting, Oct. 2016

Technical Skills

- **Computational & Modeling Skills**
- R, Python, and Matlab (statistical analysis and data processing)
- HYSPLIT trajectory modeling (using TrajStat software)
- IGOR pro (data visualization and analysis)
- CMAQ (Community Multiscale Air Quality) model simulation and analysis
- **Laboratory & Analytical Skills**
- Isotope Ratio Mass Spectrometry (IRMS) for nitrogen and oxygen isotope measurements
- Bacterial Denitrifier method for isotope analysis
- Ion Chromatography (IC) for anion and cation analysis in atmospheric aerosol samples
- Gas Chromatography with Flame Ionization Detector (GC-FID) for volatile organic compounds (VOCs) analysis
- High-Performance Liquid Chromatography (HPLC) for hydrogen peroxide (H_2O_2) analysis in atmospheric samples
- Wet laboratory techniques (sample preparation, extraction, filtration)

Acknowledgements

First, I would like to express my deepest gratitude to my advisor, Dr. Meredith Hastings, for her endless support and encouragement throughout the past five years. Through her guidance, I learned not only how to become a better scientist and researcher, but also how to lead and teach with empathy, patience, and purpose. During the time we spent together, she taught me–through her words, her actions, and simply by being who she is–what it means to live with integrity, curiosity, and compassion. These are lessons I will never forget and will carry with me throughout my life. I am also incredibly grateful to Dr. Wendell W. Walters, who has served as an advisor and mentor to me throughout my Ph.D. For five years, he has supported me alongside Meredith, always providing thoughtful advice, patient guidance, and kind encouragement. His passion for research and intuitive insight have had a profound influence on my development as a researcher. I deeply admire both Meredith and Wendell–as scientists, as mentors, and as people. If someone were to ask me what the most meaningful time in my life has been, I would say, without hesitation, it was the time I spent working and growing with them.

Next, I would also like to thank my committee members–Dr. Victor Tsai, Dr. Daniel Ibarra, Dr. Havala O. T. Pye, and Dr. Jung-Eun Lee–for their thoughtful feedback, guidance, and their generous commitment of time and support over the past five years. I am deeply grateful for their encouragement, insights, and willingness to be part of my committee. I would also like to thank my master's advisor, Prof. Meehye Lee, for her support and belief in me. She has continued to guide and encourage me from my master's program through my Ph.D., and I'm truly grateful for her steady encouragement over all these years.

I am especially grateful to Ruby Ho, our lab manager, whose dedication and support made this work possible. Despite the overwhelming number of samples I processed over the years, she

ensured that everything was analyzed smoothly and accurately. I truly appreciate her efforts in keeping the lab running efficiently and with care. I would also like to thank our lab mates–Jiajue Chai, Alexandra MacFarland, Grace Berg, Vivien Chen, Emily Joyce, and Dani Blum–for creating such a supportive and collaborative lab environment. It was a joy to share this journey with them.

I would like to thank my family–my father, mother, sister, and younger brother–for their love and support. Even though we've been thousands of miles apart, they have always stood by me, encouraging me every step of the way. I could not have completed this Ph.D. without their constant encouragement and belief in me, all the way from South Korea. I love you all so much. Finally, I would like to thank my friends–my friends back in Korea, my friends from the Korean Graduate Student Association (KGSA) at Brown, and friends in the Department of Earth, Environmental, and Planetary Sciences (DEEPs)–for always cheering me on, whether from near or far. Your support has meant more to me than words can express.

I am truly grateful to everyone who has been part of this journey. Thank you for taking it with me. This has been one of the most fulfilling and joyful experiences of my life.

Table of Contents

List of Figures

Chapter 1. Introduction

Chapter 2. Nitrate Chemistry in the Northeast US: Oxygen Isotopes Reveal Differences in Particulate and Gas Phase Formation

Chapter 4. Shift in Atmospheric Oxidation Chemistry Following the Clean Air Act

Chapter 5. Isotopic Evidence of Coal's Lingering Footprint in a Post-Coal Era

Chapter 6. Tracking Atmospheric Nitrate Chemistry Change during COVID-19 Lockdown

List of Tables

CHAPTER 1

Introduction

Heejeong Kim

Department of Earth, Environmental, and Planetary Sciences, Institute at Brown for Environment and Society, Brown University, Providence, RI 02912, USA

Nitrogen oxides (NO_x = NO + NO_2) and their oxidation product, nitrate (gas-phase nitric acid (HNO_3) and nitrate in particulate form (pNO_3)), are key reactive nitrogen species (N_r) in the atmosphere, with the potential to adversely influence air quality, climate, and human and ecosystem health[1–3]. NO_x plays an important role in regulating the oxidizing capacity of the atmosphere, controlling the production of atmospheric oxidants such as ozone (O_3) and hydroxyl radicals (OH)[3,4]. These oxidants are responsible for removing atmospheric trace gases and influence the lifetime of greenhouse gases such as methane (CH_4)[4]. Gaseous HNO_3 is a strong acid and highly water-soluble such that it readily dissolves in cloud droplets, contributing to acid rain[5,6]. Gaseous HNO_3 can also be partitioned into the particle phase of NO_3, a major inorganic component of fine particulate matter ($PM_{2.5}$), which has direct linkages to adverse effects on human health, visibility, and radiative forcing[5,7]. Exposure to NO_x and its secondary pollutants increases the risk of respiratory and cardiovascular diseases and threatens agricultural yields due to ozone-induced crop damage. In addition, dry and wet deposition of atmospheric nitrate disrupts nutrient balances in ecosystems and accelerates acidification, posing long-term risks to forests, soils, and aquatic environments[8–10]. Due to its widespread environmental, health, and economic impacts, governments have historically mandated monitoring and reporting of NO_x emissions to track pollution sources and implement regulatory measures to protect public and ecosystem health[11–13].

NO_x is emitted into the atmosphere from many sources, including both natural (e.g., lightning, soil nitrification/ denitrification, and wildfires) and anthropogenic (e.g., vehicle, fossil fuel combustion, industry, residences, and agriculture) origins[1]. Once emitted into the atmosphere, NO is rapidly oxidized to NO_2 by O_3 or peroxy radicals (HO_2 and RO_2) within a timescale of approximately 1–2 min. During the daytime, NO_2 is photolyzed back to NO by sunlight and net chemical production of NO_x is zero, which is known as a photostationary steady state (R1, 3, 4)[5,14],

$$NO + O_3 \rightarrow NO_2 + O_2 \quad \text{(R1)}$$

$$NO + RO_2\ (HO_2) \rightarrow NO_2 + RO\ (OH) \quad \text{(R2)}$$

$$NO_2 + h\nu \rightarrow NO + O(^3P) \quad \text{(R3)}$$

$$O(^3P) + O_2 \xrightarrow{M} O_3 \quad \text{(R4)}$$

where *M* is any non-reactive third body. These photochemical reactions involving NO_x, carbon monoxide, and volatile organic compounds (VOCs) lead to the formation of tropospheric O_3, which is harmful to human health, vegetation, and ecosystems due to its strong oxidation capacity[15,16]. The major sink for NO_x in the atmosphere is its oxidation to HNO_3. The dominant HNO_3 formation pathway during the daytime and/or warm season (i.e., high photochemistry season) is NO_2 oxidation by OH (R5):

$$NO_2 + OH \xrightarrow{M} HNO_3 \quad \text{(R5)}$$

On the other hand, NO_x photochemistry shuts down during the nighttime. Since NO and NO_2 are no longer in photochemical equilibrium and the main NO oxidant for nighttime is O_3 (R1), NO_2 cannot be converted back into NO. Therefore, the major nighttime and/or cold season (i.e., low photochemistry seasons) sink of NO_x is via:

$$NO_2 + O_3 \rightarrow NO_3 + O_2 \quad \text{(R6)}$$

$$NO_3 + NO_2 \xrightarrow{M} N_2O_5 \quad \text{(R7)}$$

$$N_2O_5 + H_2O \xrightarrow{aerosol} 2HNO_3 \quad \text{(R8)}$$

In aqueous environments (such as wet aerosol), HNO_3 dissolves and dissociates to form NO_3^-. Gaseous ammonia (NH_3) dissolves and protonates to form NH_4^+; and then NO_3^- and NH_4^+ can associate to form particulate ammonium nitrate (NH_4NO_3) or they can react with existing particles, increasing their size, a process known as aerosol condensation[5]. If NH_3 is sufficiently available in the atmosphere, sulfuric acid (H_2SO_4) and NH_3 first dissolve in an aqueous phase, where H_2SO_4 dissociates into sulfate ions (SO_4^{2-}) and protons (H^+), while NH_3 is protonated to NH_4^+ (R9–12). Subsequently, these ions associate to form ammonium sulfate ($(NH_4)_2SO_4$) due to the low saturation vapor pressure of H_2SO_4 through the reaction (R13). The excess NH_3 then reacts with HNO_3 to form NH_4NO_3 through reaction (R15). HNO_3 is partitioned into the aerosol phase based on thermodynamic equilibrium (i.e., $NH_4NO_3(s) \rightleftharpoons HNO_3(g) + NH_3(g)$) or via coarse-mode uptake onto sea salt particles or alkaline dust (i.e., $HNO_3(g) + NaCl(s) \rightarrow NaNO_3(s) + HCl(g)$; $HNO_3(g) + CaCO_3(s) \rightarrow Ca(NO_3)_2(s) + CO_2(g) + H_2O(g)$). The gas-to-particle partitioning rate of HNO_3/pNO_3 is mainly governed by NH_3 availability, temperature, RH, and aerosol pH (R14)[5,6,17,18]. The partitioning process is favorably shifted toward the particle phase under colder temperatures, higher RH, and higher particle pH. Therefore, in general, HNO_3 and pNO_3 are characterized by higher concentrations in the warm (Apr-Sep) and cold (Oct-Mar) seasons, respectively[5,19].

$$H_2SO_4(g) \rightarrow H_2SO_4(aq) \quad \text{(R9)}$$

$$NH_3(g) \rightarrow NH_3(aq) \quad \text{(R10)}$$

$$H_2SO_4(aq) \rightarrow 2H^+ + SO_4^{2-} \quad \text{(R11)}$$

$$NH_3(aq) + H^+ \rightarrow NH_4^+ \quad \text{(R12)}$$

$$H_2SO_4(g) + 2NH_3(g) \rightarrow (NH_4)_2SO_4(s) \quad \text{(R13)}$$

$HNO_3(g) \leftrightarrow H^+(aq) + NO_3^-(aq)$ (R14)

$HNO_3(g) + NH_3(g) \rightarrow NH_4NO_3(s)$ (R15)

NO_x pollution has been recognized as a major environmental concern and a serious health risk for humans and ecosystems in the US[11,20,21]. Human activities increasingly dominated inputs to the N_r budget over the past several decades. In particular, key contributors to the US NO_x budget include on-road mobile sources (39%), off-road mobile sources (15%), fossil fuel combustion from electric utilities (25%), and industrial sources (11%)[22]. In order to protect public health and the environment from air pollution, the Clean Air Act was enacted in the 1970s, leading to strict regulatory controls on NO_x emissions in the US[11]. As a result, the U.S. Environmental Protection Agency (EPA) reports that total annual NO_x emissions have significantly decreased since 2000's[22]. This reduction was primarily driven by substantial declines in emissions from electric utilities (59 %), industrial fuel combustion (39 %), and the transportation sector (45 %). Historically, coal combustion was the largest source of electricity generation for several decades of the US power system, but decreased their usage by 28 % (from 1037 million short tons to 738 million short tons) as natural gas became a more cost-effective and lower-emission alternative[22–24]. As a result of the transition from coal to natural gas for electricity generation, NO_x emissions decreased by 63% and 25 % for coal and natural gas, respectively, in the US.

The northeastern US remains an important region to monitor due to historically degraded air quality due to high levels of NO_x emissions and negative atmospheric nitrate deposition impacts on sensitive ecosystems [8,13,25,26]. The northeast US receives elevated inputs of N_r from heavily urbanized and industrialized local regions, as well as via regional transport from Midwestern and western states, leading to long-term environmental and health concerns. The eastern US contains major urban centers along the Northeast Corridor, including Washington, D.C., Philadelphia, New

York City, and Boston, significantly contributing to NO_x emissions from dense road networks and high traffic volumes[22]. Additionally, the Ohio and Pennsylvania regions, which account for 58 % of total US underground coal mine production, have historically been major sources of NO_x emissions in the eastern US[27], contributing to around 20 % of total NO_x emissions via long-range transport. Under the Clean Air Act Amendment, stringent regulations have led to significant reductions in NO_x emissions over the years in the northeastern US (Figure 1.1). Particularly, according to EPA NEI, NO_x emissions have decreased by 82% in the northeastern US from 2005 to 2015–a critical period for emission reductions [22,28–30]. However, despite significant local reductions in NO_x, the response to changes in endpoints such as O_3, $PM_{2.5,}$ and deposition has not followed our expectations. For example, pNO_3 concentrations have been found to be similar or to have increased in response to precursor emission reductions in the New England region [29–32] (Figure 1.2). This indicates that there are significant uncertainties regarding oxidation chemistries and feedbacks in response to emission regulations. Thus, understanding the relative contributions of NO_x emission sources and the oxidation processes responsible for their removal is crucial for air quality improvement.

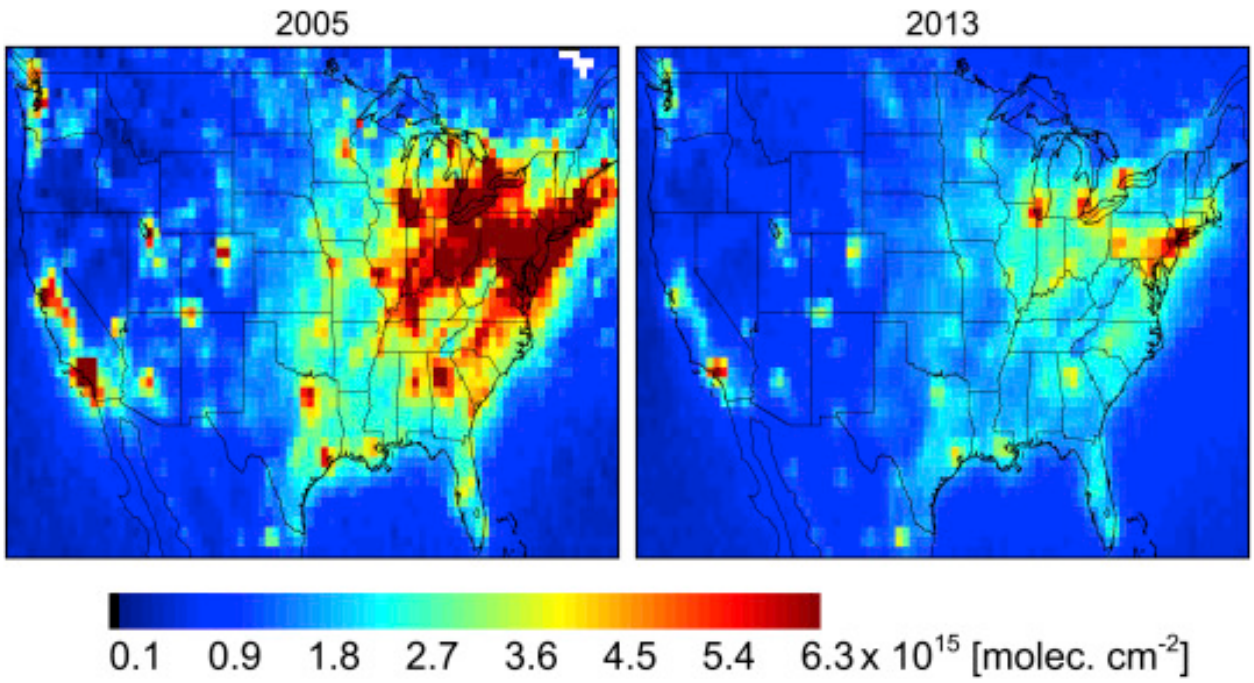

Figure 1. 1 Satellite image of annual average NO_2 in the US for 2005 and 2013. Image adapted from Lamsal et al. (2015), U.S. NO_2 trends (2005–2013): EPA Air Quality System (AQS) data versus improved observations from the Ozone Monitoring Instrument (OMI).

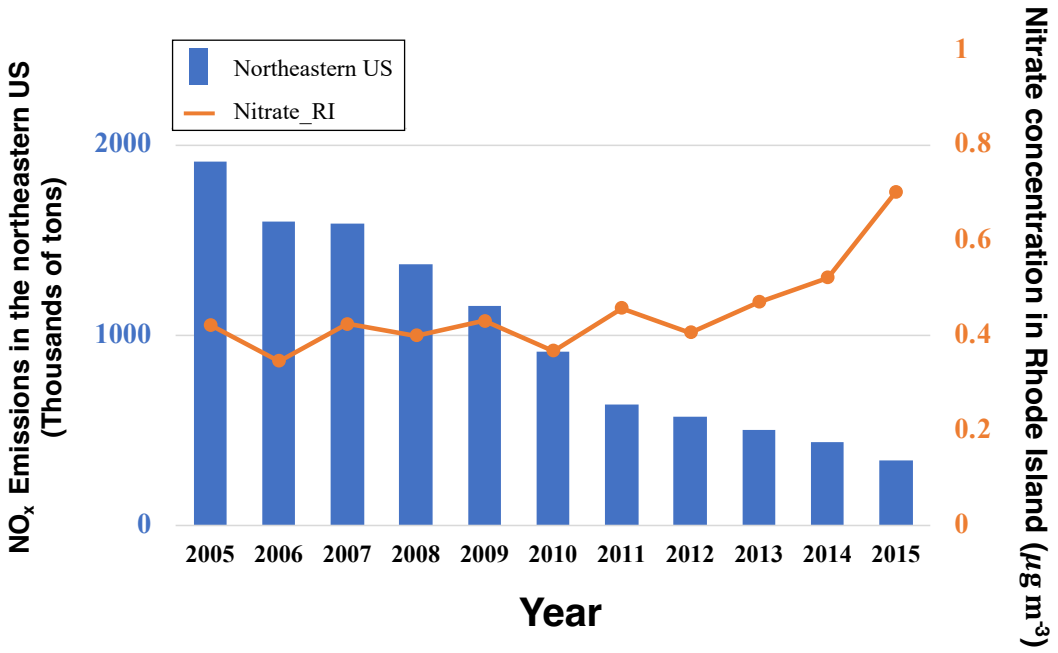

Figure 1.2. Long-term trends of NO_x emissions in the Northeastern US (CT, MA, PA, NH, NJ, NY, RI, and VT) and nitrate concentration in PM_{10}, which was collected in RI from 2005 to 2015[30].

Atmospheric chemistry and transport models are now widely used and provide essential tools for interpreting observational data, testing hypotheses about chemical reactions, and predicting future concentrations of atmospheric chemicals[33,34]. These models help understand human and natural influences on the environment and assess the impacts of emissions and chemical processes on air quality. However, accurately reproducing atmospheric compositions still remains challenging[8,31,35,36]. Atmospheric nitrate concentrations have been simulated using various chemistry models to detail spatiotemporal variabilities between precursor NO_x emissions and nitrate in the US, but models tend to underestimate or overestimate nitrate concentrations due to uncertainties in emission inventories, chemical feedbacks, and/or deposition processes. For example, the global 3D chemical transport model, GEOS-Chem, often underestimated nitrate concentration in the California area, primarily due to an underestimation of ammonia emission,

which limits ammonium nitrate formation [36]. In contrast, in the northeastern US, the model tends to overestimate nitrate concentrations [8,35]. Previous studies reveal that potential biases could be due to uncertainties in NO_x and gaseous NH_3 emission estimates, dry deposition removal rates, heterogeneous chemical production rates, and/or changing chemistry due to reductions in NO_x and sulfur dioxide emissions [29,31,35].

Stable nitrogen and oxygen isotopes of pNO_3 have been identified as a powerful observational constraint for identifying atmospheric NO_x emission sources and understanding NO_x oxidation chemistry [37–43]. The isotopic composition is expressed as δ, which is a standardized notation and quantified as δ (‰) = 1000 × ($R_{sample}/R_{reference}$ - 1). R is the ratio of the heavy isotope to the light isotope (e.g., $^{15}N/^{14}N$; $^{18}O/^{16}O$; $^{17}O/^{16}O$) in the sample and internationally recognized isotopic reference material (Nitrogen = Air N_2 and Oxygen = Vienna Standard Mean Ocean Water), respectively. The N isotopic composition ($\delta^{15}N$) of NO_x provides insight into the NO_x emission budget, as different NO_x emission sources have distinct $\delta^{15}N$ values (Figure 1.3). For example, natural gas combustion has distinctive $\delta^{15}N(NO_x)$ emission signatures near -18‰ [44], +15‰ of coal combustion [45], -32‰ of soil emissions [46], and -2‰ of vehicle emissions [47]. These source signatures are imprinted into $\delta^{15}N(NO_x)$ values and the chemical and physical processing during NO_x cycling and post-NO_2 oxidation in the atmosphere introduces isotope fractionation[43,48–50]. Therefore, $\delta^{15}N$ of pNO_3 reflects the information about precursor NO_x sources and/or NO_x oxidation chemical processing. Key isotope effects associated with nitrate formation include equilibrium isotope effects (EIEs), unidirectional kinetic isotope effects (KIEs), and photo-induced fractionation isotope effects (PHIEs) during NO_x cycling and post-NO_2 oxidation reactions[43,49,51,52]. Therefore, evaluating these effects systematically is crucial to understanding the drivers of the observed variability in $\delta^{15}N(pNO_3)$.

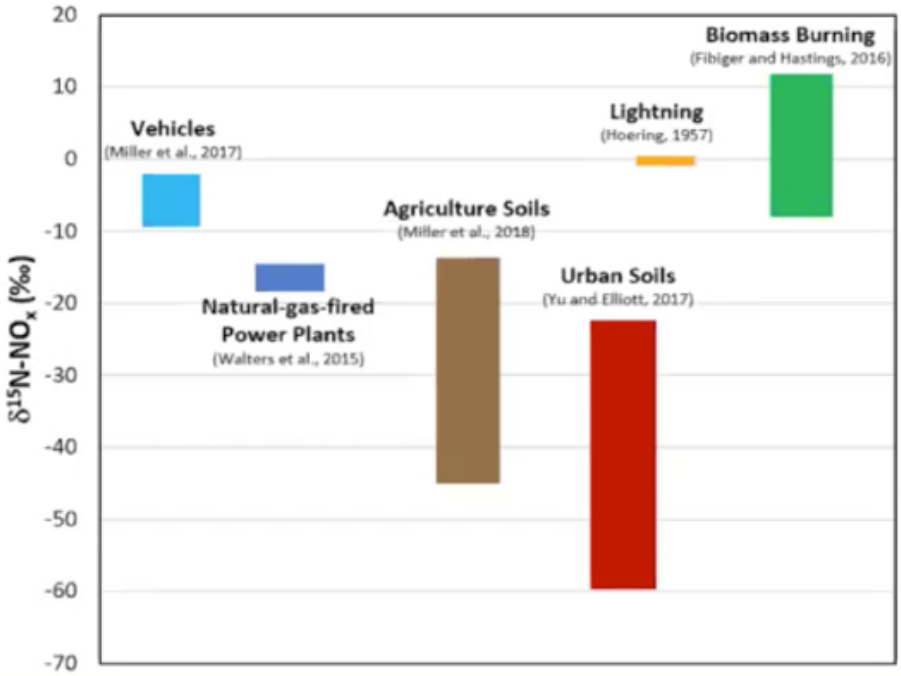

Figure 1.3. Range of $\delta^{15}N$ values for various NO_x sources. Image credit: Dr. Emily Joyce

The oxygen isotopic compositions ($\Delta^{17}O$ and $\delta^{18}O$) of NO_x are also a useful tool for tracing NO_x photochemical cycling and evaluating the changes in the daytime and nighttime oxidation chemistry involving NO_x [37,38,42,53–55]. In general, stable oxygen isotopes fractionate via a mass-dependent manner, leading to distinctive $\delta^{17}O$ and $\delta^{18}O$ signatures for the key atmospheric oxidants such as $O_2/RO_2/HO_2$, H_2O, and OH ($\delta^{17}O = 0.52 \times \delta^{18}O$; Figure 1.4). However, one notable exception is the mass-independent fractionation that occurs during O_3 formation. Fractionation of O_3 leads to an unexpected "excess" of $\delta^{17}O$ relative to $\delta^{18}O$, which is quantified and defined as $\Delta^{17}O$ ($= \delta^{17}O - 0.52 \times \delta^{18}O$) [53,56]. This effect arises because there is an intramolecular O isotope distribution with heavier isotope values (^{17}O, ^{18}O) at the terminal ends, which are preferentially transferred. Previous studies report that tropospheric O_3 has a $\Delta^{17}O$ value for bulk O_3 of ~ 26‰ and a transferrable signal of ~ 39‰, whereas the $\Delta^{17}O$ values of other oxidants such as H_2O, OH, HO_2, and RO_2 were assumed to be 0 ‰ [42,57–61]. For $\delta^{18}O$, direct observations of the $\delta^{18}O(O_3)$ vary

from 90–120‰ in the Northern Hemisphere mid-latitudes [57,58]. HO_2 and RO_2 radicals are estimated to have an O isotopic composition that reflects tropospheric O_2 (~ 23‰) [53,55]. $\delta^{18}O$ of H_2O is assumed to be -6 ‰, which is a typical mid-latitude value and represents water in the liquid phase[53]. Since direct measurements of $\delta^{18}O(OH)$ are unavailable, it is estimated based on the assumption that OH is in isotopic equilibrium with $H_2O(g)$. The equilibrium fractionation factor between OH and $H_2O(g)$ is theoretically determined as 1.0371 at 298 K, leading to an estimated $\delta^{18}O$ of OH at -43‰ [53,62]. These distinct oxygen isotopic characteristics enable us to track NO_x oxidation chemistry, providing insight into the relative contributions of different oxidation mechanisms and their variability over time and space. For example, prior experimental investigations suggest that O isotopic equilibrium is achieved between NO_x and O_3 or HO_2/RO_2 radicals during the photochemical reaction, leading to higher $\Delta^{17}O$ and $\delta^{18}O$ values of NO_2 for daytime chemistry [63,64]. In contrast, at night, NO_2 produced via primary NO directly can maintain an imprint of the oxygen source associated with the emission type (e.g., O_2 in the case of combustion), leading to lower $\Delta^{17}O$ and $\delta^{18}O$ values of NO_2. These differences in NO_2 isotopic composition are further transferred to nitrate with oxidation processes of NO_2 to pNO_3. Therefore, the $\delta^{18}O$ and $\Delta^{17}O$ of atmospheric nitrate preserve information about NO_x cycling and NO_x to nitrate oxidation process, with the dominant oxidation pathways during the process.

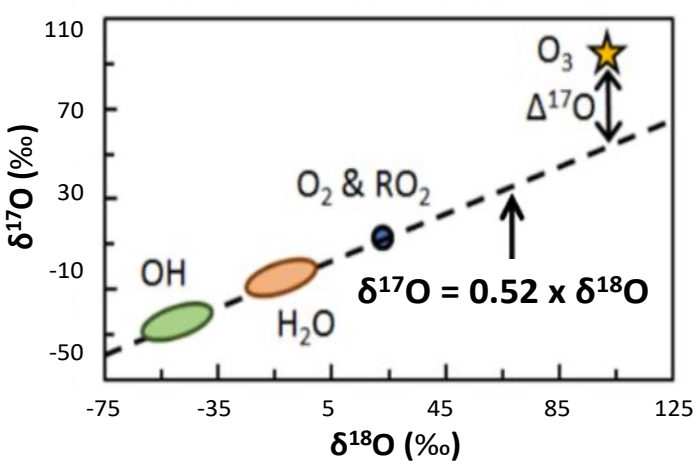

Figure 1.4. Summary of $\delta^{17}O$ and $\delta^{18}O$ values of key oxidants (OH, O_2, RO_2, and H_2O), with exceptional excess $\delta^{17}O$ of O_3 (defined as $\Delta^{17}O$). Image credit: Dr. Wendell Walters.

This thesis contains studies that aimed to comprehensively examine atmospheric nitrate chemistry in the northeastern US utilizing long-term and short-term isotope measurements along with atmospheric chemistry models. In doing so, this research has advanced the utility of stable oxygen ($\delta^{18}O$ and $\Delta^{17}O$) and nitrogen ($\delta^{15}N$) isotopic compositions of atmospheric nitrate, and their ability to quantify aspects of N_r emissions and chemistry. This research has sought to:

1. Identify NO_x emission sources to quantify each different NO_x source and assess their relative contributions to atmospheric nitrate.
2. Explore the spatiotemporal variability in NO_x oxidation chemistry and nitrate production mechanisms across urban and suburban/rural environments in the northeastern US.
3. Constrain uncertainties in atmospheric chemistry models by comparing observed isotopic compositions with predictions from the model, providing insights into model biases.
4. Evaluate the impact of long-term NO_x emission reductions on nitrate chemistry by identifying shifts in oxidation pathways over the past decade.

5. Investigate the atmospheric response to short-term emission reductions, such as the COVID-19 pandemic, to assess how abrupt changes in human activities influence nitrate formation.

To achieve these objectives, this work took advantage of a unique aerosol record. From 2005-2015, the Rhode Island Department of Management, as part of their regular monitoring to meet EPA requirements, collected particulate matter (PM_{10}; Figure 1.5) in Providence, RI (an urban site) and West Greenwich, RI (a suburban/rural site). Across the US, regular, time- and resource-intensive aerosol monitoring is conducted [28,65]. Typically, however, only 1-2 years of samples are available on the archive. When I arrived at Brown University in September 2020, I was provided access to a 10-year aerosol record for Chapters 3–5 that RI DEM had archived and had since donated to Professor Meredith Hastings' research group. This unique collection provided the basis for my research.

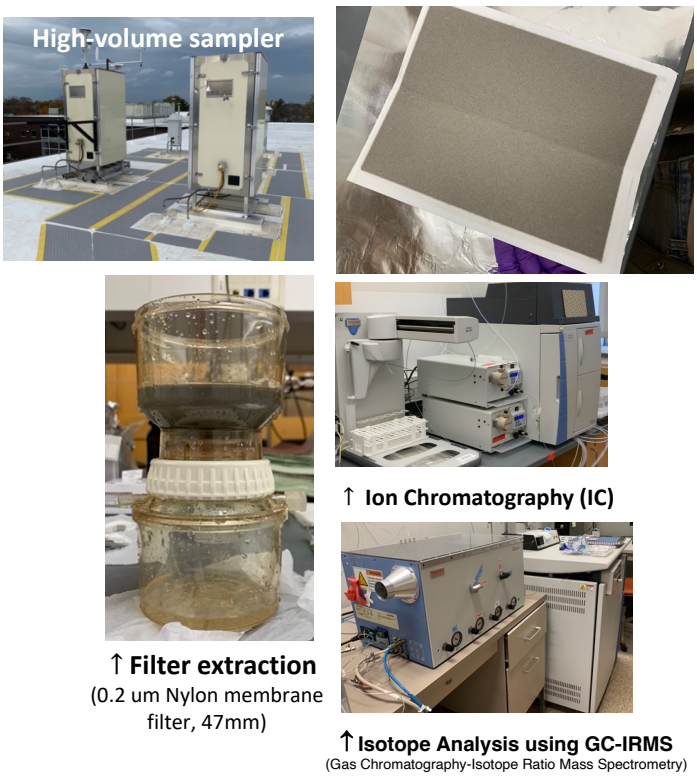

Figure 1. 5. Overview of the filter sampling protocols, including the high-vol sampler, filters after sampling, the filter extraction process, IC, and GC-IRMS.

The structure of this thesis is as follows. In Chapter 2, nitric acid (HNO_3) and particulate nitrate (pNO_3) samples collected at three different EPA Clean Air Status and Trends Network (CASTNET) sites in the northeastern US from December 2016 to 2018 were used to investigate atmospheric nitrate chemistry. Oxygen isotopic compositions of HNO_3 and pNO_3 were analyzed to explore spatial and temporal differences in HNO_3 and pNO_3 concentrations and production mechanisms in the northeastern US over 2 years. In addition, the GEOS-Chem model was used to constrain the mismatch in modeled predictions of atmospheric nitrate chemistry in the northeastern US.

In Chapters 3–5, I focus on long-term changes in nitrate chemistry using a unique record of atmospheric PM_{10} samples. Samples were collected at two different environmental sites from 2005 to 2015 in the state of Rhode Island, United States, including downtown Providence (41.82°N, − 71.41°W) and West Greenwich (41.61°N, − 71.72°W), representing an urban and suburban environment, respectively. These three chapters explore different aspects of atmospheric nitrate over the past decade in response to emission regulations. Using those samples, in Chapter 3, major inorganic components in PM_{10} were analyzed to explore the long-term changes in particle chemistry for urban and rural environments in southern New England over the decades of emissions reduction implementation. In Chapter 4, oxygen isotopic compositions ($\delta^{18}O$ and $\Delta^{17}O$) in the long-term pNO_3 record were analyzed to constrain NO_x oxidation chemistry changes over a time of large reductions in NO_x. In this study, we employed the US EPA Community Multiscale Air Quality (CMAQ) model to offer a more detailed and mechanistic understanding of the differences in nitrate formation between suburban/rural and urban areas in the northeastern US. Further, impacts on NO_x chemical lifetime were discovered that provide context for the impact of changes in NO_x oxidation chemistry in the whole northeastern US. In Chapter 5, using the same atmospheric nitrate records, nitrogen isotope composition ($\delta^{15}N$) in pNO_3 was analyzed to explore the emissions regulation impact on nitrate precursors and atmospheric chemical processing. Applying the framework developed in my prior studies, isotope fractionations during NO_x cycling and NO_x oxidation processes were quantified based on the CMAQ model output. In addition, NO_x emission estimates were constrained using a Bayesian framework-based isotope mixing model with a Markov Chain Monte Carlo (MCMC) method. These long-term records provide a new framework to test our understanding of the effectiveness of emission controls on secondary pollutants such as O_3, PM, and deposition.

Lastly, in Chapter 6, we assess the short-term response of atmospheric nitrate chemistry in response to abrupt emission reductions. The COVID-19 pandemic in 2020 led to an unprecedented reduction in human activities worldwide, resulting in a significant decrease in air pollutants and greenhouse gas emissions over a short period. Here, we analyzed nitrogen and oxygen isotopes of nitrate collected from six different environments in the northeastern US from 2019 to 2020 to understand spatiotemporal variabilities of nitrate formation during the COVID-19 lockdown.

Overall, this research provides new insights into the evolution of NO_x oxidation chemistry and nitrate formation in response to both long-term policy-driven emission reductions and short-term disruptions. Specifically, this study demonstrates that surface observation, together with the atmospheric chemistry model framework, enables isotope measurements to be utilized as quantitative constraints on NO_x emissions and atmospheric chemical processes. This work advances the understanding of atmospheric nitrate chemistry and offers a new constraint on atmospheric processes that can inform future air quality management strategies and model development.

1. References

(1) Galloway, J. N.; Dentener, F. J.; Capone, D. G.; Boyer, E. W.; Howarth, R. W.; Seitzinger, S. P.; Asner, G. P.; Cleveland, C. C.; Green, P. A.; Holland, E. A. Nitrogen Cycles: Past, Present, and Future. *Biogeochemistry* **2004**, *70* (2), 153–226.

(2) Pinder, R. W.; Davidson, E. A.; Goodale, C. L.; Greaver, T. L.; Herrick, J. D.; Liu, L. Climate Change Impacts of US Reactive Nitrogen. *Proc. Natl. Acad. Sci. U.S.A.* **2012**, *109* (20), 7671–7675. https://doi.org/10.1073/pnas.1114243109.

(3) Crutzen, P. J. The Role of NO and NO_2 in the Chemistry of the Troposphere and Stratosphere. *Annual review of earth and planetary sciences* **1979**, *7*, 443–472.

(4) Prinn, R. G. The Cleansing Capacity of the Atmosphere. *Annu. Rev. Environ. Resour.* **2003**, *28* (1), 29–57. https://doi.org/10.1146/annurev.energy.28.011503.163425.

(5) Seinfeld, J. H.; Pandis, S. N. *Atmospheric Chemistry and Physics: From Air Pollution to Climate Change*; John Wiley & Sons, 2016.

(6) Pye, H. O.; Nenes, A.; Alexander, B.; Ault, A. P.; Barth, M. C.; Clegg, S. L.; Collett Jr, J. L.; Fahey, K. M.; Hennigan, C. J.; Herrmann, H. The Acidity of Atmospheric Particles and Clouds. *Atmospheric chemistry and physics* **2020**, *20* (8), 4809–4888.

(7) Andreae, M. O.; Jones, C. D.; Cox, P. M. Strong Present-Day Aerosol Cooling Implies a Hot Future. *Nature* **2005**, *435* (7046), 1187–1190.

(8) Zhang, L.; Jacob, D. J.; Knipping, E. M.; Kumar, N.; Munger, J. W.; Carouge, C. C.; Van Donkelaar, A.; Wang, Y. X.; Chen, D. Nitrogen Deposition to the United States: Distribution, Sources, and Processes. *Atmospheric Chemistry and Physics* **2012**, *12* (10), 4539–4554.

(9) Driscoll, C. T.; Lawrence, G. B.; Bulger, A. J.; Butler, T. J.; Cronan, C. S.; Eagar, C.; Lambert, K. F.; Likens, G. E.; Stoddard, J. L.; Weathers, K. C. Acidic Deposition in the Northeastern United States: Sources and Inputs, Ecosystem Effects, and Management Strategies: The Effects of Acidic Deposition in the Northeastern United States Include the Acidification of Soil and Water, Which Stresses Terrestrial and Aquatic Biota. *BioScience* **2001**, *51* (3), 180–198.

(10) Holland, E. A.; Braswell, B. H.; Sulzman, J.; Lamarque, J.-F. NITROGEN DEPOSITION ONTO THE UNITED STATES AND WESTERN EUROPE: SYNTHESIS OF OBSERVATIONS AND MODELS. *Ecological Applications* **2005**, *15* (1), 38–57. https://doi.org/10.1890/03-5162.

(11) Https://Www.Epa.Gov/Laws-Regulations/Summary-Clean-Air-Act.

(12) Fenger, J. Air Pollution in the Last 50 Years–From Local to Global. *Atmospheric environment* **2009**, *43* (1), 13–22.

(13) Feng, J.; Chan, E.; Vet, R. Air Quality in the Eastern United States and Eastern Canada for 1990–2015: 25 Years of Change in Response to Emission Reductions of SO_2 and NO_x in the Region. *Atmospheric Chemistry and Physics* **2020**, *20* (5), 3107–3134.

(14) Leighton, P. *Photochemistry of Air Pollution*; Elsevier, 2012.

(15) Fowler, D.; Amann, M.; Anderson, R.; Ashmore, M.; Cox, P.; Depledge, M.; Derwent, D.; Grennfelt, P.; Hewitt, N.; Hov, O. *Ground-Level Ozone in the 21st Century: Future Trends, Impacts and Policy Implications*; The Royal Society, 2008.

(16) *Volatile Organic Compounds in the Atmosphere*, 1st ed.; Koppmann, R., Ed.; Wiley, 2007. https://doi.org/10.1002/9780470988657.

(17) Nenes, A.; Pandis, S. N.; Weber, R. J.; Russell, A. Aerosol pH and Liquid Water Content Determine When Particulate Matter Is Sensitive to Ammonia and Nitrate Availability. *Atmospheric Chemistry and Physics* **2020**, *20* (5), 3249–3258.
(18) Guo, H.; Sullivan, A. P.; Campuzano-Jost, P.; Schroder, J. C.; Lopez-Hilfiker, F. D.; Dibb, J. E.; Jimenez, J. L.; Thornton, J. A.; Brown, S. S.; Nenes, A. Fine Particle pH and the Partitioning of Nitric Acid during Winter in the Northeastern United States. *Journal of Geophysical Research: Atmospheres* **2016**, *121* (17), 10–355.
(19) Khoder, M. I. Atmospheric Conversion of Sulfur Dioxide to Particulate Sulfate and Nitrogen Dioxide to Particulate Nitrate and Gaseous Nitric Acid in an Urban Area. *Chemosphere* **2002**, *49* (6), 675–684.
(20) Miller, C. A.; Hidy, G.; Hales, J.; Kolb, C. E.; Werner, A. S.; Haneke, B.; Parrish, D.; Frey, H. C.; Rojas-Bracho, L.; Deslauriers, M.; Pennell, B.; Mobley, J. D. Air Emission Inventories in North America: A Critical Assessment. *Journal of the Air & Waste Management Association* **2006**, *56* (8), 1115–1129. https://doi.org/10.1080/10473289.2006.10464540.
(21) Sullivan, T. J.; Driscoll, C. T.; Beier, C. M.; Burtraw, D.; Fernandez, I. J.; Galloway, J. N.; Gay, D. A.; Goodale, C. L.; Likens, G. E.; Lovett, G. M. Air Pollution Success Stories in the United States: The Value of Long-Term Observations. *Environmental science & policy* **2018**, *84*, 69–73.
(22) Https://Www.Epa.Gov/Air-Emissions-Inventories/2020-National-Emissions-Inventory-Nei-Data.
(23) De Gouw, J. A.; Parrish, D. D.; Frost, G. J.; Trainer, M. Reduced Emissions of CO_2, NO_x, and SO_2 from U.S. Power Plants Owing to Switch from Coal to Natural Gas with Combined Cycle Technology. *Earth's Future* **2014**, *2* (2), 75–82. https://doi.org/10.1002/2013EF000196.
(24) Kim, S. -W.; Heckel, A.; McKeen, S. A.; Frost, G. J.; Hsie, E. -Y.; Trainer, M. K.; Richter, A.; Burrows, J. P.; Peckham, S. E.; Grell, G. A. Satellite-observed U.S. Power Plant NO_x Emission Reductions and Their Impact on Air Quality. *Geophysical Research Letters* **2006**, *33* (22), 2006GL027749. https://doi.org/10.1029/2006GL027749.
(25) Christiansen, A.; Mickley, L. J.; Hu, L. Constraining Long-Term NO_x Emissions over the United States and Europe Using Nitrate Wet Deposition Monitoring Networks. *Atmospheric Chemistry and Physics* **2024**, *24* (7), 4569–4589.
(26) Driscoll, C. T.; Whitall, D.; Aber, J.; Boyer, E.; Castro, M.; Cronan, C.; Goodale, C. L.; Groffman, P.; Hopkinson, C.; Lambert, K. Nitrogen Pollution in the Northeastern United States: Sources, Effects, and Management Options. *BioScience* **2003**, *53* (4), 357–374.
(27) Https://Www.Eia.Gov/Coal/Data/Browser/.
(28) CASTNET data. Https://Awsedap.Epa.Gov/Public/Single/?Appid=efa6d1bf-4cab-4e17-9e14-8046adfe9249&sheet=3495c3da-Aca4-494b-A1d8-D6d6a0571cbc&opt=currsel%2ctxmenu&bookmark=7b7e8090-0dde-43a2-B492-7e27c32f7219.
(29) Shah, V.; Jaeglé, L.; Thornton, J. A.; Lopez-Hilfiker, F. D.; Lee, B. H.; Schroder, J. C.; Campuzano-Jost, P.; Jimenez, J. L.; Guo, H.; Sullivan, A. P. Chemical Feedbacks Weaken the Wintertime Response of Particulate Sulfate and Nitrate to Emissions Reductions over the Eastern United States. *Proceedings of the National Academy of Sciences* **2018**, *115* (32), 8110–8115.
(30) Kim, H.; Walters, W. W.; Kysela, L.; Hastings, M. G. Long-Term Trends in Inorganic Aerosol Chemical Composition and Chemistry at an Urban and Rural Site in the Northeastern US. *Science of The Total Environment* **2023**, *904*, 166848.

(31) Holt, J.; Selin, N. E.; Solomon, S. Changes in Inorganic Fine Particulate Matter Sensitivities to Precursors Due to Large-Scale US Emissions Reductions. *Environmental Science & Technology* **2015**, *49* (8), 4834–4841.
(32) Jaeglé, L.; Shah, V.; Thornton, J. A.; Lopez-Hilfiker, F. D.; Lee, B. H.; McDuffie, E. E.; Fibiger, D.; Brown, S. S.; Veres, P.; Sparks, T. L. Nitrogen Oxides Emissions, Chemistry, Deposition, and Export over the Northeast United States during the WINTER Aircraft Campaign. *Journal of Geophysical Research: Atmospheres* **2018**, *123* (21), 12–368.
(33) CMAQ. Https://Www.Epa.Gov/Cmaq.
(34) Geoschem. Https://Geoschem.Github.Io.
(35) Heald, C. L.; Collett Jr, J. L.; Lee, T.; Benedict, K. B.; Schwandner, F. M.; Li, Y.; Clarisse, L.; Hurtmans, D. R.; Van Damme, M.; Clerbaux, C. Atmospheric Ammonia and Particulate Inorganic Nitrogen over the United States. *Atmospheric Chemistry and Physics* **2012**, *12* (21), 10295–10312.
(36) Walker, J. M.; Philip, S.; Martin, R. V.; Seinfeld, J. H. Simulation of Nitrate, Sulfate, and Ammonium Aerosols over the United States. *Atmospheric Chemistry and Physics* **2012**, *12* (22), 11213–11227.
(37) Hastings, M. G.; Sigman, D. M.; Lipschultz, F. Isotopic Evidence for Source Changes of Nitrate in Rain at Bermuda. *Journal of Geophysical Research: Atmospheres* **2003**, *108* (D24).
(38) Michalski, G.; Scott, Z.; Kabiling, M.; Thiemens, M. H. First Measurements and Modeling of $\Delta^{17}O$ in Atmospheric Nitrate. *Geophysical Research Letters* **2003**, *30* (16).
(39) Freyer, H. D. Seasonal Variation of $^{15}N/^{14}N$ Ratios in Atmospheric Nitrate Species. *Tellus B* **1991**, *43* (1), 30–44.
(40) Elliott, E. M.; Kendall, C.; Wankel, S. D.; Burns, D. A.; Boyer, E. W.; Harlin, K.; Bain, D. J.; Butler, T. J. Nitrogen Isotopes as Indicators of NO_x Source Contributions to Atmospheric Nitrate Deposition across the Midwestern and Northeastern United States. *Environmental Science & Technology* **2007**, *41* (22), 7661–7667.
(41) Elliott, E. M.; Kendall, C.; Boyer, E. W.; Burns, D. A.; Lear, G. G.; Golden, H. E.; Harlin, K.; Bytnerowicz, A.; Butler, T. J.; Glatz, R. Dual Nitrate Isotopes in Dry Deposition: Utility for Partitioning NO_x Source Contributions to Landscape Nitrogen Deposition. *Journal of Geophysical Research: Biogeosciences* **2009**, *114* (G4).
(42) Kim, H.; Walters, W. W.; Bekker, C.; Murray, L. T.; Hastings, M. G. Nitrate Chemistry in the Northeast US–Part 2: Oxygen Isotopes Reveal Differences in Particulate and Gas-Phase Formation. *Atmospheric Chemistry and Physics* **2023**, *23* (7), 4203–4219.
(43) Bekker, C.; Walters, W. W.; Murray, L. T.; Hastings, M. G. Nitrate Chemistry in the Northeast US–Part 1: Nitrogen Isotope Seasonality Tracks Nitrate Formation Chemistry. *Atmospheric Chemistry and Physics* **2023**, *23* (7), 4185–4201.
(44) Walters, W. W.; Tharp, B. D.; Fang, H.; Kozak, B. J.; Michalski, G. Nitrogen Isotope Composition of Thermally Produced NO_x from Various Fossil-Fuel Combustion Sources. *Environmental science & technology* **2015**, *49* (19), 11363–11371.
(45) Felix, J. D.; Elliott, E. M.; Shaw, S. L. Nitrogen Isotopic Composition of Coal-Fired Power Plant NO_x : Influence of Emission Controls and Implications for Global Emission Inventories. *Environ. Sci. Technol.* **2012**, *46* (6), 3528–3535. https://doi.org/10.1021/es203355v.
(46) Miller, D. J.; Chai, J.; Guo, F.; Dell, C. J.; Karsten, H.; Hastings, M. G. Isotopic Composition of In Situ Soil NO_x Emissions in Manure-Fertilized Cropland. *Geophysical Research Letters* **2018**, *45* (21). https://doi.org/10.1029/2018GL079619.

(47) Walters, W. W.; Goodwin, S. R.; Michalski, G. Nitrogen Stable Isotope Composition ($\delta^{15}N$) of Vehicle-Emitted NO_x. *Environmental science & technology* **2015**, *49* (4), 2278–2285.
(48) Walters, W. W.; Michalski, G. Theoretical Calculation of Nitrogen Isotope Equilibrium Exchange Fractionation Factors for Various NO_y Molecules. *Geochimica et Cosmochimica Acta* **2015**, *164*, 284–297.
(49) Li, J.; Zhang, X.; Orlando, J.; Tyndall, G.; Michalski, G. Quantifying the Nitrogen Isotope Effects during Photochemical Equilibrium between NO and NO_2: Implications for $\delta^{15}N$ in Tropospheric Reactive Nitrogen. *Atmospheric Chemistry and Physics* **2020**, *20* (16), 9805–9819.
(50) Hastings, M. G.; Casciotti, K. L.; Elliott, E. M. Stable Isotopes as Tracers of Anthropogenic Nitrogen Sources, Deposition, and Impacts. *Elements* **2013**, *9* (5), 339–344.
(51) Walters, W. W.; Simonini, D. S.; Michalski, G. Nitrogen Isotope Exchange between NO and NO_2 and Its Implications for $\delta^{15}N$ Variations in Tropospheric NO_x and Atmospheric Nitrate. *Geophysical Research Letters* **2016**, *43* (1), 440–448. https://doi.org/10.1002/2015GL066438.
(52) Miller, C. E.; Yung, Y. L. Photo-induced Isotopic Fractionation. *J. Geophys. Res.* **2000**, *105* (D23), 29039–29051. https://doi.org/10.1029/2000JD900388.
(53) Michalski, G.; Bhattacharya, S. K.; Mase, D. F. Oxygen Isotope Dynamics of Atmospheric Nitrate and Its Precursor Molecules. In *Handbook of environmental isotope geochemistry*; Springer, 2012; pp 613–635.
(54) Alexander, B.; Hastings, M. G.; Allman, D. J.; Dachs, J.; Thornton, J. A.; Kunasek, S. A. Quantifying Atmospheric Nitrate Formation Pathways Based on a Global Model of the Oxygen Isotopic Composition ($\Delta^{17}O$) of Atmospheric Nitrate. *Atmospheric Chemistry and Physics* **2009**, *9* (14), 5043–5056.
(55) Walters, W. W.; Fang, H.; Michalski, G. Summertime Diurnal Variations in the Isotopic Composition of Atmospheric Nitrogen Dioxide at a Small Midwestern United States City. *Atmospheric Environment* **2018**, *179*, 1–11.
(56) Thiemens, M. H. Mass-Independent Isotope Effects in Planetary Atmospheres and the Early Solar System. *Science* **1999**, *283* (5400), 341–345. https://doi.org/10.1126/science.283.5400.341.
(57) Vicars, W. C.; Bhattacharya, S. K.; Erbland, J.; Savarino, J. Measurement of the ^{17}O-Excess ($\Delta^{17}O$) of Tropospheric Ozone Using a Nitrite-Coated Filter. *Rapid Communications in Mass Spectrometry* **2012**, *26* (10), 1219–1231.
(58) Vicars, W. C.; Savarino, J. Quantitative Constraints on the ^{17}O-Excess ($\Delta^{17}O$) Signature of Surface Ozone: Ambient Measurements from 50°N to 50°S Using the Nitrite-Coated Filter Technique. *Geochimica et Cosmochimica Acta* **2014**, *135*, 270–287.
(59) Alexander, B.; Sherwen, T.; Holmes, C. D.; Fisher, J. A.; Chen, Q.; Evans, M. J.; Kasibhatla, P. Global Inorganic Nitrate Production Mechanisms: Comparison of a Global Model with Nitrate Isotope Observations. *Atmospheric Chemistry and Physics* **2020**, *20* (6), 3859–3877.
(60) Mauersberger, K.; Krankowsky, D.; Janssen, C. Oxygen Isotope Processes and Transfer Reactions. In *Solar System History from Isotopic Signatures of Volatile Elements*; Kallenbach, R., Encrenaz, T., Geiss, J., Mauersberger, K., Owen, T. C., Robert, F., Eds.; Space Sciences Series of ISSI; Springer Netherlands: Dordrecht, 2003; Vol. 16, pp 265–279. https://doi.org/10.1007/978-94-010-0145-8_17.

(61) Brenninkmeijer, C. A.; Janssen, C.; Kaiser, J.; Röckmann, T.; Rhee, T. S.; Assonov, S. S. Isotope Effects in the Chemistry of Atmospheric Trace Compounds. *Chemical Reviews* **2003**, *103* (12), 5125–5162.
(62) Walters, W. W.; Michalski, G. Theoretical Calculation of Oxygen Equilibrium Isotope Fractionation Factors Involving Various NOy Molecules, OH, and H_2O and Its Implications for Isotope Variations in Atmospheric Nitrate. *Geochimica et Cosmochimica Acta* **2016**, *191*, 89–101.
(63) Michalski, G.; Bhattacharya, S. K.; Girsch, G. NO_x Cycle and the Tropospheric Ozone Isotope Anomaly: An Experimental Investigation. *Atmospheric Chemistry and Physics* **2014**, *14* (10), 4935–4953.
(64) Walters, W. W.; Pye, H. O. T.; Kim, H.; Hastings, M. G. Modeling the Oxygen Isotope Anomaly ($\Delta^{17}O$) of Reactive Nitrogen in the Community Multiscale Air Quality Model: Insights into Nitrogen Oxide Chemistry in the Northeastern United States. *ACS EST Air* **2024**, acsestair.3c00056. https://doi.org/10.1021/acsestair.3c00056.
(65) Air Data.
Https://Epa.Maps.Arcgis.Com/Apps/Webappviewer/Index.Html?Id=5f239fd3e72f424f98ef3d5def547eb5&extent=-146.2334,13.1913,-46.3896,56.5319.

CHAPTER 2

Nitrate Chemistry in the Northeast US: Oxygen Isotopes Reveal Differences in Particulate and Gas Phase Formation

Heejeong Kim[1,2*], Wendell W. Walters[2], Claire Bekker[1, a], Lee T. Murray[3], and Meredith G. Hastings[1,2]

[1]Department of Earth, Environmental, and Planetary Sciences, Brown University; Providence, RI 02912, USA.

[2]Institute at Brown for Environment and Society, Brown University; Providence, RI 02912, USA

[3]Department of Earth and Environmental Sciences, University of Rochester; Rochester, NY 14627, USA

[a]Now at Environmental Health Sciences, University of California Los Angeles; Los Angeles, CA 90095

Published in *Atmospheric Chemistry and Physics* (2023),

doi: 10.5194/acp-23-4203-2023

Abstract

The northeastern US represents a mostly urban corridor impacted by high population and fossil-fuel combustion emission density. This has led to historically degraded air quality and acid rain that has been a focus of regulatory-driven emissions reductions. Detailing the chemistry of atmospheric nitrate formation is critical for improving the model representation of atmospheric chemistry and air quality. The oxygen isotopic composition of atmospheric nitrate are useful indicators in tracking nitrate formation pathways. Here, we measured oxygen isotope deltas ($\Delta(^{17}O)$ and $\delta(^{18}O)$) for nitric acid (HNO_3) and particulate nitrate (pNO_3) from three US EPA Clean Air Status and Trends Network (CASTNET) sites in the northeastern US from December 2016 to 2018. The $\Delta(^{17}O, HNO_3)$ and $\delta(^{18}O, HNO_3)$ values ranged from 12.9 ‰ to 30.9 ‰ and from 46.9 ‰ to 82.1 ‰, and the $\Delta(^{17}O, pNO_3)$ and $\delta(^{18}O, pNO_3)$ ranged from 16.6 ‰ to 33.7 ‰ and from 43.6 ‰ to 85.3 ‰, respectively. There was distinct seasonality of $\delta(^{18}O)$ and $\Delta(^{17}O)$ with higher values observed during winter compared to summer, suggesting a shift in O_3 to HO_x radical chemistry, as expected. Unexpectedly, there was a statistical difference in $\Delta(^{17}O)$ between HNO_3 and pNO_3, with higher values observed for pNO_3 (27.1±3.8) ‰ relative to HNO_3 (22.7±3.6) ‰, and significant differences in the relationship between $\delta(^{18}O)$ and $\Delta(^{17}O)$. This difference suggests atmospheric nitrate phase-dependent oxidation chemistry that is not predicted in models. Based on the output from GEOS-Chem, and both the $\delta(^{18}O)$ and $\Delta(^{17}O)$ observations, we quantify the production pathways of atmospheric nitrate. The model significantly overestimated the heterogeneous N_2O_5 hydrolysis production for both HNO_3 and pNO_3, a finding consistent with observed seasonal changes in $\delta(^{18}O)$ and $\Delta(^{17}O)$ of HNO_3 and pNO_3, though large uncertainties remain in the quantitative transfer of $\delta(^{18}O)$ from major atmospheric oxidants. This comparison provides

important insight into the role of oxidation chemistry in reconciling a commonly observed positive bias for modeled atmospheric nitrate concentrations in the northeastern US.

1. Introduction

Nitrogen oxides ($NO_x = NO + NO_2$) in the atmosphere have an important impact on air quality and human and ecosystem health (Galloway et al., 2004). NO_x plays an important role in influencing the oxidizing efficiency of the atmosphere, including the production of ozone (O_3), and leads to the formation of atmospheric nitrate (gas phase nitric acid (HNO_3) and nitrate in particulate form (pNO_3)) (Crutzen et al., 1979). HNO_3 and pNO_3 are, in turn, important contributors to dry and wet N deposition. Nitrate is a key component of particulate matter ($PM_{2.5}$), which has direct adverse effects on human respiratory and climate change, and the deposition of N to ecosystems can contribute to soil acidification and eutrophication (Camargo and Alonso, 2006; Schlesinger, 2007; Tai et al., 2010). Thus, changes in the chemistry and chemical feedbacks associated with NO_x have important implications for predicting air quality improvements and climatic responses.

The US Environmental Protection Agency (EPA) reported that NO_x emissions have decreased by 36 % in the United States from 2007 to 2015 due to effective regulations in response to the Clean Air Act and its Amendments (US EPA, 2017; CASTNET, 2019; NEI, 2017; Shah et al., 2018). However, atmospheric pNO_3 concentrations have responded sub-linearly to the dramatic NO_x emission reductions, with only a 7.8 % pNO_3 decrease over the same period in the northeastern US. Uncertainties in our understanding between NO_x reductions and the production of atmospheric nitrate challenge our ability to make effective reductions in reactive nitrogen concentrations. Major factors influencing atmospheric nitrate production include oxidant

availability, heterogeneous chemistry, gas-to-particle partitioning, and potential aerosol nitrate photolysis (Jaeglé et al., 2018; Shah et al., 2018; Kasibhatla et al., 2018).

Atmospheric nitrate concentrations have been simulated using various chemistry models to detail spatiotemporal variabilities between precursor NO_x emissions and nitrate in the US, with somewhat limited success (Walker et al., 2012; Zhang et al., 2012). In particular, the concentrations of nitrate observed in the northeastern US tend to be overestimated in models (e.g., Heald et al., 2012; Zhang et al., 2012), which is an important region to monitor due to its high population density, transport patterns and the tendency for poor air quality (Sickles and Shadwick, 2015). Modeling studies suggest that biases revealed by comparison with observations could be due to uncertainties in NO_x and gaseous ammonia (NH_3) emission estimates, dry deposition removal rates, heterogeneous chemical production rates, and changing chemistry due to reductions in NO_x and sulfur dioxide emissions (Heald et al., 2012; Holt et al., 2015; Shah et al., 2018).

The nitrate oxygen isotope deltas ($\Delta(^{17}O)$ and $\delta(^{18}O)$) have proven to provide observational constraints on the oxidation pathways that are responsible for the formation of atmospheric nitrate (Hastings et al., 2003; Michalski et al., 2003; Alexander et al., 2009). The isotopic composition is expressed as δ, which is a standardized notation and quantified as $\delta = (R_{sample}/R_{reference} - 1)$. R is the ratio of the heavy isotope to the light isotope (e.g., $^{18}O/^{16}O$; $^{17}O/^{16}O$) in the sample and internationally recognized isotopic reference material (Vienna Standard Mean Ocean Water), respectively. Several studies have suggested that the distinctive ($\Delta(^{17}O) = \delta(^{17}O) - 0.52 \times \delta(^{18}O)$) and $\delta(^{18}O)$ signatures of atmospheric oxidants such as O_3, $O_2/RO_2/HO_2$, H_2O and OH are incorporated into nitrate, tracking the oxidation chemistry of NO_x (Hastings et al., 2003; Michalski et al., 2003; Savarino et al., 2007). Traditionally, the influence of O_3 incorporation in nitrate has been quantitively tracked using only $\Delta(^{17}O)$, because of the unique mass-independent fractionation

that results in O_3 carrying excess $\delta(^{17}O)$, yielding a transferrable $\Delta(^{17}O)$ = (39±2) ‰ (Thiemens, 2006; Vicars and Savarino, 2014). However, all other atmospheric oxidants contain expected mass-dependent signatures such that all have $\Delta(^{17}O)$ value of approximately 0 ‰. The $\delta(^{18}O)$ of atmospheric oxidants could provide further insights into nitrate production mechanisms, especially in cases where oxidants other than O_3 are important, since it is distinctive for each oxidant (e.g., $\delta(^{18}O, O_3)$ = (126.3±12) ‰, $\delta(^{18}O, O_2)$ = 23 ‰, $\delta(^{18}O, OH)$ = -43 ‰ (Michalski et al., 2012; Vicars and Savarino, 2014)).

The northeastern US remains an important region to monitor due to historically degraded air quality by NO_x emissions and negative atmospheric nitrate deposition impacts on sensitive ecosystems. Changes in oxidation chemistry and chemical feedbacks associated with nitrate production and deposition have important implications for predicting air quality improvements and informing policy recommendations. In this study, using the Clean Air Status and Trends Network (CASTNET) samples, we explored spatiotemporal differences in HNO_3 and pNO_3 concentrations and production mechanisms in the northeastern US over two years. Based on these observations, we aimed to better constrain the mismatch in modeled predictions of atmospheric nitrate chemistry in the northeastern US. This is the first study to quantitatively evaluate the triple oxygen isotope composition from observations and model simulations in the northeastern US. The comparison with the combination of $\Delta(^{17}O)$ and $\delta(^{18}O)$ values, and both gaseous and particle phases of nitrate, provide a significant advance in our ability to probe the representation of oxidation chemistry in atmospheric chemistry models.

2. Methods

2.1 CASTNET Samples

Atmospheric nitrate samples were collected by the US EPA at several locations of Clean Air Status and Trends Network (CASTNET) sites in the northeastern US (Figure 2.1). Three CASTNET sites were selected: Abington, CT (ABT147, 41.84° N, -72.01° W), Connecticut Hill, NY (CTH110, 42.40° N, -76.65° W), Woodstock, NH (WST109, 43.94° N, -71.70° W). The samples were collected weekly from December 23, 2016, to December 28, 2018, using a three-stage filter pack system. Based on EPA protocols, pNO_3 was collected using a Teflon filter in the first stage of the filter pack, and gaseous HNO_3 was collected using a Nylon filter in the second stage of the filter pack. We note that due to the semi-volatile characteristic of ammonium nitrate, some pNO_3 might volatilize as HNO_3 and collect downstream of the filter pack leading to negative biases for pNO_3 and positive biases for HNO_3 collection (Hering and Cass, 1999; Ashbaugh and Eldred, 2004).

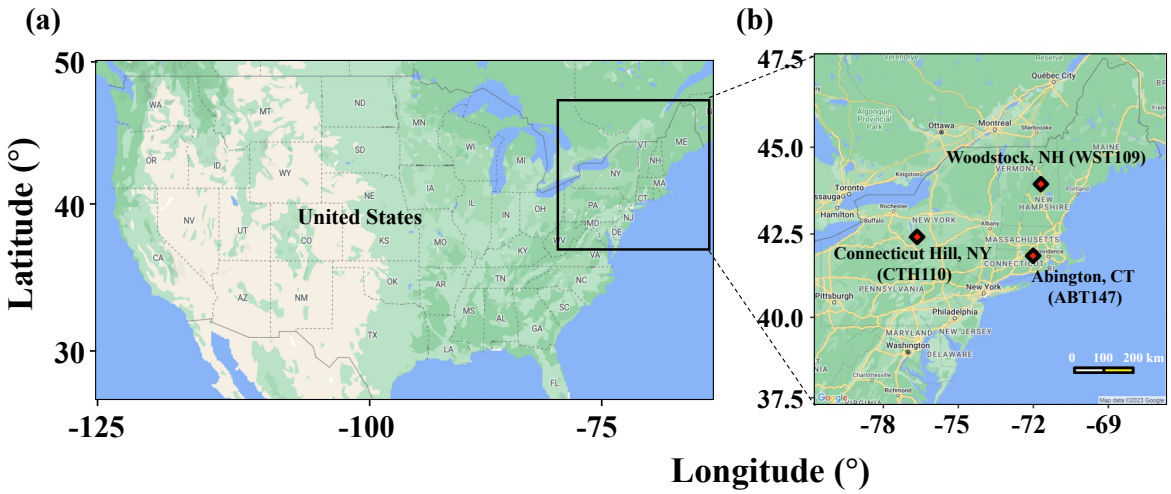

Figure 2.1. Map of the United States (a) and selected CASTNET sites (b) for this study in the northeastern US. Major cities (urban areas), transportation routes, and CASTNET sites are also indicated in (b). The image was created using Google Earth (©2023 Google).

2.2 Concentration and Isotope Analyses

Filters were extracted and measured for nitrate concentration using Ion Chromatography and then stored in the CASTNET laboratory at room temperature for up to two years. Extracted samples were shipped to Brown University in the summer of 2020. Nitrate concentrations were measured at Brown University to check for stability of nitrate using standard colorimetric methods (i.e., US EPA Method 353.2) on an automated discrete UV-Vis Analyzer (SmartChem Westco Scientific Instruments, Inc.). The limit of detection was 0.1 and 0.3 μM for nitrite and nitrate, respectively, and the pooled standard deviation of replicate quality control standards was better than 3 %. Overall, strong positive correlations were found between measured concentrations at Brown and reported CASTNET data for both HNO_3 ($y = 0.99x - 0.08$ ($R^2 = 0.99$); $p < 0.05$) and pNO_3 ($y = 1.04x + 0.09$ ($R^2 = 0.99$); $p < 0.05$) (Figure 2.2); we, therefore, consider the samples representative of their original concentrations.

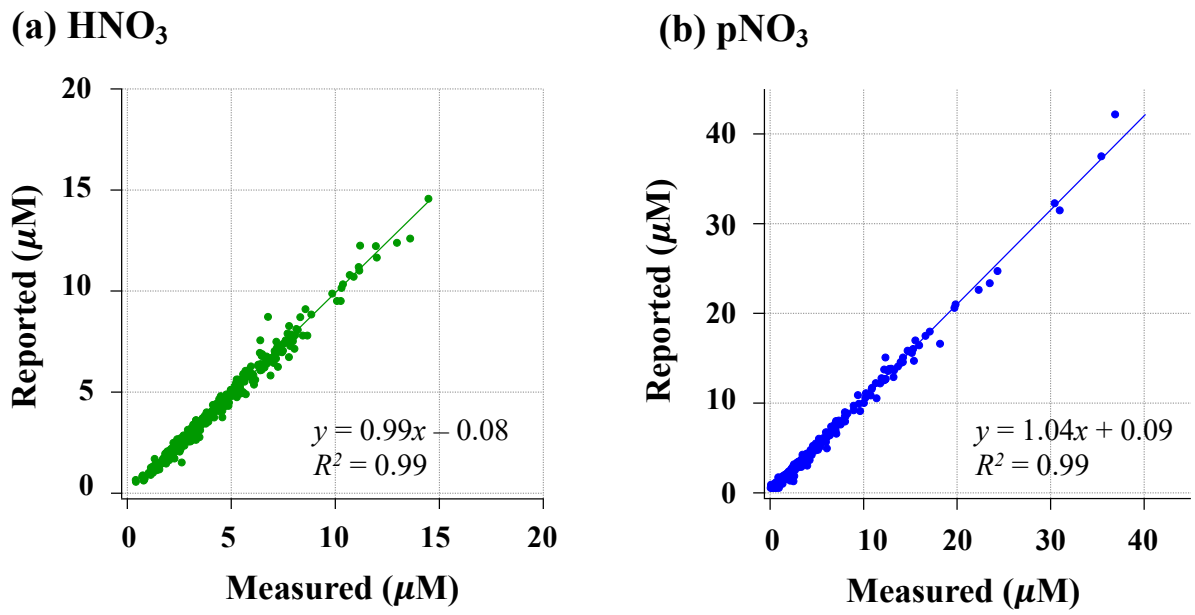

Figure 2.2. Relationship of HNO_3 (a) and pNO_3 (b) filter extract concentrations reported by CASTNET and re-measured at Brown University.

The samples were collected once a week, and equal volumes of filter extract were combined for isotope analysis to produce monthly aggregates for HNO_3 and pNO_3, respectively. Oxygen ($\delta(^{18}O)$ and $\Delta(^{17}O)$) stable isotopic compositions in HNO_3 and pNO_3 were analyzed utilizing the bacterial denitrifier method at Brown University (Sigman et al., 2001; Casciotti et al., 2002; Kaiser et al., 2007). Briefly, samples were injected into a buffer solution containing *P. aureofaciens,* which lack the nitrous oxide (N_2O) reductase enzyme, and sample nitrate was quantitatively reduced to N_2O. For $\delta(^{18}O)$ analysis, the generated N_2O is injected into a Thermo-Finnegan Delta V Plus isotope ratio mass spectrometry (IRMS) with a modified Gas Bench system after flowing through an automated extraction and purification system. Determination of $\delta(^{18}O)$ in N_2O was conducted at an *m/z* of 44, 45, and 46 and corrected using internationally recognized isotopic reference materials that included IAEA-NO_3 (25.6 ‰), USGS34 (-27.9 ‰), and USGS35 (57.5 ‰). The $\Delta(^{17}O)$ was determined in a separate analysis. The bacteria-generated N_2O was decomposed to N_2

and O_2 in a gold furnace heated to 770 ºC and analyzed at *m/z* 32, 33, and 34 to determine $^{17}O/^{16}O$ and $^{18}O/^{16}O$ ratios of the evolved O_2. The 33/32 and 34/32 mass ratios were corrected using isotopic reference materials, USGS34 (-0.29 ‰) and USGS35 (21.6 ‰), and then $\Delta(^{17}O)$ was determined from $\Delta(^{17}O) = \delta(^{17}O) - 0.52 \times \delta(^{18}O)$. Due to sample mass limitations, some samples were only analyzed for $\delta(^{18}O)$. The number of samples that were not measured for $\Delta(^{17}O)$ was 1 HNO_3 sample from CTH110, 2 HNO_3 samples from ABT147, 5 pNO_3 samples from CTH110, and 16 pNO_3 samples from WST109. The overall pooled standard deviations of isotopic reference materials and sample numbers were as followed: USGS34 ($\sigma(\delta(^{18}O))$ = 0.5 ‰ (n = 21); $\sigma(\Delta(^{17}O))$ = 1 ‰ (n = 26)); USGS35 ($\sigma(\delta(^{18}O))$ = 0.4 ‰ (n = 27); $\sigma(\Delta(^{17}O))$ = 2 ‰ (n = 26)), and IAEA-N3 ($\sigma(\delta(^{18}O))$ = 0.3 ‰ (n = 23)).

2.3 GEOS-Chem Modeling

The GEOS-Chem global model of atmospheric chemistry (Bey et al., 2001; Walker et al., 2012; 2019) was utilized to track the production of NO_2 and HNO_3 at the CASTNET sites and further to model the oxygen isotope deltas (e.g., $\delta(^{18}O)$ and $\Delta(^{17}O)$) following a previous framework (Alexander et al., 2020). Following this framework, oxidation chemistry is tagged only for HNO_3 production and is assumed to be the same for pNO_3. We use version 13.2.1 (doi:10.5281/zenodo.5500717) of the model driven by GEOS5-FP assimilated meteorology from the NASA Global Modeling and Assimilation Office (GMAO). A nested grid (0.25° latitude × 0.3125° longitude horizontal resolution; ~25 km) simulation was conducted over the northeastern United States (97°-60° W; 35°-60º N) in 2017 and 2018. Boundary conditions were from global simulations performed at 4° latitude × 5° longitude horizontal resolution for the same years after a one-year initialization. Gas- and aerosol-phase chemistry was simulated using the default "fullchem" mechanism (Bates and Jacob, 2019; Wang et al., 2021). Inorganic gas and aerosol

partitioning were conducted using version 2.2 of the ISORROPIA II thermodynamic equilibrium model (Fountoukis and Nenes, 2007).

All default anthropogenic emissions were applied, which is primarily version 2.0 of the Community Emissions Data System (Hoesly et al., 2018) as implemented by McDuffie et al. (2020). Natural emissions respond to local meteorology and include biogenic VOCs from terrestrial plants and the ocean (Millet et al., 2010; Guenther et al., 2012; Hu et al., 2015; Breider et al., 2017), NO_x from lightning and soil microbial activity (Murray et al., 2012; Hudman et al., 2012), mineral dust (Ridley et al., 2012), and sea salt (Jaeglé et al., 2011; Huang and Jaeglé, 2017). Biomass burning emissions were monthly means from version 4.1s of the Global Fire Emissions Database (GFED4.1s; van der Werf et al., 2017). Wet deposition for water-soluble aerosols is described by Liu et al. (2001) and by Amos et al. (2012) for gases. Dry deposition is based on the resistance-in-series scheme of Wesely (1989). Diagnostics were implemented to archive the total production and loss pathways of NO_y, NO_x, NO_2, $RONO_2$, HNO_3 and pNO_3, including the net flux of mass between HNO_3 and pNO_3 in ISOROPPIA II. We evaluated model performance for simulating concentrations and isotope deltas ($\delta(^{18}O)$ and $\Delta(^{17}O)$) using the Normalized Mean Bias (B) metric (Eq.1):

$$B = (\sum (\bar{Q}_m - \bar{Q}_o) / \sum \bar{Q}_o) \quad \text{(Eq.1)}$$

where $\bar{Q}_m$ = modeled quantities and $\bar{Q}_o$ = observed quantities.

2.4 $\delta(^{18}O)$ and $\Delta(^{17}O)$ Calculations Based on Model Outputs

The oxygen isotope deltas ($\delta(^{18}O)$ and $\Delta(^{17}O)$) of nitrate were calculated based on oxygen isotope mass-balance using production rate outputs from the GEOS-Chem global 3-D model and compared with our observations. Expected $\delta(^{18}O)$ and $\Delta(^{17}O)$ ranges resulting from nitrate

production pathways have been previously described and calculated using oxygen mass-balance (Alexander et al., 2009, 2020; Michalski et al., 2003; Morin et al., 2011; Carter et al., 2021). Briefly, the $\delta(^{18}O)$ and $\Delta(^{17}O)$ of nitrate are determined by both NO_x photochemical cycling and nitrate formation reactions (Alexander et al., 2009; Walters et al., 2018). During NO_x photochemical cycling, the oxygen isotopic compositions of NO_x are determined by the relative production rates of NO_2 via reaction of NO with O_3, peroxy and hydroperoxyl radicals, and halogen oxides (XO; BrO, ClO). The proportional contribution of O_3 during NO oxidation is denoted as A and is calculated using

$$A = (k(O_3+NO)\,[O_3] + k(XO+NO)[XO])/(k(O_3+NO)[O_3] + k(XO+NO)[XO] + k(HO_2+NO)[HO_2] + k(RO_2+NO)[RO_2]) \quad \text{(Eq. 2)}$$

where k is the respective rate constant for NO oxidation via O_3, XO, HO_2, and RO_2. The $\Delta(^{17}O)$ value of the terminal oxygen atom in O_3 (O_3^*) is assumed to be (39±2) ‰ based on observations, while all other oxidants are assumed to be 0 ‰ (Vicars et al., 2012; Vicars and Savarino, 2014; Alexander et al., 2020). $\delta(^{18}O)$ and $\Delta(^{17}O)$ values of nitrate from each production pathway were then determined using O mass-balance based on the O transfer from varying oxidants involved in its formation (Table 2.1).

The GEOS-Chem global model has been previously used to quantify nitrate production pathways based on $\Delta(^{17}O)$ (Alexander et al., 2009, 2020), but this has not been done for $\delta(^{18}O)$. Using a similar framework as for $\Delta(^{17}O)$, we expect that $\delta(^{18}O)$ of NO_2 reflects isotopic signatures of both O_3 and O_2, as it has been assumed that the O isotopic composition of RO_2 and HO_2 is equal to O_2 (Michalski et al, 2012; Walters et al., 2018). Accordingly, the values of $\delta(^{18}O, NO_2)$ can be predicted by the proportional contribution of O_3 and both HO_2 and RO_2 during NO_x cycling with their distinct $\delta(^{18}O)$ values of O_3 and O_2 (Eq. 3; Table 2.1).

$$\delta(^{18}O, NO_2) = A(\delta(^{18}O, O_3*)) + (1\text{-}A)(\delta(^{18}O, O_2)) \quad \text{(Eq.3)}$$

Table 2.1. Equations for $\delta(^{18}O)$ and $\Delta(^{17}O)$ calculations by different nitrate formation pathways.

Gas-phase reactions	$\boldsymbol{\Delta^{17}O(tNO_3)}$	$\boldsymbol{\delta^{18}O(tNO_3)}$
NO_2 + OH	$\frac{2}{3}A\Delta^{17}O(O_3*)$	$\frac{2}{3}\delta^{18}O(NO_2) + \frac{1}{3}\delta^{18}O(OH)$
NO_3 + Hydrocarbons	$(\frac{2}{3}A+\frac{1}{3})\Delta^{17}O(O_3*)$	$\frac{2}{3}\delta^{18}O(NO_2) + \frac{1}{3}\delta^{18}O(O_3*)$
Heterogeneous reactions		
N_2O_5 hydrolysis (water + Cl^-)	$(\frac{2}{3}A+\frac{1}{6})\Delta^{17}O(O_3*)$	$\frac{4}{6}\delta^{18}O(NO_2) + \frac{1}{6}\delta^{18}O(O_3*) + \frac{1}{6}\delta^{18}O(H_2O)$
NO_3 hydrolysis	$(\frac{2}{3}A+\frac{1}{3})\Delta^{17}O(O_3*)$	$\frac{2}{3}\delta^{18}O(NO_2) + \frac{1}{3}\delta^{18}O(O_3*)$
NO_2 hydrolysis	$(\frac{2}{3}A+\frac{1}{3})\Delta^{17}O(O_3*)$	$\frac{2}{3}\delta^{18}O(NO_2) + \frac{1}{3}\delta^{18}O(H_2O)$
$RONO_2$ hydrolysis	$\frac{1}{3}A\Delta^{17}O(O_3*)$	$\frac{2}{3}\delta^{18}O(NO_2) + \frac{1}{3}\delta^{18}O(NO_2)$
XNO_3 hydrolysis (X = Br + Cl + I)	$(\frac{2}{3}A+\frac{1}{3})\Delta^{17}O(O_3*)$	$\frac{2}{3}\delta^{18}O(NO_2) + \frac{1}{3}\delta^{18}O(O_3*)$

The $\delta(^{18}O)$ values of O_3 and O_2 are adopted from previous studies that determined $\delta(^{18}O, O_3^*)$ and $\delta(^{18}O, O_2)$ as 126.3 ‰ and 23 ‰ (Vicars and Savarino, 2014; Kroopnick and Craig, 1972, respectively). For the calculation of $\delta(^{18}O)$ of nitrate, the value of $\delta(^{18}O)$ of $H_2O(l)$ is assumed to be -6 ‰, which is a typical mid-latitude value and represents water in the liquid phase incorporated into nitrate formation associated with heterogeneous reactions by N_2O_5 or NO_2 hydrolysis (Michalski et al, 2012). The $\delta(^{18}O)$ value of OH can be dependent on both O_3 and $H_2O(g)$, as well as environmental conditions since oxygen in OH can exchange with $H_2O(g)$ (Dubey et al. 1997). Fractionation factors associated with the O transfer into NO_y products are unknown and therefore were not considered. The $\delta(^{18}O)$ of $H_2O(g)$ was estimated based on the equilibrium between $H_2O(l)$ and $H_2O(g)$ with a temperature-dependent fractionation factor (1.0094 at 298K); it is assumed that OH and $H_2O(g)$ exist in isotopic equilibrium, which has a theoretically determined fractionation factor (1.0371 at 298K) and leads to an estimate of $\delta(^{18}O, OH)$ of -43 ‰ (Michalski et al, 2012; Walters and Michalski, 2016). We note that the typical annual temperature for the northeast US is approximately 287 K, yielding a $\delta(^{18}O, OH)$ of -45 ‰; for comparison purposes with prior publications, we utilize -43 ‰, which makes little difference in the quantitative results below. In the final step, $\delta(^{18}O)$ or $\Delta(^{17}O)$ of total atmospheric nitrate were calculated based on the monthly-averaged production rates from GEOS-Chem and the seven major reactions that produce nitrate in the model (Table 2.1) to compare with observations.

3. Results and Discussion

3.1 Spatiotemporal Variations of Atmospheric Nitrate Concentration

Figure 2.3 shows the monthly averaged spatiotemporal variations of HNO_3 and pNO_3 mass concentration (denoted as γ). The observed (o) HNO_3 concentrations ($\gamma_o(HNO_3)$) ranged from 0.11

μg m^{-3} to 0.88 μg m^{-3}, with a mean value of 0.46 μg m^{-3} across the three CASTNET sites. The observed pNO_3 concentrations ($\gamma_o(pNO_3)$) ranged from 0.04 μg m^{-3} to 2.01 μg m^{-3}, with a mean value of 0.50 μg m^{-3}, and showed clear seasonality at all three sites with averaged higher values (0.75±0.52) μg m^{-3} in the cold season (October to March) and lower values (0.25±0.17) μg m^{-3} in the warm season (April to September), which were significantly different ($p < 0.01$). On the other hand, $\gamma_o(HNO_3)$ was seasonally invariable with (0.42±0.17) μg m^{-3} for cold season and (0.50±0.24) μg m^{-3} for warm season that was not statistically different ($p > 0.05$). Averaged $\gamma_o(HNO_3)$ was generally lower than pNO_3 across the sites, but the difference was statistically insignificant ($p > 0.05$). Both $\gamma_o(HNO_3)$ and $\gamma_o(pNO_3)$ indicated spatial variability with higher values at ABT147 and CTH110 than the WST109 site. The mean annual $\gamma_o(HNO_3)$ and $\gamma_o(pNO_3)$ were (0.61±0.15) μg m^{-3} and (0.66±0.34) μg m^{-3} at ABT147, (0.55±0.13) μg m^{-3} and (0.68±0.58) μg m^{-3} at CTH110, and (0.22±0.06) μg m^{-3} and (0.17±0.13) μg m^{-3} at WST109, respectively.

The modeled (m) HNO_3 concentrations ($\gamma_m(HNO_3)$) ranged from 0.20 μg m^{-3} to 2.36 μg m^{-3}, with a mean value of 0.82 μg m^{-3} and modeled pNO_3 concentrations ($\gamma_m(pNO_3)$) ranged from 0.20 μg m^{-3} to 5.27 μg m^{-3}, with a mean value of 1.89 μg m^{-3}. Contrary to our observed data, no consistent spatial variability was observed for $\gamma_m(HNO_3)$ and $\gamma_m(pNO_3)$. The mean $\gamma_m(HNO_3)$ and $\gamma_m(pNO_3)$ were (1.09±0.62) μg m^{-3} and (1.73±1.13) μg m^{-3} at ABT147, (0.74±0.46) μg m^{-3} and (2.42±1.71) μg m^{-3} at CTH110, and (0.64±0.22) μg m^{-3} and (1.52±1.24) μg m^{-3} at WST109, respectively. However, there are significant seasonal model biases for the HNO_3 and pNO_3. The model significantly overestimates pNO_3 during the winter (3-9 times) and overestimates HNO_3 during the summer (2-3 times).

As stated above, there can be negative biases for pNO_3 and positive biases for HNO_3 collection, but these should be reduced by comparing the model to total atmospheric nitrate ($tNO_3 = HNO_3 + pNO_3$). Still, the simulated tNO_3 concentration ($\gamma_m(tNO_3)$) with GEOS-Chem is notably overestimated relative to observations ($\gamma_o(tNO_3)$; B = 182 %; Figure 2.3). While the simulated pNO_3 well reproduce the observed seasonality (high concentrations in the cold season and vice versa), it highly overestimated the concentrations for most of the year (B = 276 %; Figure 2.3). The simulated HNO_3 did not capture the observed relative lack of seasonality, instead showing clear seasonality with generally high concentrations in the warm season and low in the cold season. The lack of agreement between GEOS-Chem and nitrate observations is consistent with previously reported results in other studies (Heald et al., 2012; Zhang et al., 2012; Walker et al., 2012). Uncertainties in N_2O_5 hydrolysis rate, emission estimates, or dry and wet deposition removal rates have been suggested as possible causes for predicted nitrate biases. For instance, Luo et al., 2019; 2020 reported dramatic improvement of nitric acid and nitrate biases by updating wet scavenging parameterization in the GEOS-Chem model; however, this update leads to biases in oxidized nitrogen wet deposition between model predictions and observations.

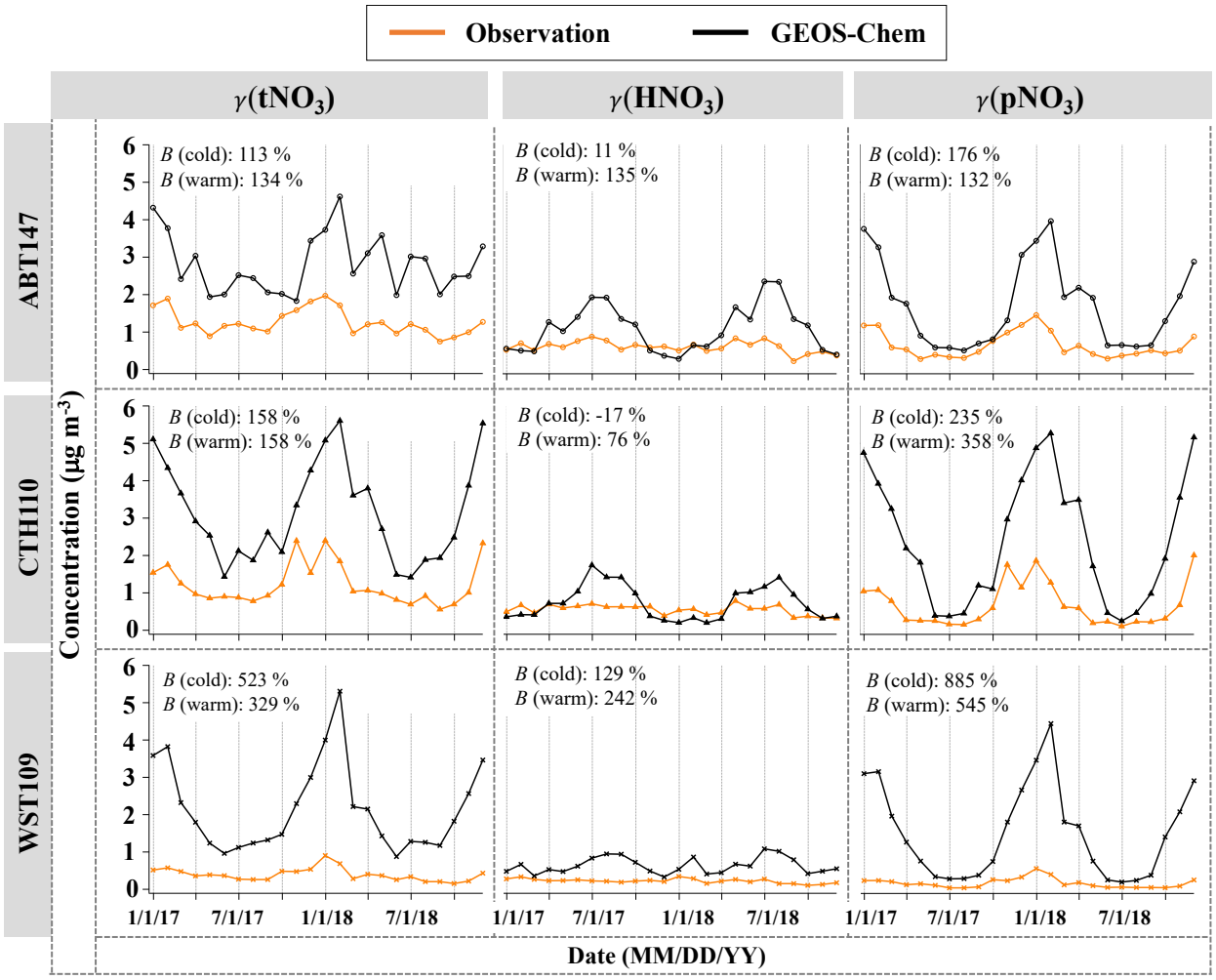

Figure 2.3. Time series of monthly mean total nitrate, HNO_3, and pNO_3 concentrations (γ) observed and simulated at ABT147, CTH110, and WST109 CASTNET sites. B refers to the normalized mean bias for comparison of the model to observations (see section 2.3 in Methods).

3.2 Oxygen Isotopic Compositions – Oxidation Chemistry and Phase Difference

The oxygen isotopic compositions in atmospheric nitrate are used to evaluate NO_x oxidation chemistry and to assess seasonal changes in nitrate formation mechanisms. For the CASTNET sites, the $\Delta(^{17}O, HNO_3)$ and $\Delta(^{17}O, pNO_3)$ values ranged from 12.9 ‰ to 30.9 ‰ and from 16.6 ‰ to 33.7 ‰, with a mean value of (22.7±3.6) ‰ and (27.1±3.8) ‰, respectively (Figure 2.4). The $\delta(^{18}O, HNO_3)$ and $\delta(^{18}O, pNO_3)$ values ranged from 46.9 ‰ to 82.1 ‰ and from 43.6 ‰ to 85.3

‰, with a mean value of (68.1±7.1) ‰ and (68.2±8.3) ‰, respectively (Figure 2.5). These observations are in the range of previously reported values in polluted mid-latitudes: $\delta(^{18}O, HNO_3)$ and $\delta(^{18}O, pNO_3)$ in CASTNET sites in Ohio, Pennsylvania, and New York from April 2004 to March 2005 ranged from 51.6 ‰ to 94.0 ‰ and from 45.2 ‰ to 92.7 ‰ (Elliott et al., 2009), respectively. They are also consistent with observations of polluted air masses in Canada from September 2010 to January 2014, which were from 62.4 to 81.7 ‰ for $\delta(^{18}O, HNO_3)$, from 19.3 to 29.0 ‰ for $\Delta(^{17}O, HNO_3)$, from 48.4 to 83.2 ‰for $\delta(^{18}O, pNO_3)$, and from 13.8 to 30.5 ‰ for $\Delta(^{17}O, pNO_3)$ (Savard et al., 2018).

Previous studies and modeling results have indicated that the seasonality of oxygen isotopic compositions in HNO_3 and pNO_3 is driven by a shift in oxidation chemistry (e.g., Hastings et al., 2003; Michalski et al, 2012; Alexander et al., 2009; 2020). Globally, the seasonality reflects a shift in O_3 to HO_x radical chemistry during winter to summer, respectively. Wintertime has higher NO + O_3 branching ratios than summer, which has increased NO + RO_2/HO_2. The high values of $\delta(^{18}O)$ and $\Delta(^{17}O)$ in HNO_3 and pNO_3 during the cold season are caused by the increased incorporation of O_3 into the nitrate product through N_2O_5 heterogeneous hydrolysis on aerosols (Figures 2.4 and 2.5). In contrast, the dominance of gas-phase production by the NO_2 + OH reaction dilutes the isotopic influence of O_3 during warm seasons leading to the low values of $\delta(^{18}O)$ and $\Delta(^{17}O)$ in HNO_3 and pNO_3. Spatial variability is observed in $\delta(^{18}O)$ and $\Delta(^{17}O)$ of HNO_3, with highest values at CTH110 ($\delta(^{18}O)$: (71.5±5.6) ‰ (n = 24) and $\Delta(^{17}O)$: (25.0±3.1) ‰ (n = 23)) followed by ABT147 ($\delta(^{18}O)$: (70.1±4.8) ‰ (n = 24) and $\Delta(^{17}O)$: (23.1±2.2) ‰ (n = 24)) and WST109 ($\delta(^{18}O)$: (62.8±7.7) ‰ (n = 24) and $\Delta(^{17}O)$: (20.2±3.7) ‰ (n = 24)). However, $\delta(^{18}O)$ and $\Delta(^{17}O)$ of pNO_3 were not significantly different across the stations: for ABT147 ($\delta(^{18}O)$: (68.6±7.1) ‰ (n = 24) and

$\Delta(^{17}O)$: (26.4±3.6) ‰ (n = 22)); CTH110 ($\delta(^{18}O)$: (69.1±8.9) ‰ (n = 24) and $\Delta(^{17}O)$: (26.8±4.1) ‰ (n = 19)); and WST109 ($\delta(^{18}O)$: (66.8±8.7) ‰ (n = 24) and $\Delta(^{17}O)$: (29.4±2.9) ‰ (n = 10)).

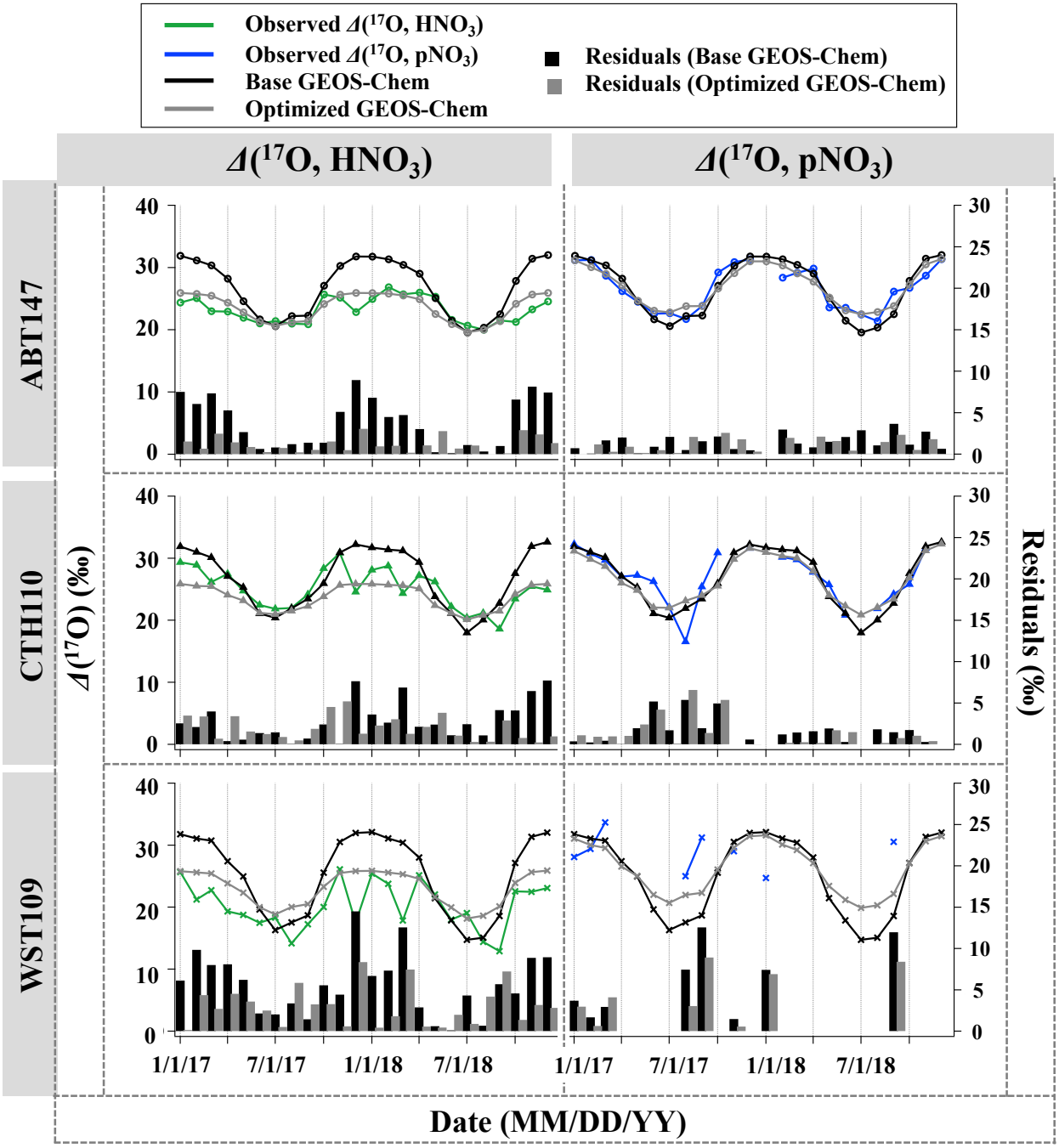

Figure 2.4. Time series of the monthly mean for observed and calculated $\Delta(^{17}O)$ for HNO_3 and pNO_3 over ABT147, CTH110, and WST109 CASTNET sites. Calculated $\Delta(^{17}O)$ using base (black) and optimized (grey) GEOS-Chem are shown in the plot together. Bars indicate the residuals between calculation and observation.

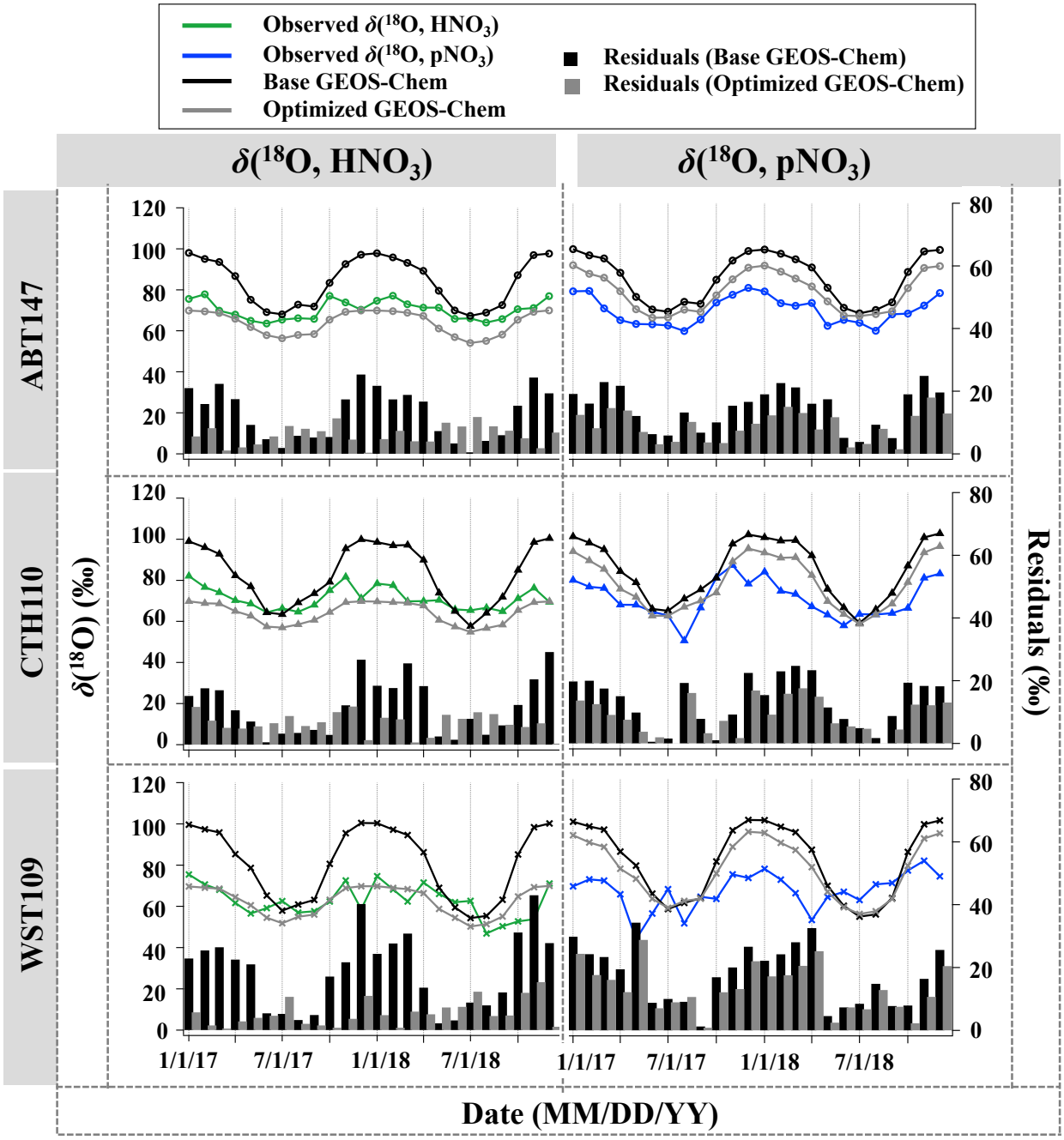

Figure 2.5. Time series of the monthly mean for observed and calculated $\delta(^{18}O)$ for HNO_3 and pNO_3 over ABT147, CTH110, and WST109 CASTNET sites. Calculated $\delta(^{18}O)$ using base (black) and optimized (grey) GEOS-Chem are shown in the plot together. Bars indicate the residuals between calculation and observation.

Our observations indicate a significant phase-dependent difference in oxidation chemistry between HNO_3 and pNO_3 that is unexpected (Figure 2.6). Many modeled mechanisms of gas- and aqueous-phase chemistry produce HNO_3, then HNO_3 is partitioned into the aerosol phase based on thermodynamic equilibrium (i.e., $NH_4NO_3(s) \rightleftharpoons HNO_3(g) + NH_3(g)$) or coarse uptake. Conventional understanding would expect $\Delta(^{17}O)$ of HNO_3 and pNO_3 to be the same (e.g., Alexander., 2020). However, observed $\Delta(^{17}O, pNO_3)$ tends to be significantly higher than $\Delta(^{17}O, HNO_3)$ ($p < 0.01$ at ABT and CTH, $p = 0.088$ at WST). The difference between $\Delta(^{17}O, pNO_3)$ and $\Delta(^{17}O, HNO_3)$ was larger in the cold season than in the warm season. For example, on average, $\Delta(^{17}O, pNO_3)$ was (5.1±2.6 ‰) higher than $\Delta(^{17}O, HNO_3)$ during the cold months, while $\Delta(^{17}O, pNO_3)$ was (2.7±4.7 ‰) higher than $\Delta(^{17}O, HNO_3)$ during warm months. This phase difference in $\Delta(^{17}O)$ cannot be explained by potential sample biases caused by volatilization, which leads to mass-dependent fractionation. This difference might be related to the differences in particulate nitrate size-dependent production pathways. Previous studies of size-segregated $\Delta(^{17}O, pNO_3)$ indicated higher values for coarse pNO_3 (aerodynamic diameter (D_a) > 0.95 μm) relative to fine pNO_3 (D_a < 0.95 μm) that was concluded to reflect the increased importance of heterogeneous N_2O_5 hydrolysis on coarse particles relative to fine particles (Vicars et al., 2013). The CASTNET pNO_3 samples reflect total suspended particles (TSP) such that increased importance of N_2O_5 heterogeneous chemistry for coarse particulate nitrate formation could explain the higher $\Delta(^{17}O, pNO_3)$ values we observe relative to $\Delta(^{17}O, HNO_3)$.

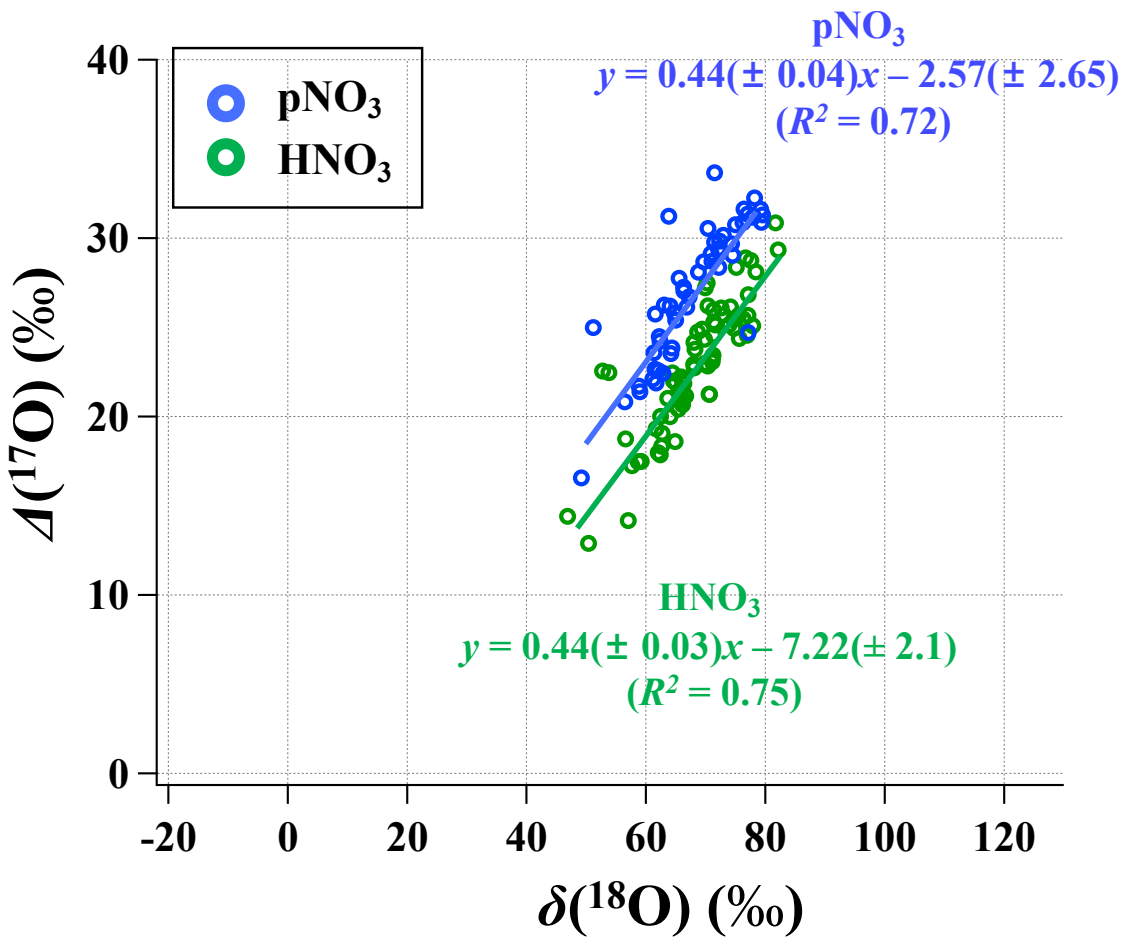

Figure 2.6. Relationship between the monthly mean ($\delta(^{18}O)$ and $\Delta(^{17}O)$) for observed HNO_3 (green) and pNO_3 (blue) across all CASTNET sites with correlation coefficient (R^2) and slope

Positive linear relationships between $\delta(^{18}O)$ and $\Delta(^{17}O)$ were observed for HNO_3 and pNO_3 across the CASTNET sites, with similar slopes but different oxygen isotopic signatures indicated by different intercepts (Figure 2.6). For the relationship of $\delta(^{18}O)$ and $\Delta(^{17}O)$, the high end-member should result from O_3, and the lower end-member depends on the isotopic signature of the atmospheric oxidants involved. The transferable $\delta(^{18}O)$ signatures of atmospheric oxidants are not fully understood yet, reflecting a complex combination of atmospheric oxidant source signatures and isotope fractionation during reaction and incorporation into the nitrate end-product. While

ozone has a notably high $\Delta(^{17}O)$ value ((39±2) ‰; Vicars and Savarino, 2014), $\Delta(^{17}O)$ values of other atmospheric oxidants such as $O_2/RO_2/HO_2$, H_2O and OH are equal to or close to 0 ‰ (Michalski et al., 2012; Walters et al., 2019). Overall, our results suggest more O_3 is incorporated during the formation of pNO_3 than HNO_3. We further analyze the oxidation chemistry involved in atmospheric nitrate formation based on output from the GEOS-Chem chemical transport model.

3.3 Quantifying atmospheric nitrate oxidation chemistry using $\Delta(^{17}O)$

Observations of the oxygen isotopic composition were utilized to quantify the relative importance of different nitrate formation pathways and to assess model representation of the chemistry of nitrate formation. Using atmospheric nitrate production rates from the GEOS-Chem model ("base case"), $\Delta(^{17}O)$ was calculated within a grid cell corresponding to our CASTNET sites and compared with observed $\Delta(^{17}O, HNO_3, pNO_3)$ at each site (Figure 2.4). We note that the previous $\Delta(^{17}O)$ GEOS-Chem framework tags NO_2 and HNO_3 production and assumes that pNO_3 production is similar to HNO_3 due to thermodynamic equilibrium. Thus, we compared the simulated $\Delta(^{17}O, HNO_3)$ from GEOS-Chem to our $\Delta(^{17}O, HNO_3)$ and $\Delta(^{17}O, pNO_3)$ observations. The averaged residuals over the collection period for each site were 3.9 ‰, 2.8 ‰, and 5.6 ‰ for $\Delta(^{17}O, HNO_3)$, and 1.5 ‰, 1.7 ‰, and 6.1 ‰ for $\Delta(^{17}O, pNO_3)$ at ABT147, CTH110, and WST109, respectively (Figure 2.4). Calculated $\Delta(^{17}O)$ based on GEOS-Chem output reproduced the observed temporal variations well (Figure 2.4), although the model better captured the lower observed $\Delta(^{17}O)$ during warmer months versus the higher values observed in the cooler months (Table 2.2). The GEOS-Chem model also does not capture observed spatial $\Delta(^{17}O)$ variabilities. For instance, higher $\Delta(^{17}O)$ values (especially for HNO_3) were observed at CTH110 compared to WST109; while no significant spatial $\Delta(^{17}O)$ differences were predicted from GEOS-Chem. The model prediction was sensitive to the type of nitrate; the calculated $\Delta(^{17}O)$ showed a better

agreement with observed $\Delta(^{17}O)$ of pNO_3 ($y = 0.55\ x + 12.62$ ($R^2 = 0.48$)) than $\Delta(^{17}O)$ of HNO_3 ($y = 0.46\ x + 10.68$ ($R^2 = 0.44$)) at all CASTNET sites (B = -2 % and 15 %, respectively) (Figure 2.7).

Table 2.2. Summary of the residuals between observed and calculated oxygen isotope deltas by season using the base and optimized GEOS-Chem, respectively.

Residuals		**$\Delta(^{17}O$, $HNO_3)$**	**$\Delta(^{17}O$, $pNO_3)$**	**$\delta(^{18}O$, $HNO_3)$**	**$\delta(^{18}O$, $pNO_3)$**
Base GEOS-Chem	Annual	4.1 ‰	2.3 ‰	15.5 ‰	15.9 ‰
	Cold	6.2 ‰	1.7 ‰	23.1 ‰	20.4 ‰
	Warm	2.0 ‰	2.8 ‰	7.9 ‰	11.4 ‰
Optimized GEOS-Chem	Annual	2.0 ‰	1.7 ‰	6.2 ‰	10.4 ‰
	Cold	2.3 ‰	1.4 ‰	5.7 ‰	13.2 ‰
	Warm	1.8 ‰	2.0 ‰	6.7 ‰	7.7 ‰

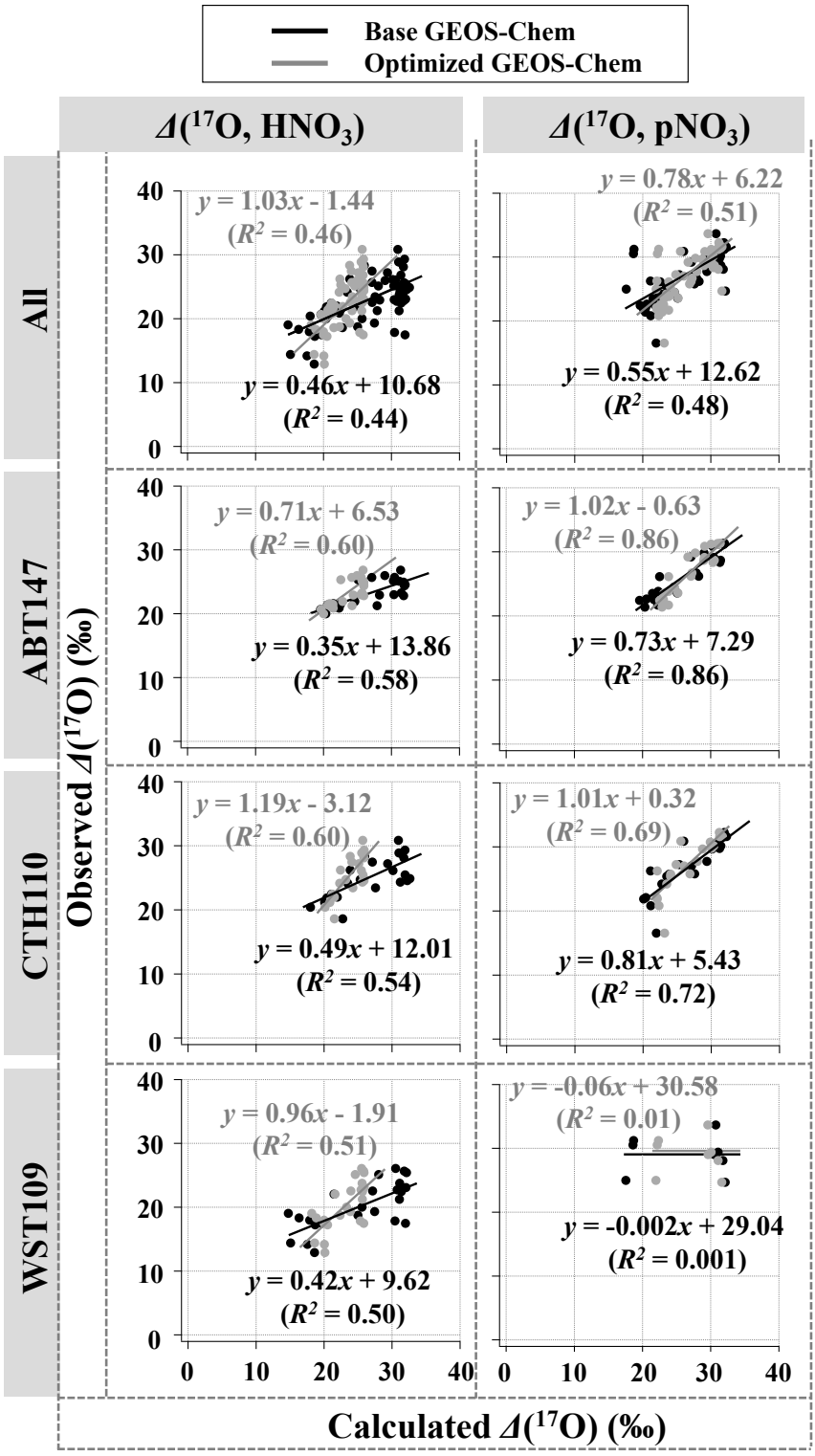

Figure 2.7. Correlation between observed and calculated $\Delta(^{17}O)$ for HNO_3 and pNO_3 using base GEOS-Chem (black) and optimized GEOS-Chem (grey) by each site.

Several studies have used $\Delta(^{17}O)$ to quantify and/or constrain modeled chemical mechanisms. Here, GEOS-Chem nitrate production rates and thus calculated $\Delta(^{17}O)$ were optimized to find the lowest residual sum of squares between the calculated and observed $\Delta(^{17}O)$. This optimization algorithm constrains the relative rates of nitrate formation pathways simulated by GEOS-Chem. Additionally, the optimization was conducted for HNO_3 and pNO_3 separately. Calculated $\Delta(^{17}O)$ from the base GEOS-Chem model was generally 1.15 times higher than observed $\Delta(^{17}O, HNO_3)$ and 0.98 times lower than $\Delta(^{17}O, pNO_3)$ across all CASTNET sites. After optimization, the residuals between observed and calculated $\Delta(^{17}O)$ dramatically decreased (Figure 2.4), especially in the cold season (Table 2.2). Moreover, the linear relationships had slopes much closer to the 1:1 line (i.e., from 0.46 to 1.03 for HNO_3 and from 0.55 to 0.78 for pNO_3; Figure 2.7) than the base GEOS-Chem model across the three CASTNET site (the relationships for each site before and after optimization are shown in Figure 2.7). On a subannual basis, the $\Delta(^{17}O)$ comparison for the cold season showed better improvement than the warm season, especially for $\Delta(^{17}O, HNO_3)$.

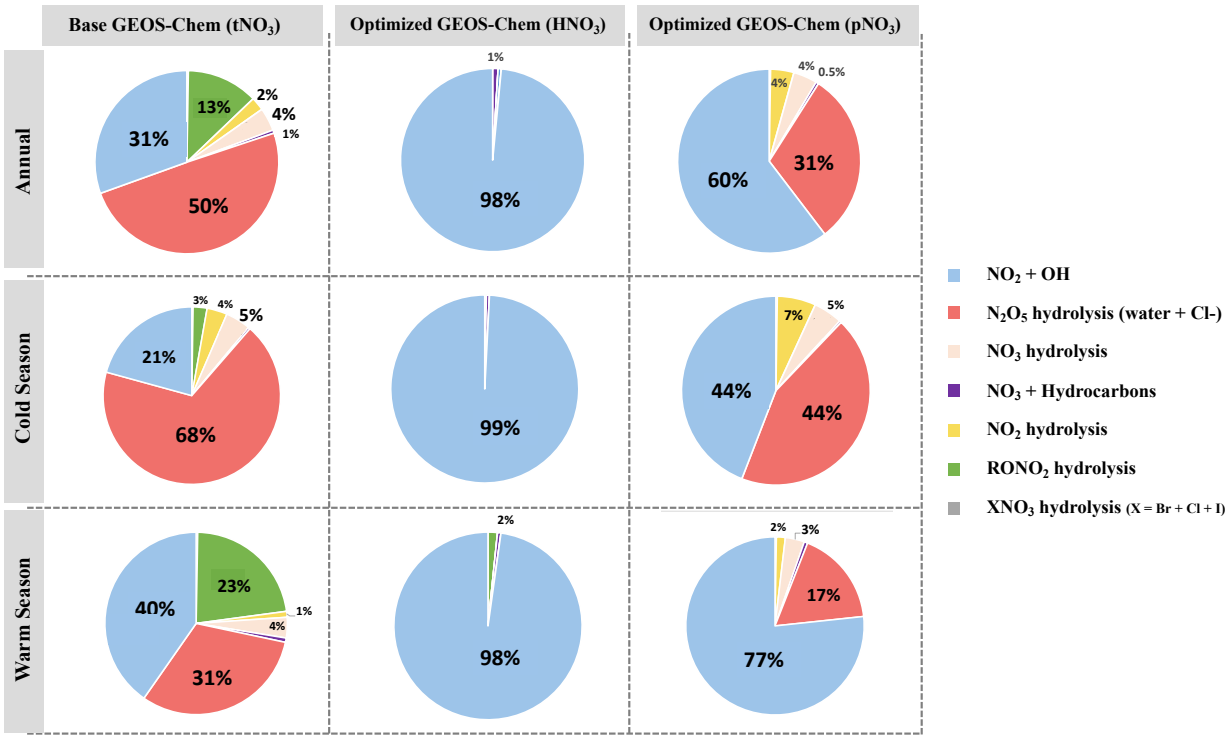

Figure 2.8. Relative proportions for major nitrate production pathways by season from base GEOS-Chem output (HNO_3 + pNO_3), optimized GEOS-Chem for HNO_3 production only, and optimized GEOS-Chem for pNO_3 production only based on comparison with observations across the three CASTNET sites. Annual refers to the full two-year record (Dec 2016-Dec 2018). The cold and warm seasons refer to Oct-Mar and Apr-Sep, respectively.

The dominant annual pathway for nitrate formation in the GEOS-Chem model ("base case") was N_2O_5 hydrolysis, which accounts for 50 % (Figure 2.8), followed by NO_2 + OH (31 %) and $RONO_2$ hydrolysis (13 %) across all CASTNET sites. Nitrate production via the reaction of XNO_3 hydrolysis and NO_3 + HC was small (< 1 %) at all sites. Strong seasonality in nitrate production was observed, as expected, with high portions of N_2O_5 hydrolysis in winter and NO_2 + OH in summer (Figure 2.8).

After optimization, the dominant pathway for nitrate formation in GEOS-Chem changed compared to the base case. For $\Delta(^{17}O, pNO_3)$, NO_2 + OH (60 %) was the dominant pathway for nitrate formation in the optimized GEOS-Chem calculation, followed by N_2O_5 hydrolysis (31 %)

and NO_3 hydrolysis (4 %) (Figure 2.8). At the same time, $\Delta(^{17}O, HNO_3)$ was almost entirely driven by NO_2 + OH reaction (98 %) in the optimized GEOS-Chem case (Figure 2.8). The optimized GEOS-Chem calculations suggest that the fraction of nitrate produced by N_2O_5 hydrolysis was significantly overestimated in the GEOS-Chem base case. In the base case, N_2O_5 hydrolysis dominated nitrate production, especially in the cold season with a fraction of over 68 % at all CASTNET sites (Figure 2.8). This may also partly explain major nitrate concentration overestimates, particularly in the cold season.

3.4 Modeling $\delta(^{18}O)$ of Atmospheric Nitrate

The GEOS-Chem model $\delta(^{18}O)$ was also calculated in the same manner as $\Delta(^{17}O)$ (Figure 2.5). Unlike the calculated $\Delta(^{17}O)$, calculated $\delta(^{18}O)$ showed remarkably positive biases compared with measured $\delta(^{18}O)$ of HNO_3 (B = 22 %) and pNO_3 (B = 21 %). The averaged residuals for $\delta(^{18}O, HNO_3)$ at each site were 13.9 ‰, 12.9 ‰, and 19.6 ‰, and for $\delta(^{18}O, pNO_3)$ were 15.4 ‰, 14.2 ‰, and 18.2 ‰ at ABT147, CTH110, and WST109, respectively (Fig. 2.5, Table 2.2). Modeling the $\delta(^{18}O)$ values of nitrate is more challenging than $\Delta(^{17}O)$ because not all oxidant $\delta(^{18}O)$ values have been directly observed and fractionation factors associated with the O transfer into NO_y products are unknown. Uncertainty in $\delta(^{18}O)$ values could be a major factor causing disagreement between observed and calculated $\delta(^{18}O)$. Additionally, uncertainties in the gas-phase and aerosol scheme related to tNO_3 production in GEOS-Chem could account for the discrepancy. Still, as with $\Delta(^{17}O)$, the calculated $\delta(^{18}O)$ showed far more disagreement with observations during cooler months than warmer months (Table 2.2).

Newly optimized nitrate production in GEOS-Chem was also applied to $\delta(^{18}O)$ calculation and compared with previous results. As with $\Delta(^{17}O)$, a slope of the regression line between (optimized) calculated and observed $\delta(^{18}O)$ became closer to 1 (i.e., from 0.30 to 0.74 for HNO_3 and from 0.39

to 0.49 for pNO_3; Figure 2.9) and residuals improved at each site after the optimization (Figure 2.5). Overall, the optimized GEOS-Chem $\delta(^{18}O)$ calculation showed better agreement than the base GEOS-Chem model (B = -6 % for $\delta(^{18}O, HNO_3)$ and B = 13 % for $\delta(^{18}O, pNO_3)$). The most significant improvement, as shown by the residuals, is during the cold season.

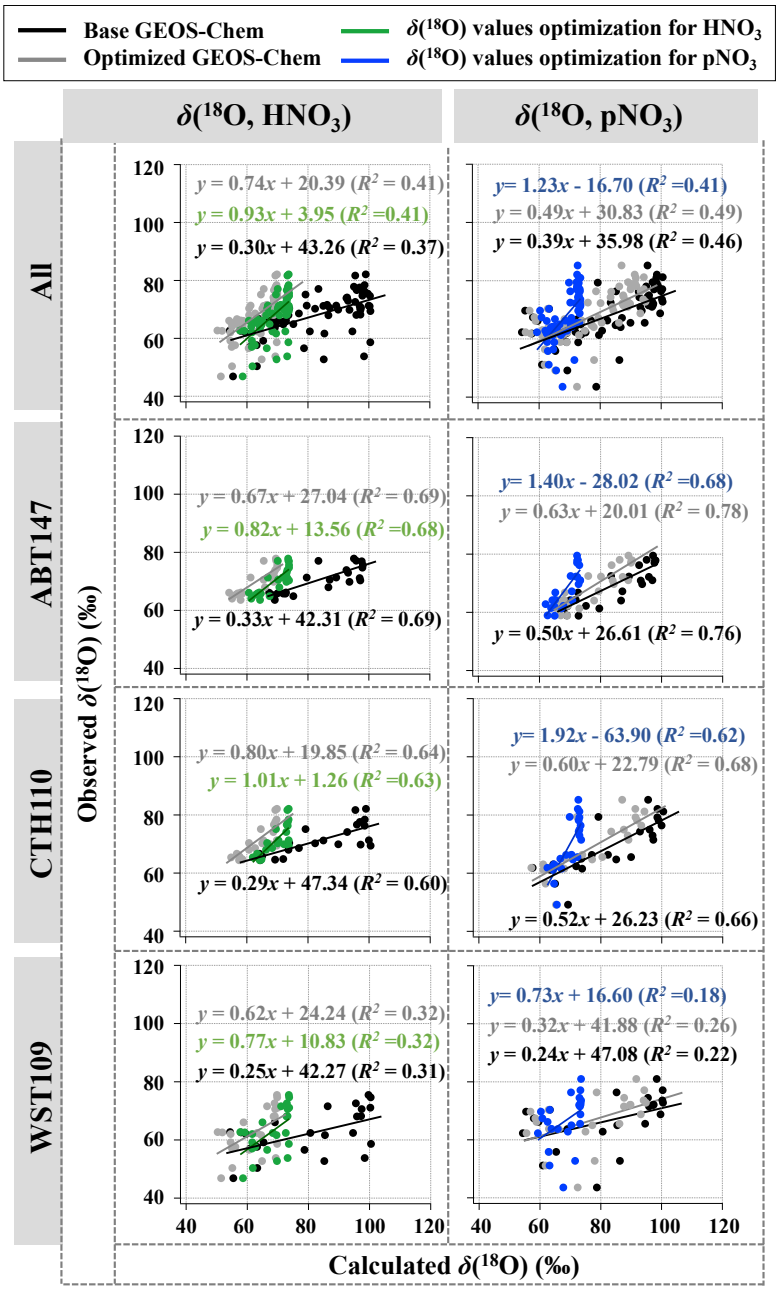

Figure 2.9. Correlation between observed and calculated δ(^{18}O) for HNO_3 and pNO_3 by each site. Calculated δ(^{18}O) values using base GEOS-Chem, optimized GEOS-Chem, and optimized δ(^{18}O) values indicated as black, grey, and green (for HNO_3) or blue (for pNO_3), respectively.

3.5 $\delta(^{18}O)$ Optimization of Atmospheric Oxidants

After optimization of relative nitrate production rates in GEOS-Chem based on $\Delta(^{17}O)$, we applied the optimized chemical production to calculate $\delta(^{18}O)$ but still observed discrepancy between observed and predicted $\delta(^{18}O)$. The discrepancy could be related to variable and somewhat unconstrained $\delta(^{18}O)$ values of atmospheric oxidants important for nitrate formation. To test this, the assumed (literature) $\delta(^{18}O)$ values of oxidants were optimized by selecting the best linear fit between the observations and calculated $\delta(^{18}O$, HNO_3 and $pNO_3)$ (Figure 2.10). After optimization for $\delta(^{18}O)$ of oxidants, the discrepancy between observation and calculation was dramatically reduced (Figure 2.9) with a decrease in *B* from 21 to 1 %. The optimization predicted $\delta(^{18}O)$ of H_2O values similar to what was expected (-6.5 ‰ vs. -6.0 ‰), however different values were predicted for $\delta(^{18}O)$ of O_2, OH, and O_3 (Table 2.3). A typical mid-latitude value (-6 ‰) of $\delta(^{18}O$, $H_2O)$ was selected in this study. We note that the $\delta(^{18}O$, $H_2O)$ will vary seasonally; however, the calculated $\delta(^{18}O)$ value of nitrate was insensitive to this value because of the relatively minor role that H_2O contributes to O atoms of atmospheric nitrate. For $\delta(^{18}O)$ of O_2, OH, and O_3, it is possible that this reflects isotope effects associated with the incorporation of these oxidants during nitrate production, rather than further issues with model chemistry since the relative production rates here are constrained based on $\Delta(^{17}O)$. The $\delta(^{18}O$, $O_2)$ was the best fit with calculated $\delta(^{18}O)$ of nitrate values when assuming a value of 11.1 ‰ (vs. the well-known 23 ‰). Since atmospheric O_2 is incorporated into nitrate via NO oxidation by HO_2 and RO_2 radicals, it was assumed that the $\delta(^{18}O)$ value of RO_2 and HO_2 is equal to O_2 such that this does not consider any potential isotope effects associated with HO_2 and RO_2 formation and reaction with NO. The optimized value of 11 ‰ reflects the O atom derived from RO_2/HO_2 reactions incorporated into NO_2. Thus, our

optimized value might suggest that RO_2/HO_2 singly substituted with ^{18}O (e.g., $R^{18}O^{16}O$, $H^{18}O^{16}O$) reacts slower than the ^{16}O isotopologues (e.g., $R^{16}O_2$ or $H^{16}O_2$).

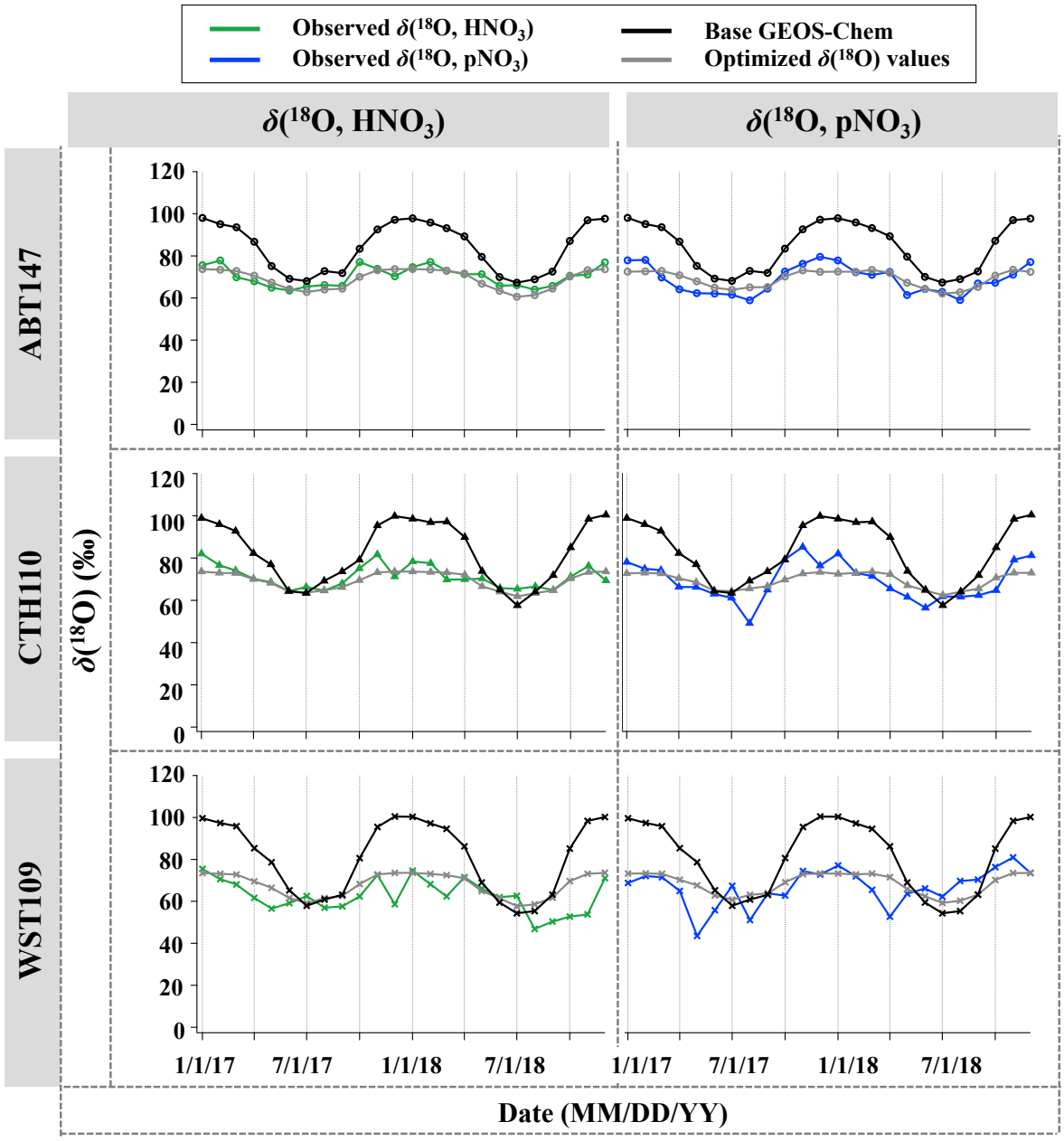

Figure 2.10. Time series of observed and calculated $\delta(^{18}O)$ for HNO_3 and pNO_3 for ABT147, CTH110, and WST109 sites. Calculated $\delta(^{18}O)$ using base GEOS-Chem (black) and using optimized $\delta(^{18}O)$ values (grey) are shown in the plot together.

Table 2.3. δ(^{18}O) values for each oxidant before and after optimization based on different scenarios

Atmospheric Oxidants	Assumed $\delta^{18}O$ (‰)	Optimized $\delta^{18}O$ (‰)			
		Non-fixed	Fixed O_3^*	Fixed O_3^* and H_2O	Fixed O_3^*, H_2O, and O_2
O_3^*	126.3	89.9	–	–	–
H_2O	-6.0	-6.5	-180.7	–	–
$O_2/RO_2/HO_2$	23.0	11.1	40.9	44.4	–
OH	-43.0	42.2	-31.3	-39.4	-36

The observed $\delta(^{18}O)$ of O_3 and OH for the CASTNET samples were the best fit with calculated $\delta(^{18}O)$ when assuming values of 89.9 ‰ for $\delta(^{18}O, O_3)$ and 42.2 ‰ for $\delta(^{18}O, OH)$, respectively. In the previous section, we noted that NO_2 + OH and N_2O_5 hydrolysis reactions were the dominant pathways for nitrate formation, indicating that OH and O_3 play an important role in determining the $\delta(^{18}O)$ value in nitrate. Indeed, optimizing $\delta(^{18}O)$ values to find the best agreement between observation and calculation is largely dependent on $\delta(^{18}O)$ values of O_3 and OH (see also Table 2.3). The optimized $\delta(^{18}O, O_3^*)$ value (89.9 ‰) was lower than the average reported $\delta(^{18}O, O_3^*)$ ((~126±12) ‰; Vicars and Savarino, 2014), though the $\delta(^{18}O, O_3)$ is known to vary with temperature and pressure, and could also potentially be fractionated during reactions (Brenninkmeijer et al., 2004). For example, Walters and Michalski (2016) calculated an isotopic enrichment factor near -20 ‰ associated with O_3 transfer in its reaction with NO, which would lower the transferable $\delta(^{18}O)$ of O_3, consistent with our predictions. The isotope effect for NO +

O_3 reaction is the only one currently known; in other words, no other $\delta(^{18}O)$ isotope effects associated with O_3 reaction with NO_y (e.g., $NO_2 + O_3$) have been calculated. Further, there is potential for equilibrium isotope effects between N_2O_5, NO_2, and NO_3 that could also impart a mass-dependent $\delta(^{18}O)$ fractionation. While difficult to pinpoint the exact isotope effects occurring, our optimized value predicts an elevated $\delta(^{18}O)$ value derived from O_3 compared to the other oxidants, consistent with our expectation.

For $\delta(^{18}O, OH)$, the optimized value dramatically increased compared to the initial assumed value (-43.0 ‰). The initial $\delta(^{18}O, OH)$ value is based on several assumptions that may not be correct regarding isotope exchange with $H_2O(g)$. Additionally, Fang et al. (2021) suggested that $\delta(^{15}N)$ of nitrate is largely controlled by an isotope effect in the $NO_2 + OH$ pathway, and it could be conceivable that $\delta(^{18}O)$ may be affected by a similar isotope effect as well. Overall, the optimization of $\delta(^{18}O, OH)$ is highly dependent on the $\delta(^{18}O, O_3^*)$ (see Table 2.3), which makes sense given the proportional control of the $NO_2 + OH$ and N_2O_5 hydrolysis reactions. Despite the uncertainty in the transferrable $\delta(^{18}O)$ from major oxidants, the comparison between predicted and observed $\delta(^{18}O)$ and $\Delta(^{17}O)$ both suggest a larger relative importance of NO_2 +OH chemistry than reflected in the model simulations. We note here that this finding is consistent with our companion study (acp-2022-621) of $\delta(^{15}N, HNO_3)$ and $\delta(^{15}N, pNO_3)$ as well.

Overall, the observed differences in the oxygen isotopic composition of HNO_3 and pNO_3, the observed relationships of $\delta(^{18}O)$ and $\Delta(^{17}O)$ in the different nitrate phases, and the significant mismatch with the global model base case challenge our current representation of nitrate chemistry in atmospheric chemistry models. Generally, the GEOS-Chem $\Delta(^{17}O)$ simulations were biased high relative to observations, indicating the over-incorporation of O_3 during nitrate formation. The largest discrepancies in the model-observation comparisons, particularly for pNO_3, occur in winter.

Our optimized chemistry, constrained by the observed $\delta(^{18}O)$ and $\Delta(^{17}O)$, suggested that the heterogenous production of nitrate via N_2O_5 chemistry is currently significantly overestimated. While our focus is on the northeastern US, an area of important environmental change due to regulated emissions reductions, this finding has implications for the global modeling of atmospheric nitrate and oxidation chemistry.

4. Conclusions

Using a combination of concentration and isotopic analyses, we evaluated atmospheric nitrate formation pathways in the northeastern US in 2017–2018. The GEOS-Chem model showed large positive biases for HNO_3 and pNO_3 concentrations, an important issue that is common in atmospheric chemistry models. The observed oxygen isotopic compositions ($\Delta(^{17}O)$ and $\delta(^{18}O)$) revealed a more important relative role of NO_2+OH chemistry and indicated that the model chemistry overpredicted heterogeneous hydrolysis of N_2O_5 for atmospheric nitrate in the northeastern US. We also observed nitrate-phase differences in $\Delta(^{17}O)$ and $\delta(^{18}O)$, which are not captured in current models. Further investigation of size-segregated nitrate chemistry is recommended to improve model prediction of nitrate formation.

Additionally, this finding has important implications for predicting oxidation chemistry in the atmosphere. For instance, the production of nitrate via heterogeneous hydrolysis of N_2O_5 represents a radical termination process, such that a much-reduced importance of this reaction could yield more radical chemistry with an impact on oxidant concentrations. Indeed, an important mechanism for converting NO_x to atmospheric nitrate could affect controlling the oxidizing efficiency, which directly influences the atmospheric oxidation budget and many atmospheric pollutants' (notably greenhouse gases) lifetime in the atmosphere. Thus, better constraining their

chemistries and feedbacks is crucial to understanding atmospheric nitrate production pathways and its connection to atmospheric oxidation chemistry.

Traditionally, $\Delta(^{17}O)$ has been used to quantitatively assess nitrate production pathways. The use of $\delta(^{18}O)$ as well can enhance our understanding of the oxidants contributing to nitrate formation, particularly for distinguishing oxidants that have similar $\Delta(^{17}O)$ values (i.e., all are near 0 ‰ except ozone). However, our study also observed a discrepancy between observed and calculated $\delta(^{18}O)$ values, even after accounting for an optimized chemical production based on $\Delta(^{17}O)$. The best match of the observations suggests that the transferrable $\delta(^{18}O)$ values of oxidants may vary more than is currently suggested in the literature. Improved constraints, particularly on the isotopic composition of OH and variability in $\delta(^{18}O, O_3)$ would add critical value to modeling and interpretation of major oxidation chemistry in the atmosphere.

5. Acknowledgments

We thank Ruby Ho for sampling and laboratory assistance. We are grateful to the US EPA CASTNET program and staff for their cooperation in this study and assistance with receiving archived samples for isotopic analysis.

6. Reference

Alexander, B., Hastings, M. G., Allman, D. J., Dachs, J., Thornton, J. A., and Kunasek, S. A.: Quantifying atmospheric nitrate formation pathways based on a global model of the oxygen isotopic composition ($\Delta^{17}O$) of atmospheric nitrate, Atmos. Chem. Phys., 9, 5043–5056, https://doi.org/10.5194/acp-9-5043-2009, 2009.

Alexander, B., Sherwen, T., Holmes, C. D., Fisher, J. A., Chen, Q., Evans, M. J., and Kasibhatla, P.: Global inorganic nitrate production mechanisms: comparison of a global model with nitrate isotope observations, Atmos. Chem. Phys., 20, 3859–3877, https://doi.org/10.5194/acp-20-3859-2020, 2020.

Amos, H. M., Jacob, D. J., Holmes, C. D., Fisher, J. A., Wang, Q., Yantosca, R. M., Corbitt, E. S., Galarneau, E., Rutter, A. P., and Gustin, M. S.: Gas-particle partitioning of atmospheric Hg (II) and its effect on global mercury deposition, Atmos. Chem. Phys., 12, 591–603, https://doi.org/10.5194/acp-12-591-2012, 2012.

Ashbaugh, L. L. and Eldred, R. A.: Loss of Particle Nitrate from Teflon Sampling Filters: Effects on Measured Gravimetric Mass in California and in the IMPROVE Network, J. Air Waste Manag. Assoc., 54, 93–104, https://doi.org/10.1080/10473289.2004.10470878, 2004.

Bates, K. H. and Jacob, D. J.: A new model mechanism for atmospheric oxidation of isoprene: global effects on oxidants, nitrogen oxides, organic products, and secondary organic aerosol, Atmos. Chem. Phys., 19, 9613–9640, https://doi.org/10.5194/acp-19-9613-2019, 2019.

Bekker, C., Walters, W. W., Murray, L. T., and Hastings, M. G.: Nitrate chemistry in the northeast US part I: nitrogen isotope seasonality tracks nitrate formation chemistry, Atmos. Chem. Phys. Discuss. [preprint], https://doi.org/10.5194/acp-2022-621, in review, 2022.

Bey, I., Jacob, D. J., Yantosca, R. M., Logan, J. A., Field, B. D., Fiore, A. M., Li, Q., Liu, H. Y., Mickley, L. J., and Schultz, M. G.: Global modeling of tropospheric chemistry with assimilated meteorology: Model description and evaluation, J. Geophys. Res.-Atmos., 106, 23073–23095, https://doi.org/10.1029/2001JD000807, 2001.

Breider, T. J., Mickley, L. J., Jacob, D. J., Ge, C., Wang, J., Payer Sulprizio, M., Croft, B., Ridley, D. A., McConnell, J. R., and Sharma, S.: Multidecadal trends in aerosol radiative forcing over the Arctic: Contribution of changes in anthropogenic aerosol to Arctic warming since 1980, J. Geophys. Res.-Atmos., 22, 3573–3594, https://doi.org/10.1002/2016JD025321, 2017.

Brenninkmeijer, C. A., Janssen, C., Kaiser, J., Röckmann, T., Rhee, T. S., and Assonov, S. S.: Isotope effects in the chemistry of atmospheric trace compounds, Chem. Rev., 103, 5125–5162, https://doi.org/10.1021/cr020644k, 2003.

Camargo, J. A. and Alonso, Á.: Ecological and toxicological effects of inorganic nitrogen pollution in aquatic ecosystems: a global assessment, Environ. Int., 32, 831–849, https://doi.org/10.1016/j.envint.2006.05.002, 2006.

Carter, T. (Tess) S., Joyce, E. E., and Hastings, M. G.: Quantifying Nitrate Formation Pathways in the Equatorial Pacific Atmosphere from the GEOTRACES Peru-Tahiti Transect, ACS Earth Space Chem., 5, 2638–2651, https://doi.org/10.1021/acsearthspacechem.1c00072, 2021.

Casciotti, K. L., Sigman, D. M., Hastings, M. G., Böhlke, J. K., and Hilkert, A.: Measurement of the oxygen isotopic composition of nitrate in seawater and freshwater using the denitrifier method, Anal. Chem., 74, 4905–4912, https://doi.org/10.1021/ac020113w, 2002.

CASTNET (Clean Air Status and Trends Network), Retrieved from the United States Environmental Protection Agency, available at https://www.epa.gov/castnet, last access: 27 February 2023.

Crutzen, P. J.: The role of NO and NO_2 in the chemistry of the troposphere and stratosphere, Annu. Rev. Earth Planet. Sci., 7, 443–472, https://doi.org/10.1146/annurev.ea.07.050179.002303, 1979.

Dubey, M. K., Mohrschladt, R., Donahue, N. M., and Anderson, J. G.: Isotope specific kinetics of hydroxyl radical (OH) with water (H_2O): Testing models of reactivity and atmospheric fractionation, J. Phys. Chem. A, 101, 1494–1500, https://doi.org/10.1021/jp962332p, 1997.

Elliott, E. M., Kendall, C., Boyer, E. W., Burns, D. A., Lear, G. G., Golden, H. E., Harlin, K., Bytnerowicz, A., Butler, T. J., and Glatz, R.: Dual nitrate isotopes in dry deposition: Utility for partitioning NO_x source contributions to landscape nitrogen deposition, J. Geophys. Res.-Biogeo, 114, https://doi.org/10.1029/2008JG000889, 2009.

Fang, H., Walters, W. W., Mase, D., and Michalski, G.: i_NRACM: incorporating ^{15}N into the Regional Atmospheric Chemistry Mechanism (RACM) for assessing the role photochemistry plays in controlling the isotopic composition of NO_x, NO_y, and atmospheric nitrate, Geosci. Model Dev., 14, 5001–5022, https://doi.org/10.5194/gmd-14-5001-2021, 2021.

Fountoukis, C. and Nenes, A.: ISORROPIA II: a computationally efficient thermodynamic equilibrium model for K^+–Ca^{2+}–Mg^{2+}–NH^{4+}–Na^+–SO_4^{2-}–NO_3^-–Cl^-–H_2O aerosols, Atmos. Chem. Phys., 7, 4639–4659, https://doi.org/10.5194/acp-7-4639-2007, 2007.

Galloway, J. N., Dentener, F. J., Capone, D. G., Boyer, E. W., Howarth, R. W., Seitzinger, S. P., Asner, G. P., Cleveland, C. C., Green, P. A., and Holland, E. A.: Nitrogen cycles: past, present, and future, Biogeochemistry, 70, 153–226, https://doi.org/10.1007/s10533-004-0370-0, 2004.

Guenther, A. B., Jiang, X., Heald, C. L., Sakulyanontvittaya, T., Duhl, T. any, Emmons, L. K., and Wang, X.: The Model of Emissions of Gases and Aerosols from Nature version 2.1 (MEGAN2. 1): an extended and updated framework for modeling biogenic emissions, Geosci. Model Dev., 5, 1471–1492, https://doi.org/10.5194/gmd-5-1471-2012, 2012.

Hastings, M. G., Sigman, D. M., and Lipschultz, F.: Isotopic evidence for source changes of nitrate in rain at Bermuda, J. Geophys. Res.-Atmos., 108, https://doi.org/10.1029/2003JD003789, 2003.

Heald, C. L., Collett Jr, J. L., Lee, T., Benedict, K. B., Schwandner, F. M., Li, Y., Clarisse, L., Hurtmans, D. R., Van Damme, M., and Clerbaux, C.: Atmospheric ammonia and particulate inorganic nitrogen over the United States, Atmos. Chem. Phys., 12, 10295–10312, https://doi.org/10.5194/acp-12-10295-2012, 2012.

Hering, S. and Cass, G.: The magnitude of bias in the measurement of $PM_{2.5}$ arising from volatilization of particulate nitrate from Teflon filters, J. Air Waste Manag. Assoc., 49, 725–733, https://doi.org/10.1080/10473289.1999.10463843, 1999.

Hoesly, R. M., Smith, S. J., Feng, L., Klimont, Z., Janssens-Maenhout, G., Pitkanen, T., Seibert, J. J., Vu, L., Andres, R. J., and Bolt, R. M.: Historical (1750–2014) anthropogenic emissions of reactive gases and aerosols from the Community Emissions Data System (CEDS), Geosci. Model Dev., 11, 369–408, https://doi.org/10.5194/gmd-11-369-2018, 2018.

Holt, J., Selin, N. E., and Solomon, S.: Changes in inorganic fine particulate matter sensitivities to precursors due to large-scale US emissions reductions, Environ. Sci. Technol., 49, 4834–4841, https://doi.org/10.1021/acs.est.5b00008, 2015.

Hu, L., Millet, D. B., Baasandorj, M., Griffis, T. J., Turner, P., Helmig, D., Curtis, A. J., and Hueber, J.: Isoprene emissions and impacts over an ecological transition region in the US Upper Midwest inferred from tall tower measurements, J. Geophys. Res.-Atmos., 120, 3553–3571, https://doi.org/10.1002/2014JD022732, 2015.

Huang, J. and Jaeglé, L.: Wintertime enhancements of sea salt aerosol in polar regions consistent with a sea ice source from blowing snow, Atmos. Chem. Phys., 17, 3699–3712, https://doi.org/10.5194/acp-17-3699-2017, 2017.

Hudman, R. C., Moore, N. E., Martin, R. V., Russell, A. R., Mebust, A. K., Valin, L. C., and Cohen, R. C.: Steps towards a mechanistic model of global soil nitric oxide emissions: implementation and space based-constraints, Atmos. Chem. Phys., 12, 7779-7795, https://doi.org/10.5194/acp-12-7779-2012, 2012.

Jaeglé, L., Quinn, P. K., Bates, T. S., Alexander, B., and Lin, J.-T.: Global distribution of sea salt aerosols: new constraints from in situ and remote sensing observations, Atmos. Chem. Phys., 11, 3137–3157, https://doi.org/10.5194/acp-11-3137-2011, 2011.

Jaeglé, L., Shah, V., Thornton, J. A., Lopez-Hilfiker, F. D., Lee, B. H., McDuffie, E. E., Fibiger, D., Brown, S. S., Veres, P., and Sparks, T. L.: Nitrogen oxides emissions, chemistry, deposition, and export over the Northeast United States during the WINTER aircraft campaign, J. Geophys. Res.-Atmos., 123, 12–368, https://doi.org/10.1029/2018JD029133, 2018.

Kaiser, J., Hastings, M. G., Houlton, B. Z., Röckmann, T., and Sigman, D. M.: Triple oxygen isotope analysis of nitrate using the denitrifier method and thermal decomposition of N_2O, Anal. Chem., 79, 599–607, https://doi.org/10.1021/ac061022s, 2007.

Kasibhatla, P., Sherwen, T., Evans, M. J., Carpenter, L. J., Reed, C., Alexander, B., Chen, Q., Sulprizio, M. P., Lee, J. D., and Read, K. A.: Global impact of nitrate photolysis in sea-salt aerosol on NO_x, OH, and O_3 in the marine boundary layer, Atmos. Chem. Phys., 18, 11185–11203, https://doi.org/10.5194/acp-18-11185-2018, 2018.

Kroopnick, P. and Craig, H.: Atmospheric oxygen: isotopic composition and solubility fractionation, Science, 175, 54–55, https://doi.org/10.1126/science.175.4017.54, 1972.

Liu, H., Jacob, D. J., Bey, I., and Yantosca, R. M.: Constraints from ^{210}Pb and ^{7}Be on wet deposition and transport in a global three-dimensional chemical tracer model driven by assimilated meteorological fields, J. Geophys. Res.-Atmos., 106, 12109–12128, https://doi.org/10.1029/2000JD900839, 2001.

Luo, G., Yu, F., and Moch, J. M.: Further improvement of wet process treatments in GEOS-Chem v12.6.0: impact on global distributions of aerosols and aerosol precursors, Geosci. Model Dev., 13, 2879–2903, https://doi.org/10.5194/gmd-13-2879-2020, 2020.

Luo, G., Yu, F., and Schwab, J.: Revised treatment of wet scavenging processes dramatically improves GEOS-Chem 12.0.0 simulations of surface nitric acid, nitrate, and ammonium over the United States, Geosci. Model Dev., 12, 3439–3447, https://doi.org/10.5194/gmd-12-3439-2019, 2019.

McDuffie, E. E., Smith, S. J., O'Rourke, P., Tibrewal, K., Venkataraman, C., Marais, E. A., Zheng, B., Crippa, M., Brauer, M., and Martin, R. V.: A global anthropogenic emission inventory of atmospheric pollutants from sector- and fuel-specific sources (1970–2017): an application of the Community Emissions Data System (CEDS), Earth Syst. Sci. Data, 12, 3413–3442, https://doi.org/10.5194/essd-12-3413-2020, 2020.

Michalski, G., Bhattacharya, S. K., and Mase, D. F.: Oxygen isotope dynamics of atmospheric nitrate and its precursor molecules, in: Handbook of environmental isotope geochemistry, Springer, 613–635, https://doi.org/10.1007/978-3-642-10637-8_30, 2012.

Michalski, G., Scott, Z., Kabiling, M., and Thiemens, M. H.: First measurements and modeling of $\Delta^{17}O$ in atmospheric nitrate, Geophys. Res. Lett., 30, https://doi.org/10.1029/2003GL017015, 2003.

Millet, D. B., Guenther, A., Siegel, D. A., Nelson, N. B., Singh, H. B., de Gouw, J. A., Warneke, C., Williams, J., Eerdekens, G., Sinha, V., Karl, T., Flocke, F., Apel, E., Riemer, D. D., Palmer, P. I., and Barkley, M.: Global atmospheric budget of acetaldehyde: 3-D model analysis and constraints from in-situ and satellite observations, Atmos. Chem. Phys., 10, 3405–3425, https://doi.org/10.5194/acp-10-3405-2010, 2010.

Morin, S., Sander, R., and Savarino, J.: Simulation of the diurnal variations of the oxygen isotope anomaly ($\Delta^{17}O$) of reactive atmospheric species, Atmos. Chem. Phys., 11, 3653–3671, https://doi.org/10.5194/acp-11-3653-2011, 2011.

Murray, L. T., Jacob, D. J., Logan, J. A., Hudman, R. C., and Koshak, W. J.: Optimized regional and interannual variability of lightning in a global chemical transport model constrained by LIS/OTD satellite data, J. Geophys. Res.-Atmos., 117, https://doi.org/10.1029/2012JD017934, 2012.

NEI (National Emissions Inventory): Retrieved from United States Environmental Protection Agency, available at https://www.epa.gov/air-emissions-inventories/national-emissions-inventory-nei, last access: 27 February 2023.

Ridley, D. A., Heald, C. L., and Ford, B.: North African dust export and deposition: A satellite and model perspective, J. Geophys. Res.-Atmos., 117, https://doi.org/10.1029/2011JD016794, 2012.

Savard, M. M., Cole, A. S., Vet, R., and Smirnoff, A.: The $\Delta^{17}O$ and $\delta^{18}O$ values of atmospheric nitrates simultaneously collected downwind of anthropogenic sources–implications for polluted air masses, Atmos. Chem. Phys., 18, 10373–10389, https://doi.org/10.5194/acp-18-10373-2018, 2018.

Savarino, J., Kaiser, J., Morin, S., Sigman, D. M., and Thiemens, M. H.: Nitrogen and oxygen isotopic constraints on the origin of atmospheric nitrate in coastal Antarctica, Atmos. Chem. Phys., 7, 1925–1945, https://doi.org/10.5194/acp-7-1925-2007, 2007.

Schlesinger, R. B.: The health impact of common inorganic components of fine particulate matter ($PM_{2.5}$) in ambient air: a critical review, Inhal. Toxicol., 19, 811–832, https://doi.org/10.1080/08958370701402382, 2007.

Shah, V., Jaeglé, L., Thornton, J. A., Lopez-Hilfiker, F. D., Lee, B. H., Schroder, J. C., Campuzano-Jost, P., Jimenez, J. L., Guo, H., and Sullivan, A. P.: Chemical feedbacks weaken the wintertime response of particulate sulfate and nitrate to emissions reductions over the eastern United States, Proc. Natl. Acad. Sci., 115, 8110–8115, https://doi.org/10.1073/pnas.1803295115, 2018.

Sickles, I. I. and Shadwick, D. S.: Air quality and atmospheric deposition in the eastern US: 20 years of change, Atmos. Chem. Phys., 15, 173–197, https://doi.org/10.5194/acp-15-173-2015, 2015.

Sigman, D. M., Casciotti, K. L., Andreani, M., Barford, C., Galanter, M., and Böhlke, J. K.: A bacterial method for the nitrogen isotopic analysis of nitrate in seawater and freshwater, Anal. Chem., 73, 4145–4153, https://doi.org/10.1021/ac010088e, 2001.

Tai, A. P., Mickley, L. J., and Jacob, D. J.: Correlations between fine particulate matter ($PM_{2.5}$) and meteorological variables in the United States: Implications for the sensitivity of $PM_{2.5}$ to climate change, Atmos. Environ., 44, 3976–3984, https://doi.org/10.1016/j.atmosenv.2010.06.060, 2010.

Thiemens, M. H.: History and applications of mass-independent isotope effects, Annu. Rev. Earth Planet. Sci., 34, 217–262, https://doi.org/10.1146/annurev.earth.34.031405.125026, 2006.

US EPA (Environmental Protection Agency): Our nation's air, available at https://gispub.epa.gov/air/trendsreport/ 2017, last access: 27 February 2023.

van der Werf, G. R., Randerson, J. T., Giglio, L., van Leeuwen, T. T., Chen, Y., Rogers, B. M., Mu, M., van Marle, M. J. E., Morton, D. C., Collatz, G. J., Yokelson, R. J., and Kasibhatla, P. S.: Global fire emissions estimates during 1997–2016, Earth Syst. Sci. Data, 9, 697–720, https://doi.org/10.5194/essd-9-697-2017, 2017.

Vicars, W. C. and Savarino, J.: Quantitative constraints on the ^{17}O-excess ($\Delta^{17}O$) signature of surface ozone: Ambient measurements from 50°N to 50°S using the nitrite-coated filter technique, Geochim. Cosmochim. Acta, 135, 270–287, https://doi.org/10.1016/j.gca.2014.03.023, 2014.

Vicars, W. C., Bhattacharya, S. K., Erbland, J., and Savarino, J.: Measurement of the ^{17}O-excess ($\Delta^{17}O$) of tropospheric ozone using a nitrite-coated filter, Rapid Commun. Mass Spectrom., 26, 1219–1231, https://doi.org/10.1002/rcm.6218, 2012.

Vicars, W. C., Morin, S., Savarino, J., Wagner, N. L., Erbland, J., Vince, E., Martins, J. M. F., Lerner, B. M., Quinn, P. K., Coffman, D. J., and others: Spatial and diurnal variability in reactive nitrogen oxide chemistry as reflected in the isotopic composition of atmospheric

nitrate: Results from the CalNex 2010 field study, J. Geophys. Res.-Atmos., 118, https://doi.org/10.1002/jgrd.50680, 2013.

Walker, J. M., Philip, S., Martin, R. V., and Seinfeld, J. H.: Simulation of nitrate, sulfate, and ammonium aerosols over the United States, Atmos. Chem. Phys., 12, 11213–11227, https://doi.org/10.5194/acp-12-11213-2012, 2012.

Walker, J. T., Beachley, G., Amos, H. M., Baron, J. S., Bash, J., Baumgardner, R., Bell, M. D., Benedict, K. B., Chen, X., and Clow, D. W.: Toward the improvement of total nitrogen deposition budgets in the United States, Sci. Total Environ., 691, 1328–1352, https://doi.org/10.1016/j.scitotenv.2019.07.058, 2019.

Walters, W. W. and Michalski, G.: Theoretical calculation of oxygen equilibrium isotope fractionation factors involving various NO_y molecules, OH, and H_2O and its implications for isotope variations in atmospheric nitrate, Geochim. Cosmochim. Acta, 191, 89–101, https://doi.org/10.1016/j.gca.2016.06.039, 2016.

Walters, W. W., Fang, H., and Michalski, G.: Summertime diurnal variations in the isotopic composition of atmospheric nitrogen dioxide at a small midwestern United States city, Atmos. Environ., 179, 1–11, https://doi.org/10.1016/j.atmosenv.2018.01.047, 2018.

Walters, W. W., Michalski, G., Böhlke, J. K., Alexander, B., Savarino, J., and Thiemens, M. H.: Assessing the seasonal dynamics of nitrate and sulfate aerosols at the South Pole utilizing stable isotopes, J. Geophys. Res.-Atmos., 124, 8161–8177, https://doi.org/10.1029/2019JD030517, 2019.

Wang, X., Jacob, D. J., Downs, W., Zhai, S., Zhu, L., Shah, V., Holmes, C. D., Sherwen, T., Alexander, B., and Evans, M. J.: Global tropospheric halogen (Cl, Br, I) chemistry and its impact on oxidants, Atmos. Chem. Phys., 21, 13973–13996, https://doi.org/10.5194/acp-21-13973-2021, 2021.

Wesely, M. L. and Lesht, B. M.: Comparison of RADM dry deposition algorithms with a site-specific method for inferring dry deposition, Water, Air, and Soil Pollution, 44, 273–293, https://doi.org/10.1007/BF00279259, 1989.

Zhang, L., Jacob, D. J., Knipping, E. M., Kumar, N., Munger, J. W., Carouge, C. C., Van Donkelaar, A., Wang, Y. X., and Chen, D.: Nitrogen deposition to the United States: distribution, sources, and processes, Atmos. Chem. Phys., 12, 4539–4554, https://doi.org/10.5194/acp-12-4539-2012, 2012.

CHAPTER 3

Long-term Trends in Inorganic Aerosol Chemical Composition and Chemistry at an Urban and Rural Site in the Northeastern US

Heejeong Kim[1,2], Wendell W. Walters[1,2,a], Lizzy Kysela[3], and Meredith G. Hastings[1,2]

[1]Department of Earth, Environmental, and Planetary Sciences, Brown University, Providence, RI 02912, USA.
[2]Institute at Brown for Environment and Society, Brown University, Providence, RI 02912, USA.
[3]Center for Sustainability and the Global Environment, University of Wisconsin-Madison, Madison, WI 53726, USA.
[a]now at: Department of Chemistry and Biochemistry, University of South Carolina, Columbia, SC 29208, USA.

Published in *Science of The Total Environment* (2023),

doi: 10.1016/j.scitotenv.2023.166848

Abstract

Atmospheric nitrate and sulfate are major inorganic particulate matter components that impact human and ecosystem health and air quality. Over the last several decades, emissions of the precursor gases, nitrogen oxides (NO_x = NO + NO_2) and sulfur dioxide (SO_2), have dramatically decreased in the US in response to federal regulations. However, the response in concentrations of particulate nitrate (pNO_3) and sulfate (pSO_4) have not followed predictions due to complex non-linear chemistry feedbacks that may differ amongst environments (i.e., urban vs. rural). In this study, we explored the long-term response of particle chemistry for urban and rural environments in southern New England, a region historically impacted by NO_x and SO_2 emissions. Particulate matter (PM_{10}) samples collected via the same method from 2005 to 2015 at urban and rural locations in Rhode Island were analyzed for their major inorganic components, and air mass trajectories and statistical analysis were used to identify source regions over time. Our results indicated a significant urban-rural aerosol chemical composition gradient for sampling locations within 40 km. Over time, as anthropogenic influences have decreased, the relative contribution of marine and crustal sources has increased greatly, impacting fine and coarse particle chemistry in recent years. Total mass concentrations of chemical species, particularly anthropogenic pSO_4 and particulate ammonium (pNH_4), have shown dramatic decreases over the ten years at both the urban and rural sites; however, pNO_3 concentration increased by 95 % and 57 % in the urban and rural sites, respectively, despite significant NO_x emission reductions. Our results demonstrate that changes in chemical mechanisms due to the decrease in SO_2 emissions contributed to decreases in pNH_4, along with enhanced pNO_3 concentration. Furthermore, the change in SO_2 emissions has significantly impacted the atmospheric lifetime and transport distance of pNH_4, favoring more localized contributions in recent years.

1. Introduction

Atmospheric particulate matter (PM) is a critical atmospheric pollutant originating from various natural (e.g., sea salt particles and wind-blown dust) and anthropogenic activities (e.g., industrial activities, vehicle, and combustion processes) (O'Dowd et al., 1997; Manisalidis et al., 2020; Lenschow et al., 2001; Harrison et al., 1997). PM_{10}, a particle with diameters smaller than 10 μm, has potential adverse air quality and climate change impacts as well as human and ecosystem health (Seinfeld et al, 1998; Fuzzi et al., 2015; Camargo and Alonso, 2006; Schlesinger, 2007). For example, high concentrations of PM_{10} are directly associated with the acidity of clouds, visibility degradation, and solar radiation transfer, which can lead to poor air quality and affect the atmosphere's radiative properties (Pye et al., 2020; Hyslop, 2009; Andreae et al., 2005). In terms of health effects, epidemiological studies have shown that the level of PM_{10} has a direct connection with respiratory illnesses such as asthma, pulmonary damage, or mortality rate (Donaldson et al., 2000; Wilson and Suh, 1997; Scanlon et al., 2000; Berico et al., 1997; Dominici et al., 2002; Orellano et al., 2020). Further, inorganic components in PM_{10}, such as particulate sulfate (pSO_4), particulate nitrate (pNO_3), and particulate ammonium (pNH_4), negatively impact sensitive ecosystems causing eutrophication, soil acidification, and forest degradation (Van Breemen and Van Dijk, 1988; Bobbink et al., 1998).

Over the past several decades, emissions of the precursor gases, sulfur dioxide (SO_2), and nitrogen oxides ($NO_x = NO + NO_2$), deriving from industrialization and urbanization, have caused severe PM_{10} pollution in the US. The Clean Air Act Amendments (CAAA) of 1990 were implemented in the US to reduce major environmental threats such as acid rain, urban air pollution, and toxic air emissions. In response to the CAAA in the US, SO_2 and NO_x emissions were successfully controlled with a total decrease of 73 % and 43 %, respectively, between 2005 and

2015, leading to a decrease in average PM_{10} concentrations at the national level (US EPA, 2017; NEI, 2017; Shah et al., 2018; Jaeglé et al., 2018). The US Environmental Protection Agency (EPA) has continuously monitored PM_{10} concentrations throughout the country to improve air quality and set the national air quality standards for PM_{10} (24-hour standards with one-expected exceedance forms and levels of 150 μg m^{-3}; US EPA, 2017). Long-term monitoring of speciated air pollutants has been conducted at several national monitoring networks in the US, including the Clean Air Status and Trends Network (CASTNET), the Chemical Speciation Network (CSN), the Interagency Monitoring of Protected Visual Environments (IMPROVE), the National Atmospheric Deposition Program (NADP), and the Ammonia Monitoring Network (AMoN). However, these networks utilize different techniques for sample collection depending on the network goals, such that it can be challenging to integrate data and compare measurements across the various monitoring networks. For example, the CASTNET program monitors total suspended particles (TSP) collected on a Teflon filter, primarily in rural locations, while the CSN program collects fine PM ($PM_{2.5}$) using Nylon filters in urban locations. The different types of filters have different collection biases and artifacts, making it difficult to make quantitative comparisons across networks and landscapes (i.e., urban versus rural). Compared to several national monitoring networks, our PM_{10} records are simultaneously sampled using the same methodology between rural and urban locations which motivated this research.

The northeastern US has been an important region to monitor as its high population density and transport patterns have affected the degradation of air quality (Sickles li and Shadwick, 2015). Reductions of SO_2 and NO_x in the northeastern US have been even more impressive, with decreases of 46 % and 82 %, respectively, since 2005 (NEI, 2017). However, the responses in pSO_4 and pNO_3 concentrations have not been as strong as the precursor emission reduction due to the

complex non-linear chemistry feedback that may differ for varying environments (i.e., urban versus rural and summer versus winter). For example, atmospheric chemistry model (GEOS-Chem) simulation results showed that as SO_2 and NO_x emissions decrease, aerosol pH and oxidation efficiency increase, leading to more effective secondary aerosol formation, especially for pNO_3 (Shah et al., 2018; Guo et al., 2016; Holt et al., 2015). Consequently, pNO_3 concentrations are expected to increase in the northeastern US as SO_2 emissions continuously decrease. A comprehensive understanding of aerosol chemical composition changes is clearly needed to design the emission reduction policy that can also target future particulate matter reductions.

This study aims to understand the connection between precursor emissions changes and spatiotemporal variabilities of inorganic species in PM_{10} utilizing aerosol samples that were simultaneously collected using the same protocol at an urban and rural site in the northeastern US between 2005 to 2015. In the northeastern US, particle pollution levels are exacerbated by the combination of high population density, heavily-developed industrial and transportation sectors, and natural influences (e.g., marine and crustal), making it difficult to target effective strategies for mitigating air quality. This study aims to explore key uncertainties in the production mechanisms of major anthropogenic inorganic species (e.g., pNO_3, pSO_4, and pNH_4; note that all components of particulate matter are referred to as pX, where X represents nitrate, sulfate, ammonium, sodium, etc.) in response to emission regulation implementation with an emphasis on seasonal and spatial patterns. By comparing urban and rural areas, it is possible to better understand the impacts of different emission sources and their changes on the chemistry of inorganic species in PM_{10}. Detailing the changes in oxidation chemistry and chemical feedbacks associated with the production and deposition of inorganic species can have important implications for testing

chemical model mechanisms, better predicting air quality improvements, and informing future policy recommendations.

2. Methods

2.1 Sampling and Chemical Analysis

PM_{10} samples were collected at two different environmental sites in the state of Rhode Island, United States, including downtown Providence (41.82° N, -71.41° W) and West Greenwich (41.61° N, -71.72° W), representing an urban and rural environment, respectively (Fig. 3.1). Providence has a population of 191,000 and is an urban-mixed-use region that includes commercial buildings, residential buildings, highways, and industry (Fig. 3.1b). West Greenwich has a population of 6,500, and the measurement site is in a meadow surrounded by trees. Forest and recreation fields are the major land use type in this area (Fig. 3.1b). Sample collections were conducted by the Rhode Island Department of Environmental Management (RI-DEM) and Rhode Island Department of Health (RI-DOH) using a high-volume sampler with a flow rate of 1.13 m^3 min^{-1}. Filter samples were collected on a quartz-fiber filter every six days for 24 hours, following EPA protocols (USEPA-Method IO-2.1, 1999) from 2005 to 2015. Samples were measured for total mass concentration of PM_{10} and stored at room temperature until transferred to Brown University in the summer of 2019.

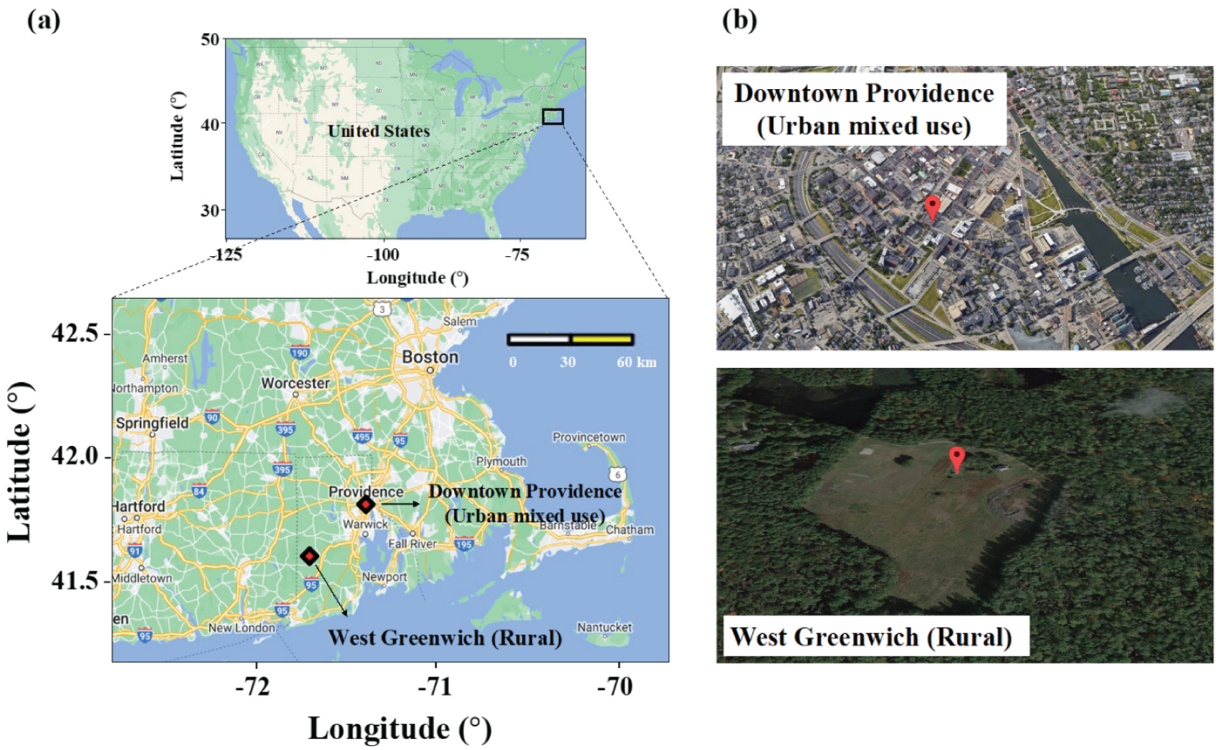

Figure 3.1. Map of the (a) United States and Rhode Island and (b) two sampling sites in Rhode Island. Major cities (urban areas), transportation routes, and sampling sites are also indicated. The image was created using Google Earth (©2023 Google).

Filter samples were extracted and analyzed for ion concentrations at Brown University. Briefly, filter cuts were taken and transferred to triple DI-rinsed Nalgene bottles and extracted in 100 mL of ultra-high purity water (MQ > 18.2 MΩ). Bottles were placed on a mechanical shaker table overnight. Filters were removed from the bottles, and then the extracted solution was filtered with a 0.2 μm Nylon Filter and placed in a freezer until subsequent analysis. A subset of filters was extracted a second time with a separate volume of 100 mL. The second extraction was found to have ion concentrations always below detection limits, such that we assume our extraction technique fully characterizes the ion concentrations. The entire 2005-2015 record was extracted for the Providence location. A subset of samples was extracted for the endpoints of the West Greenwich record, including 2005-2006 and 2014-2015.

Major inorganic ion concentrations (i.e., sodium (Na^+), potassium (K^+), calcium (Ca^{2+}), ammonium (NH_4^+), magnesium (Mg^{2+}), fluoride (F^-), chloride (Cl^-), nitrate (NO_3^-), and sulfate (SO_4^{2-})) were analyzed using ion chromatography (Dionex Integrion HPIC) employing suppressed conductivity detection. Anions were determined using a Dionex AS19-4μm guard column (4 × 50 mm) and analytical column (4 × 250 mm) with 20 mM KOH as eluent and a flow rate of 1 mL min^{-1}. Cations were analyzed using a Dionex CS-16 guard column (5 × 50 mm) analytical column (5 × 250 mm). Eluent of 30 mM methane sulfonic acid (MSA) was used to detect cations with a pump flow rate of 1 mL min^{-1}. Working standards of two different concentrations were analyzed every six samples for quality control. The limit of detection (LOD) for cations was 5.3 μM, 3.2 μM, 5.2 μM, 4.8 μM, and 4.7 μM for Na^+, NH_4^+, K^+, Mg^{2+}, and Ca^{2+}, respectively and the LOD for anions was 0.6 μM, 1.7 μM, 1.2 μM, and 4.0 μM for F^-, Cl^-, NO_3^-, and SO_4^{2-}, respectively. The average relative standard deviations (RSD) of replicate quality control standards were less than 3.4 % for all analyzed ions. For high NH_4^+ concentrations, over 250 μM, samples were rerun using standard colorimetric methods (i.e., US EPA Method 353.2) on an automated discrete UV-Vis Analyzer (SmartChem Westco Scientific Instruments, Inc.).

2.2 Sea salt and crustal calculation

The contributions of sea salt, crustal dust, and anthropogenic emissions to the PM_{10} inorganic concentrations were calculated following previous studies (Huang et al., 2008; Meng et al., 2019; Nah et al., 2021). (Note again that all components of particulate matter are referred to as pX, where X represents nitrate, sulfate, ammonium, sodium, etc).The concentration unit was converted from the concentration in solution (μM) to the concentration in the air ($\mu g\ m^{-3}$), based on the extraction volume and the amount of sampled air, which typically corresponded to 1700 m^3 for each filter. The measured pNO_3, pNH_4, and pF were assumed to be solely derived from

anthropogenic sources in this study. Other ions such as pCl, pSO_4, and soluble nonvolatile cations (NVCs, such as pNa, pK, pCa, and pMg) are expected to derive from marine or crustal origins (Sun et al., 2006; Jayarathne et al., 2014; Meng et al., 2019); thus, their contributions were calculated separately. For example, pCl in PM_{10} is generally considered to originate from sea salt with pNa or anthropogenic sources. The ratio of pCl and pNa originating from sea salt typically has a value of 1.8 (McInnes et al., 1994): if the ratio is greater, it is assumed that additional anthropogenic sources are contributing pCl (e.g., combustion processes). However, in our study, the observed pCl/pNa ratios were much lower than 1.8, indicating strong pCl depletion in the study areas, such that pNa was considered a better tracer of sea salt (see section 4.1). The sea salt (*SS*) origin of pCa, pMg, pK, and pSO_4 can be estimated using volume-weighted concentration ($\mu g\ m^{-3}$) as follows (Eq. 1 – Eq. 4; Kennish, 2019; Huang et al., 2008; Nah et al., 2021):

$$[pCa]_{SS} = 0.037 \times pNa \quad \text{(Eq. 1)}$$

$$[pMg]_{SS} = 0.012 \times pNa \quad \text{(Eq. 2)}$$

$$[pK]_{SS} = 0.037 \times pNa \quad \text{(Eq. 3)}$$

$$[pSO_4]_{SS} = 0.25 \times pNa \quad \text{(Eq. 4)}$$

In addition to sea salt, pMg, pCa, pK, and pSO_4 were considered to have a crustal origin. The contribution of crustal sources to PM_{10} was quantified using non-sea salt (*NSS*) or crustal pMg as a reference. The crustal contribution of pCa, pK, and pSO_4 was calculated as follows (Eq. 5 – Eq. 7):

$$[pMg]_{NSS} = [pMg]_{crustal} = [pMg]_{total} - [pMg]_{SS} \quad \text{(Eq. 5)}$$

$$[pCa]_{crustal} = [pMg]_{NSS} \times 1.87 \quad \text{(Eq. 6)}$$

$$[pK]_{crustal} = [pMg]_{NSS} \times 0.48 \quad \text{(Eq. 7)}$$

where 1.87 and 0.48 represent the equivalent ratio of pCa/pMg and pK/pMg in the crust, respectively (Huang et al., 2008). Mineral dust derived from calcium sulfate ($CaSO_4$) contributes to the supply of pSO_4; thus, $[pSO_4]_{crustal}$ was calculated using the pCa/pSO_4 mass-ratio (Eq. 8; Delmas, 1981).

$$[pSO_4]_{crustal} = 0.47 \times [pCa]_{crustal} \quad \text{(Eq. 8)}$$

The anthropogenic contributions of components with multiple origins, including pCa, pK, and pSO_4, were calculated as the difference between the measured total and the amount of sea salt and crustal contribution (Eq. 9 – Eq. 11; Meng et al., 2019).

$$[pSO_4]_{anthropogenic} = [pSO_4]_{total} - [pSO_4]_{SS} - [pSO_4]_{crustal} \quad \text{(Eq. 9)}$$

$$[pCa]_{anthropogenic} = [pCa]_{total} - [pCa]_{SS} - [pCa]_{crustal} \quad \text{(Eq. 10)}$$

$$[pK]_{anthropogenic} = [pK]_{total} - [pK]_{SS} - [pK]_{crustal} \quad \text{(Eq. 11)}$$

If the calculated components of crustal and anthropogenic sources were negative, the values were substituted with 0 μg m^{-3}. These treatments of negative concentrations affected ~ 0.4 % of the total data set for $[pMg]_{crustal,}$ leading to a 0.001 μg m^{-3} increase in the averaged concentration of $[pMg]_{crustal}$. Further, for anthropogenic source calculations, the treatment of negative concentrations affected 2 %, 10 %, and 28 % of the total data set for $[pSO_4]_{anthropogenic}$, $[pCa]_{anthropogenic}$, and $[pK]_{anthropogenic}$, respectively. Though negative values account for a large portion of the anthropogenic sources data set, substitution to 0 μg m^{-3} leads to only 0.001 μg m^{-3}, 0.006 μg m^{-3}, and 0.007 μg m^{-3} increase in total averaged concentration of $[pSO_4]_{anthropogenic}$, $[pCa]_{anthropogenic}$, and $[pK]_{anthropogenic}$, respectively.

2.3 Back trajectory and PSCF analysis

Air-mass back trajectories were traced using the hybrid single-particle Lagrangian integrated trajectory (HYSPLIT) model with the North American Regional Reanalysis (NARR) 12 km dataset (Stein et al., 2015). 72-hour backward trajectories of air masses arriving at 1000 m above ground level were calculated every 6 hours for the two sampling sites (Providence and West Greenwich, RI). Back trajectories were analyzed from 2005 to 2006, 2009 to 2010, and 2014 to 2015 for Providence and from 2005 to 2006 and 2014 to 2015 for West Greenwich. The trajectory data was collated with the main measured anthropogenic components, including pNO_3, pSO_4, and pNH_4 concentration data at a weekly resolution to compute the potential source contribution function (PSCF), which is a probability function indicating possible source locations (Ashbaugh et al., 1985; Zeng and Hopke, 1989; Wang et al., 2006). The PSCF analysis was calculated and plotted using the Trajstat software (Wang et al., 2009). The domain was 20 ~ 70°N and 40 ~ 110°W with horizontal resolutions of 1° × 1°. PSCF is defined as

$$PSCF_{ij} = \frac{m_{ij}}{n_{ij}} \qquad \text{(Eq. 12)}$$

where i is latitude, j is longitude, n_{ij} is the number of trajectories endpoints that fall in the grid cell, and m_{ij} is the number of trajectories endpoints above the criterion value of pollutants reaching the grid cell. To reduce the uncertainty in the cells with a small n_{ij} value, the PSCF values were multiplied by a weight function (i.e., W_{ij}) as follows:

$$\text{Weighted PSCF (WPSCF)} = W_{ij} \times \text{PSCF} \qquad \text{(Eq. 13)}$$

W_{ij} is defined as below.

$$W_{ij} = \begin{cases} 1.00, & 80 < n_{ij} \\ 0.70, & 20 < n_{ij} \leq 80 \\ 0.42, & 10 < n_{ij} \leq 20 \\ 0.05, & n_{ij} \leq 10 \end{cases} \qquad \text{(Eq. 14)}$$

2.4 Emissions inventory

The US EPA National Emissions Inventory (NEI) reports national emissions data by locations, sectors, and years. We used emission inventory data to investigate the trends in anthropogenic emissions of SO_2, NO_x, and ammonia (NH_3) for our record from 2005 to 2015 (https://www.epa.gov/air-emissions-inventories/air-pollutant-emissions-trends-data, last access: April 11, 2023). Annual emissions inventory data of SO_2, NO_x, and NH_3 were obtained for the northeastern US, including Connecticut, New Jersey, New York, Pennsylvania, Massachusetts, New Hampshire, Rhode Island, and Vermont. This region was chosen because the back trajectory data indicated significant transport to the study sites from this area.

3. Results

3.1 Inorganic chemical compositions of PM_{10}

Prior chemical composition measurements are not available for the filters used in this study. The stability and preservation of the filter samples were therefore examined via ion charge balance. The charge equivalence ratio of the sum of anions to cations exhibited a strong linear correlation for all samples ($R^2 = 0.98$; $p < 0.01$) with a slope of 1.13 ± 0.006 (Fig. 3.2). This result is likely indicative that the PM_{10} compositions have been well-preserved. We note that it is challenging to compare and contrast results from this study to results from networks such as the CSN because of the difference in collection techniques. Here we are focused on comparing the relative changes

over time in two different environments (urban vs. rural) that utilized the same sampling protocols such that the records are directly comparable.

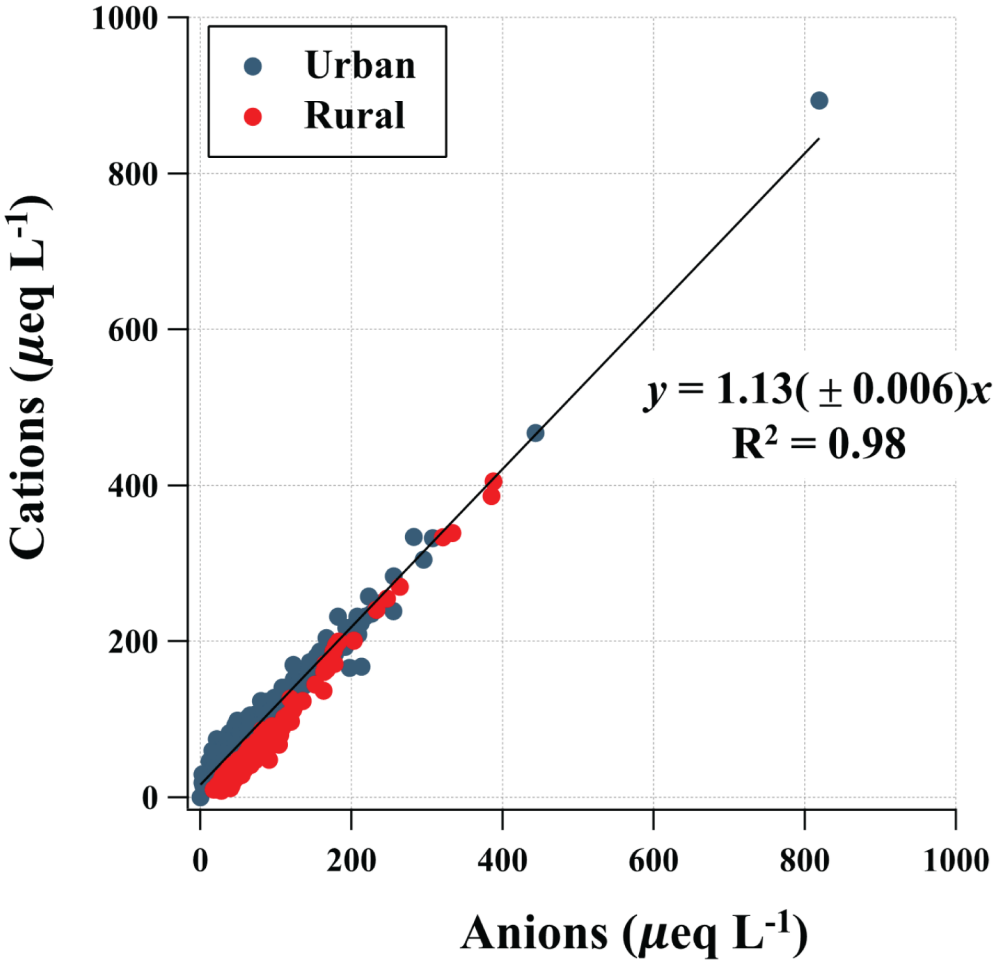

Figure 3. 2. Total cations versus total anions equivalence for all of the PM_{10} samples (n = 873) in Rhode Island from 2005 to 2015.

The time series of inorganic chemical compositions of PM_{10} observed in urban and rural areas in RI from 2005 to 2015 are presented in Fig. 3.3. For the entire measurement period, pSO_4 and pNa were the most abundant components of PM_{10} in both urban and rural areas in terms of mass fraction (Fig. S3.1). The pSO_4 and pNa account for 47 % and 21 % in the urban site and 52 % and 18 % in the rural site of the total inorganic compositions, with median values of 1.6 $\mu g\ m^{-3}$

and 0.8 μg m^{-3} for urban and 1.5 μg m^{-3} and 0.7 μg m^{-3} for rural, respectively. On the other hand, in terms of mole fraction, pNa was the most abundant species in the urban (37 %), followed by pSO_4 (20 %) and pNH_4 (18 %), while pNH_4 (36 %) was the highest in the rural area followed by pNa (29 %) and pSO_4 (21 %).

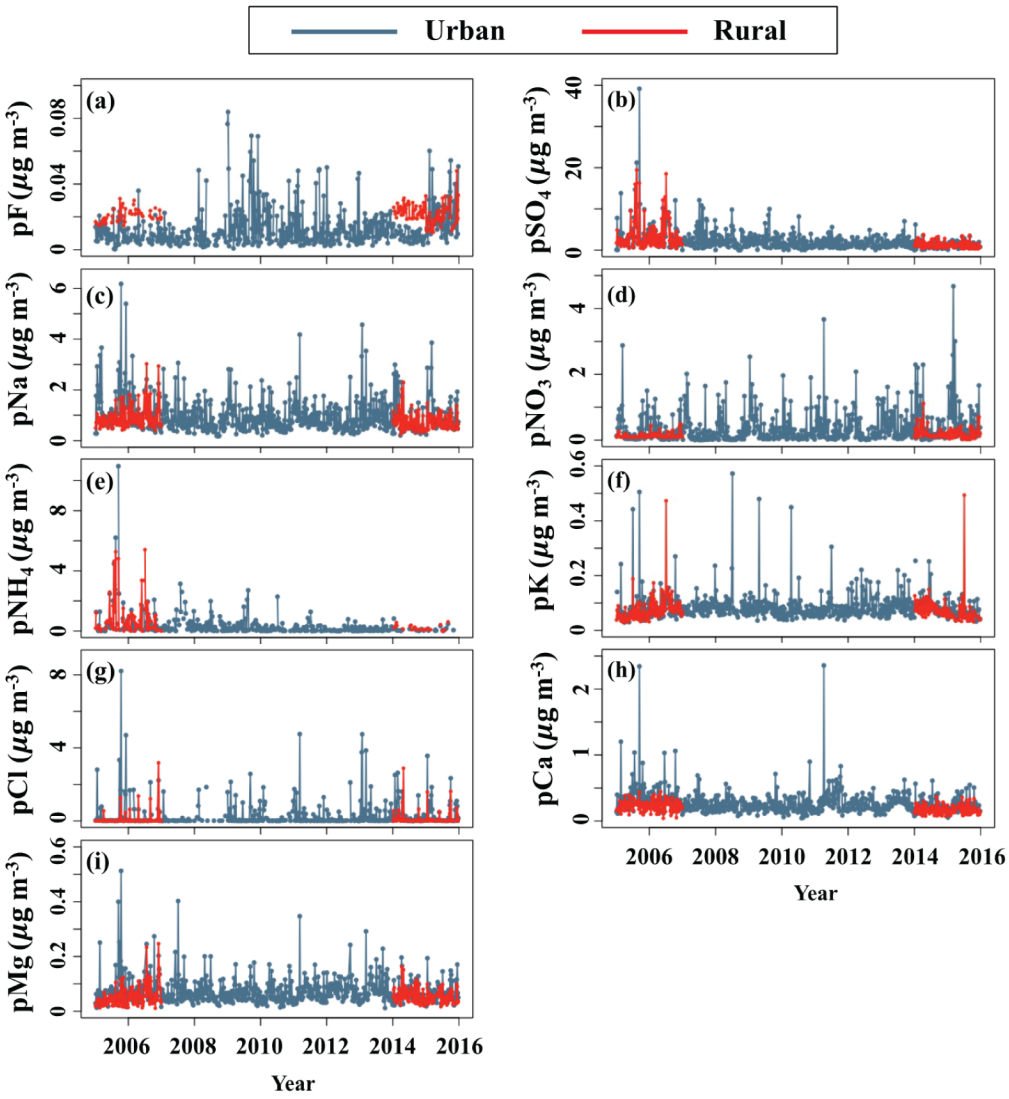

Figure 3. 3. Time series of the concentrations of inorganic components (e.g., pF, pSO_4, pNa, pNO_3, pNH_4, pK, pCl, pCa, and pMg) of PM_{10} observed in RI from 2005 to 2015.

Short-term events with elevated inorganic concentrations characterized both the urban and rural records. High concentrations of pSO_4 were frequently observed in conjunction with elevated pNH_4 concentrations at the urban site, especially in the early years of the aerosol record (Figs 3.3b, 3.3e). For example, the maximum pSO_4 and pNH_4 concentrations reached 39.2 μg m^{-3} and 11.0 μg m^{-3} in September 2005. In the urban area, a strong correlation between pSO_4 and pNH_4 exists for the entire period (R^2 = 0.93). Similarly, pNa and pCl are also well correlated (R^2 = 0.77), with a local maximum in concentrations of both species occurring in October 2005 at the urban site. Significant correlations were also observed between pSO_4 and pCa (R^2 = 0.60), pNa and pMg (R^2 = 0.58), and pNa and pNO_3 (R^2 = 0.57). In the rural area, a strong correlation was found between pSO_4 and pNH_4 (R^2 = 0.97), but their high concentration events did not overlap with the timing of those in the urban area. Moreover, high pNa concentrations in the rural area were observed with high pMg concentrations. Indeed, pNa had a stronger correlation with pMg (R^2 = 0.81) than with pCl (R^2 = 0.58). Significant correlations were also observed between pSO_4 and pCa (R^2 = 0.59) and pMg and pCl (R^2 = 0.50). The correlations for other species can be found in Fig. S3.2.

Significant spatial differences between the urban and rural sites were observed (Fig. 3.4). The spatial comparison was conducted for 2005, 2006, 2014, and 2015, which were available years for both sites. The total mass concentration of inorganic compositions in the urban area was usually higher than in the rural area ($p < 0.05$). In addition to total mass, there were differences in the inorganic components of PM_{10} between the urban and rural sites. In the rural site, pF was significantly higher than in the urban site ($p < 0.01$; Table S3.1). The average pNH_4 concentrations were higher than in the urban area, but this was not found to be statistically significantly different ($p = 0.25$). On the other hand, significantly higher concentrations of pNO_3 ($p < 0.01$) and sea salt aerosol compositions such as pNa, pCl, pMg, and pCa ($p < 0.01$) were observed in the urban area

relative to the rural area, as expected due to the location of the sites relative to the coastline (Fig. 3.1).

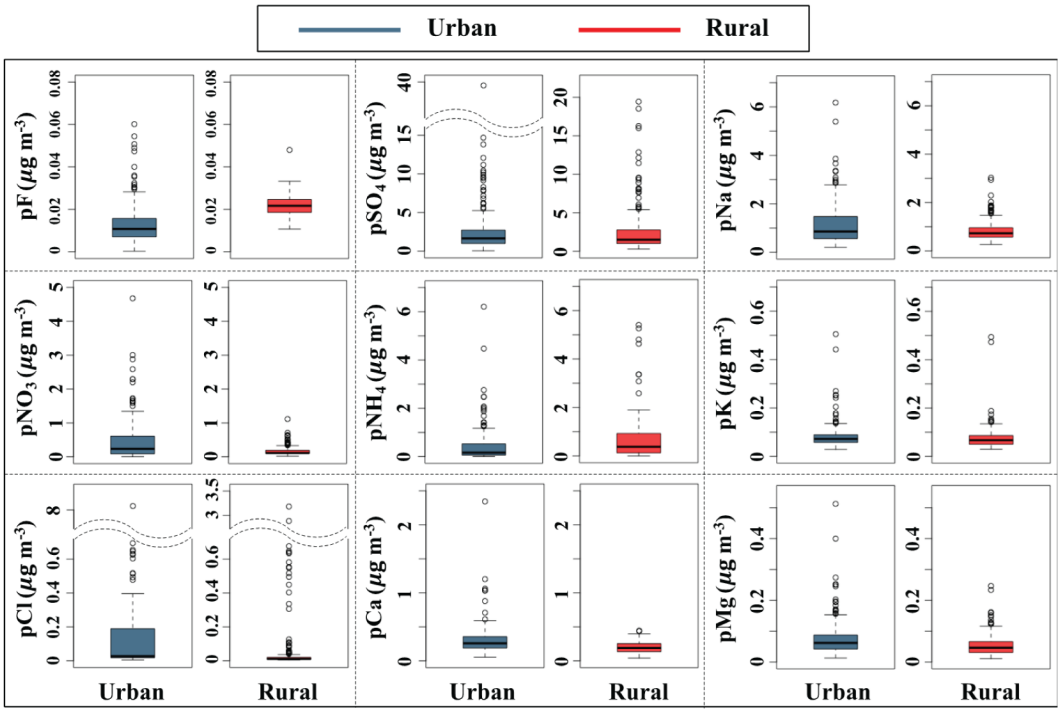

Figure 3.4. Box plots summarizing the distribution (lower extreme, lower quartile, median, upper quartile, and upper extreme) of inorganic chemical compositions of PM_{10} for urban and rural areas. The plot is for 2005, 2006, 2014, and 2015, which were available years for both urban and rural sites.

From 2005 to 2015, the total mass of inorganic chemical compositions of PM_{10} considerably decreased (Fig. 3.5a), though the percent change has dramatically slowed during the most recent 5 years (from 2011 to 2015). For the entire sampling period (2005 to 2015), the total mass of inorganic compositions decreased from 8.1 (± 8.4) $\mu g\ m^{-3}$ to 3.8 (± 2.2) $\mu g\ m^{-3}$ and from 5.3 (± 5.3) $\mu g\ m^{-3}$ to 2.6 (± 1.1) $\mu g\ m^{-3}$ for urban and rural areas, respectively. However, in the early years (2005 to 2010), the average rate of change downward in the total mass concentration of ions was -14% yr^{-1}. In contrast, in the most recent years (2011-2015), the total mass

concentration oscillates between increases and decreases, resulting in an overall change of only -2% during this period.

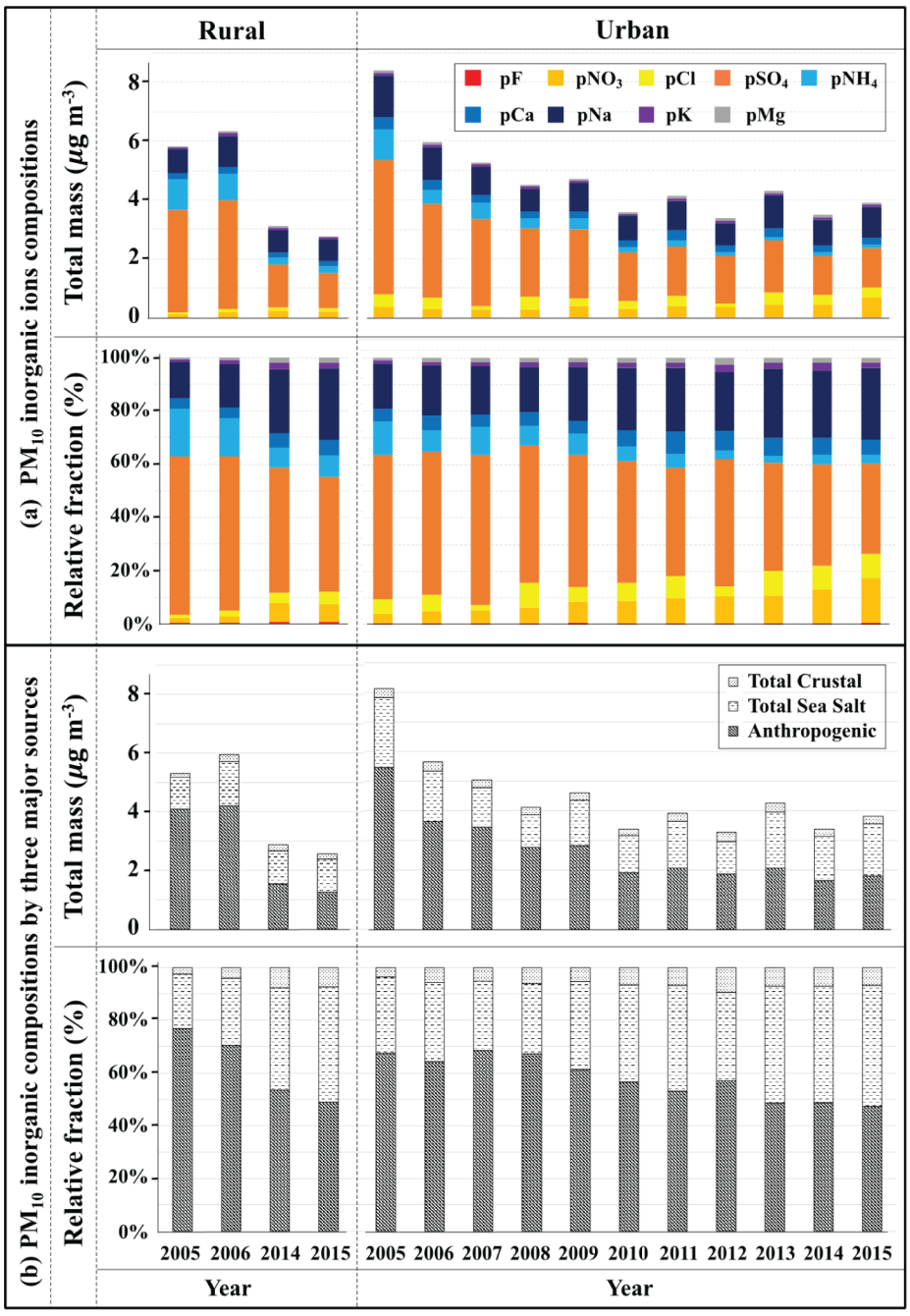

Figure 3.5. Temporal variations of total mass concentration and relative fraction of (a) PM_{10} inorganic ion compositions and (b) the compositions by major sources such as crustal, sea salt, and anthropogenic from 2005 to 2015 for urban and rural areas.

Major components of inorganic contributions to PM_{10} mass have also changed with time (Fig. 3.5a). In the early years, the major component comprising PM_{10} was pSO_4; however, pSO_4 mass has dramatically decreased in urban and rural areas in the more recent years of the aerosol record. Additionally, pNH_4 showed elevated concentrations in the early years but was barely detected at the urban and rural sites in the most recent years (2011-2015). Overall, pNH_4 and pSO_4 concentrations in PM_{10} decreased by 88 % and 70 %, and 78 % and 65 % in urban and rural areas, respectively. In contrast to the decreasing trend in pSO_4 and pNH_4 concentrations, pNO_3 concentrations have increased by 90 % and 57 % for urban and rural areas, respectively. The primary sea-salt and crustal inorganic PM_{10} components, including pNa, pK, pMg, pCa, and pCl indicated a consistent mass contribution throughout the record. As a result, the relative contributions of various inorganic components to PM_{10} have changed over time. At the beginning of the aerosol record, pSO_4 accounted for nearly two-thirds of the total PM_{10} mass, but the proportion decreased to 30 % in recent years. In concert, the relative proportions of pNa, pCl, pCa, and pNO_3 increased up to 60 % in the urban and rural areas.

The seasonality of major inorganic and anthropogenic components of pNO_3, pSO_4, and pNH_4 have changed over time from 2005 (red) to 2015 (blue) (Fig. 3.6). For pNO_3, concentrations were higher in the cold season (from Oct to Mar) than in the warm season (from Apr to Sep), and this seasonality has become more prominent in recent years. We note that recent spatiotemporal variations of pNO_3 concentrations in the northeastern US region are similar (Bekker et al., 2023; Kim et al., 2023). Contrary to pNO_3, the monthly average pSO_4 and pNH_4 concentrations have well-correlated seasonal variations over time, which were high in the warm season and low in the cold season in the early years. Comparison of the annual seasonality of pSO_4 and pNH_4 demonstrated considerable variability from the early to late 2000s. The largest decrease in pSO_4

and pNH_4 concentrations occurred in the warm season, resulting in a lack of seasonality in the latest years of the record.

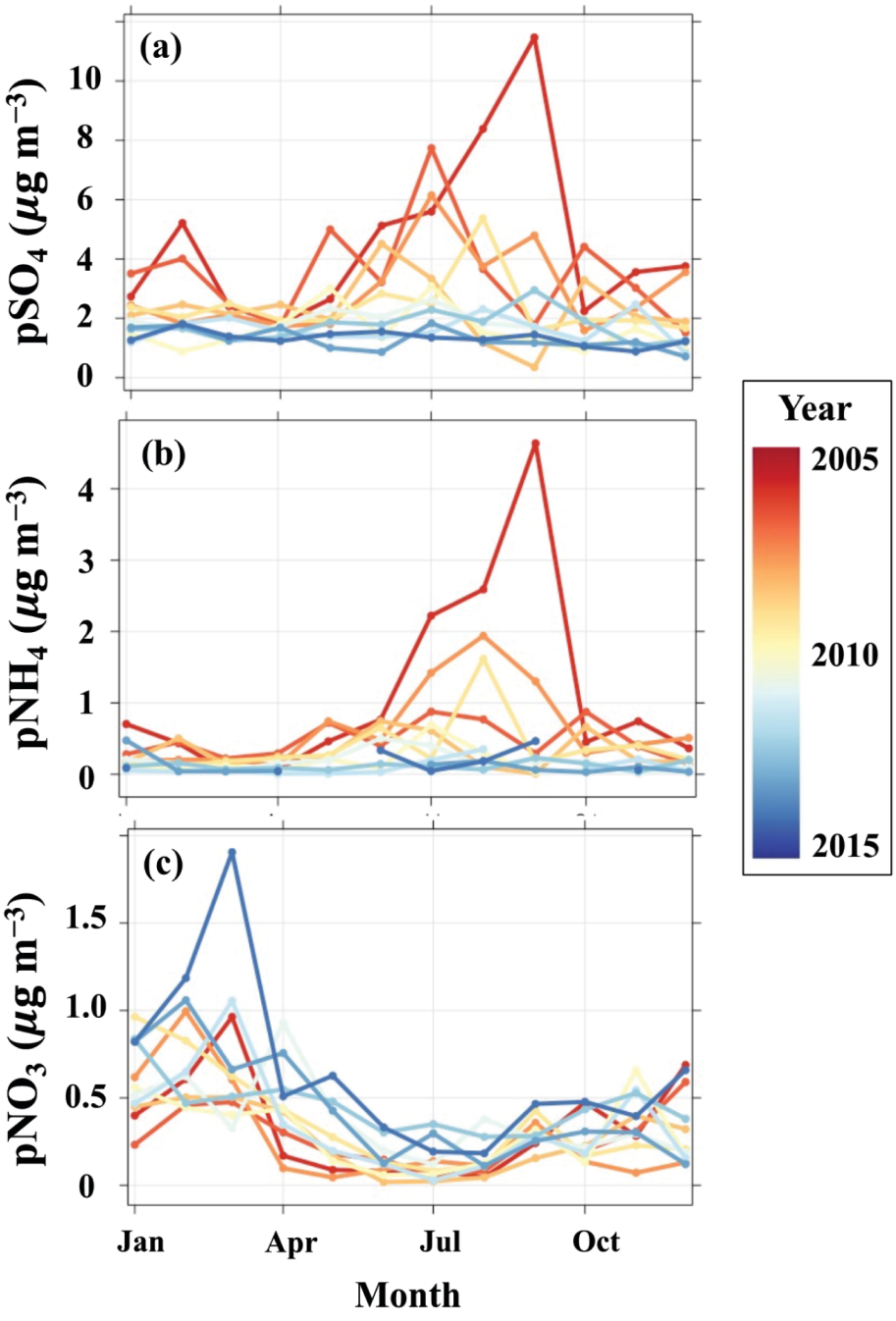

Figure 3. 6. Seasonal variations of (a) pSO_4, (b) pNH_4, and (c) pNO_3 in PM_{10} from 2005 (red) to 2015 (blue).

3.2 Source apportionment

The total marine, crustal, and anthropogenic contributions to the ionic components in PM_{10} for the ten-year record were calculated for the urban and rural sites (Fig. 3.5b). Overall, the anthropogenic inorganic contribution was the dominant source accounting for 60 % and 66 % at the urban and rural sites, respectively, followed by sea salt (34 % for urban and 29 % for rural) and crustal (6 % for urban and 5 % rural) sources (Fig. S3.3). Between the beginning and ending years of the time series, total anthropogenic contribution prominently decreased from 67 % to 47 % and from 77 % to 49 % in the urban and rural sites, respectively (Fig. 3.5b). In particular, anthropogenic pSO_4 accounted for a large portion of total anthropogenic contributions at the beginning of the record but dramatically decreased from 4.1 to 1.0 μg m^{-3} and from 3.2 to 1.0 μg m^{-3} for the urban and rural site, respectively. This change in mass corresponded to a decrease of 75 % and 70 % for the urban and rural sites, respectively. Due to the changes in anthropogenic contributions, the relative fraction of the crustal source to inorganic PM_{10} increased by a factor of 1.9 for the urban and a factor of ~3 for the rural site, and the sea salt source increased by 1.6 times for the urban site and 2.1times for the rural site. The relative contribution of sea salt and crustal sources increased despite their mass contributions remaining consistent throughout the record, which averaged 1.6 μg m^{-3} and 1.2 μg m^{-3} for sea salt and 0.3 μg m^{-3} and 0.2 μg m^{-3} for crustal at the urban and rural sites, respectively.

3.3 Potential source contribution function (PSCF) analysis

PSCF analysis was applied to identify potential sources regions of the main anthropogenic components (i.e., pNO_3, pSO_4, and pNH_4) for the 2005-2006 (beginning), 2009-2010 (middle), and 2014-2015 (end) periods of the record for Providence and 2005-2006 (beginning) and 2014-

2015 (end) for West Greenwich. The calculated PSCF values of pNO_3, pSO_4, and pNH_4 from 2005 to 2015 are shown in Fig. 3.7. The color in the maps corresponds to a probability, indicating the likelihood of a source region for a given species measured at the receptor site. The PSCF results identified the northeastern US (e.g., Connecticut, New Jersey, New York, Pennsylvania, Massachusetts, New Hampshire, Rhode Island, and Vermont) as the main sources region contributing to pNO_3, pSO_4, and pNH_4 in PM_{10} in RI. No major differences in spatial distributions of the calculated PSCF values were found between urban and rural areas (see PSCF results for West Greenwich in Fig. S3.4). Generally, PSCF results between pNO_3 and pSO_4 showed similar patterns in RI, but pNH_4 showed different tendencies. The main potential source areas of pNO_3 and pSO_4 were consistent between 2005-2015, with an average area of 458,000 km^2 and extending as much as 3,000 km from the receptor site. However, the potential source area for pNH_4 gradually diminished from 2005 to 2015, with a source contribution area of 280,150 km^2 to 22,850 km^2. Furthermore, the greatest transport distance from 2005-2006 to 2014-2015 diminished from 3,300 km to 1,300 km, respectively. Thus, the potential sources contributing to pNH_4 for 2014-2015 were more localized than in previous years. Overall, no significant transport or source-contributing region changes were identified for pNO_3 or pSO_4.

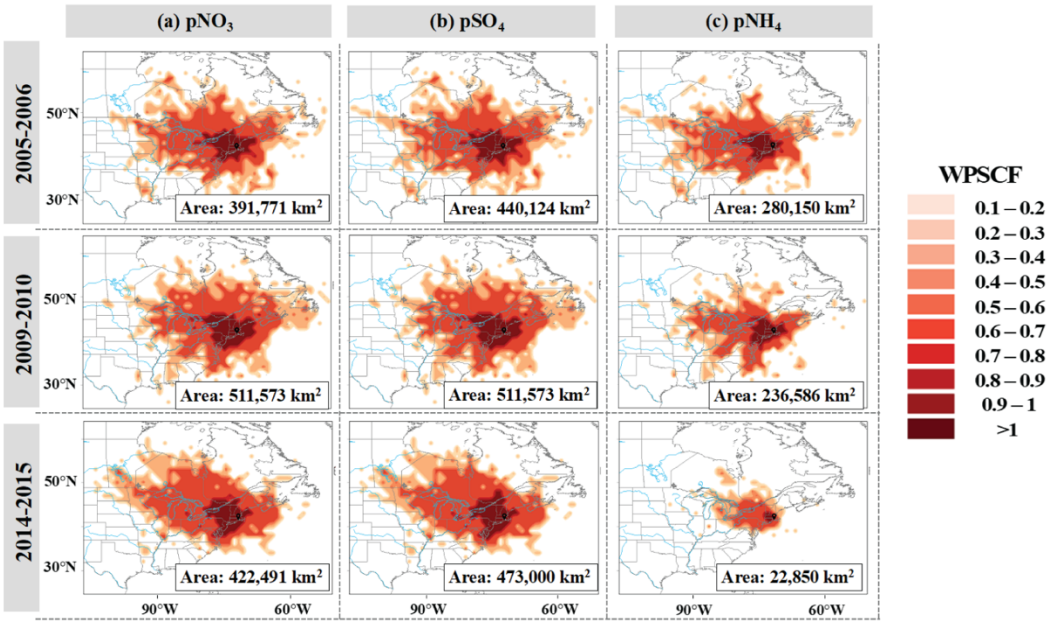

Figure 3.7. Annual mean WPSCF maps for (a) pNO_3, (b) pSO_4, and (c) pNH_4 for 2005-2006 (beginning), 2009-2010 (middle), and 2014-2015 (end).

The annual trends of the major inorganic PM_{10} anthropogenic precursor emissions, including NO_x, SO_2, and NH_3, from 2005 to 2015 for the contiguous US and the northeastern US (e.g., Connecticut, New Jersey, New York, Pennsylvania, Massachusetts, New Hampshire, Rhode Island, and Vermont) are shown in Fig. 3.8. Considerable reductions of national NO_x and SO_2 emissions have been observed throughout the US, with a total decrease of 43 % and 73 % between 2005 and 2015. Both NO_x and SO_2 emissions in the northeastern US followed the reductions by 82 % and 46 %, respectively. On the other hand, NH_3 emissions have shown little change in the US. NH_3 emissions remained relatively consistent across the US, with slight increases until 2010 and then a slight decrease until 2015. Contrary to the nationwide trend, NH_3 emissions have decreased in the northeastern US, though the relative reduction (35 %) was much lower than the NO_x and SO_2 reductions.

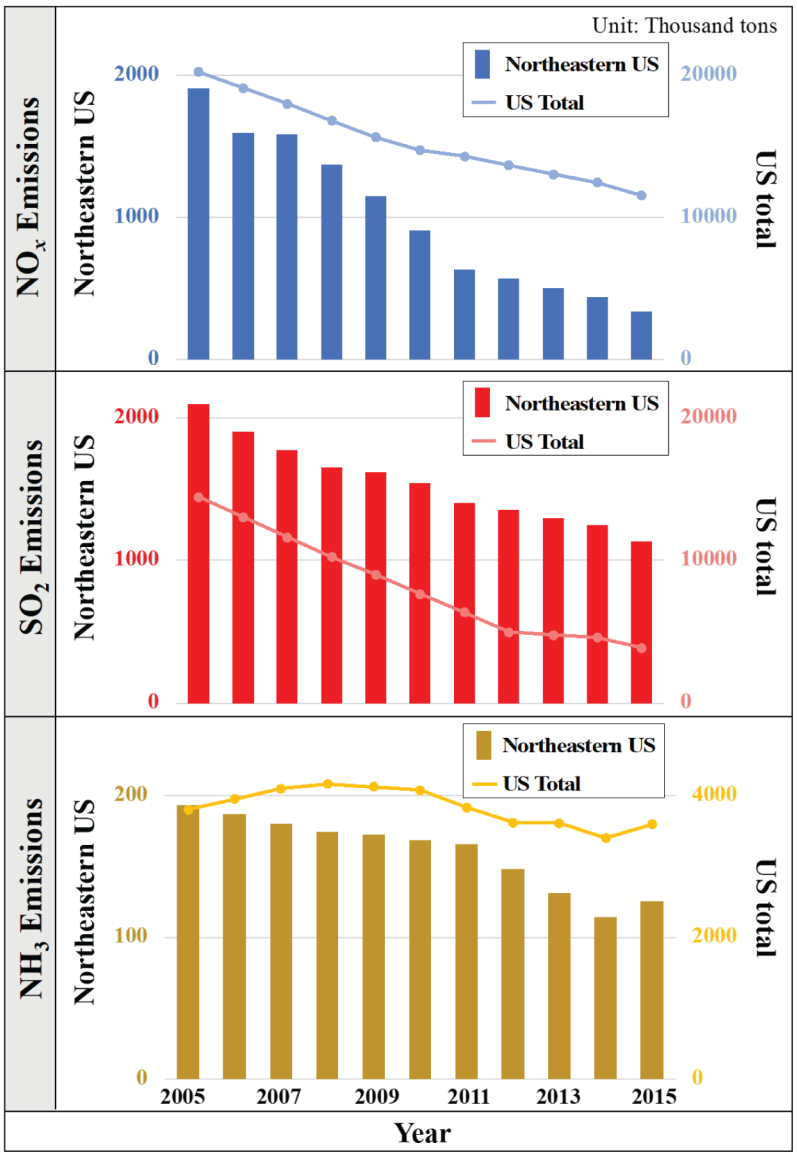

Figure 3. 8. Temporal variations for NO_x, SO_2, and NH_3 emissions in the northeastern US and total US from 2005 to 2015.

4. Discussion

4.1 Natural Sources of Inorganic PM_{10}

Over the past decade, the total mass concentration of PM_{10} from natural sources in RI has shown no significant variability, indicating a consistent contribution of crustal and sea salt sources (e.g., pCl, pSO_4, and non-volatile cations (NVCs)). However, their relative contribution to the inorganic aerosol compositions has increased due to the decrease in anthropogenic contribution in recent years. The relative importance of sea salt has gradually increased and accounted for nearly 45 % of the total mass of inorganic PM_{10} in recent years for both urban and rural sites. Moreover, sea salt aerosol compositions such as pNa, pCl, and pMg were strongly correlated in this region, suggesting that the study area is heavily influenced by the nearby marine environment (Fig. S3.2).

Sodium chloride (NaCl), magnesium chloride ($MgCl_2$), and calcium chloride ($CaCl_2$) are all major components of sea salt particles. In particular, NaCl is the most abundant component in sea salt aerosols contributing to more than 80 % of the mass. Interestingly, our record shows that pCl/pNa ratios in the study region (0.19 for the urban and 0.08 for the rural) were significantly lower than typical seawater (1.81; McInnes et al., 1994), suggesting an "aged" sea salt with a dominance of pCl depletion. The estimated pCl depletion (Eq. 15) was approximately 89 % for the urban and 95 % for the rural area, with seasonal variation ranging from 86 % in the cold season to up to 98 % in the warm season. This depletion was larger than that reported in previous studies. For example, Zhao and Gao, (2008) reported that pCl depletion varied from 14 % to 96 % depending on the particle size in Newark, New Jersey, US. In Italy, Cesari et al., (2018) also reported that pCl was depleted by about 60 %, suggesting the presence of aged sea spray at an urban background site.

% Chloride Depletion = (1.81 × pNa – pCl)/(1.81 × pNa) × 100 % (Eq. 15)

The pCl in sea salt particles can undergo acid displacement leading to the formation of gas-phase hydrochloric acid (HCl). At the same time, NVCs in sea salt interact with sulfuric acid (H_2SO_4) and nitric acid (HNO_3) by strongly modulating the aerosol acidity (Guo et al., 2018), resulting in fine and coarse aerosol formation, including sodium sulfate (Na_2SO_4; R1), sodium nitrate ($NaNO_3$; R2), and calcium sulfate ($CaSO_4$):

$2NaCl\ (s) + H_2SO_4\ (g) \rightarrow 2HCl\ (g) + Na_2SO_4\ (s)$ (R1)

$NaCl\ (s) + HNO_3\ (g) \rightarrow HCl\ (g) + NaNO_3\ (s)$ (R2)

A stronger correlation between pNa and pNO_3 (R^2 = 0.57 at the urban and 0.43 at the rural site) was observed compared to the correlation between pNa and pSO_4 (R^2 = 0.33 for the urban and 0.36 for the rural). These observations suggest that pCl was primarily displaced in the form of $NaNO_3$ by the reaction between HNO_3 and sea salt than Na_2SO_4 in this region. HCl, which is produced by pCl depletion has higher volatility relative to HNO_3, resulting in little impact on the pH (Guo et al., 2018). Further, our record also indicated that pSO_4 was well correlated with pCa (R^2 = 0.60 for the urban and 0.59 for the rural). These correlations suggest that the NVCs, particularly pNa and pCa, play an important role in neutralizing H_2SO_4 and HNO_3 in addition to pNH_4 during this period. Moreover, in recent years (e.g., 2014-2015), the correlation coefficient between pNa and pNO_3 reached up to 0.80 in the urban area (Fig. S3.6). Due to the massive reduction in atmospheric acid precursors, chloride depletion diminished from 2005 to 2015; though, it was still important for pNO_3 incorporation into aerosol. This might be related to the fact that a decrease in H_2SO_4 concentration from the SO_2 emissions reduction allows more NVCs to react with HNO_3 compared to the previous years. Therefore, our results highlight that the relative role

of $NaNO_3$ is more important to aerosol formation than in previous years, which contributes to the increase in local pNO_3 concentration together with ammonium nitrate (NH_4NO_3) in recent years. Overall, the increasing contribution of sea salt in our sites underscores the importance of pCl depletion and NVCs in controlling aerosol formation in our study area.

4.2 Anthropogenic Changes of Major Inorganic Species in PM_{10}

4.2.1. Potential Source Region Changes Between 2005 to 2015

The northeastern US and its surroundings have been identified as the main potential source region of anthropogenic pSO_4 and pNO_3, which has remained quite consistent over the 10 years (Fig. 3.7). According to the US Energy Information Administration, SO_2 and NO_x emissions from electricity generation, coal-fired power plants, domestic combustion, and manufacturing processes have been considerably cut since 1990 under the CAAA in the US (US EPA, 2017; US EIA, 2018). However, the NEI estimates that the relative SO_2 fossil-fuel combustion emissions in New England have shifted from coal-dominated (52.6% in 2008) to oil-dominated (81.6% in 2014) in recent years (NEI, 2017), with oil burning still contributing importantly to NO_x emissions. Additionally, the transportation sector still accounts for more than half of the total NO_x emissions in this region (NEI, 2017). Thus, even though precursor emissions have dramatically decreased in this region, the relative contribution to near-surface pSO_4 or pNO_3 concentration could vary depending on the emission sources over time. Note that PSCF is determined by the relative importance of the emissions from the source areas to the receptor sites, rather than the absolute amount of emissions. Therefore, given that the PSCF results consistently point to the northeastern US and its surroundings as the major sources region of pSO_4 and pNO_3 over the years, regional influences via long-range transport continue to be important in determining PM_{10} composition. However, our results also indicate clear changes in chemical influences on PM_{10} composition.

In contrast to pNO_3 and pSO_4, pNH_4 shows a significant change in the source region contribution based on the PSCF analysis. While the potential source region for pNH_4 was similar to pNO_3 and pSO_4 in the early years, it has become much more localized in recent years. Gaseous NH_3 plays an important role in neutralizing acid gases in the atmosphere and is converted into pNH_4 through gas-to-particle conversion (Seinfeld and Pandis., 2016). Accordingly, the lifetime of total ammonium, NH_x (NH_3 + pNH_4), can be determined by the reactions with acid gases, leading to the formation of pSO_4 and pNO_3 in the atmosphere. The localized trend of pNH_4 from PSCF in recent years implies that the lifetime of NH_x has decreased substantially across the years due to the reduction of pSO_4. Reduced SO_2 emissions changed the aerosol pH, affecting the equilibrated partitioning of semivolatile compounds, such as NH_4NO_3, which has increased in recent years. Due to the semivolatile characteristics of NH_4NO_3, the gas-to-particle partitioning of NH_x favors NH_3 remaining in the gas phase at the higher pH of recent years, consequently leading to a more localized source contribution to pNH_4.

Agriculture activities such as livestock waste management and fertilizer production are known to be dominant NH_3 emission sources in the US (NEI, 2017). However, in urban areas, NH_3 from vehicles and fuel-combustion emissions have been identified as important sources (Decina et al., 2017; Walters et al., 2020; 2022). As the NH_x lifetime changes with SO_2 emission change, the main source of gas-phase NH_3 for pNH_4 formation has also changed. In the early years of the observations, elevated PSCF probabilities for pNH_4 indicated that potentially significant pNH_4 source regions originated from the northeastern US, including the midwestern US and southeastern Canada, which have significant agricultural-related NH_3 emissions. Thus, long-range transport from the agriculture sector was likely the primary source of NH_3 to our measurement site in the early years. On the other hand, localized PSCF probabilities in recent years imply that potential

sources of pNH_4 have been confined within the northeastern US. This indicates that as NH_x long-range transport decreased, local NH_x emissions, such as vehicles and fuel-combustion emissions, have become increasingly important in our study sites. This is consistent with recent isotopic investigations conducted in RI, which show an important role for non-agriculture sources such as mobile and fuel-combustion emissions contributing to pNH_4 in the northeastern US (Walters et al., 2020; 2022).

4.2.2. Spatial Differences in Anthropogenic Inorganic Species

As a result of SO_2 emissions reduction in the US, the mass fraction of pSO_4 from anthropogenic sources has decreased from 2005 to 2015, implying the effectiveness of emission regulations in combating anthropogenic pSO_4 pollution. pSO_4 had no spatial difference between the urban and the rural sites ($p > 0.05$), suggesting similar background levels across the sites over the ten-year aerosol record. pNH_4 concentrations significantly decreased by nearly 96 % at both sites (Fig. 3.5a), which was considerably higher than the reduction in NH_3 emissions in the northeastern US (34.8 %). While the spatial differences of pNH_4 were insignificant between the urban and rural areas in the early years ($p = 0.35$), significant spatial differences were observed for pNH_4 in recent years ($p < 0.05$).

Throughout the record, significant spatial differences were observed for pNO_3 despite the close location of the two sites ($p < 0.01$). Higher pNO_3 concentration was always observed in the urban site than in the rural site, which indicates that local NO_x emissions are important sources of particulate pNO_3 concentrations in the urban area. On the other hand, low NO_x concentrations in the rural area well represent the rural background of pNO_3. Surprisingly, the pNO_3 concentration trend did not follow the large NO_x emissions reduction, as pNO_3 increased over the ten-year aerosol record. Overall, the changes in pSO_4, pNH_4, and pNO_3 that did not always follow the change in

precursor emissions highlight the importance of the non-linear chemistry associated with their formation. This chemistry is important to understand to make recommendations for decreasing the concentrations of these significant anthropogenic components of PM.

4.2.3. Changes in Seasonality

The influences of emission regulations on major anthropogenic inorganic species (e.g., pNO_3, pSO_4, and pNH_4) were well reflected in seasonality changes of the aerosol record. For example, while summertime pSO_4 peaks were mainly observed in the early years (e.g., 2005-2007), no significant seasonality was observed in recent years (e.g., 2013-2015). In the polluted mid-latitudes, SO_2 is oxidized to pSO_4 not only through gaseous hydroxyl radical (OH) but also through aqueous S(IV) oxidation in clouds involving hydrogen peroxide (H_2O_2), ozone (O_3), or oxygen (O_2), with a dependence on aerosol acidity (R3-R6; Alexander et al., 2009; Stockwell and Calvert, 1983; Harris et al., 2013).

$$SO_2 + 2OH \rightarrow H_2SO_4\,(g) \qquad (R3)$$

$$SO_2 + O_2 + H_2O \rightarrow H_2SO_4\,(aq) \qquad (R4)$$

$$SO_2 + H_2O_2 \rightarrow H_2SO_4\,(aq) \qquad (R5)$$

$$H_2SO_4 \rightarrow SO_4^{2-} + 2H^+ \qquad (R6)$$

In the eastern US, model simulations suggest that S(IV) oxidation via H_2O_2 in cloud water contributes to 46 % of pSO_4 formation, and gas phase reaction with OH is 35 % (Shah et al., 2018). Our observations of summertime pSO_4 peaks in the early aerosol record (e.g., 2005-2007) imply that the oxidants were sufficiently available to fully oxidize SO_2 to pSO_4 due to the photochemical production of oxidants relevant to SO_2 oxidation. On the other hand, SO_2 oxidation in winter early in the aerosol record was likely limited by oxidant availability, specifically in cloud water, due to

reduced sunlight and high SO_2 concentrations relative to oxidant availability. Compared to summertime, we observed small wintertime pSO_4 peaks in the early years of the aerosol record that might be related to high SO_2 emissions due to increased seasonal heating demands. Compared to the early years of the aerosol record, pSO_4 peaks have been considerably flattened in recent years (e.g., 2013-2015) in both winter and summer. Wintertime SO_2 oxidation has become less limited by the availability of oxidants due to the reduction of SO_2 emissions, such that a greater proportion of SO_2 emissions have been oxidized during winter in recent years. This change in oxidation chemistry explains the relative change in pSO_4 concentrations that decreased less during winter (61 %) compared to summer (76 %) for 2005-2015.

The seasonality of pNH_4 closely followed pSO_4 and exhibited a dramatic change despite a limited change in precursor NH_3 emissions (Figs 3.6, 3.8). NH_3 plays an important role in controlling aerosol acidity by neutralizing H_2SO_4, HNO_3, and HCl (Seinfeld and Pandis., 2016). When NH_3 is sufficiently available, NH_3 preferentially neutralizes H_2SO_4 to form ammonium bisulfate (NH_4HSO_4) and ammonium sulfate ($(NH_4)_2SO_4$) due to the low saturation vapor pressure of H_2SO_4 by the reaction (R7) (Seinfeld and Pandis., 2016). The excess NH_3 then reacts with HNO_3 to form NH_4NO_3 through reaction (R8). Therefore, the pSO_4 and pNO_3 formation is sensitive to NH_3 concentration, temperature, and relative humidity (RH).

$$H_2SO_4\ (g) + 2NH_3\ (g) \rightarrow (NH_4)_2SO_4\ (s) \qquad \text{(R7)}$$

$$HNO_3\ (g) + NH_3\ (g) \rightarrow NH_4NO_3\ (s) \qquad \text{(R8)}$$

Given the observed strong correlation between pSO_4 and pNH_4 (R^2 = 0.96), high pNH_4 concentration in the summer in the early years is associated with enhanced NH_4HSO_4 and $(NH_4)_2SO_4$ formation. In the early years, anthropogenic inorganic PM_{10} was dominated by

NH_4HSO_4 and $(NH_4)_2SO_4$, leading to high aerosol acidity (low pH). However, as SO_2 emissions have decreased in recent years, the seasonality of pNH_4 diminished. In more recent years, the reaction with HNO_3 to form NH_4NO_3 has become important for pNH_4 formation and, therefore, more important for fine mode PM, leading to an increase in particle pH for PM_{10}. This is supported by the significantly increased correlation coefficient between pNO_3 and pNH_4 (from -0.24 to 0.56) from 2005 to 2015, especially in the urban area (Fig. S3.6). In the early years, when SO_2 concentrations were high, pNH_4 concentrations and coarse mode acidity were dependent upon the availability of SO_2 in this region. Whereas in the recent years of the aerosol record, NH_3 has been a more important factor in controlling fine pNO_3 concentration by the reaction with HNO_3 (R8).

Compared to pSO_4 and pNH_4, the pNO_3 seasonality has become more pronounced in recent years. In general, pNO_3 was characterized by higher concentration in the cold season than in the warm season. The gas-to-particle partitioning rate of HNO_3/pNO_3 is mainly governed by temperature, RH, and aerosol pH (R9). The partitioning to pNO_3 is favorably shifted toward the particle phase at colder temperatures, higher RH, and higher particle pH (Seinfeld and Pandis., 2016). During the early years of the aerosol record, high pSO_4 content led to acidic aerosol pH, causing HNO_3/pNO_3 partitioning to favor the gaseous phase, leading to low pNO_3 concentration.

$$HNO_3\ (g) \leftrightarrow H^+ + NO_3^- \qquad \text{(R9)}$$

In the more recent years of the aerosol record, pNO_3 concentrations have continuously increased, despite the reduction of NO_x emissions. This non-linear response in pNO_3 concentration in the northeastern US might be related to changes in the relative contribution from local production, long-range transport, or chemical mechanisms associated with pNO_3 formation (Bekker et al., 2023; Kim et al., 2023). In terms of chemical influences, as pSO_4 concentration decreases, particle pH increases, creating more favorable conditions to shift from gaseous HNO_3 to pNO_3, resulting

in higher concentrations and significant seasonality of pNO_3 in the more recent years of the aerosol record.

In Guo et al., 2016 and Shah et al., 2018, the fraction of pNO_3 was simulated as a function of particle pH and temperature over the eastern US using a PM thermodynamic model. The pNO_3 fraction was sensitive to both aerosol pH and temperature change. In particular, the pNO_3 fraction exponentially increases under the same temperature as aerosol pH increases. In these model simulations, the pNO_3 fraction in an early year (e.g., 2007) was less significant than in a recent year (e.g., 2015) due to the low particle pH caused by high pSO_4 content. Further, the pNO_3 fraction was modeled to be insensitive to temperature in the early year, consistent with our record. However, the temperature sensitivity has gradually increased as pH increased due to the decrease in SO_2 emissions. Therefore, pNO_3 formation has become more sensitive to temperature under changing atmospheric acidity due to emission regulations, leading to greater NH_4NO_3 formation at colder temperatures. This change contributes to the more pronounced seasonality of pNO_3 in wintertime in more recent years of the aerosol record. Overall, pNO_3 formation is limited by the availability of NH_3 and NVCs in the eastern US (Shah et al., 2018; Guo et al., 2018; Park et al., 2004), and further, chemical feedbacks driven by emission reductions impact pNO_3 enhancement as pSO_4 decreases.

5. Conclusion

We observed significant spatial-temporal variations of inorganic chemical species in PM_{10} in urban and rural areas in southern New England from 2005 to 2015. Overall, we found that anthropogenic and natural sources influence aerosol formation in our study area. In response to emission regulation, the reduction of acid rain precursors (i.e., SO_2 and NO_x) and NH_3 emissions

have changed aerosol acidity over the years. Our records show that pSO_4 from anthropogenic sources has considerably decreased, implying the effectiveness of emission control on pSO_4 concentrations. Conversely, the reduction in SO_2 emissions promotes pNO_3 formation by releasing excess NH_3, decreasing aerosol acidity. Despite the significant reduction in NO_x emissions, pNO_3 has reversely responded with an increase of 76 % from 2005 to 2015. The lack of a pNO_3 decrease was driven by the chemical mechanism associated with pNO_3 partitioning. Our results indicated that the potential source regions contributing to pSO_4 and pNO_3 remain relatively unchanged over time, but better constraints are needed to pinpoint precursor emission source changes in these regions.

Compared to pSO_4 and pNO_3, the fate of pNH_4 was more affected by interaction with other gases, aerosols, and fine particles. The reduction in SO_2 emissions has resulted in excess NH_3 being available to neutralize HNO_3, leading to an increase in fine pNO_3 with a reduction in pNH_4. Further, the relative importance of urban NH_3 emissions is gradually increasing in recent years, which might continuously affect the neutralizing and oxidizing capacity of the atmosphere as well as $PM_{2.5}$ and PM_{10} concentrations in the future. Our observations support modeling studies that have suggested that pNO_3 would continue to increase since 2015, due to changes in atmospheric acidity (e.g., Shah et al., 2018). Additionally, regulating both local and transported sources of NH_x emissions may represent a more effective way to mitigate air quality, considering pNO_3 formation is limited by the availability of NH_3 in the northeastern US.

It is also critical to detail the role natural sources, such as sea salt and crustal material, play as they significantly affect aerosol chemistry at our study sites. The pNa and pCl act as an indicator of sea salt influence, and low pCl/pNa ratios suggested that pCl depletion (about 79 % of Cl^- at both sites) was dominant in the study region. Depleted pCl in sea salt aerosol allows more NVCs

to react with H_2SO_4 and HNO_3 with aerosol acidity neutralization, leading to a strong correlation between pNa and pNO_3. Overall, natural sources (e.g., sea salt and crustal) play an important role, and their influence on local production of fine and coarse PM levels has increased as anthropogenic emissions have decreased. Our results provide crucial insights into the complex relationship between atmospheric aerosol chemistry and emissions reduction. Considering similarities seen in recent aerosol chemistry across the northeastern US region (Bekker et al., 2023; Kim et al., 2023), these findings are likely broadly applicable, especially in urban coastal regions where significant NO_x, SO_2, and NH_3 emissions are present such as in western Europe and eastern China.

6. Acknowledgments

We thank Ruby Ho for laboratory assistance. We are grateful to the Rhode Island Department of Environmental Management (RI-DEM) and the Rhode Island Department of Health (RI-DOH).

7. References

Alexander, B., Hastings, M.G., Allman, D.J., Dachs, J., Thornton, J.A., Kunasek, S.A., 2009. Quantifying atmospheric nitrate formation pathways based on a global model of the oxygen isotopic composition ($\Delta^{17}O$) of atmospheric nitrate. Atmospheric Chemistry and Physics 9, 5043–5056.

Andreae, M.O., Jones, C.D., Cox, P.M., 2005. Strong present-day aerosol cooling implies a hot future. Nature 435, 1187–1190.

Ashbaugh, L.L., Malm, W.C., Sadeh, W.Z., 1985. A residence time probability analysis of sulfur concentrations at Grand Canyon National Park. Atmospheric Environment (1967) 19, 1263–1270.

Bekker, C., Walters, W.W., Murray, L.T., Hastings, M.G., 2023. Nitrate chemistry in the northeast US–Part 1: Nitrogen isotope seasonality tracks nitrate formation chemistry. Atmospheric Chemistry and Physics 23, 4185–4201.

Berico, M., Luciani, A., Formignani, M., 1997. Atmospheric aerosol in an urban area—measurements of TSP and PM_{10} standards and pulmonary deposition assessments. Atmospheric Environment 31, 3659–3665.

Bobbink, R., Hornung, M., Roelofs, J.G., 1998. The effects of air-borne nitrogen pollutants on species diversity in natural and semi-natural European vegetation. Journal of ecology 86, 717–738.

Camargo, J.A., Alonso, Á., 2006. Ecological and toxicological effects of inorganic nitrogen pollution in aquatic ecosystems: a global assessment. Environment international 32, 831–849.

Cesari, D., De Benedetto, G.E., Bonasoni, P., Busetto, M., Dinoi, A., Merico, E., Chirizzi, D., Cristofanelli, P., Donateo, A., Grasso, F.M., 2018. Seasonal variability of $PM_{2.5}$ and PM_{10} composition and sources in an urban background site in Southern Italy. Science of the Total Environment 612, 202–213.

Decina, S.M., Templer, P.H., Hutyra, L.R., Gately, C.K., Rao, P., 2017. Variability, drivers, and effects of atmospheric nitrogen inputs across an urban area: emerging patterns among human activities, the atmosphere, and soils. Science of the Total Environment 609, 1524–1534.

Dominici, F., Daniels, M., Zeger, S.L., Samet, J.M., 2002. Air pollution and mortality: estimating regional and national dose-response relationships. Journal of the American Statistical Association 97, 100–111.

Donaldson, K., Ian Gilmour, M., MacNee, W., 2000. Asthma and PM_{10}. Respiratory research 1, 12–15.

Fuzzi, S., Baltensperger, U., Carslaw, K., Decesari, S., Denier van der Gon, H., Facchini, M.C., Fowler, D., Koren, I., Langford, B., Lohmann, U., 2015. Particulate matter, air quality and climate: lessons learned and future needs. Atmospheric chemistry and physics 15, 8217–8299.

Guo, H., Nenes, A., Weber, R.J., 2018. The underappreciated role of nonvolatile cations in aerosol ammonium-sulfate molar ratios. Atmospheric Chemistry and Physics 18, 17307–17323.

Guo, H., Sullivan, A.P., Campuzano-Jost, P., Schroder, J.C., Lopez-Hilfiker, F.D., Dibb, J.E., Jimenez, J.L., Thornton, J.A., Brown, S.S., Nenes, A., 2016. Fine particle pH and the partitioning of nitric acid during winter in the northeastern United States. Journal of Geophysical Research: Atmospheres 121, 10–355.

Harris, E., Sinha, B., Van Pinxteren, D., Tilgner, A., Fomba, K.W., Schneider, J., Roth, A., Gnauk, T., Fahlbusch, B., Mertes, S., 2013. Enhanced role of transition metal ion catalysis during in-cloud oxidation of SO_2. science 340, 727–730.

Harrison, R.M., Deacon, A.R., Jones, M.R., Appleby, R.S., 1997. Sources and processes affecting concentrations of PM_{10} and $PM_{2.5}$ particulate matter in Birmingham (UK). Atmospheric environment 31, 4103–4117.

Holt, J., Selin, N.E., Solomon, S., 2015. Changes in inorganic fine particulate matter sensitivities to precursors due to large-scale US emissions reductions. Environmental Science & Technology 49, 4834–4841.

Huang, K., Zhuang, G., Xu, C., Wang, Y., Tang, A., 2008. The chemistry of the severe acidic precipitation in Shanghai, China. Atmospheric Research 89, 149–160.

Hyslop, N.P., 2009. Impaired visibility: the air pollution people see. Atmospheric Environment 43, 182–195.

Jaeglé, L., Shah, V., Thornton, J.A., Lopez-Hilfiker, F.D., Lee, B.H., McDuffie, E.E., Fibiger, D., Brown, S.S., Veres, P., Sparks, T.L., 2018. Nitrogen oxides emissions, chemistry, deposition, and

export over the Northeast United States during the WINTER aircraft campaign. Journal of Geophysical Research: Atmospheres 123, 12–368.

Jayarathne, T., Stockwell, C.E., Yokelson, R.J., Nakao, S., Stone, E.A., 2014. Emissions of fine particle fluoride from biomass burning. Environmental science & technology 48, 12636–12644.

Kennish, M.J., 2019. Practical handbook of marine science. crc press.

Kim, H., Walters, W.W., Bekker, C., Murray, L.T., Hastings, M.G., 2023. Nitrate chemistry in the northeast US–Part 2: Oxygen isotopes reveal differences in particulate and gas-phase formation. Atmospheric Chemistry and Physics 23, 4203–4219.

Lenschow, P., Abraham, H.-J., Kutzner, K., Lutz, M., Preuß, J.-D., Reichenbächer, W., 2001. Some ideas about the sources of PM_{10}. Atmospheric environment 35, S23–S33.

Manisalidis, I., Stavropoulou, E., Stavropoulos, A., Bezirtzoglou, E., 2020. Environmental and health impacts of air pollution: a review. Frontiers in public health 14.

McInnes, L.M., Covert, D.S., Quinn, P.K., Germani, M.S., 1994. Measurements of chloride depletion and sulfur enrichment in individual sea-salt particles collected from the remote marine boundary layer. Journal of Geophysical Research: Atmospheres 99, 8257–8268.

Meng, Y., Zhao, Y., Li, R., Li, J., Cui, L., Kong, L., Fu, H., 2019. Characterization of inorganic ions in rainwater in the megacity of Shanghai: Spatiotemporal variations and source apportionment. Atmospheric Research 222, 12–24.

Nah, T., Yang, J., Wang, J., Sullivan, A.P., Weber, R.J., 2021. Fine Aerosol Acidity and Water during Summer in the Eastern North Atlantic. Atmosphere 12, 1040.

NEI (National Emissions Inventory): Retrieved from the United States Environmental Protection Agency, https://www.epa.gov/air-emissions-inventories/2017-national-emissions-inventory-nei-data (last access: 24 April 2023), 2017.

O'Dowd, C.D., Smith, M.H., Consterdine, I.E., Lowe, J.A., 1997. Marine aerosol, sea-salt, and the marine sulphur cycle: A short review. Atmospheric Environment 31, 73–80.

Orellano, P., Reynoso, J., Quaranta, N., Bardach, A., Ciapponi, A., 2020. Short-term exposure to particulate matter (PM_{10} and $PM_{2.5}$), nitrogen dioxide (NO_2), and ozone (O_3) and all-cause and cause-specific mortality: Systematic review and meta-analysis. Environment international 142, 105876.

Park, R.J., Jacob, D.J., Field, B.D., Yantosca, R.M., Chin, M., 2004. Natural and transboundary pollution influences on sulfate-nitrate-ammonium aerosols in the United States: Implications for policy. Journal of Geophysical Research: Atmospheres 109.

Pye, H.O., Nenes, A., Alexander, B., Ault, A.P., Barth, M.C., Clegg, S.L., Collett Jr, J.L., Fahey, K.M., Hennigan, C.J., Herrmann, H., 2020. The acidity of atmospheric particles and clouds. Atmospheric chemistry and physics 20, 4809–4888.

Scanlon, P.D., Connett, J.E., Waller, L.A., Altose, M.D., Bailey, W.C., Sonia Buist, A., e Lung Health Study Research Group, D.P.T. for th, 2000. Smoking cessation and lung function in mild-

to-moderate chronic obstructive pulmonary disease: the Lung Health Study. American Journal of respiratory and critical care medicine 161, 381–390.

Schlesinger, R.B., 2007. The health impact of common inorganic components of fine particulate matter ($PM_{2.5}$) in ambient air: a critical review. Inhalation toxicology 19, 811–832.

Seinfeld, J.H., 1998. Clouds, contrails and climate. Nature 391, 837–838.

Seinfeld, J.H., Pandis, S.N., 2016. Atmospheric chemistry and physics: from air pollution to climate change. John Wiley & Sons.

Shah, V., Jaeglé, L., Thornton, J.A., Lopez-Hilfiker, F.D., Lee, B.H., Schroder, J.C., Campuzano-Jost, P., Jimenez, J.L., Guo, H., Sullivan, A.P., 2018. Chemical feedbacks weaken the wintertime response of particulate sulfate and nitrate to emissions reductions over the eastern United States. Proceedings of the National Academy of Sciences 115, 8110–8115.

Sickles Ii, J.E., Shadwick, D.S., 2015. Air quality and atmospheric deposition in the eastern US: 20 years of change. Atmospheric Chemistry and Physics 15, 173–197.

Stein, A.F., Draxler, R.R., Rolph, G.D., Stunder, B.J., Cohen, M.D., Ngan, F., 2015. NOAA's HYSPLIT atmospheric transport and dispersion modeling system. Bulletin of the American Meteorological Society 96, 2059–2077.

Stockwell, W.R., Calvert, J.G., 1983. The mechanism of the HO-SO_2 reaction. Atmospheric Environment (1967) 17, 2231–2235.

Sun, Y., Zhuang, G., Tang, A., Wang, Y., An, Z., 2006. Chemical characteristics of $PM_{2.5}$ and PM_{10} in haze-fog episodes in Beijing. Environmental science & technology 40, 3148–3155.

US EIA (Energy Information Administration), 2018: Changes in coal sector led to less SO_2 and NO_x emissions from electric power industry, https://www.eia.gov/todayinenergy/detail.php?id=37752 (last access: 24 April 2023).

US EPA (Environmental Protection Agency), 2017: Our nation's air, https://gispub.epa.gov/air/trendsreport/2017 (last access: 24 April 2023).

USEPA—Method IO-2.1, 1999. "IO Compendium Method IO-2.1: Compendium of Methods for the Determination of Inorganic Compounds in Ambient Air: Sampling of Ambient Air for Total Suspended Particulate Matter (SPM) and PM_{10} Using High Volume (HV) Sampler." EPA/625/R-96/010a.

Van Breemen, N., Van Dijk, H.F.G., 1988. Ecosystem effects of atmospheric deposition of nitrogen in the Netherlands. Environmental pollution 54, 249–274.

Walters, W.W., Karod, M., Willcocks, E., Baek, B.H., Blum, D.E., Hastings, M.G., 2022. Quantifying the importance of vehicle ammonia emissions in an urban area of northeastern USA utilizing nitrogen isotopes. Atmospheric Chemistry and Physics 22, 13431–13448.

Walters, W.W., Song, L., Chai, J., Fang, Y., Colombi, N., Hastings, M.G., 2020. Characterizing the spatiotemporal nitrogen stable isotopic composition of ammonia in vehicle plumes. Atmospheric Chemistry and Physics 20, 11551–11567.

Wang, Y.Q., Zhang, X.Y., Arimoto, R., 2006. The contribution from distant dust sources to the atmospheric particulate matter loadings at XiAn, China during spring. Science of the Total Environment 368, 875–883.

Wang, Y.Q., Zhang, X.Y., Draxler, R.R., 2009. TrajStat: GIS-based software that uses various trajectory statistical analysis methods to identify potential sources from long-term air pollution measurement data. Environmental Modelling & Software 24, 938–939.

Wilson, W.E., Suh, H.H., 1997. Fine particles and coarse particles: concentration relationships relevant to epidemiologic studies. Journal of the Air & Waste Management Association 47, 1238–1249.

Zeng, Y., Hopke, P.K., 1989. A study of the sources of acid precipitation in Ontario, Canada. Atmospheric Environment (1967) 23, 1499–1509.

Zhao, Y., Gao, Y., 2008. Acidic species and chloride depletion in coarse aerosol particles in the US east coast. Science of the total Environment 407, 541–547.

8. Supplementary

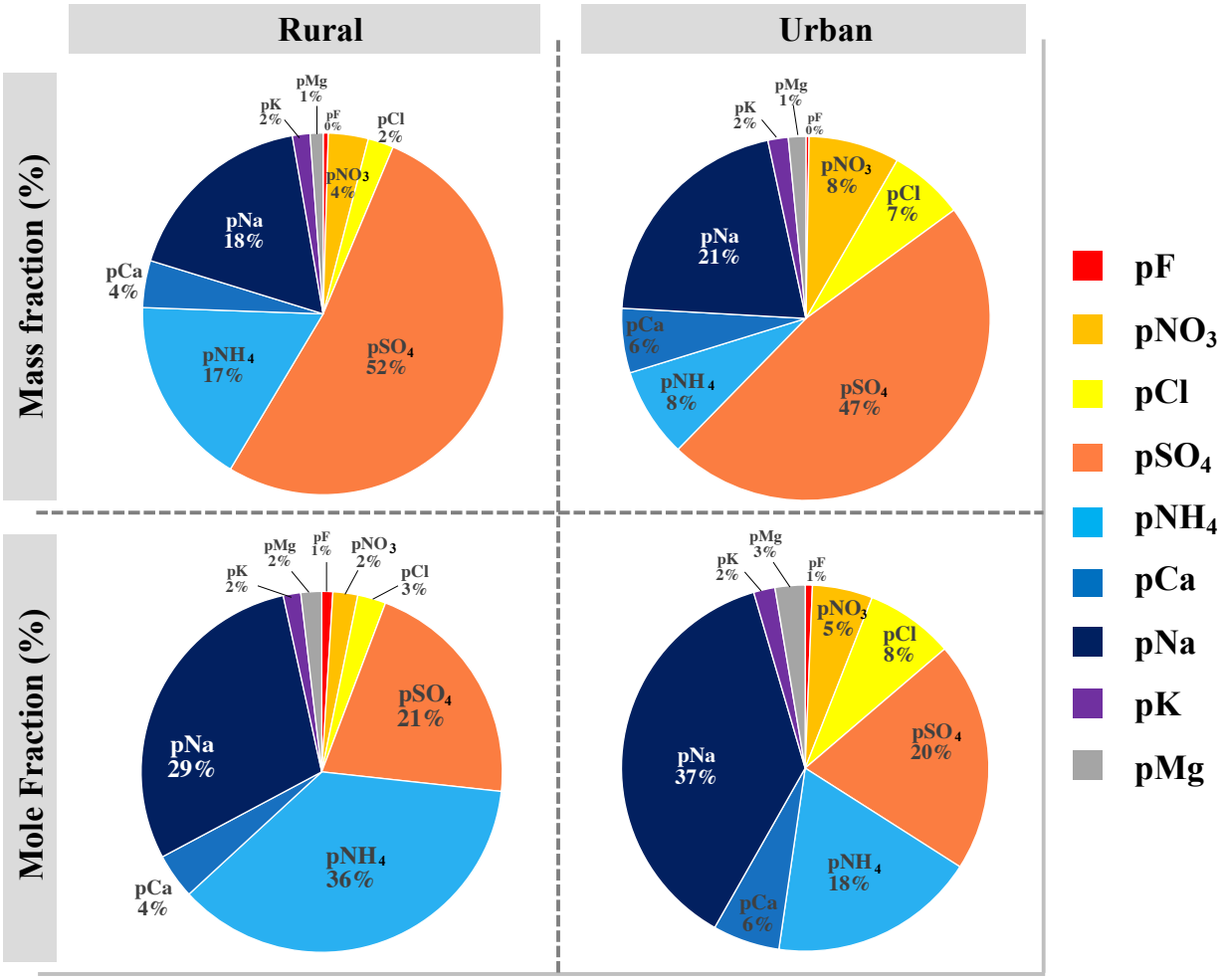

Figure S3.1. Relative mass and mole fraction (%) of PM_{10} inorganic ion compositions for rural and urban areas over the entire period (2005-2015).

Rural

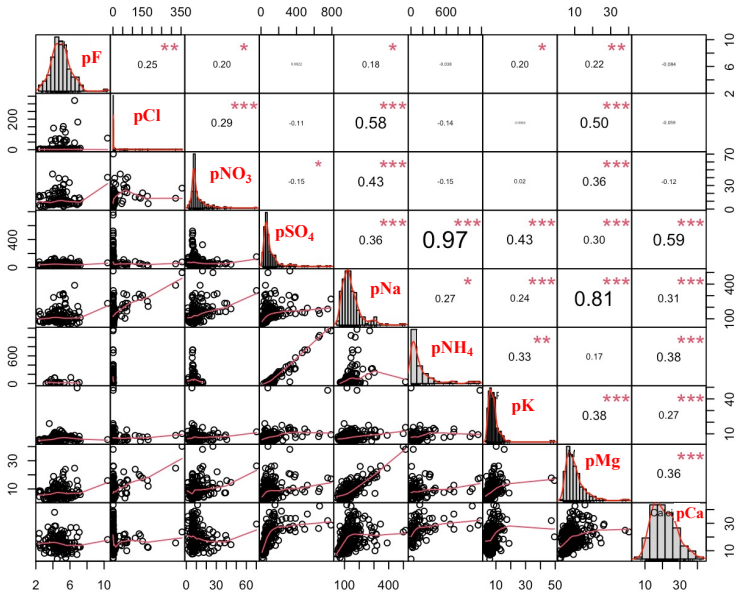

Urban

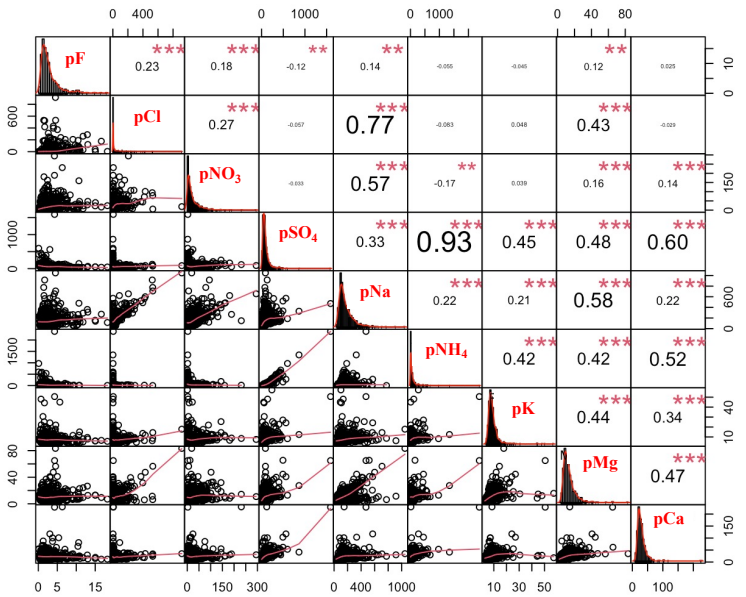

Figure S3.2. Pearson correlation coefficients for PM_{10} inorganic ion compositions for entire periods for rural and urban areas. The star symbol (*) indicates the significance level of the correlation coefficient between two variables.

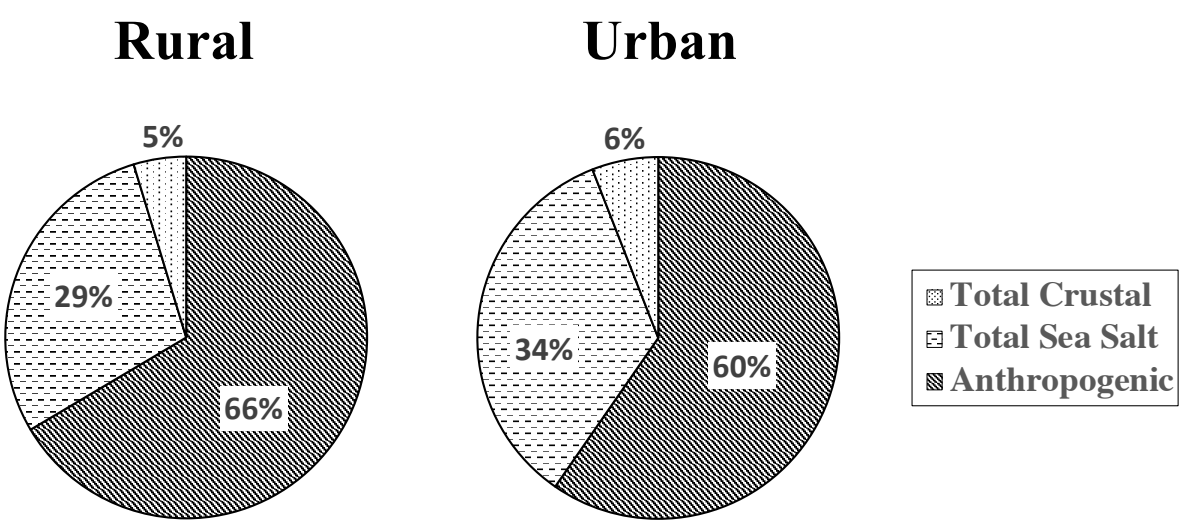

Figure S3.3. The relative fraction of PM_{10} inorganic compositions by major sources such as crustal, sea salt, and anthropogenic for urban and rural areas over the entire period (2005-2015).

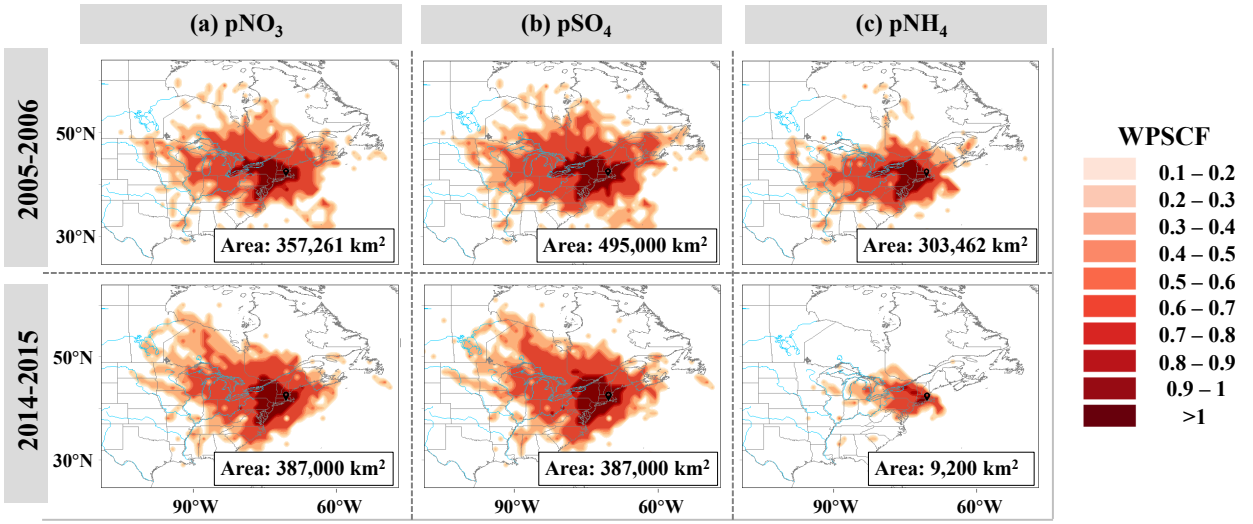

Figure S3.4. Annual mean weighted potential source contribution function (WPSCF) maps for pNO_3, pSO_4, and pNH_4 for 2005-2006 (beginning) and 2014-2015 (end) for the rural area.

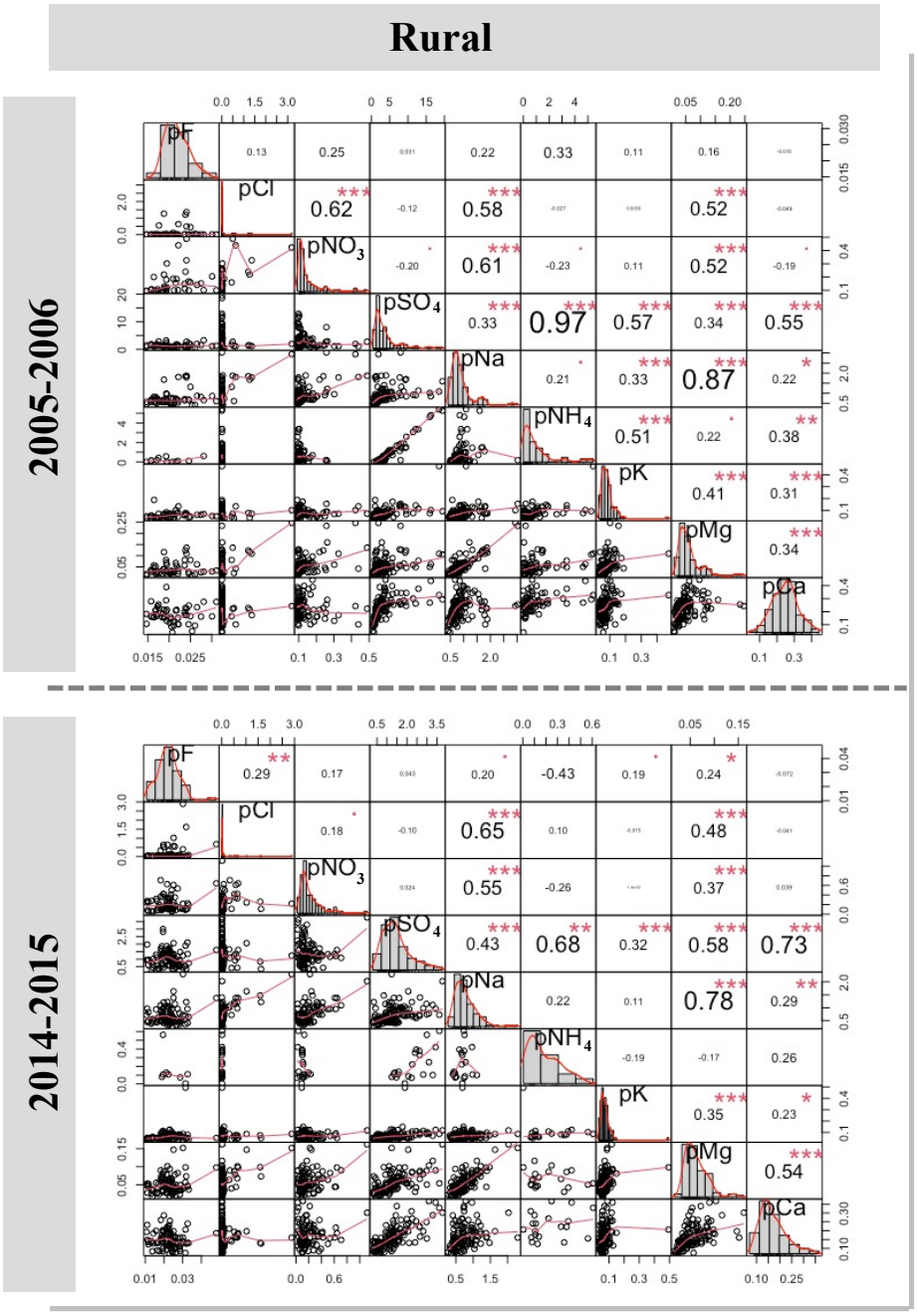

Figure S3.5. Pearson correlation coefficients for PM_{10} inorganic ion compositions for 2005-2006 (beginning) and 2014-2015 (end) for the rural area. The star symbol (*) indicates the significance level of the correlation coefficient between two variables.

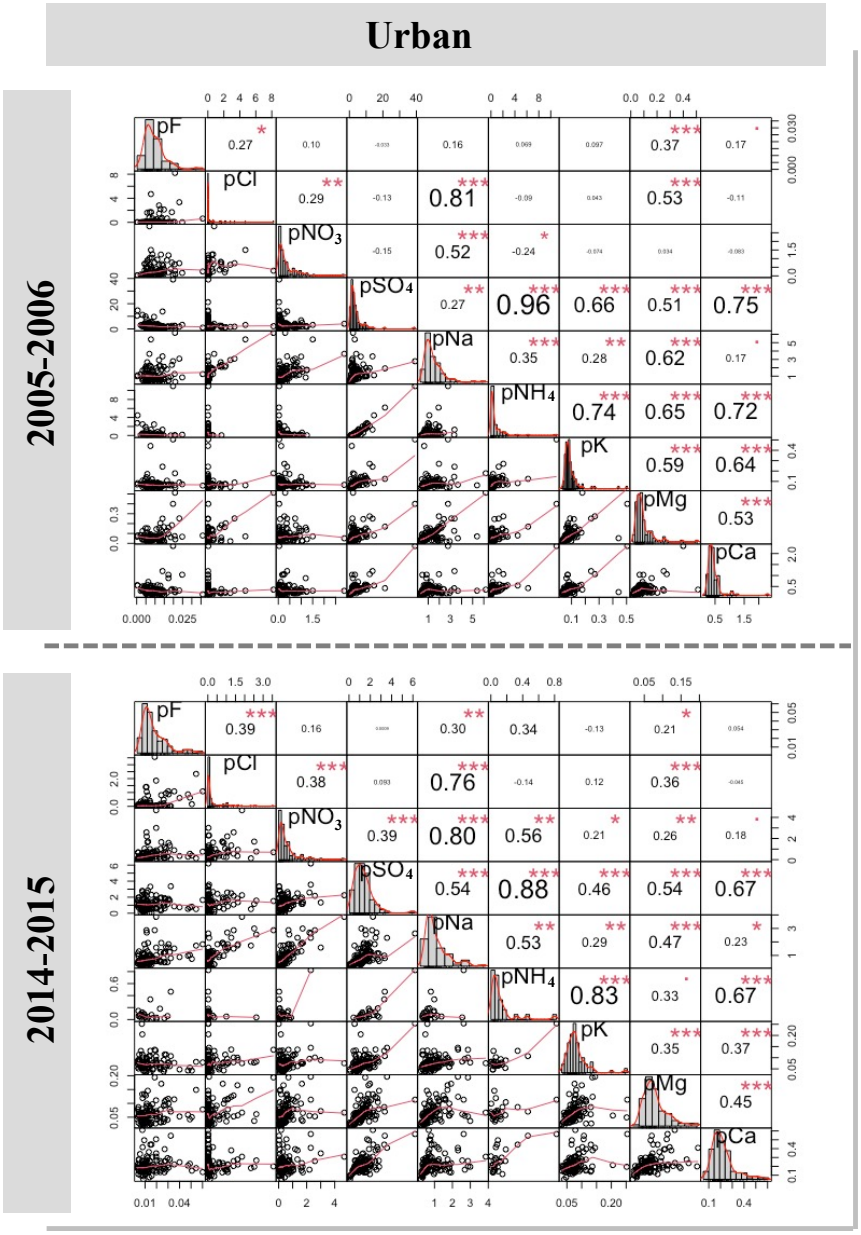

Figure S3.6. Pearson correlation coefficients for PM_{10} inorganic ion compositions for 2005-2006 (beginning) and 2014-2015 (end) for the urban area. The star symbol (*) indicates the significance level of the correlation coefficient between two variables.

Table S3.1. Summary of ANOVA (ANalysis Of VAriance) p values between urban and rural areas for PM_{10} inorganic ion compositions for 2005-2006 (beginning), 2014-2015 (end), and entire periods (2005-2015).

Urban vs. Rural	pF	pCl	pNO_3	pSO_4	pNa	pNH_4	pK	pMg	pCa
2005-2006	$p < 0.01$	$p < 0.01$	$p < 0.01$	$p = 0.70$	$p < 0.01$	$p = 0.35$	$p < 0.01$	$p < 0.01$	$p < 0.01$
2014-2015	$p < 0.01$	$p < 0.01$	$p < 0.01$	$p = 0.88$	$p < 0.01$	$p < 0.05$	$p = 0.22$	$p < 0.01$	$p < 0.01$
All	$p < 0.01$	$p < 0.01$	$p < 0.01$	$p = 0.16$	$p < 0.01$	$p = 0.25$	$p = 0.46$	$p < 0.01$	$p < 0.01$

Table S3.2. Summary of ANOVA (ANalysis Of VAriance) p values between different periods for pNO_3, $[pSO_4]$ anthropogenic, pNH_4, total sea salt, and total crustal for urban and rural areas.

Species	Urban			Rural
	* Period 1 vs 2	Period 2 vs 3	Period 1 vs 3	Period 1 vs 3
$[pNO_3]$	$p = 0.78$	$p < 0.01$	$p < 0.01$	$p < 0.01$
$[pSO_4]$ anthropogenic	$p < 0.01$	$p < 0.01$	$p < 0.01$	$p < 0.01$
$[pNH_4]$	$p < 0.05$	$p = 0.08$	$p < 0.05$	$p < 0.05$
Total Sea Salt	$p < 0.01$	$p = 0.16$	$p = 0.09$	$p = 0.07$
Total Crustal	$p < 0.05$	$p = 0.06$	$p = 0.41$	$p = 0.48$

* Period 1: 2005-2006 / Period 2: 2009-2010 / Period 3: 2014-2015

CHAPTER 4

Shift in Atmospheric Oxidation Chemistry Following the Clean Air Act

Heejeong Kim[1,2], Wendell W. Walters[3,4], Havala, O. T. Pye[4], Kristen M. Foley[4], Meredith G. Hastings[1,2]

[1]Department of Earth, Environment, and Planetary Sciences, Brown University, Providence, RI 02912, USA.

[2]Institute at Brown for Environment and Society, Brown University, Providence, RI 02912, USA.

[3]Department of Chemistry and Biochemistry, University of South Carolina, Columbia, SC 29208, USA.

[4]Office of Research and Development, U.S. Environmental Protection Agency, Durham, NC 27703, USA.

Under review for publication in [*Nature Geoscience*]

Abstract

The successful implementation of the US Clean Air Act has reduced nitrogen oxide (NO_x) emissions, with important improvements in air quality and acid deposition. However, predicting the impact of emission reductions on tropospheric chemistry remains challenging, as NO_x influences oxidant concentrations and aerosol formation. Here, we quantified oxygen isotopes in nitrate from a unique 2005-2015 aerosol record in the northeastern US to constrain chemistry changes over a time of large reductions in NO_x. Comparison with the isotope record indicates that the US EPA air quality model accurately simulates NO_x oxidation chemistry. Between 2005 and 2015, the observation and model results show a shift toward increased nighttime oxidation of NO_x. Our analysis reveals that emission regulations have driven this shift in oxidation chemistry, which has led to a shorter NO_x lifetime and enhanced aerosol formation rate in urban areas. This explains the continued elevated wintertime nitrate that plagues air quality in the eastern US despite significant NO_x decreases. The isotopic constraint on oxidizing chemistry greatly enhances our ability to test and predict the effectiveness of emissions reductions on oxidation chemistry.

1. Introduction

Nitrogen oxides (NO_x = nitric oxide (NO) + nitrogen dioxide (NO_2)) are an important component of the atmosphere with implications for climate, air quality, and environmental health[1,2]. The photochemical cycling of NO_x plays an important role in atmospheric oxidation capacity by controlling the production of major tropospheric oxidants such as the hydroxyl radical (OH) and the criteria pollutant ozone (O_3)[3,4]. These oxidants are responsible for removing atmospheric trace gases and influence the lifetime of greenhouse gases such as methane (CH_4)[5]. NO_x oxidation products include nitric acid (HNO_3) and organic nitrates ($RONO_2$) (collectively, nitrate), which contribute to particulate nitrate (hereafter, pNO_3) and represent a significant and

increasing component of fine particulate matter ($PM_{2.5}$)[6,7]. In addition, atmospheric dry and wet deposition of nitrate provides a source of fixed nitrogen to terrestrial and aquatic landscapes with important implications for ecosystem health[1]. Regulations have been implemented in the United States and other regions to decrease NO_x emissions, particularly from anthropogenic fossil fuel combustion sources, to improve air quality and combat deposition[7–9]. However, predicting the response of changes in endpoints such as O_3, $PM_{2.5,}$ and deposition to emission regulations remains challenging due to complex non-linear chemical feedbacks associated with NO_x chemistry. For example, recent wintertime observations of pNO_3 in the northeastern US revealed that concentrations have not changed or have actually increased between 2005 to 2015, despite a significant decrease (~35%) in NO_x emissions[7,10]. This non-linear response in pNO_3 concentrations to NO_x emission reductions has been suggested (via modeling) to be linked with wintertime NO_x chemistry in the region[11,12], as well as associated with an observed decrease in atmospheric acidity driven by sulfur dioxide (SO_2) emission reduction, such that a greater proportion of HNO_3 partitions into the aerosol phase[7,10].

Beyond a shift in aerosol thermodynamics, changes in NO_x oxidation chemistry and the atmosphere's oxidative capacity affect the efficiency of NO_x conversion to atmospheric nitrate. Top-down, satellite-based observations have been employed to estimate alterations in NO_x lifetimes and, consequently, oxidation efficiency, which have indicated variable changes across major urban centers in the US[13]. These observations provide critical insight into the role of shifting O_3 production regimes from NO_x-saturated to NO_x-limited in response to emission regulations; however, these estimates were confined to spring and summertime conditions and were based on assumptions with large uncertainty involving steady-state HO_x (≡OH + hydroperoxyl radical (HO_2) + organic peroxy radicals (RO_2)) and NO_x conditions[13]. The accuracy of atmospheric chemistry

models hinges on the models' ability to accurately simulate chemical changes. For instance, the GEOS-Chem model has been shown to overpredict HNO_3 formation via N_2O_5 hydrolysis in the northeastern US, with important implications for accurately modeling atmospheric oxidants, especially in wintertime[14].

Observational constraints on oxidative chemistry are essential to enhance our understanding of the connections between changes in emissions and oxidation chemistry. The stable oxygen isotope composition, commonly reported using delta notation ($\Delta^{17}O$ and $\delta^{18}O$; see method section), has proven to provide novel observational constraints on NO_x chemistry. Atmospheric O_3 possesses an excess of ^{17}O, due to mass-independent fractionation during its formation[15]. This ^{17}O excess is defined as $\Delta^{17}O$ (= $\delta^{17}O - 0.52 \times \delta^{18}O$) and is transferred into oxidation products involving reactions with O_3. The $\Delta^{17}O$ of the terminal and transferrable O atom of O_3 (O_3*) has been measured to be 39±2‰[16], while all other oxidants associated with NO_x chemistry, including HO_2 and RO_2 radicals, water (H_2O), and OH have a $\Delta^{17}O$ near (or assumed to be near) 0‰[17]. Thus, $\Delta^{17}O$ provides quantitative insights into the relative role of O_3 involvement in NO_x oxidation chemistry[18]. Conventionally, $\Delta^{17}O$ has been used to evaluate NO_x oxidation chemistry[18,19], although $\delta^{18}O$, with a large range of different values amongst atmospheric oxidants, provides potential for further detailing NO_x oxidation chemistry[14,20]. For example, $\delta^{18}O(O_3*)$ has been measured to be 126.3±12‰, $\delta^{18}O(H_2O_{(l)})$ is observed near –6‰ for northern mid-latitudes, $\delta^{18}O(RO_2/HO_2)$ is assumed to follow $\delta^{18}O(O_2)$ = 23‰, and $\delta^{18}O(OH)$ has been suggested to be near –45‰ (due to OH isotope equilibrium with $H_2O_{(g)}$)[14,21]. In addition to the transferrable $\delta^{18}O$ signal, $\delta^{18}O$ is known to undergo isotope fractionation and while not all fractionations have been directly quantified *ab initio* investigations suggest that the reaction of NO_x with various oxidants

should lead to no more than a 20‰ change.[22] This fractionation is relatively small compared to the wide range of $\delta^{18}O$ values (>120‰).

Using the oxygen isotopic composition of an archived aerosol record from 2005 to 2015 in the northeastern US, we constrain the chemical production mechanisms for pNO_3 over a time of important emission changes. A new isotope framework, including a mechanism to track primary emission of NO versus photochemically cycled NO, was developed for the US EPA Community Multiscale Air Quality (CMAQ) model that serves as a tool for understanding the regulatory attainment of air pollutants[23]. Tracking the primary emission versus the secondary production of NO was vital to accurately model $\Delta^{17}O$ of NO_x[24]. This framework was adapted to predict both $\Delta^{17}O$ and $\delta^{18}O$ compared to the pNO_3 observations from 2005 to 2015. Based on a comparison between observations and model simulations, we constrain the impact of NO_x emission regulations on atmospheric oxidative processing and NO_x lifetime in the northeastern US, a region of historically degraded air quality[25,26].

Materials and Methods

1.1 Sampling and Chemical Analysis

Coarse mode (PM_{10}) samples were collected at two sites in Rhode Island, United States, from 2005 to 2015: downtown Providence (41.82°N, -71.41°W) and West Greenwich (41.61°N, -71.72°W). The Providence, RI, US site represents an urban-mixed-use region, including commercial buildings, residential buildings, highways, and industry. In contrast, the West Greenwich, RI, US site represents a suburban environment, within a forest, and with minimal anthropogenic point sources nearby. Sample collections were conducted by the Rhode Island Department of Environmental Management (RI-DEM) and Rhode Island Department of Health

(RI-DOH) using a high-volume sampler on a quartz-fiber filter every six days for 24 hours, following EPA protocols (USEPA-Method IO-2.1 1999). The filter samples were shipped to Brown University and separately extracted in ultra-high purity water (> 18 MΩ). The entire 2005–2015 record was extracted for the Providence location. A subset of samples was extracted for the endpoints of the West Greenwich record, including 2005–2006 and 2014–2015. Nitrate (NO_3^-) concentrations were determined using ion chromatography (Dionex Integrion HPIC). Working standards of two different concentrations were analyzed for quality control every six samples. The average relative standard deviations (RSD) of replicate quality control standards were less than 3.4 %. A detailed methodology for sampling and chemical analysis is described in Kim et al., 2023[10].

1.2 Oxygen isotope of nitrate analysis

The water-soluble pNO_3 from the filter extracts were analyzed for their stable oxygen isotopes utilizing the bacterial denitrifier method at Brown University[35,36]. Oxygen isotope compositions are denoted using delta notation (*δ),* which is quantified as $\delta = (R_{sample}/R_{reference} - 1)$, where R is the ratio of the heavy isotope to the light isotope (e.g., $^{18}O/^{16}O$; $^{17}O/^{16}O$). Briefly, the extracted NO_3^- samples were injected into a buffer solution containing *Pseudomonas aureofaciens* that lack the nitrous oxide (N_2O) reductase enzyme and quantitatively reduces NO_3^- (and NO_2^-) to N_2O. The generated N_2O was extracted, purified, and concentrated using a customized GasBench interface and then continuously flowed into an Isotope Ratio Mass Spectrometer (IRMS) for *m/z* determination at 44, 45, and 46 for $\delta^{18}O$ ($\delta^{15}N$) determination. In a separate batch analysis, the generated N_2O was thermally decomposed to N_2 and O_2 by flowing the N_2O through a gold tube heated to 770 ℃ and then analyzed via IRMS at *m/z* 32, 33, and 34 for $\Delta^{17}O$ determination. Following the identical treatment principle, samples were calibrated using internationally

recognized isotopic reference material (Vienna Standard Mean Ocean Water) that included IAEA-NO-3, USGS34, and USGS35 with $\delta^{18}O$ values of 25.6 ‰, -27.9 ‰, and 57.6 ‰, respectively, and USGS34 and USGS35 for $\Delta^{17}O$ with values of -0.29 ‰ and 21.6 ‰, respectively[37]. The $\Delta^{17}O$ was calculated using the linear definition ($\Delta^{17}O = \delta^{17}O - 0.52 \times \delta^{18}O$) commonly used for nitrate with atmospheric origin[21,38]. Samples with a concentration less than 3 μmol L^{-1}, were not analyzed for $\Delta^{17}O$ and $\delta^{18}O$ due to the limited volume. The overall pooled standard deviations (σ) of isotopic reference materials were as follows: USGS34 ($\sigma(\delta^{18}O)$ = 0.5 ‰; $\sigma(\Delta^{17}O)$ = 1.8 ‰); USGS35 ($\sigma(\delta^{18}O)$ = 0.4 ‰; $\sigma(\Delta^{17}O)$ = 2.2 ‰), and IAEA-NO-3 ($\sigma(\delta^{18}O)$ = 0.3 ‰). Insignificant $\Delta^{17}O$ and $\delta^{18}O$ spatial differences were observed between an urban (Providence, RI) and suburban (West Greenwich, RI) site, likely due to their proximity (i.e., within 40 km); thus, we focus our analysis primarily on the urban site due to its more complete record (i.e., every six days versus monthly at the suburban site). The relative uncertainty (%) for the observations is defined as:

Relative uncertainty (%) = (Analytical Uncertainty (σ)/Average Value ($\overline{x}$))×100% (Eq. 2)

where $\overline{x}$ was defined as the average of all measurements over all years. Relative uncertainties were 0.6 % and 7.9 % for $\delta^{18}O$ and $\Delta^{17}O$, respectively.

1.3 CMAQ model description and simulations of oxygen isotopes

The CMAQ v5.4 was utilized to simulate the NO_2 and HNO_3 formation pathways and model the oxygen isotope compositions (e.g., $\delta^{18}O$ and $\Delta^{17}O$) of HNO_3 as recently described[23,24]. The CMAQ model simulation was based on replicated runs from the US EPA's Air QUAlity TimE Series Project (EQUATES)[30,39]. Briefly, the model used the Carbon Bond 6 revision 3 gas-phase mechanisms and version 7 of the aerosol module chemical mechanism (cb6r3-ae07) with the

addition of chlorine chemistry[40–42], and the NO_x photochemical cycling (NPC) adaptation, recently developed to more accurately simulate $\Delta^{17}O$ of NO_2 and HNO_3[24]. The model simulations included the bidirectional ammonia (NH_3) exchange[43,44], the Surface Tiled Aerosol Gaseous Exchange (STAGE) dry deposition[40,45–48], Weather Research and Forecasting (WRF) model version 4.1.1 meteorology[49], and emission inputs based on the EQUATES methods, which are based on the 2017 national emissions inventory (NEI) methods and year-specific emissions data when available or 2017 data that has been scaled for the simulation year[30,50,51]. Model simulations were conducted for the northeastern US domain at a horizontal resolution of 12×12 km for 2005, 2010, and 2015. Daily averaged data from the model was used to compare the model and observations. We selected identical dates for each (i.e., the model is sampled over the same date and time resolution as the observations).

Fractional production rates of NO_2 and HNO_3 formation were quantified using Integrated Reaction Rate (IRR) analysis within the Process Analysis (PA) script in CMAQ and used for the calculation of $\Delta^{17}O$ and $\delta^{18}O$ based on oxygen isotope mass balance via previously reported frameworks[14,19,21,24,52]. The $\Delta^{17}O$ and $\delta^{18}O$ of HNO_3 are determined by NO_x photochemical cycling and HNO_3 formation reaction. Here, we simulated $\Delta^{17}O$ and $\delta^{18}O$ of HNO_3 based on production rates within the grid cell corresponding to our sampling sites for the lowest 1,000 m of the atmosphere (Extended Data Table 4.1). We assume that the oxygen isotope composition of aerosol nitrate is approximately equal to HNO_3 due to rapid thermodynamic equilibrium and because the vast majority of aerosol nitrate extracted in water should have derived from HNO_3[52]. For the $\Delta^{17}O$ calculation, the transferrable terminal O from O_3 (O_3^*) was assumed to be 39±2 ‰, consistent with recent near-surface observations[16] and the $\Delta^{17}O$ values of other oxidants such as H_2O, OH, HO_2, and RO_2 were assumed to be 0 ‰, consistent with photochemical $\Delta^{17}O$ model expectations[17]. We

consider ±5 % uncertainty for modeled $\Delta^{17}O(pNO_3)$ in this study. For the $\delta^{18}O$ calculation, the following values were assumed for the various oxidants involved in NO_2 and HNO_3 formation: $\delta^{18}O(O_3^*)$ = (126.3±12) ‰, $\delta^{18}O(O_2)$ = 23 ‰, $\delta^{18}O(H_2O)$ = -6 ‰, and $\delta^{18}O(OH)$ = -43 ‰[14,21]. We consider ±10 % uncertainty for modeled $\delta^{18}O(pNO_3)$.

To account for primary NO and secondary NO produced from NO_2 photolysis, the newly modified cb6r3-ae07 (NPC) mechanism was also applied[24]. In short, NO produced via NO_2 photolysis was tagged as NO_{photo}, which is photochemically cycled by oxidants and reflects the oxygen isotopic signature of oxidants involved in NO_x photochemical cycling. In contrast, primary NO is assumed to carry an O-atom from source emissions with a $\Delta^{17}O(NO)$ value of 0 ‰ and $\delta^{18}O(NO)$ value of 23 ‰, assuming that the O-atom in NO stems from O_2. Overall, the simulated $\Delta^{17}O$ and $\delta^{18}O$ values of HNO_3 were predicted by the proportional contribution of O_3 relative to other oxidants based on the averaged relative NO_2 and HNO_3 production rates from the CMAQ model. This approach enables tracking of the production rates of NO_2 and HNO_3 at a reaction-specific level, providing quantitative insights into NO_x oxidation chemistry. The statistical parameters, including the correlation coefficient (R) and normalized mean bias (*NMB;* (Eq. 3)), are selected to evaluate model performance.

$$NMB = (\sum (Q_m - Q_o) / \sum Q_o) \qquad \text{(Eq. 3)}$$

where Q_m = modeled quantities and Q_o = observed quantities.

1.4 Ozone (O_3) Production Efficiency Calculation

Over the 10-year record, the model results indicated that ozone (O_3) concentration has increased in major urban areas in the northeastern US. Using the CMAQ model output, we

quantified O_3 production efficiency (OPE (ε); Eq. 4), which represents the chain length associated with NO_x in the process of O_3 production. OPE is calculated as:

$$\varepsilon = \frac{P(O_3)}{L(NO_x)} \qquad \text{(Eq. 4)}$$

where $P(O_3)$ is the production rate of O_3, and $L(NO_x)$ is the loss rate of NO_x. $P(O_3)$ is the sum of the $NO + HO_2/RO_2$ production rates, while $L(NO_x)$ is the sum of the HNO_3 and $RONO_2$ production rates. Overall, the calculated annual OPE is 3.7 for 2005 and 5.6 for 2015 (Fig.S4. 5). Seasonally, OPE increased from 2.2 to 3.0 and from 5.3 to 8.3 for the cold and warm seasons, respectively, from 2005 to 2015.

1.5 Statistical Analysis

To assess long-term trends in observed $\Delta^{17}O$ and $\delta^{18}O$ of pNO_3, we applied a weighted least squares (WLS) regression with weights based on the inverse squared total error to account for measurement uncertainty. Both raw data and annual averaged data were considered for the regression analysis (Fig. 4.2). In addition, we conducted deseasonalization using the "stl" function (Seasonal-Trend decomposition using locally weighted scatterplot smoothing (LOESS)) in the openair package in R . This method decomposes the time series into *trend*, *seasonal*, and *residual* components, effectively removing seasonal variability to highlight the underlying long-term trend. The *trend* component captures the underlying long-term trend in the data for understanding changes over time. The *seasonal* component identifies and isolates recurring patterns within each year, accounting for seasonal fluctuations of $\Delta^{17}O$ and $\delta^{18}O$ of pNO_3. The *residual* component represents the remaining unexplained variability, removing both long-term and seasonal influences on isolate noise or other non-systematic variations. By removing the seasonal component, we can more accurately analyze the underlying trend of $\Delta^{17}O$ and $\delta^{18}O$ of pNO_3 over time, which is

particularly useful for assessing the effects of chemistry changes in response to emission reductions. The statistical significance of the trend was then assessed using a two-sided *t*-test on the regression slope for both observation and simulation results. To assess the statistical meaningfulness of the observed trend, we also applied the method proposed by Bryhn & Dimberg (2011), which evaluates trend meaningfulness based on R^2 and p-value criteria of >0.65 and <0.05 for time intervals ranging from 2 to 30, respectively[29]. Using their developed Excel macro add-in, we evaluated whether the $\delta^{18}O(pNO_3)$ long-term trend, which indicated the observed long-term trend was statistically meaningful (Table. S4.1).

1.6 Ancillary Near-Surface Observations

Near-surface observation data of gaseous and particle pollutants (e.g., O_3, NO_x, pNO_3, and isoprene) and meteorological factors (e.g., temperature and relative humidity) from the Chemical Speciation Network (CSN) and the Interagency Monitoring of Protected Visual Environments (IMPROVE) are used to validate CMAQ model performance. For example, to support our observation, which is conducted in Providence, RI, NO_x, pNO_3, isoprene, and meteorological data are used from the CSN and IMPROVE networks around the Providence (site ID: 44-007-1010; 44-007-0012; 44-007-0022). Note that O_3 was only historically monitored for the warm season (Mar-Sep) in the Providence area, so O_3 in Providence was not utilized in this study. In addition, we have evaluated the oxidation chemistry in the entire northeastern US domain. To validate model performance in the northeastern US, we have compared near-surface O_3, NO_x, pNO_3, and isoprene observation data from major urban cities, including Boston, MA (25-025-0042), New York Cities (36-005-0110), and Washington, DC (11-001-0043), versus suburban/rural areas, including the suburban in MA (25-013-0008), rural in NY (36-041-0005) and rural in ME (23-003-1100).

2. Results and Discussion

2.1 Observed trends and seasonal variability of oxygen isotopes

The oxygen isotopes of water-soluble pNO_3 track strong seasonal variability in NO_x oxidation, with a long-term shift in response to emission changes in the northeastern US from 2005 to 2015 (Fig. 4.1). This seasonality is similar across New England sites based on the isotopic composition of recent HNO_3 and pNO_3 samples from the CASTNET monitoring network[14,27]. The observed $\Delta^{17}O$ (n=524) and $\delta^{18}O$ (n=532) of pNO_3 exhibit relatively higher values in the cold season (Oct to Mar) and lower values in the warm season (Apr to Sep), reflecting a shift from O_3– to HO_x–dominated NO_x oxidation chemistry, consistent with previous studies in the polluted mid-latitudes[14,27,28]. During winter, NO_2 is formed primarily via $NO+O_3$, and HNO_3 is formed primarily via N_2O_5 heterogeneous hydrolysis on aerosols (i.e., NO_2+O_3 forms NO_3 that reacts with NO_2 to form N_2O_5). These reactions result in a greater proportion of O_3 incorporated into pNO_3 during the cold season, leading to relatively high $\Delta^{17}O$ and $\delta^{18}O$ values. During the summer, the increased photochemical production of HO_x radicals leads to an increase in NO_2 formation via $NO+HO_2/RO_2$, and NO_2+OH dominates nitrate production, leading to relatively lower $\Delta^{17}O$ and $\delta^{18}O$ values[19,24].

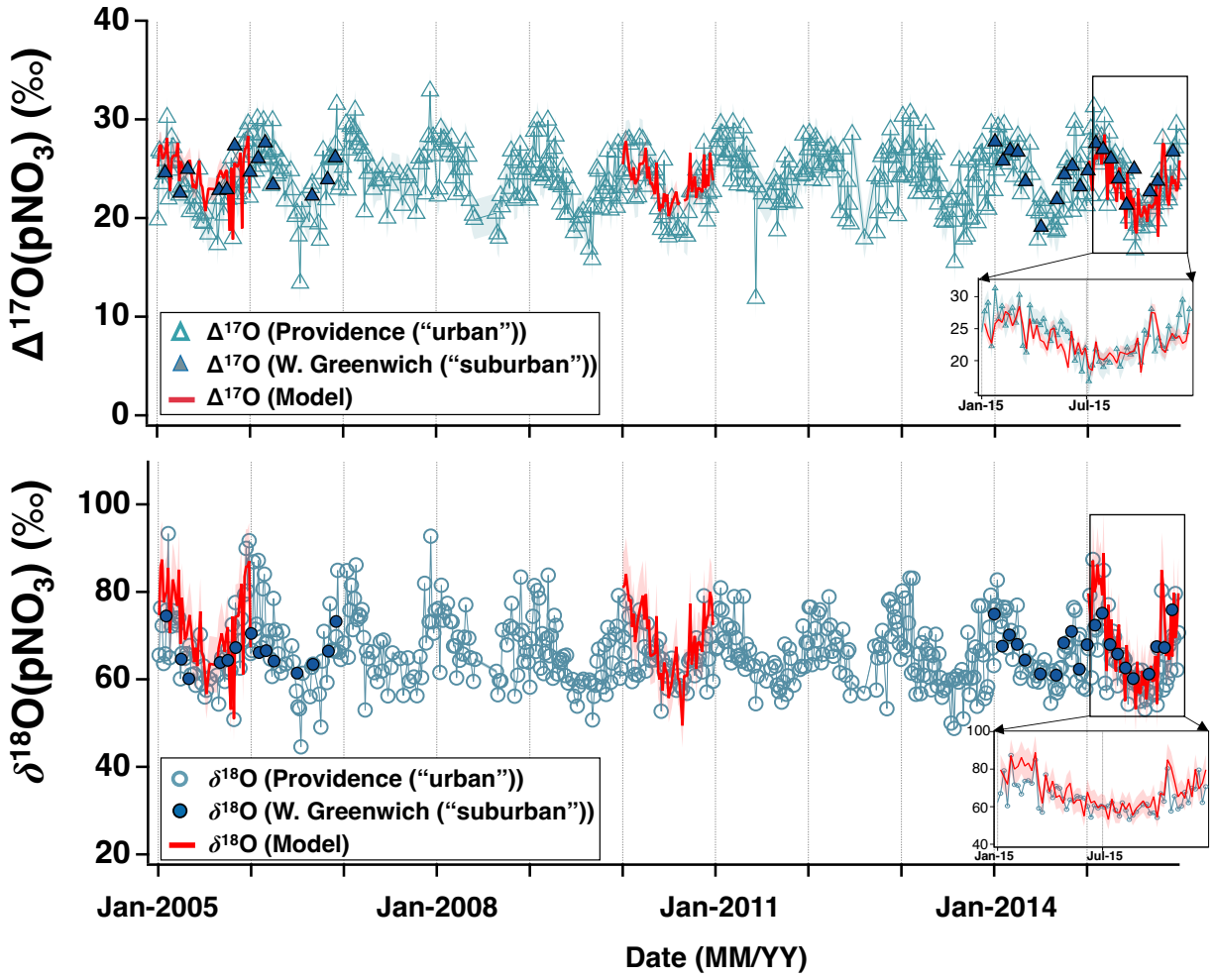

Figure 4.1. The observed (data points) and modeled (line) $\Delta^{17}O$ and $\delta^{18}O$ of pNO_3 in Providence and West Greenwich, RI, from 2005 to 2015. The Providence data represents a sample collected every six days. The West Greenwich data represents samples collected every six days merged into mass-weighted monthly mixtures due to sample mass limitations. The shaded areas surrounding observed $\Delta^{17}O$ and $\delta^{18}O$ data denote the $\pm1\sigma$ analytical error (±2 ‰ for $\Delta^{17}O$ and ±0.4 ‰ for $\delta^{18}O$). The CMAQ model output is selected for the same date as the observation and is shown for 2005, 2010, and 2015. The shaded areas surrounding modeled $\Delta^{17}O$ and $\delta^{18}O$ denote the uncertainty of the oxygen isotope composition of atmospheric oxidants involved in NO_x chemistry (±5% for $\Delta^{17}O$ and ±10% for $\delta^{18}O$).

The long-term observations also reveal a significant annual decreasing trend in $\delta^{18}O(pNO_3)$ based on a weighted least squares (WLS) regression (Fig. 4.2a; $p<0.01$). This long-term decreasing trend in $\delta^{18}O(pNO_3)$ is driven by change in the cold season ($p<0.01$), while no significant trend

was detected for the warm season (Fig. S4. 1a-2a). A deseasonalized time series analysis was also conducted and still reveals a significant decrease in $\delta^{18}O(pNO_3)$, suggesting that the observed trend is driven not only by interannual seasonal fluctuations but also by shifts in nitrate formation pathways (Extended Data Fig. 4.1). Following the approach of Bryhn and Dimberg (2011), which recommends $R^2 > 0.65$ and $p < 0.05$ as criteria for statistical meaningfulness, we find that this trend is both statistically significant and meaningful when dividing the dataset into seven equal intervals (R^2=0.71, p=0.02; Table.S4.1)[29]. No annual or seasonal statistically significant long-term trend was observed in $\Delta^{17}O$, although this may be due to the larger relative uncertainty of the $\Delta^{17}O$ measurements of 7.9% compared to $\delta^{18}O$ of 0.6% (see Eq. 2, Method section for details).

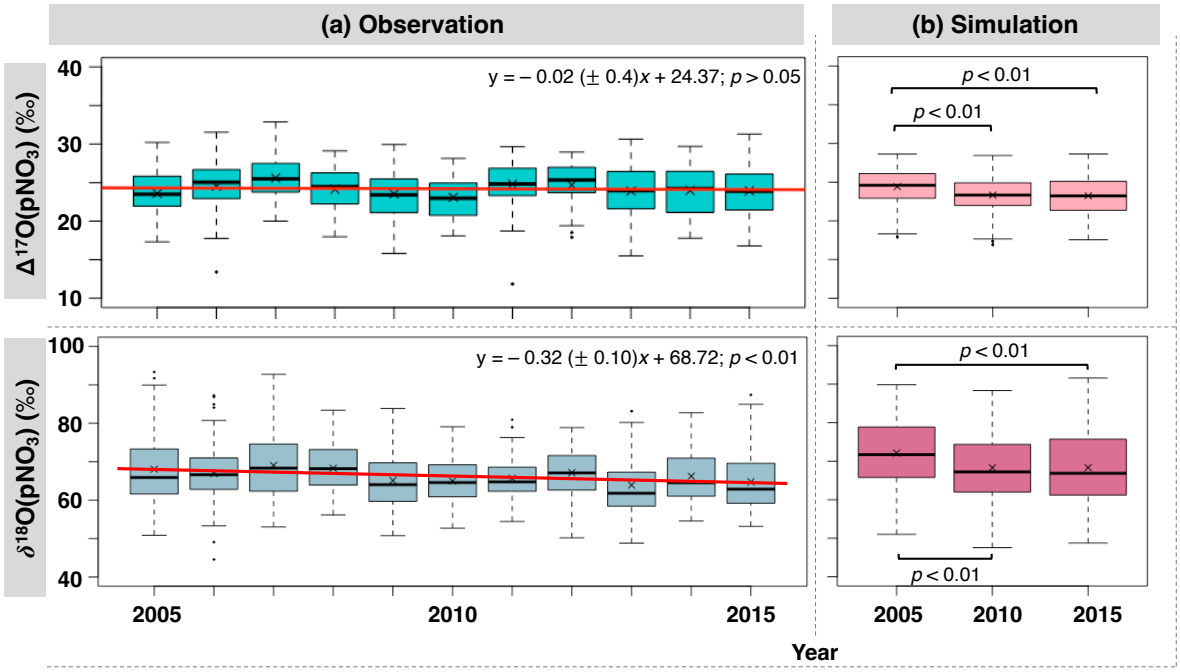

Figure 4.2. Box-and-whiskers plot describing the annual distribution of observed and modeled $\Delta^{17}O$ (top) and $\delta^{18}O$ (bottom) of pNO_3 from 2005 to 2015 in Providence, RI. The middle line and x marker in each box represent the median and mean values, respectively. The upper and lower ends of the box indicate the 25th and 75th percentiles and the whiskers extend from the box to the minimum and maximum values, excluding outliers (open circles). The solid red line represents the weighted least squares (WLS) regression trends for the observations, with the slope, its standard error, intercept, and the p-value (based on a two-sided t-test) indicated.

2.2 Shift in NO_x oxidation chemistry between 2005-2015

To detail NO_x oxidation changes over time, CMAQ model simulations from replicated runs of the US EPA's Air QUAlity TimE Series Project (EQUATES)[30], which have shown overall excellent agreement with reactive nitrogen concentrations, were used to calculate $\Delta^{17}O$ and $\delta^{18}O$ of pNO_3 for the years 2005, 2010, and 2015 (Fig. 4.1; Extended Data Fig. 4.2). The simulated pNO_3 and NO_x concentrations matched well with observed seasonal variability and magnitude (Extended Data Fig. 4.3); NO_x and O_3 were also well captured in the simulations across the northeastern US (Extended Data Fig. 4.4). A linear regression between the model and isotope observations yields a slope of 0.46($\pm$0.05), r=0.61, and a Normalized Mean Bias (*NMB)* of only 1% for $\Delta^{17}O$; for $\delta^{18}O$ it yields a slope of 0.84($\pm$0.07), r=0.71, and a *NMB* of 6% (Eq.3). This is a very reasonable *NMB*, given that the relative standard deviation of the measurements of $\Delta^{17}O(O_3*)$ and $\delta^{18}O(O_3*)$ are 5% and 16%, respectively. While the $\delta^{18}O$ value is expected to be influenced by fractionation processes that depend on temperature, we do not observe any impactful trends in temperature over time (Fig. S4.4). Therefore, we also do not expect the $\delta^{18}O$ values of the various oxidants to have shifted significantly over time.

The simulated $\Delta^{17}O$ and $\delta^{18}O$ values of pNO_3 predict a significant decreasing trend from 2005 to 2015 (Fig. 4.2), consistent with $\delta^{18}O$ observations. The different observed trends of $\Delta^{17}O$ and $\delta^{18}O$ of pNO_3 may be related to the precision of the analytical methods, meaning that it is possible that a real decline signal in $\Delta^{17}O$ may be obscured by the higher noise levels in $\Delta^{17}O$ measurements, as previously noted. $\delta^{18}O(pNO_3)$ shows a larger annual mean shift of 3.8‰ from 2005 to 2015 compared to the model $\Delta^{17}O$ shift of 1.2‰. This may also imply that the $\delta^{18}O$ provides a more sensitive constraint for interpreting long-term variability in NO_x oxidation chemistry under these study conditions. Based on the overall agreement between the modeled and observed $\Delta^{17}O$ and

$\delta^{18}O$ as evidenced by the low *NMB*, the CMAQ simulations were considered an accurate representation of our study site, allowing for the evaluation of connections between emission regulations and the drivers of observed long-term changes in NO_x oxidation chemistry.

The simulations indicate a shift in the relative importance of NO_x oxidation pathways from 2005 to 2015 in response to NO_x emission reductions (Fig. 4.3a). In this study, NO denoted primary NO directly emitted from emission sources and NO_{photo} was used to track secondary NO produced from NO_2 photolysis during photochemical cycling (see Method section). Using these two species, NO_2 produced via primary NO directly can maintain an imprint of the oxygen source associated with the emission type (e.g., O_2 in the case of combustion). In contrast, the oxygen isotope composition of NO_2 produced via NO_{photo} will reflect the oxidants involved in NO photochemical cycling and oxidation. For Providence, RI, the formation of NO_2 was dominated by $NO_{photo}+O_3$, averaging a contribution of 79% over all simulations, followed by $NO+O_3$ (17%). While $NO_{photo}+O_3$ dominated NO_2 production, an increased contribution from primary $NO+O_3$ was seen between 2005 to 2015 in both the warm and cold seasons. This suggests that the relative nighttime NO oxidation, when the oxygen isotopes of NO_2 do not reach photochemical equilibrium, became increasingly significant during the study period. Indeed, in the northeastern US, monthly average O_3 concentrations were significantly higher in 2015 compared to 2005, particularly during nighttime and colder months, for both modeled and near-surface observations (Extended Data Fig. 4.5; Fig. S4.5-6). This trend can be explained by incomplete nighttime O_3 titration by NO, as NO_x emissions decreased in urban areas in the northeastern US and the molar NO_2/NO_x ratio increased (Fig. S4.5-6). In 2005, simulated NO_2 concentrations exceeded O_3 during the colder months, whereas in 2015, O_3 concentrations surpassed NO_2 throughout the year. Further, CMAQ predicted an increase in annual O_3 production efficiency (OPE) from 3.7 to 5.6 from 2005 to 2015 (Fig. S4.5;

Method section), which resulted in a decrease in modeled $\Delta^{17}O$ and $\delta^{18}O$ values of NO_2 because of the increased contribution of primary $NO+O_3$ chemistry relative to $NO_{photo}+O_3$. All in all, the model analysis, constrained by the oxygen isotope observations, indicated that nighttime oxidation of NO and NO_2 has become more efficient in response to emission regulations.

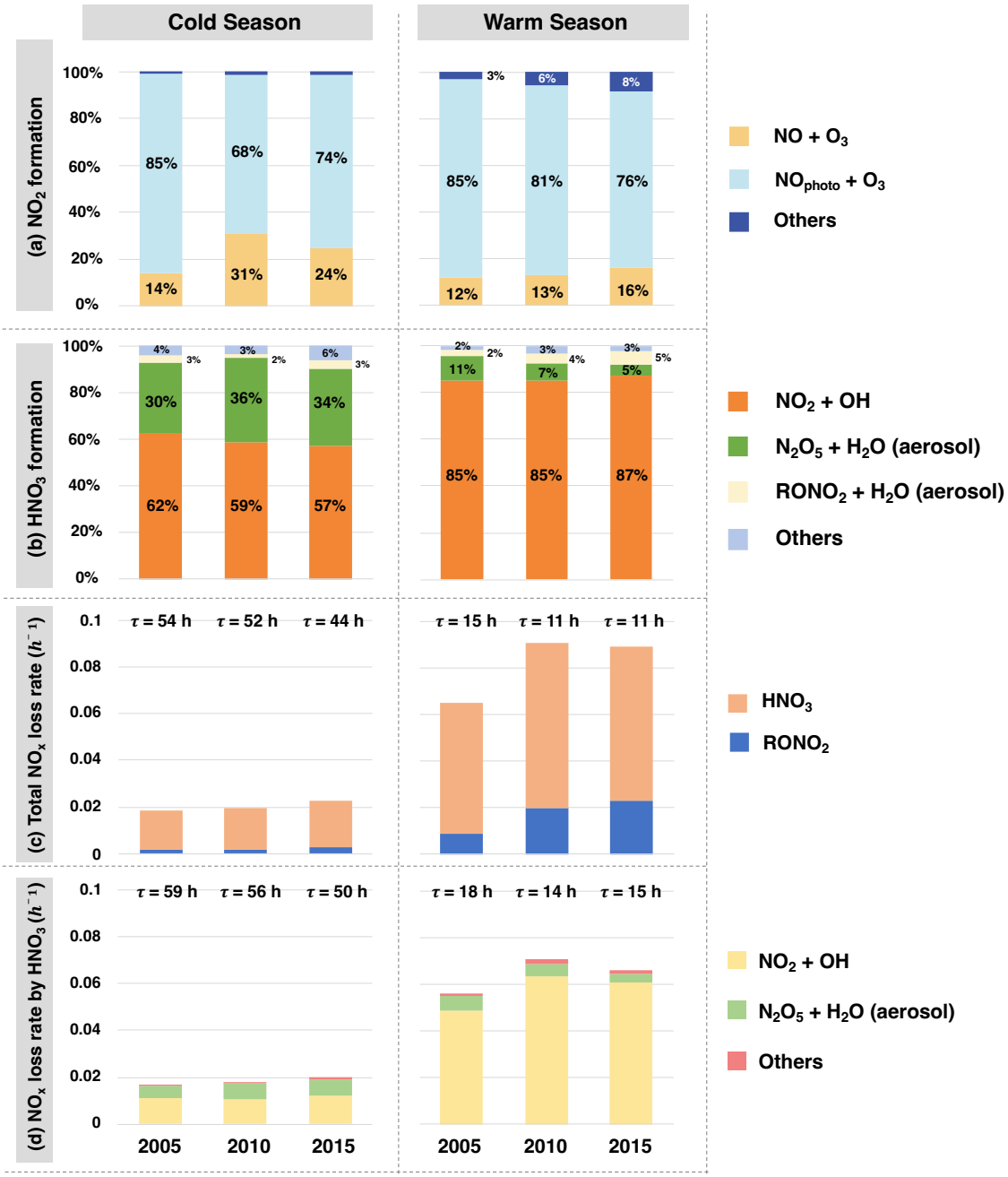

Figure 4.3. Fractional pathways of formation for (a) NO_2 and (b) HNO_3, along with the rate of (c) total NO_x loss (h^{-1}), and (d) NO_x loss rate by HNO_3 formation for cold and warm seasons in 2005, 2010, and 2015 in Providence, RI based on the US EPA CMAQ model. Note that NO refers to primary emissions while NO_{photo} refers to secondary NO production (see Methods for details). A detailed breakdown of other NO_2 and HNO_3 formation pathways is provided in Table S4.1.

Across all model runs, simulated HNO_3 formation was annually dominated by NO_2+OH (78 %) followed by the N_2O_5 hydrolysis pathway (18%) (Fig. 4.3b). The average relative contribution of N_2O_5 hydrolysis was more important in the cold season, accounting for 33% of HNO_3 formation compared to only 8% during the warm season. Between 2005 and 2015, the CMAQ model indicated that the relative role of N_2O_5 hydrolysis in HNO_3 formation increased during the cold season, and the importance of the NO_2+OH pathway decreased. This change suggests that N_2O_5 hydrolysis may have previously been limited by the availability of O_3, as observed in polluted regions in the US[12] and China[31]. The increased O_3 oxidation efficiency would be expected to increase $\Delta^{17}O$ and $\delta^{18}O$ of HNO_3 under conventional isotope mass-balance frameworks. However, this effect is counterbalanced by the predicted decrease in $\Delta^{17}O$ and $\delta^{18}O$ of NO_2 due to an increased contribution of O atoms from primary NO emissions. The overall enhanced nighttime oxidation efficiency of primary NO (i.e., $\Delta^{17}O$ = 0‰) by O_3 is key to the predicted reduction in $\Delta^{17}O$ and $\delta^{18}O$ values of pNO_3. On average, these chemistry changes are predicted to lower $\Delta^{17}O$ and $\delta^{18}O$ across the northeastern US from 2005 to 2015 with spatial variabilities seemingly driven by urban versus rural settings (Fig. 4.4a and b).

2.3 Spatial changes in NO_x lifetime

The increased importance of O_3 in NO_x oxidation resulting from emission regulations substantially impacts NO_x lifetime, NO_x oxidation efficiency, and shifts in oxidation capacity in the northeastern US. To quantitively understand the impact of changes in NO_x oxidation chemistry, NO_x lifetime[31] was calculated as the total mass of reactive N species (NO, NO_2, NO_3, $2N_2O_5$, HONO, HNO_4, $ClNO_2$, PAN) divided by the total loss rate of terminal NO_x sinks (production of HNO_3 and $RONO_2$) from the CMAQ output.

$$\tau = \frac{\text{Total mass of reactive N } (\text{ppb}_v)}{\text{Total loss rate of terminal NO}_x \text{ sinks } (\text{ppb}_v/\text{h})} \quad \text{(Eq. 1)}$$

The NO_x loss rate in Providence, RI, was mainly governed by HNO_3 formation, with an increased contribution of $RONO_2$ in the warm season, particularly in the more recent years of simulations (Fig. 4.3c; Extended Data Fig. 4.6). Overall, and as expected, NO_x lifetime was much longer in the cold season (average of 47h) than the warm season (average of 11h) because of the relatively lower oxidant concentrations during the wintertime[12,31]. In the cold season, NO_2+OH accounted for roughly 56% of total NO_x chemical loss, followed by heterogeneous uptake of N_2O_5 (31% of total loss) averaged over all modeled years (Fig. 4.3d). In the warm season, total NO_x was mostly lost via NO_2+OH (71%) followed by $RONO_2$ formation (20%). $RONO_2$ in the model includes monofunctional organic nitrates, multifunctional organic nitrates, and reaction with isoprene, accounting for 63%, 22%, and 14% of total $RONO_2$ formation, respectively. The relative portion of organic nitrate contribution to HNO_3 production via $RONO_2$ hydrolysis (4%) was small, but it is notable that its contribution systematically increased from 2005 to 2015 (Fig. 4.3c). Indeed, the NO_x chemical lifetime decrease in the warm season from 2005 to 2015 is primarily due to the increased importance of $RONO_2$ formation. For example, $RONO_2$ formation accounted for approximately 9% of the total NO_x loss rate for the cold season over all years, whereas their contribution during the warm season substantially increased from 14% to 26% between 2005 and 2015 (Fig. 4.3c; Extended Data Fig. 4.6). This shift in NO_x loss pathways was primarily driven by decreasing NO_x concentrations, which increased the relative importance of $RONO_2$ formation compared to HNO_3 production. As NO_x concentrations decreased, the chemical environment increasingly favored RO_2 radical reactions with NO, leading to more $RONO_2$ formation. Model simulations and surface observations indicated some increase in major biogenic VOC (BVOC) concentrations (e.g., α-pinene and isoprene) in the warm season from 2005 to 2015 (Fig. S4.7-8),

while the NO_x loss rate via $RONO_2$ formation increased by approximately 155% over the same period (Fig. S4.7d). This suggests that changes in chemical regimes driven by changing NO_x concentrations had a far greater impact on $RONO_2$ production than VOC emissions alone. This trend underscores the importance of understanding the environmental fate of $RONO_2$, including its role in renoxification, deposition, and terminal atmospheric loss[32–34].

Over time, the model simulation for Providence, RI, indicated a substantial decrease in NO_x lifetime during the winter from 54h to 44h (-19%). However, across the entire northeastern US domain, the model simulated lifetime of NO_x exhibited a relatively consistent mean lifetime of 19.5h (2005) to 20.4h (2015) (Fig. 4.4c; see Extended Data Fig. 4.7 for seasonality). Investigating this further, we found a pronounced spatial contrast in NO_x oxidation chemistry and lifetime changes between urban areas (e.g., the northeastern corridor from Washington, DC to Boston) compared to suburban/rural areas (outside this corridor) in the northeastern US (Extended Data Fig. 4.8-9; Fig. S4.9). As in Providence in 2005, nitrate formation in other urban regions was dominated by the NO_2+OH pathway (71%), while N_2O_5 hydrolysis played a key role in suburban/rural areas (e.g., ~42%; Extended Data Fig. 4.9). However, the importance of N_2O_5 hydrolysis in suburban/rural areas then declined to 32% in 2015, amidst a relative increase in $RONO_2$ formation and increased BVOC emissions, shifting nitrate formation toward NO_2+OH and $RONO_2$ hydrolysis pathways in more recent years. Furthermore, the response of O_3 to NO_x reductions is different in the urban versus suburban/rural areas in the model.

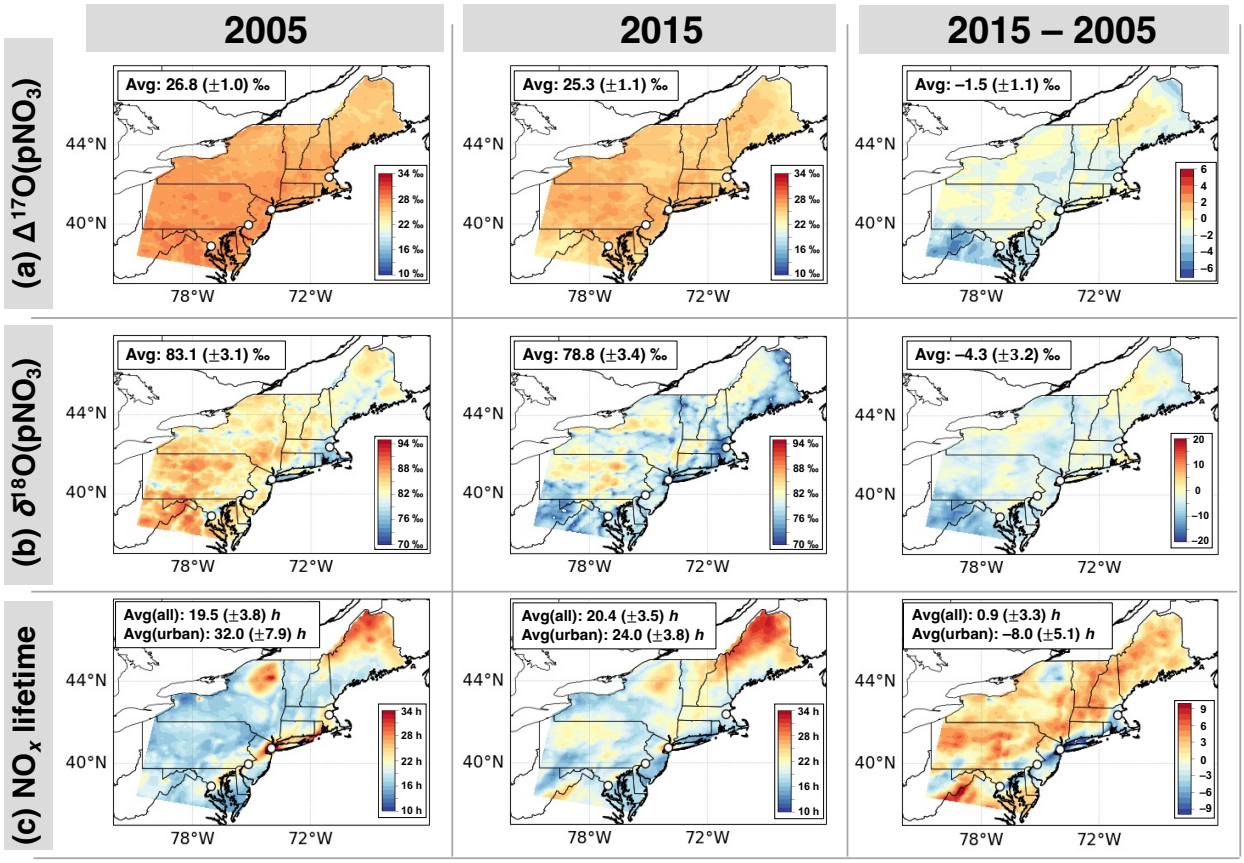

Figure 4.4. The CMAQ simulated (a) $\Delta^{17}O$ and (b) $\delta^{18}O$ of pNO_3 and (c) calculated NO_x lifetime (τ) over the northeastern US domain for 2005 and 2015 and their difference (2015 – 2005). White circles indicate the locations of major cities in the northeastern US, including Boston, MA; New York City, NY; Philadelphia, PA; and Washington, DC. The τ_{urban} is the average NO_x lifetime for the major cities in the northeastern US, including Providence, RI.

Overall, urban regions experienced enhanced O_3 production efficiency and more efficient conversion of NO to NO_2 and NO_2 to pNO_3, both of which contributed to a shortened NO_x lifetime and boosted pNO_3 formation efficiency in recent years. In urban regions with significant anthropogenic emissions, similar trends of decreasing NO_x lifetime, particularly during winter, were simulated between 2005 to 2015, whereas suburban/rural areas showed a more variable response (Fig. 4.4; Extended Data Fig. 4.7). This is supported by near-surface observations in urban areas that show a higher mean nitrate oxidation ratio (NOR) in 2015 versus 2005, indicative

of more efficient conversion of NO_x to pNO_3 (Fig. S4.10). For areas outside of the urban core in the northeastern US, limited observations of simultaneous pNO_3 and NO_x indicate a variable response in NOR. For example, in rural northeast Maine (46.69°N, –68.03°W), the mean NOR did not change between 2005 and 2015, while in a suburban/rural location in southwest Massachusetts (42.19°N, –72.55°W) NOR increased under the influence of the nearby northeastern corridor (Fig. S4.10).

In conclusion, oxygen isotopes provide powerful observational constraints on NO_x oxidation chemistry, offering a more detailed and mechanistic understanding of the differences in nitrate formation between suburban/rural and urban areas. By combining the unique observational constraint of oxygen isotope data with concentration observations and modeling, we gain deeper insight into the oxidation processes at work. These insights are particularly important since NO_x/pNO_3 chemistry are the result of several competing reactions. Our findings suggest that emission regulation amendments have increased NO_x oxidation efficiency to inorganic and organic nitrate in heavily urbanized locations in the northeastern US. These findings are further supported by additional ancillary analysis of near-surface concentrations of O_3, NO_x, pNO_3, and NOR. This shift in chemistry contributes to the high wintertime pNO_3 concentrations that continue to plague major urban cities in the northeastern US despite major reductions in NO_x[7,10]. Atmospheric oxidation efficiency changes and their impact on pollutant lifetime may have also contributed to a redistribution of acid and nutrient deposition. This work provides a new framework to test our understanding of the effectiveness of emission controls on endpoints such as O_3, PM, and deposition.

3. Acknowledgments

We thank Ruby Ho for laboratory assistance. We thank the Rhode Island Department of Environmental Management (RI-DEM) and the Rhode Island Department of Health (RI-DOH) for filter collection.

4. References

1. Galloway, J. N. *et al.* Nitrogen cycles: past, present, and future. *Biogeochemistry* **70**, 153–226 (2004).
2. Pinder, R. W. *et al.* Climate change impacts of US reactive nitrogen. *Proc. Natl. Acad. Sci. U.S.A.* **109**, 7671–7675 (2012).
3. Crutzen, P. J. The role of NO and NO_2 in the chemistry of the troposphere and stratosphere. *Annual review of earth and planetary sciences* **7**, 443–472 (1979).
4. Prinn, R. G. The Cleansing Capacity of the Atmosphere. *Annu. Rev. Environ. Resour.* **28**, 29–57 (2003).
5. Newsome, B. & Evans, M. Impact of uncertainties in inorganic chemical rate constants on tropospheric composition and ozone radiative forcing. *Atmospheric Chemistry and Physics* **17**, 14333–14352 (2017).
6. Seinfeld, J. H. & Pandis, S. N. *Atmospheric Chemistry and Physics: From Air Pollution to Climate Change*. (John Wiley & Sons, 2016).
7. Shah, V. *et al.* Chemical feedbacks weaken the wintertime response of particulate sulfate and nitrate to emissions reductions over the eastern United States. *Proceedings of the National Academy of Sciences* **115**, 8110–8115 (2018).
8. Sullivan, T. J. *et al.* Air pollution success stories in the United States: The value of long-term observations. *Environmental science & policy* **84**, 69–73 (2018).
9. Li, H. *et al.* Rapid transition in winter aerosol composition in Beijing from 2014 to 2017: response to clean air actions. *Atmospheric Chemistry and Physics* **19**, 11485–11499 (2019).
10. Kim, H., Walters, W. W., Kysela, L. & Hastings, M. G. Long-term trends in inorganic aerosol chemical composition and chemistry at an urban and rural site in the northeastern US. *Science of The Total Environment* **904**, 166848 (2023).
11. Jaeglé, L. *et al.* Nitrogen oxides emissions, chemistry, deposition, and export over the Northeast United States during the WINTER aircraft campaign. *Journal of Geophysical Research: Atmospheres* **123**, 12–368 (2018).
12. Kenagy, H. S. *et al.* NO_x Lifetime and NO_y Partitioning During WINTER. *JGR Atmospheres* **123**, 9813–9827 (2018).
13. Laughner, J. L. & Cohen, R. C. Direct observation of changing NO_x lifetime in North American cities. *Science* **366**, 723–727 (2019).
14. Kim, H., Walters, W. W., Bekker, C., Murray, L. T. & Hastings, M. G. Nitrate chemistry in the northeast US–Part 2: Oxygen isotopes reveal differences in particulate and gas-phase formation. *Atmospheric Chemistry and Physics* **23**, 4203–4219 (2023).

15. Thiemens, M. H. Mass-Independent Isotope Effects in Planetary Atmospheres and the Early Solar System. *Science* **283**, 341–345 (1999).
16. Vicars, W. C. & Savarino, J. Quantitative constraints on the ^{17}O-excess ($\Delta^{17}O$) signature of surface ozone: Ambient measurements from 50°N to 50°S using the nitrite-coated filter technique. *Geochimica et Cosmochimica Acta* **135**, 270–287 (2014).
17. Lyons, J. R. Transfer of mass-independent fractionation in ozone to other oxygen-containing radicals in the atmosphere. *Geophysical Research Letters* **28**, 3231–3234 (2001).
18. Michalski, G., Scott, Z., Kabiling, M. & Thiemens, M. H. First measurements and modeling of $\Delta^{17}O$ in atmospheric nitrate. *Geophysical Research Letters* **30**, (2003).
19. Alexander, B. *et al.* Global inorganic nitrate production mechanisms: comparison of a global model with nitrate isotope observations. *Atmospheric Chemistry and Physics* **20**, 3859–3877 (2020).
20. Hastings, M. G., Sigman, D. M. & Lipschultz, F. Isotopic evidence for source changes of nitrate in rain at Bermuda. *Journal of Geophysical Research: Atmospheres* **108**, (2003).
21. Michalski, G., Bhattacharya, S. K. & Mase, D. F. Oxygen isotope dynamics of atmospheric nitrate and its precursor molecules. in *Handbook of environmental isotope geochemistry* 613–635 (Springer, 2012).
22. Walters, W. W. & Michalski, G. Ab initio study of nitrogen and position-specific oxygen kinetic isotope effects in the NO+ O_3 reaction. *The Journal of chemical physics* **145**, (2016).
23. Walters, W. W., Tharp, B. D., Fang, H., Kozak, B. J. & Michalski, G. Nitrogen isotope composition of thermally produced NO_x from various fossil-fuel combustion sources. *Environmental science & technology* **49**, 11363–11371 (2015).
24. Walters, W. W., Pye, H. O. T., Kim, H. & Hastings, M. G. Modeling the Oxygen Isotope Anomaly ($\Delta^{17}O$) of Reactive Nitrogen in the Community Multiscale Air Quality Model: Insights into Nitrogen Oxide Chemistry in the Northeastern United States. *ACS EST Air* acsestair.3c00056 (2024) doi:10.1021/acsestair.3c00056.
25. Sickles Ii, J. E. & Shadwick, D. S. Air quality and atmospheric deposition in the eastern US: 20 years of change. *Atmospheric Chemistry and Physics* **15**, 173–197 (2015).
26. Brown, S. S. *et al.* Variability in Nocturnal Nitrogen Oxide Processing and Its Role in Regional Air Quality. *Science* **311**, 67–70 (2006).
27. Elliott, E. M. *et al.* Dual nitrate isotopes in dry deposition: Utility for partitioning NO_x source contributions to landscape nitrogen deposition. *Journal of Geophysical Research: Biogeosciences* **114**, (2009).
28. Wang, Y. *et al.* Influences of Atmospheric Pollution on the Contributions of Major Oxidation Pathways to $PM_{2.5}$ Nitrate Formation in Beijing. *JGR Atmospheres* **124**, 4174–4185 (2019).
29. Bryhn, A. C. & Dimberg, P. H. An operational definition of a statistically meaningful trend. *PLoS One* **6**, e19241 (2011).
30. Foley, K. M. *et al.* 2002–2017 anthropogenic emissions data for air quality modeling over the United States. *Data in Brief* **47**, 109022 (2023).
31. Shah, V. *et al.* Effect of changing NO_x lifetime on the seasonality and long-term trends of satellite-observed tropospheric NO_2 columns over China. *Atmospheric Chemistry and Physics* **20**, 1483–1495 (2020).
32. Romer Present, P. S., Zare, A. & Cohen, R. C. The changing role of organic nitrates in the removal and transport of NO_x. *Atmospheric Chemistry and Physics* **20**, 267–279 (2020).

33. Ng, N. L. *et al.* Nitrate radicals and biogenic volatile organic compounds: oxidation, mechanisms, and organic aerosol. *Atmospheric chemistry and physics* **17**, 2103–2162 (2017).
34. Desai, N. S. *et al.* Impact of Heatwaves and Declining NO_x on Nocturnal Monoterpene Oxidation in the Urban Southeastern United States. *JGR Atmospheres* **129**, e2024JD041482 (2024).
35. Casciotti, K. L., Sigman, D. M., Hastings, M. G., Böhlke, J. K. & Hilkert, A. Measurement of the oxygen isotopic composition of nitrate in seawater and freshwater using the denitrifier method. *Analytical chemistry* **74**, 4905–4912 (2002).
36. Kaiser, J., Hastings, M. G., Houlton, B. Z., Röckmann, T. & Sigman, D. M. Triple oxygen isotope analysis of nitrate using the denitrifier method and thermal decomposition of N_2O. *Analytical Chemistry* **79**, 599–607 (2007).
37. Böhlke, J. K., Mroczkowski, S. J. & Coplen, T. B. Oxygen isotopes in nitrate: new reference materials for ^{18}O:^{17}O:^{16}O measurements and observations on nitrate-water equilibration. *Rapid Comm Mass Spectrometry* **17**, 1835–1846 (2003).
38. Miller, M. F. Isotopic fractionation and the quantification of ^{17}O anomalies in the oxygen three-isotope system: an appraisal and geochemical significance. *Geochimica et Cosmochimica Acta* **66**, 1881–1889 (2002).
39. Benish, S. E. *et al.* Long-term regional trends of nitrogen and sulfur deposition in the United States from 2002 to 2017. *Atmospheric Chemistry and Physics* **22**, 12749–12767 (2022).
40. Appel, K. W. *et al.* The Community Multiscale Air Quality (CMAQ) model versions 5.3 and 5.3. 1: system updates and evaluation. *Geoscientific model development* **14**, 2867–2897 (2021).
41. Sarwar, G., Simon, H., Bhave, P. & Yarwood, G. Examining the impact of heterogeneous nitryl chloride production on air quality across the United States. *Atmospheric Chemistry and Physics* **12**, 6455–6473 (2012).
42. Yarwood, G. *et al.* Updates to the Carbon Bond mechanism for version 6 (CB6). in *9th Annual CMAS Conference, Chapel Hill, NC* 11–13 (2010).
43. Pleim, J. E., Ran, L., Appel, W., Shephard, M. W. & Cady-Pereira, K. New Bidirectional Ammonia Flux Model in an Air Quality Model Coupled With an Agricultural Model. *J Adv Model Earth Syst* **11**, 2934–2957 (2019).
44. Bash, J. O., Cooter, E. J., Dennis, R. L., Walker, J. T. & Pleim, J. E. Evaluation of a regional air-quality model with bidirectional NH_3 exchange coupled to an agroecosystem model. *Biogeosciences* **10**, 1635–1645 (2013).
45. Clifton, O. E. *et al.* A single-point modeling approach for the intercomparison and evaluation of ozone dry deposition across chemical transport models (Activity 2 of AQMEII4). *Atmospheric Chemistry and Physics* **23**, 9911–9961 (2023).
46. Walker, J. T. *et al.* Atmospheric deposition of reactive nitrogen to a deciduous forest in the southern Appalachian Mountains. *Biogeosciences* **20**, 971–995 (2023).
47. Hogrefe, C. *et al.* An analysis of CMAQ gas-phase dry deposition over North America through grid-scale and land-use-specific diagnostics in the context of AQMEII4. *Atmospheric Chemistry and Physics* **23**, 8119–8147 (2023).
48. Wu, Z. *et al.* Estimating source-sink distributions and fluxes of reactive nitrogen and sulfur within a mixed forest canopy. *Agricultural and Forest Meteorology* **333**, 109386 (2023).
49. Beck, J. *et al.* An evaluation of a hybrid, terrain-following vertical coordinate in the WRF-based RAP and HRRR models. *Weather and Forecasting* **35**, 1081–1096 (2020).

50. Zhang, Y. *et al.* A Measurement-Model Fusion Approach for Improved Wet Deposition Maps and Trends. *JGR Atmospheres* **124**, 4237–4251 (2019).
51. Xing, J. *et al.* Historical gaseous and primary aerosol emissions in the United States from 1990 to 2010. *Atmospheric Chemistry and Physics* **13**, 7531–7549 (2013).
52. Alexander, B. *et al.* Quantifying atmospheric nitrate formation pathways based on a global model of the oxygen isotopic composition ($\Delta^{17}O$) of atmospheric nitrate. *Atmospheric Chemistry and Physics* **9**, 5043–5056 (2009).
53. Carslaw, D. C. & Ropkins, K. Openair—an R package for air quality data analysis. *Environmental Modelling & Software* **27**, 52–61 (2012).
54. Cleveland, R. B., Cleveland, W. S., McRae, J. E. & Terpenning, I. STL: A seasonal-trend decomposition. *J. off. Stat* **6**, 3–73 (1990).

5. Extended data & Supplementary

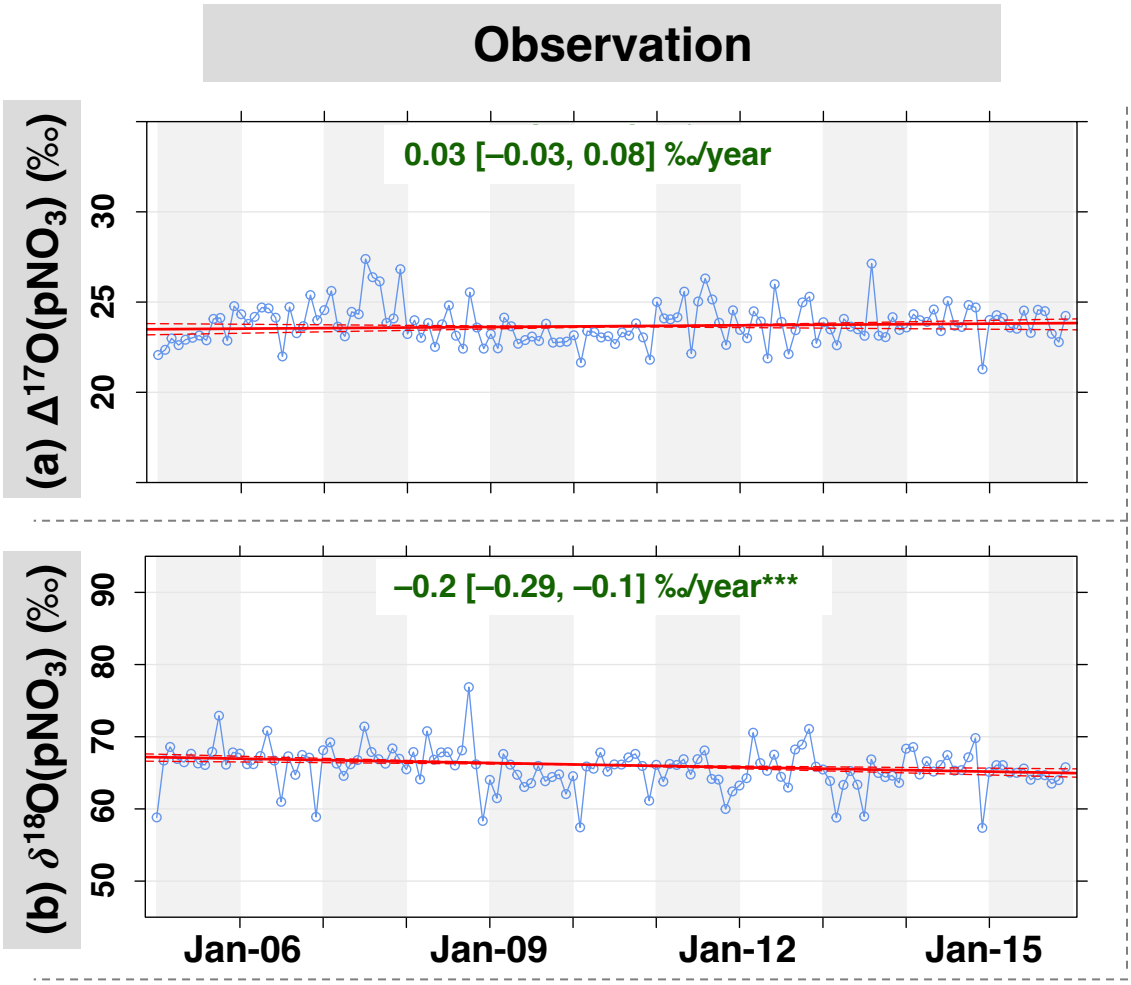

Extended Data Figure 4.1. Trends in observed (a) $\Delta^{17}O$ and (b) $\delta^{18}O$ of pNO_3 from 2005 to 2015 in Providence, RI. These plots show deseasonalized monthly mean isotope values, with the solid red line indicating the trend estimate and the dashed red lines representing the 95% confidence intervals. The overall trend is displayed at the top with the slope. The asterisks (***) indicate that the trend is significant at the 0.001 level. Deseasonalization was conducted using the stl function (Seasonal-Trend decomposition using locally weighted scatterplot smoothing (LOESS)) in the openair package in R[1,2]. Details can be found in the Method section.

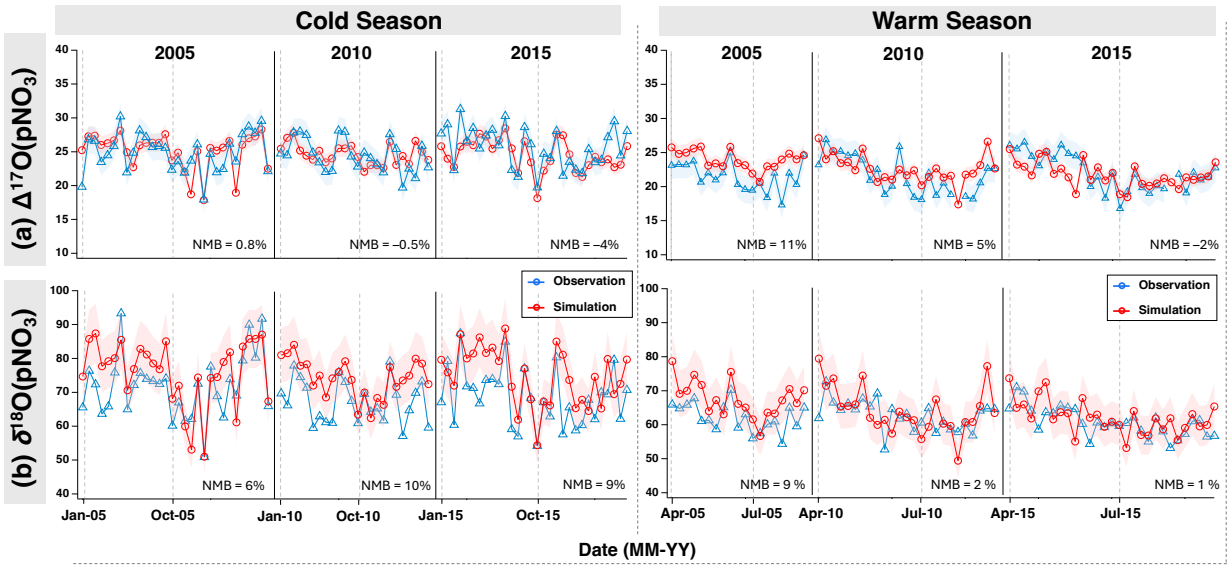

Extended Data Figure 4.2. Time series of observed and modeled (a) $\Delta^{17}O$ and (b) $\delta^{18}O$ of pNO_3 for the cold and warm seasons over time. Normalized mean biases (NMB) are indicated within the plots. The shaded areas surrounding observed $\Delta^{17}O$ and $\delta^{18}O$ data (blue) denote the ±1σ analytical error (±2 ‰ for $\Delta^{17}O$, ±0.4 ‰ for $\delta^{18}O$). The shaded areas surrounding modeled $\Delta^{17}O$ and $\delta^{18}O$ (red) denote the uncertainty of the oxygen isotope composition of atmospheric oxidants involved in NO_x chemistry (±5 % for $\Delta^{17}O$ and ±10 % for $\delta^{18}O$).

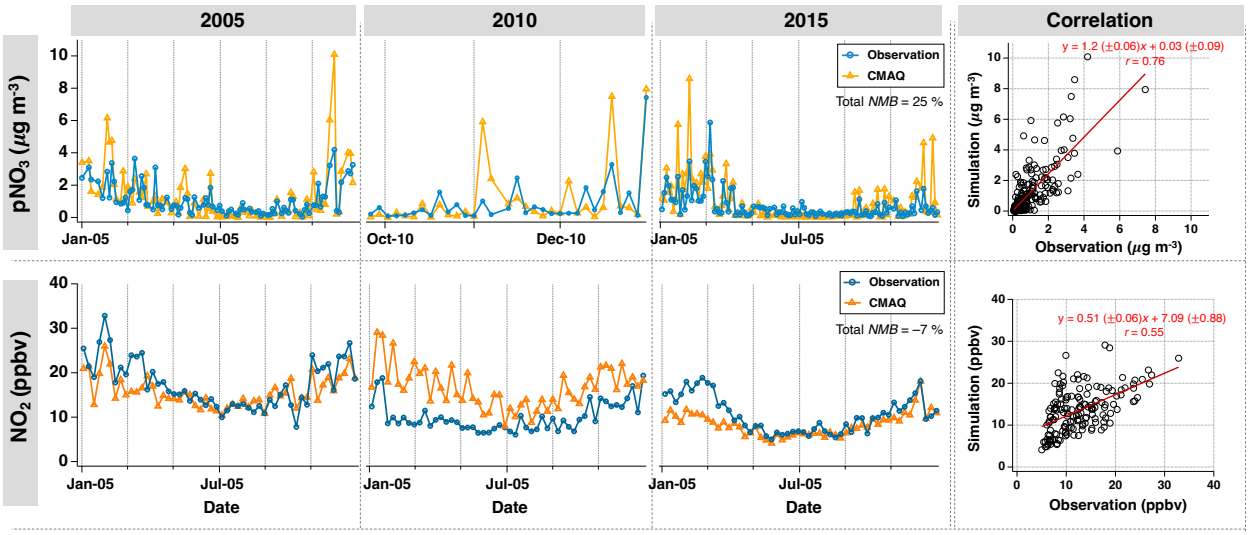

Extended Data Figure 4.3. Time series of weekly mean $PM_{2.5}$ total nitrate and NO_2 concentrations observed (blue) and simulated (orange) with their correlations. The slope, correlation coefficient (r), and normalized mean biases (NMB) are indicated within the plots. Surface measurement data of total nitrate in $PM_{2.5}$ and NO_2 are from the Chemical Speciation Network (CSN) in Providence, RI. Note that observation data of total nitrate in $PM_{2.5}$ for 2010 is not available from Jan to Sep.

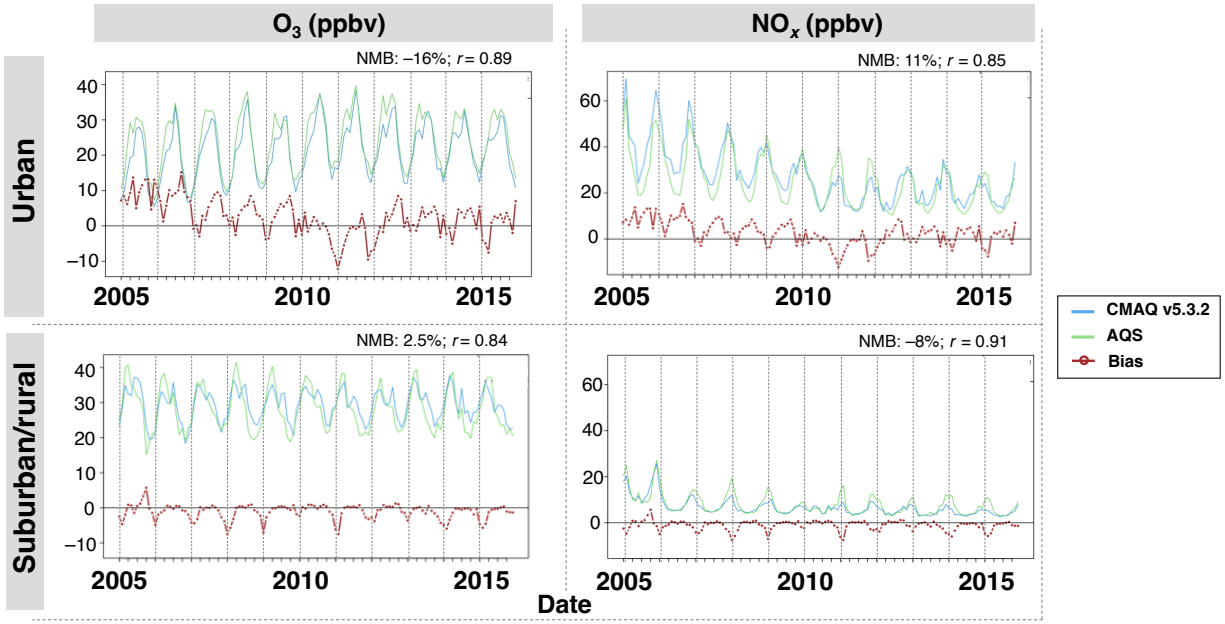

Extended Data Figure 4.4. Time series of monthly mean O_3 and NO_x concentrations observed (green) and simulated (blue) with biases between model and observation. Model performance evaluation metrics such as the normalized mean biases (NMB) and correlation coefficient (r) are indicated within the plots (note that evaluation metrics are averaged for 2005, 2010, and 2015 years only). Urban includes Boston, MA, New York Cities, and Washington, DC datasets, while suburban/rural includes the suburban area in MA and rural area in NY. Surface O_3 and NO_x observation data is from EPA air quality monitoring networks.

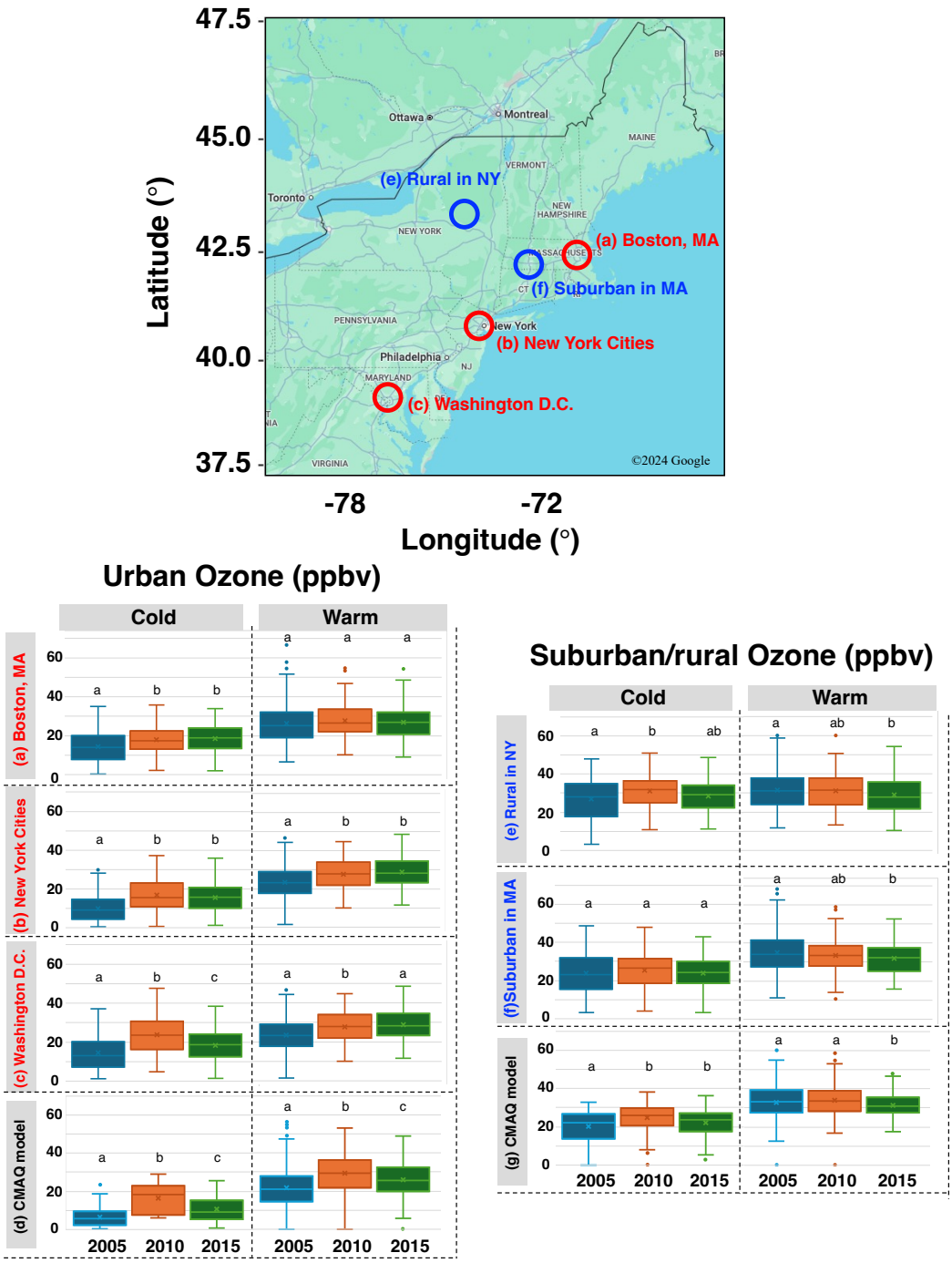

Extended Data Figure 4.5. Box-and-whiskers plot describing the seasonal surface O_3 distribution from observations (a-c, e-f) and simulation (d) and (g)) for 2005, 2010, and 2015. Major urban areas include (a) Boston, MA (42.33°N, –71.08°W), (b) New York (40.81°N, –73.90°W), and (c) Washington, DC (38.92°N, –77.01°W); suburban and rural stations include (f) MA (42.19°N, –72.56°W) and (e) NY (43.45°N, –74.52°W), respectively. CMAQ model results are averaged for (d) urban and (g) rural areas. Similar lowercase letters in the plots represent statistically similar values (based on a two-sided t-test). Note that Providence is not included here because O_3 was only historically monitored for the warm season (Mar-Sep).

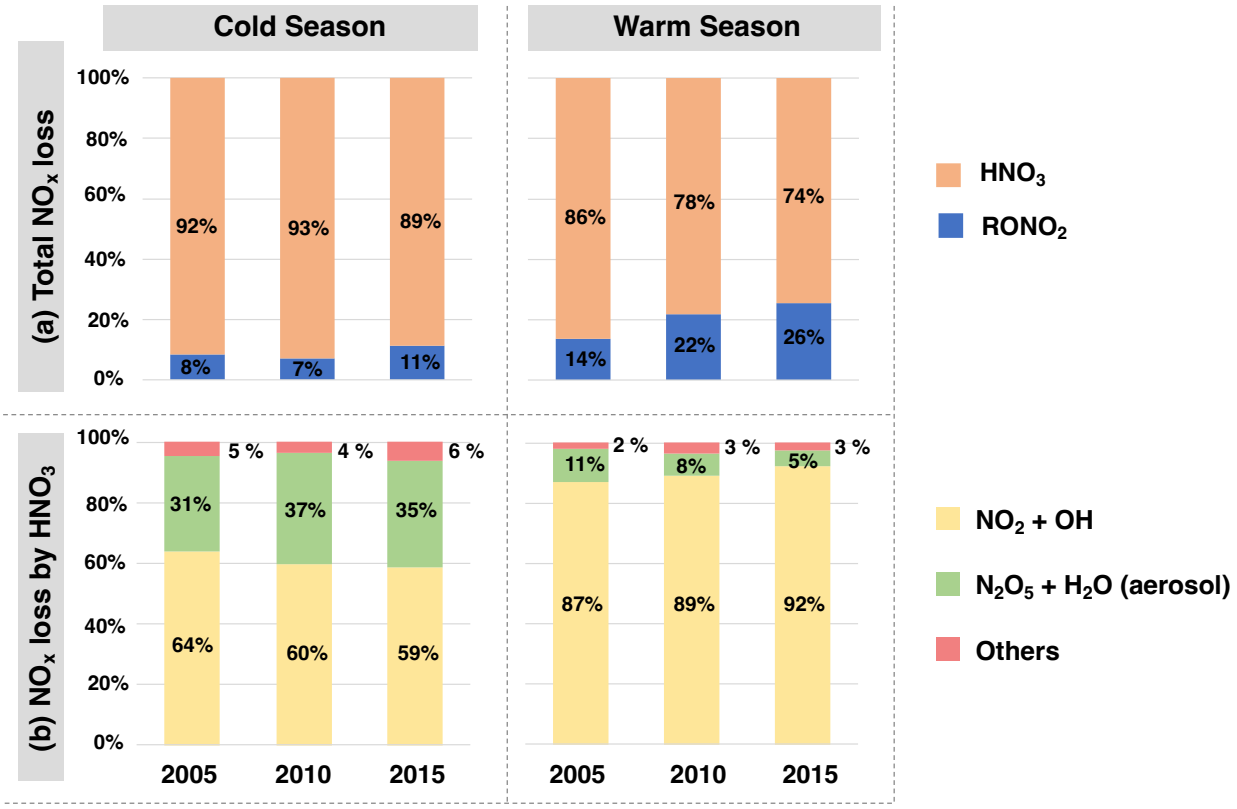

Extended Data Figure 4.6. Fractional loss pathways for (a) total NO_x, and (b) NO_x loss via HNO_3 formation for cold and warm seasons in Providence, RI. A detailed breakdown of other NO_2 and HNO_3 formation pathways is provided in Extended Data Table 4.1.

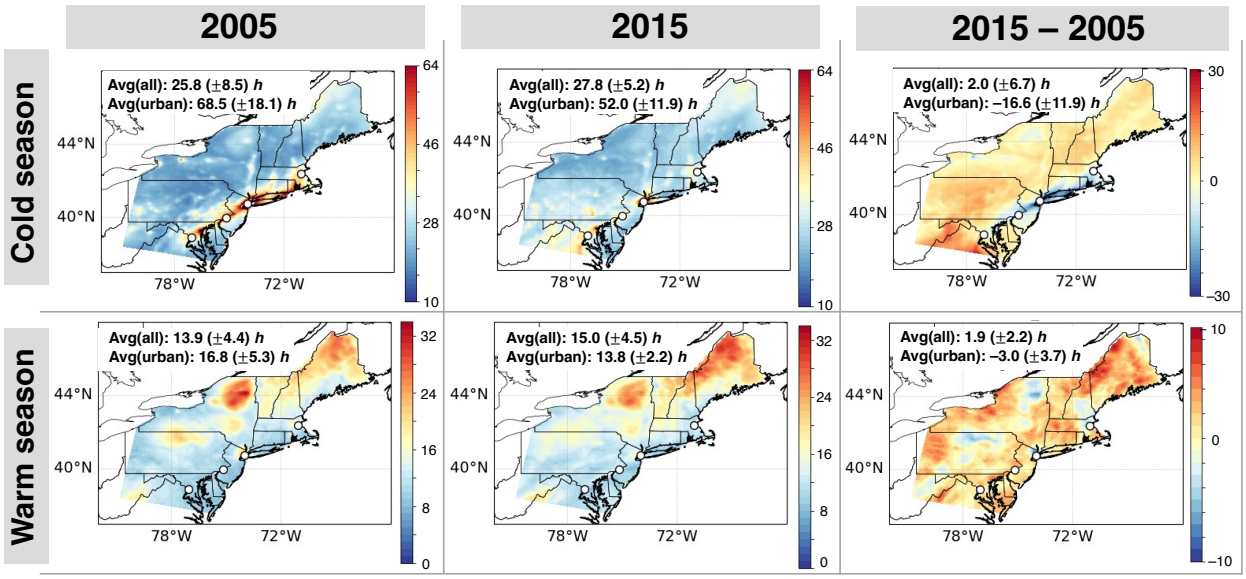

Extended Data Figure 4.7. Calculated NO_x lifetime over the northeastern US domain for cold and warm seasons for 2005 and 2015, along with their difference. The circles indicate the locations of major cities in the northeastern US, including Boston, MA; New York City, NY; Philadelphia, PA; and Washington, DC. The averaged NO_x lifetime for the major cities is shown as "Avg(urban)" (τ_{urban}) for the northeastern US and includes Providence, RI.

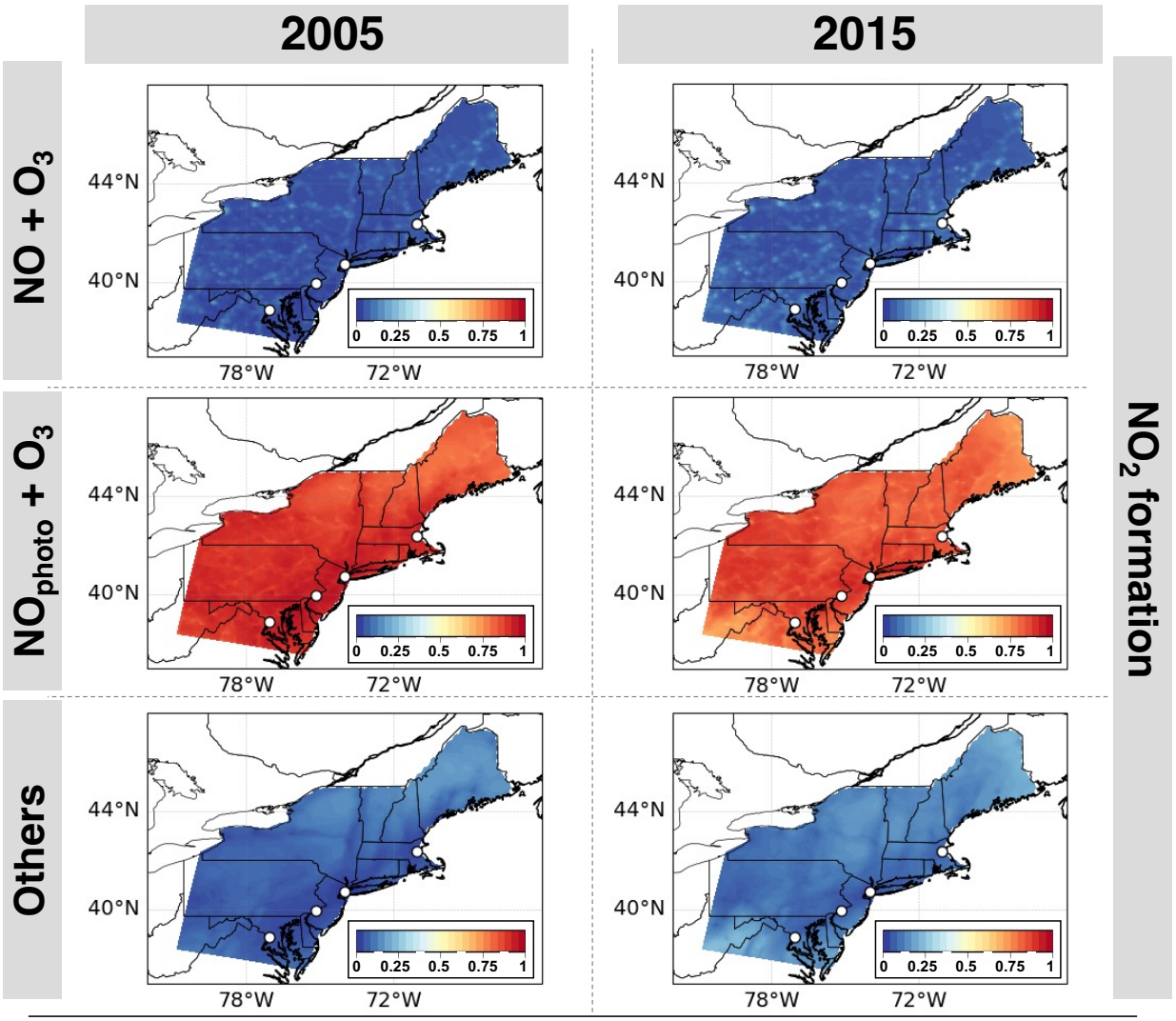

Extended Data Figure 4.8. Fractional pathways for NO_2 formation over the northeastern US domain for 2005 and 2015. A detailed breakdown of other NO_2 and HNO_3 formation pathways is provided in Extended Data Table 4.1.

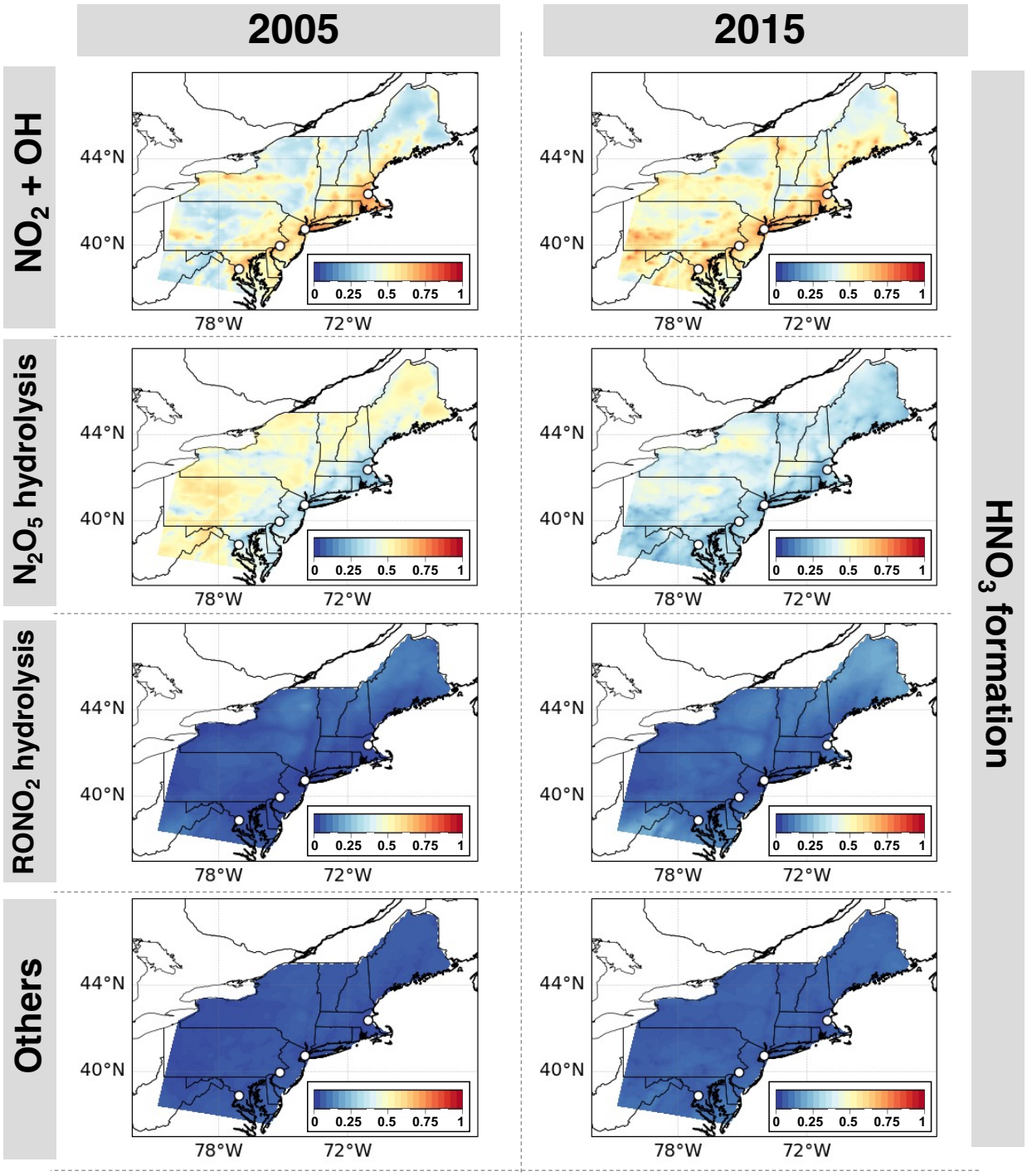

Extended Data Figure 4.9. Fractional pathways for HNO_3 formation over the northeastern US domain for 2005 and 2015. A detailed breakdown of other NO_2 and HNO_3 formation pathways is provided in Extended Data Table 4.1.

Extended Data Table 4.1. Oxygen isotope mass-balance equations for $\Delta^{17}O$ and $\delta^{18}O$ calculation by different NO_2 and HNO_3 formation pathways.

Species	Pathway	$\Delta^{17}O$ Transfer Factor	$\delta^{18}O$ Transfer Factor
NO_2	$NO + O_3$	$(1/2)\Delta^{17}O(O_3^*)$	$(1/2)\delta^{18}O(NO) + (1/2)\delta^{18}O(O_3^*)$
	$NO + HO_2$	0	$(1/2)\delta^{18}O(NO) + (1/2)\delta^{18}O(HO_2)$
	$NO + RO_2$	0	$(1/2)\delta^{18}O(NO) + (1/2)\delta^{18}O(RO_2)$
	$NO + ClO$	$(1/2)\Delta^{17}O(O_3^*)$	$(1/2)\delta^{18}O(NO) + (1/2)\delta^{18}O(O_3^*)$
	$NO_{photo} + O_3$	$\Delta^{17}O(O_3^*)$	$\delta^{18}O(O_3)$
	$NO_{photo} + HO_2$	0	$\delta^{18}O(HO_2)$
	$NO_{photo} + RO_2$	0	$\delta^{18}O(RO_2)$
	$NO_{photo} + ClO$	$\Delta^{17}O(O_3^*)$	$\delta^{18}O(ClO)$
HNO_3	$NO_2 + OH$	$(2/3)\Delta^{17}O(NO_2)$	$(2/3)\delta^{18}O(NO_2) + (1/3)\delta^{18}O(OH)$
	$NO_3 + VOC$	$(2/3)\Delta^{17}O(NO_2) + (1/3)\Delta^{17}O(O_3^*)$	$(2/3)\delta^{18}O(NO_2) + (1/3)\delta^{18}O(O_3^*)$
	$N_2O_5 + H_2O(g)$	$(2/3)\Delta^{17}O(NO_2) + (1/6)\Delta^{17}O(O_3^*)$	$(2/3)\delta^{18}O(NO_2) + (1/6)\delta^{18}O(O_3^*) + (1/6)\delta^{18}O(H_2O)$
	$N_2O_5 + H_2O$ (aerosol)	$(2/3)\Delta^{17}O(NO_2) + (1/6)\Delta^{17}O(O_3^*)$	$(2/3)\delta^{18}O(NO_2) + (1/6)\delta^{18}O(O_3^*) + (1/6)\delta^{18}O(H_2O)$
	$NO_2 + H_2O$ (aerosol)	$(2/3)\Delta^{17}O(NO_2)$	$(2/3)\delta^{18}O(NO_2) + (1/3)\delta^{18}O(H_2O)$
	$ClNO_3 + H_2O$ (aerosol)	$(2/3)\Delta^{17}O(NO_2) + (1/3)\Delta^{17}O(O_3^*)$	$(2/3)\delta^{18}O(NO_2) + (1/3)\delta^{18}O(O_3^*)$
	$RONO_2 + H_2O$ (aerosol) (from $RO_2 + NO$)	$(1/3)\Delta^{17}O(NO_2)$	$(1/3)\delta^{18}O(NO_2) + (2/3)\delta^{18}O(O_2)$
	$RONO_2 + H_2O$ (aerosol) (from $R + NO_3$)	$(2/3)\Delta^{17}O(NO_2) + (1/3)\Delta^{17}O(O_3^*)$	$(2/3)\delta^{18}O(NO_2) + (1/3)\delta^{18}O(O_3^*)$

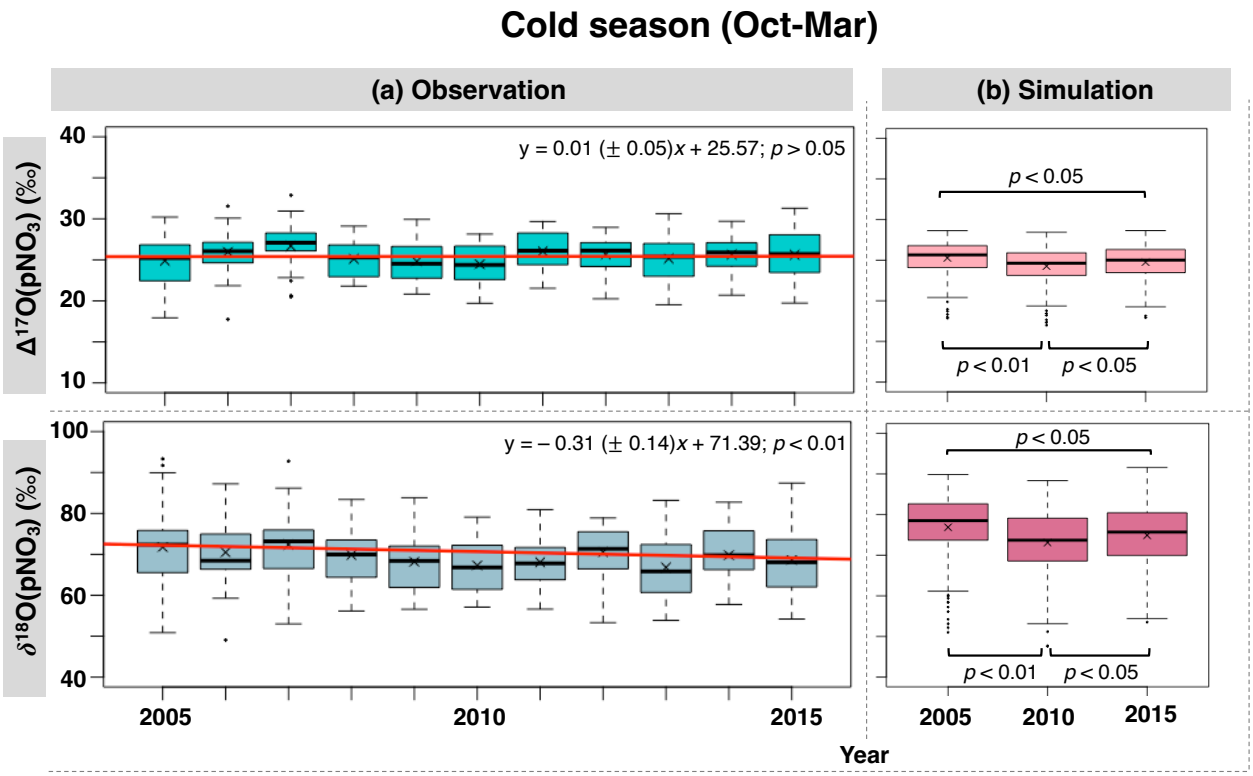

Figure S4.1. Box-and-whiskers plot describing the cold season distribution of observed and modeled $\Delta^{17}O$ (top) and $\delta^{18}O$ (bottom) of pNO_3 from 2005 to 2015 in Providence, RI. The middle line and "x" symbol in each box represent the median and mean values, respectively. The upper and lower ends of the box indicate the 25th and 75th percentiles and the whiskers extend from the box to the minimum and maximum values, excluding outliers (open circles). The solid red line represents the weighted least squares (WLS) regression trends for the observations, with the slope, its standard error, intercept, and the p-value (based on a two-sided t-test) indicated.

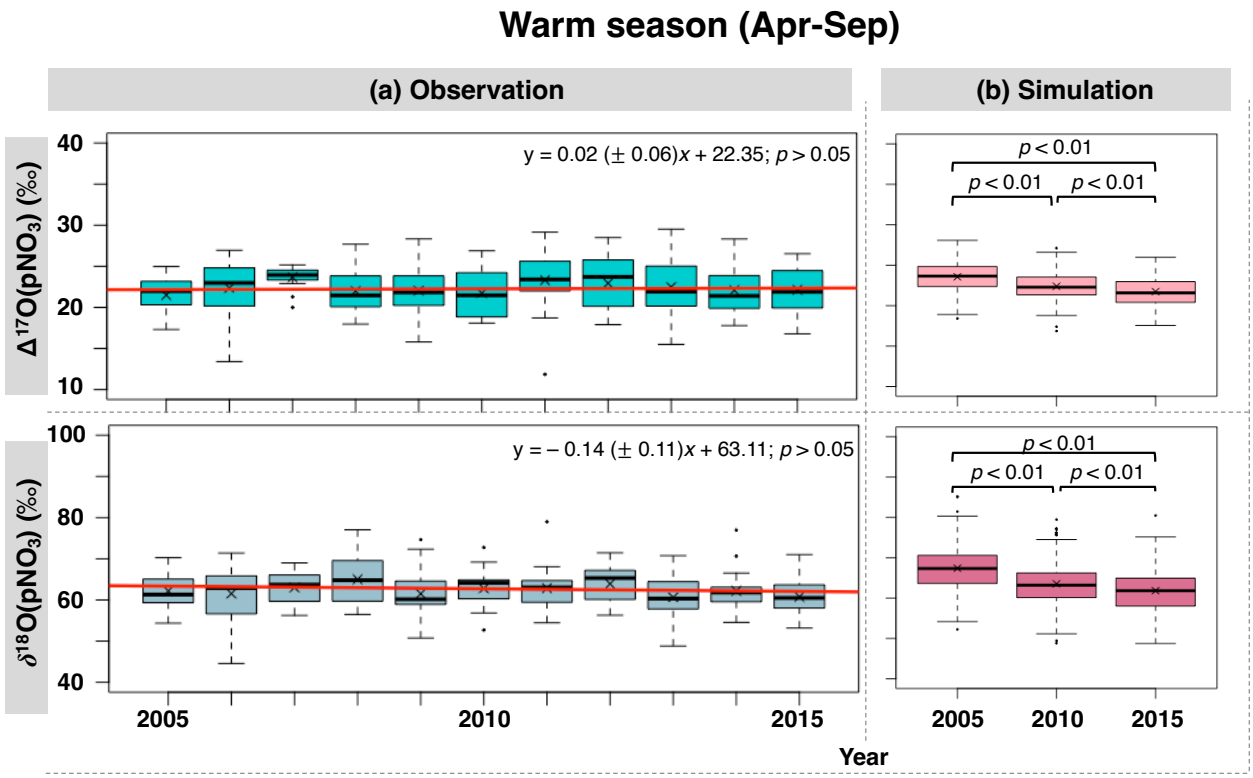

Figure S4.2. Box-and-whiskers plot describing the warm season distribution of observed and modeled $\Delta^{17}O$ (top) and $\delta^{18}O$ (bottom) of pNO_3 from 2005 to 2015 in Providence, RI. The middle line and "x" symbol in each box represent the median and mean values, respectively. The upper and lower ends of the box indicate the 25th and 75th percentiles and the whiskers extend from the box to the minimum and maximum values, excluding outliers (open circles). The solid red line represents the WLS regression trends for the observations, with the slope, its standard error, intercept, and the p-value (based on a two-sided t-test) indicated.

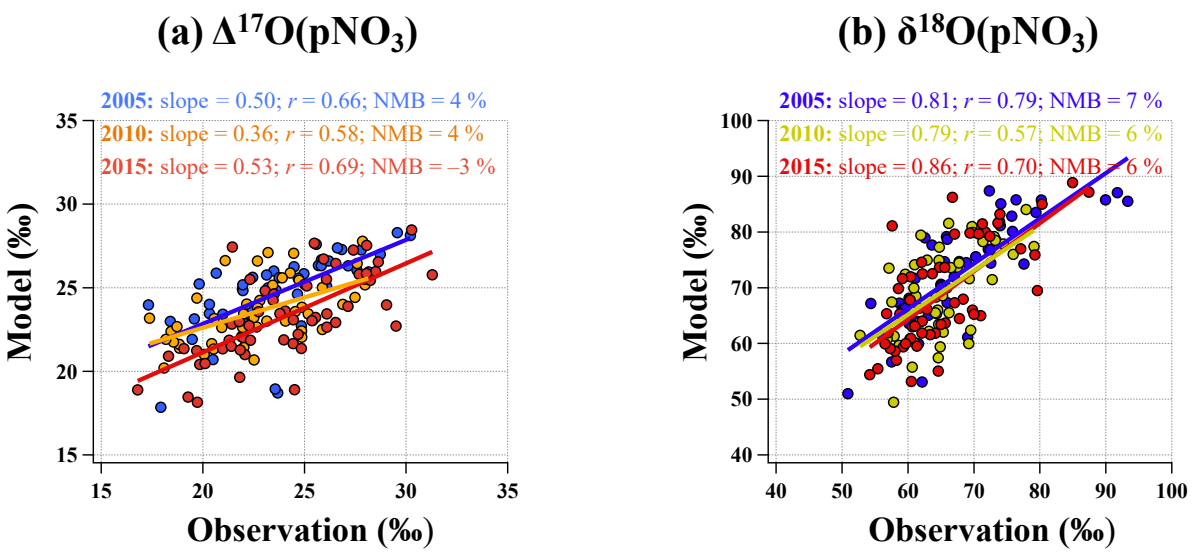

Figure S4.3. Correlation between observed and modeled $\Delta^{17}O$ and $\delta^{18}O$ of pNO_3 for Providence, RI, for the years 2005, 2010, and 2015.

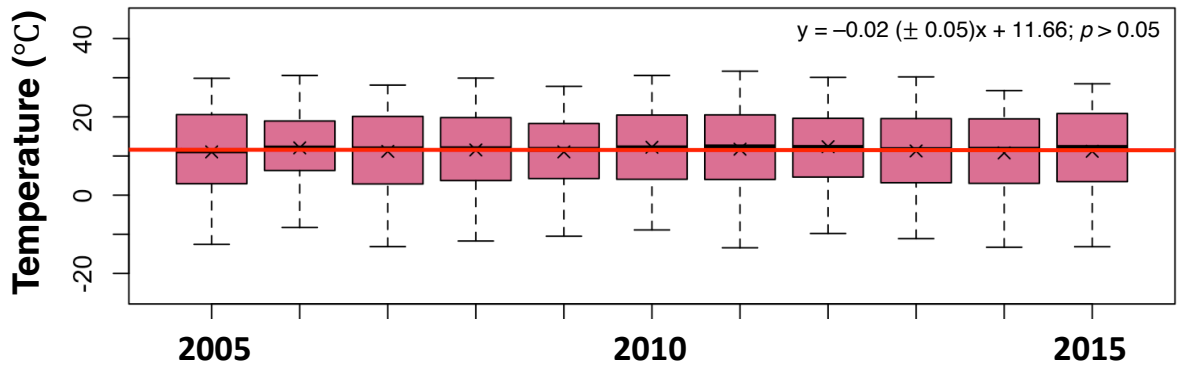

Figure S4.4. Box-and-whiskers plots describing the distribution of observed temperature (year-round) from 2005 to 2015 in Providence, RI. The middle line in each box represents the median value, while the upper and lower ends of the box indicate the 25th and 75th percentiles, respectively. The whiskers extend from the box to the minimum and maximum values with mean value marked as "x". Surface measurement data of temperature is from the CSN site in Providence, RI.

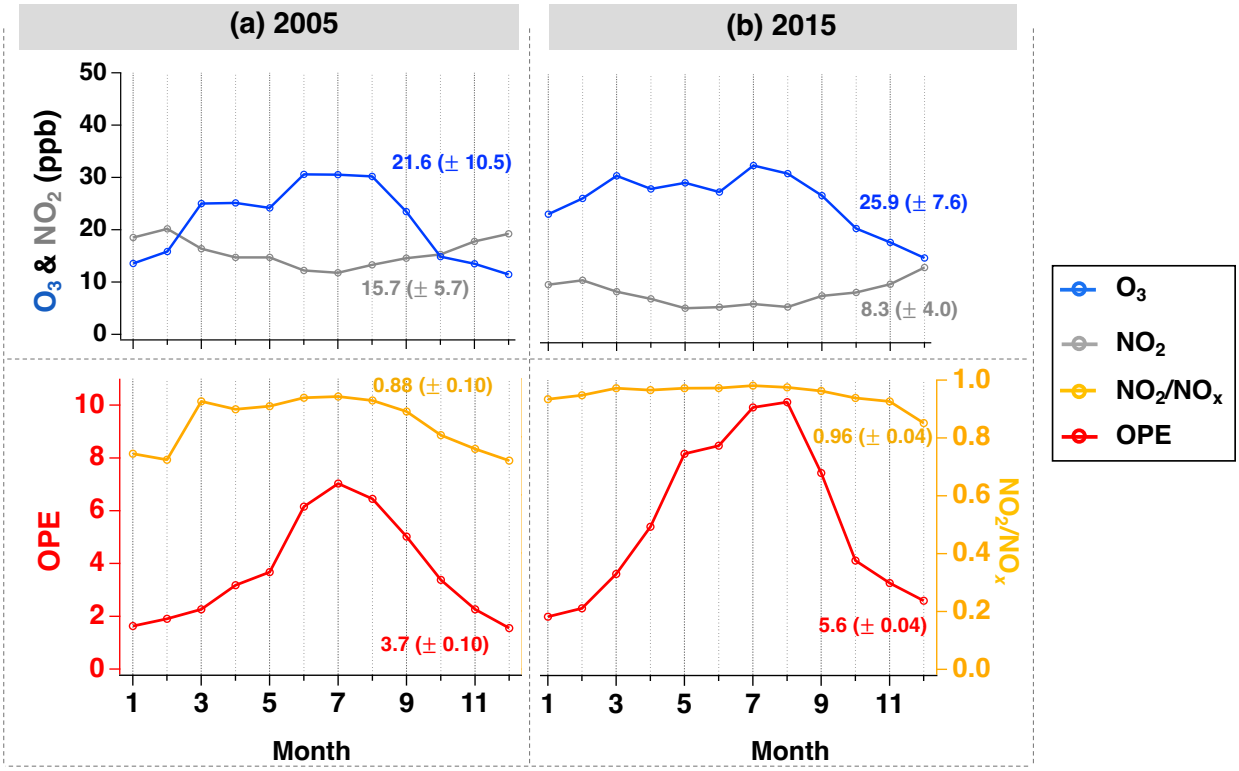

Figure S4.5. Near-surface monthly averaged O_3 and NO_2 concentrations, along with O_3 production efficiency (OPE) and NO_2/NO_x in Providence, RI for 2005 and 2015, as simulated using CMAQ. Overall averages with standard deviation are indicated in the plots. In 2005, NO_2 levels exceeded O_3 during the winter months due to the titration of O_3. In 2015, O_3 concentrations exceeded NO_2 concentrations throughout the entire year.

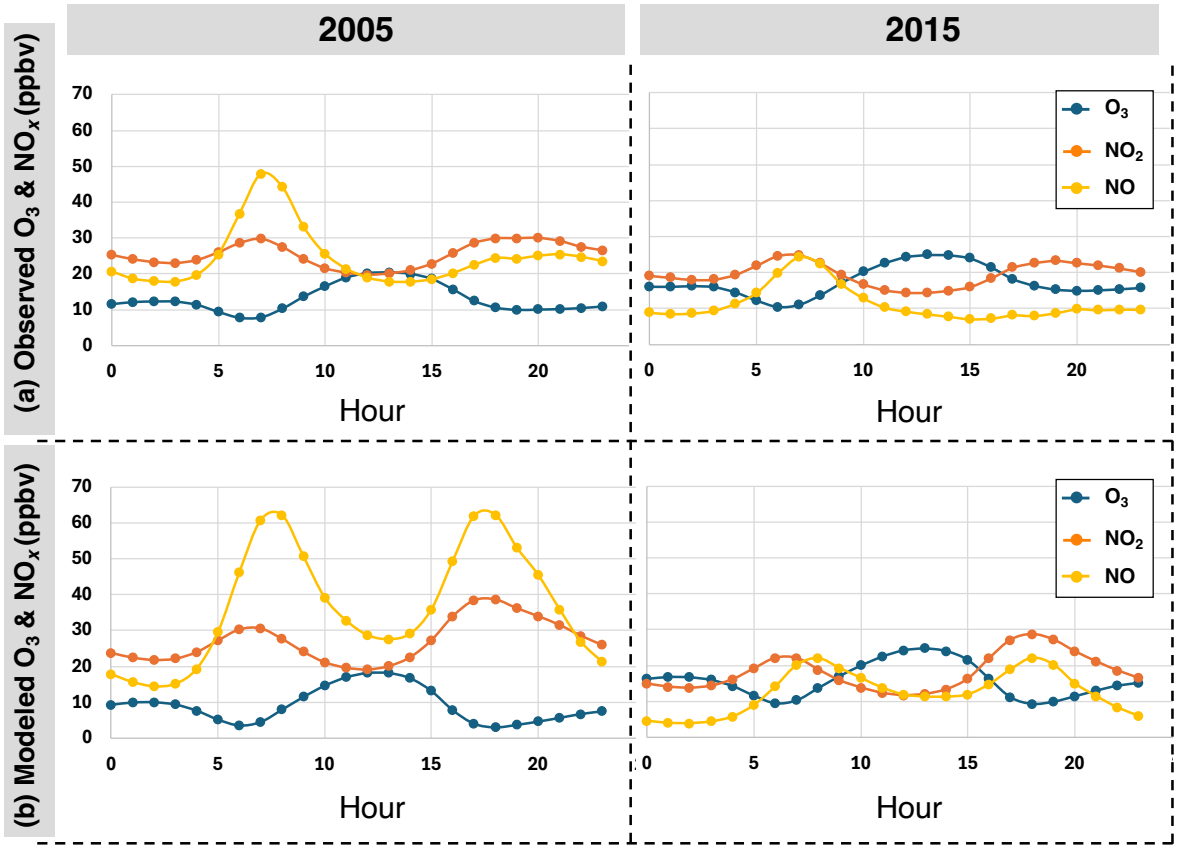

Figure S4.6. Near-surface hourly averaged wintertime O_3, NO_2, and NO concentrations in major urban areas including Boston, MA (42.33°N, –71.08°W), New York (40.81°N, –73.90°W), and Washington, DC (38.92°N, –77.01°W) from (a) observations and (b) simulation for 2005 and 2015.

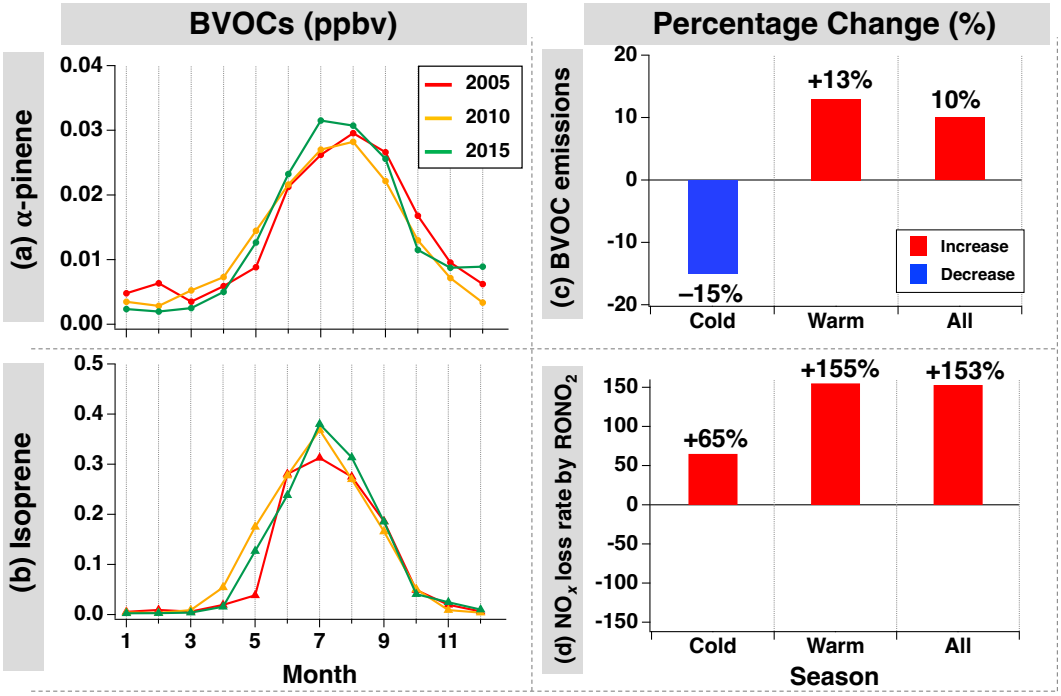

Figure S4.7. Monthly variations of biogenic volatile organic compound (BVOC) concentrations, including (a) α-pinene and (b) isoprene, based on the US EPA CMAQ model, along with (c) their percentage changes by season from 2005 to 2015. Additionally, (d) the percentage change of total NO_x loss rate by $RONO_2$ formation from 2005 to 2015 is included.

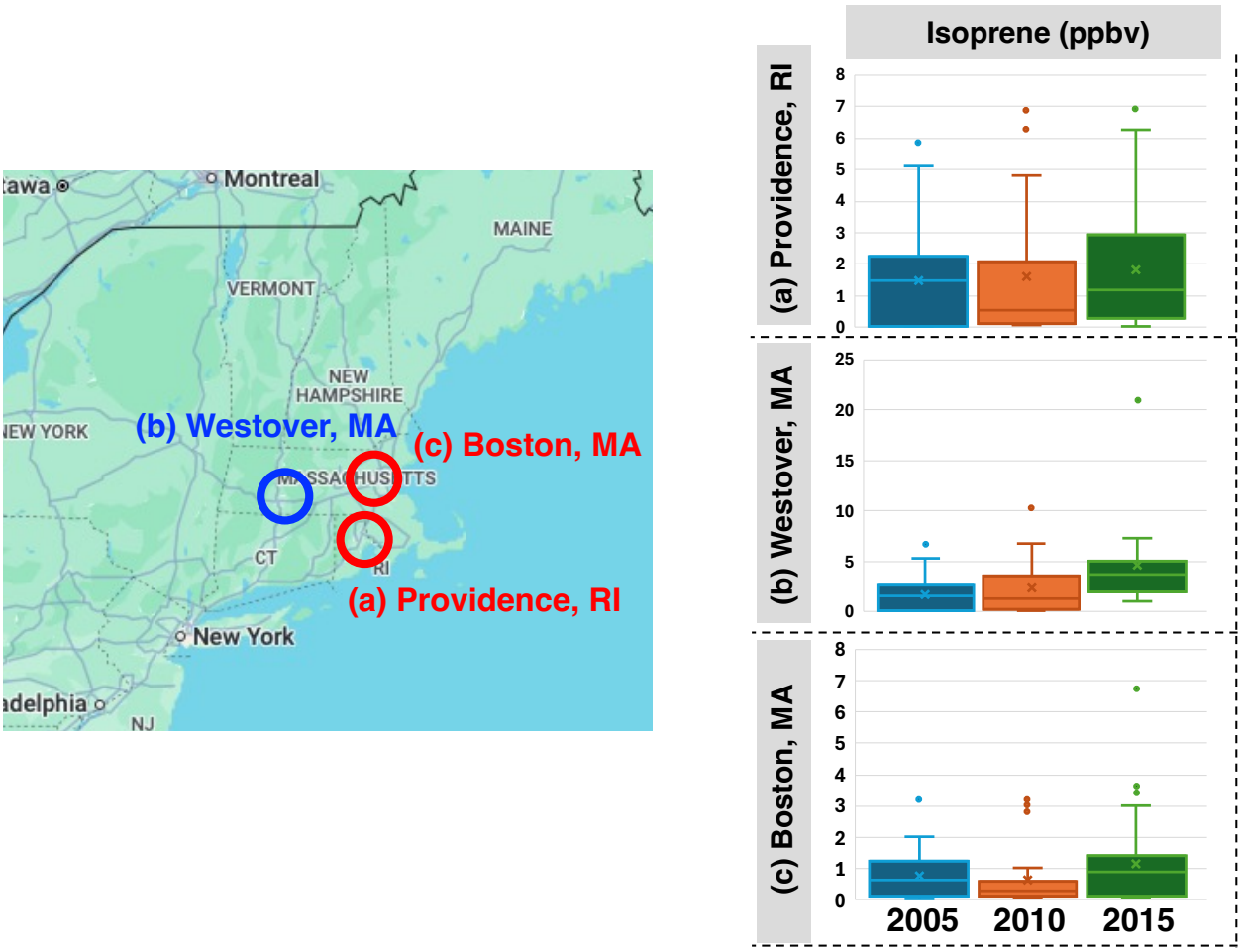

Figure S4.8. Box-and-whiskers plot describing the warm season isoprene distribution for 2005, 2010, and 2015 in major urban cities in the northeastern US, including Providence, RI and Boston, MA, and the rural areas in MA. The map image was created using Google Earth (©2024 Google). Surface isoprene observation data is from the CSN in Providence, RI, Boston, MA, and the rural areas (WESTOVER AFB) in MA.

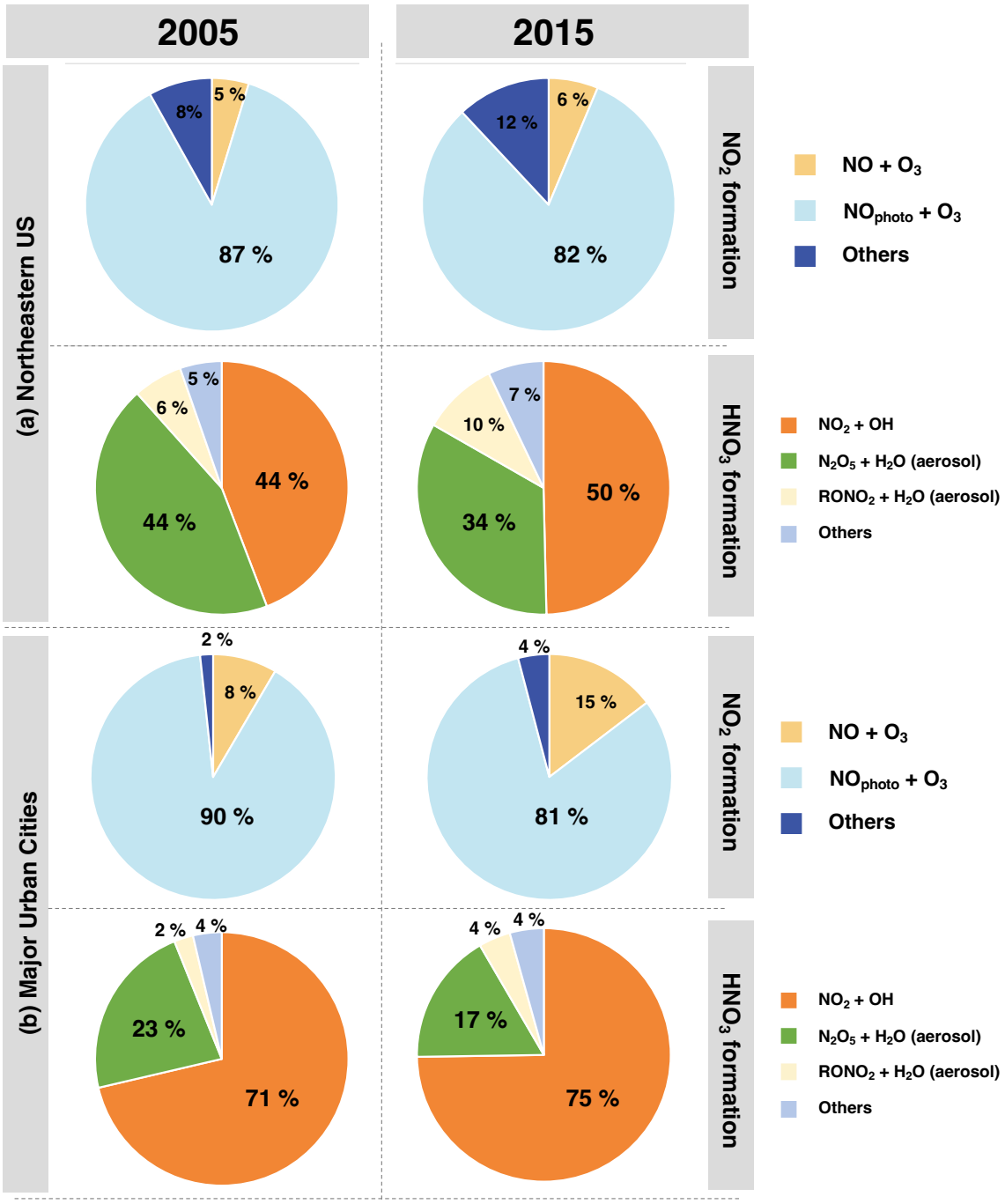

Figure S4.9. Fractional pathways for NO_2 and HNO_3 formation for (a) the Northeastern US domain and (b) the major urban cities in the Northeastern US for 2005 and 2015. A detailed breakdown of other NO_2 and HNO_3 formation pathways is provided in Extended Data Table 4.1.

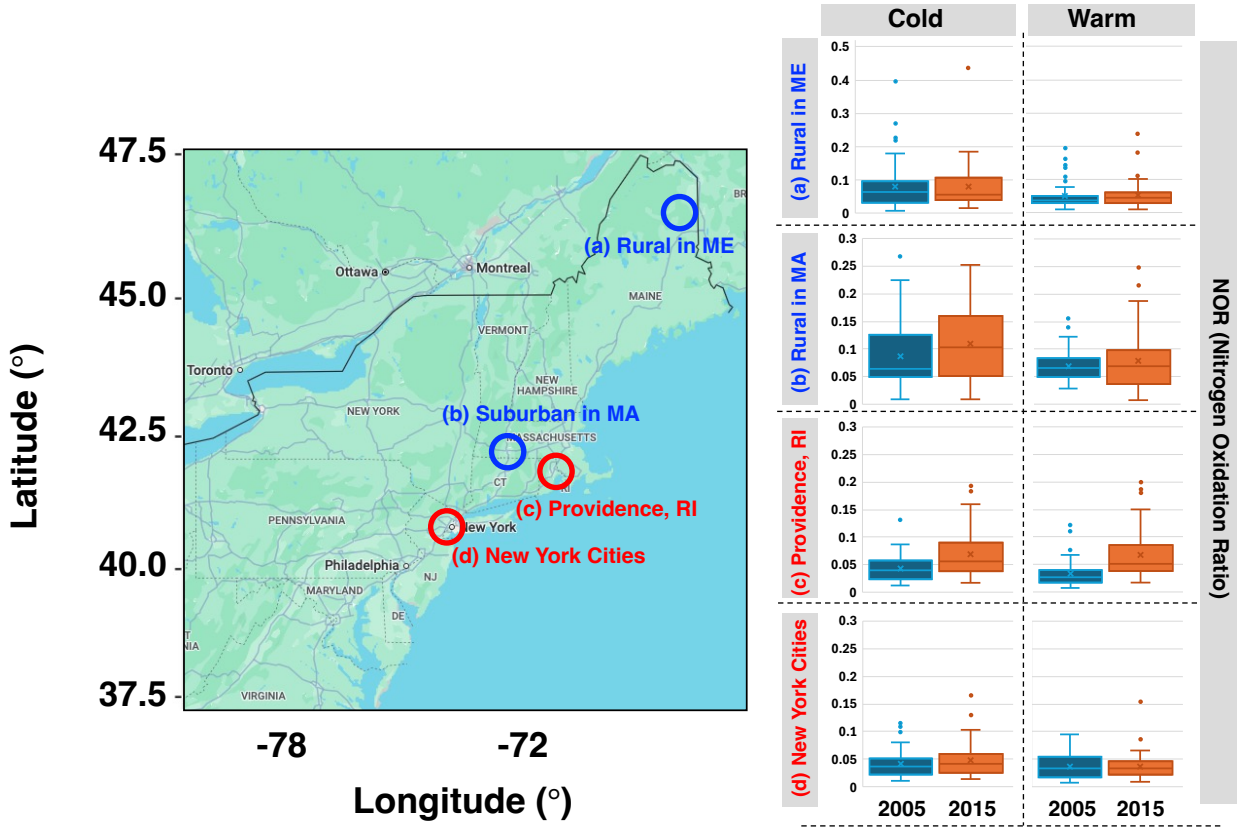

Figure S4.10. Box-and-whiskers plot describing Nitrogen Oxidation Ratio (NOR) distribution by seasons for 2005 and 2015 in major urban cities (Providence, RI and New York City) and suburban/rural sites (suburban area in MA and rural area in ME). NOR is calculated by observed pNO_3 divided by the sum of observed pNO_3 and observed NO_x to assess NO_x to pNO_3 conversion efficiency. Urban data is from the CSN sites and suburban/rural data is from the IMPROVE (Interagency Monitoring of Protected Visual Environments) networks. Note that pNO_3 data is not available for 2005 in rural area in ME, so we replaced it with 2006 data. NOR has increased in the urban areas in recent years, especially in the cold season in response to emission reduction, while no significant trends were observed from the suburban/rural sites.

Table S4.1. Evaluation of trend meaningfulness using the method of Bryhn & Dimberg (2011). The R^2 and p-values were calculated for different interval lengths to determine whether the observed trend is statistically meaningful ($R^2 > 0.65$ and $p < 0.05$). Intervals that meet these criteria are marked as 'Yes' under Meaningfulness

Intervals	R square	p value	Meaningfulness
3	0.9388	0.1592	No
4	0.8951	0.0539	No
5	0.7014	0.0767	No
6	0.6335	0.0582	No
7	0.7058	0.0180	Yes
8	0.3421	0.1278	No
9	0.7279	0.0034	Yes

CHAPTER 5

Isotopic Evidence of Coal's Lingering Footprint in a Post-Coal Era

Heejeong Kim[1,2], Wendell W. Walters[3,4], Havala, O. T. Pye[4], Kristen M. Foley[4], Meredith G. Hastings[1,2]

[1]Department of Earth, Environment, and Planetary Sciences, Brown University, Providence, RI 02912, USA.

[2]Institute at Brown for Environment and Society, Brown University, Providence, RI 02912, USA.

[3]Department of Chemistry and Biochemistry, University of South Carolina, Columbia, SC 29208, USA.

[4]Office of Research and Development, U.S. Environmental Protection Agency, Durham, NC 27703, USA.

In preparation for submission to the *Proceedings of the National Academy of Sciences (PNAS)*

Abstract

The transition from coal to natural gas as a primary fuel for electric power generation has dramatically reduced NO_x emissions in the United States. However, substantial uncertainties still remain in current NO_x emission inventories, complicating the accurate assessment of emission trends and regulatory effectiveness. In fact, particulate nitrate (pNO_3) concentrations in the northeastern US have not responded as expected due to NO_x emission decreases. Here, we utilized nitrogen isotopes in nitrate ($\delta^{15}N(pNO_3)$) from a unique 2005-2015 aerosol record in the eastern US to directly link NO_x emission regulations to air quality and environmental responses. Simulations with the US EPA air quality model quantify seasonal variations of $\delta^{15}N(pNO_3)$ due to isotope fractionations that track with NO_x oxidation chemistry. Over the long term, a decreasing shift in $\delta^{15}N(pNO_3)$ reflects the gradual phase out of coal; however, the observations suggest that coal emissions of NO_x are underrepresented in national emission estimates. Our isotopic investigation enables a more accurate evaluation of the effectiveness of emission control strategies and can help refine regulatory efforts to mitigate air pollution.

1. Introduction

Nitrogen oxides (NO_x) are key drivers of air pollution, contributing to the formation of short-lived climate pollutants (SLCPs) such as tropospheric ozone and fine particulate matter ($PM_{2.5}$), which negatively impact air quality, public and ecosystem health, and climate(1, 2). Exposure to NO_x and its secondary pollutants increases the risk of respiratory and cardiovascular diseases and threatens agricultural yields due to ozone-induced damage(1, 3). In addition, dry and wet deposition of NO_x disrupts nutrient balances in ecosystems and accelerates acidification, posing long-term risks to forests, soils, and aquatic environments(4, 5). These impacts contribute to broader economic consequences as well, by increasing healthcare costs, reducing work

productivity, disrupting food security, and straining environmental and industrial systems(6–9). Due to its widespread environmental, health, and economic impacts, governments have historically mandated monitoring and reporting of NO_x emissions and implemented regulatory measures to protect public and ecosystem health(10, 11).

Under the Clean Air Act amendment in the United States, regulatory policies have played a pivotal role in driving down NO_x emissions in the eastern US, one of the most urbanized and industrialized regions in the country. The US Environmental Protection Agency (EPA) National Emission Inventory (NEI) reports the total NO_x emissions in the eastern US declined by approximately 53 % between 2005 to 2015, primarily from major anthropogenic sectors like transportation, industry, and energy production. Transportation sectors remain the dominant NO_x source in this region, accounting for 60 % of total NO_x emissions from major urban centers along the Northeast Corridor, including Washington, D.C., Philadelphia, New York City, and Boston (Fig. S5.1). Moreover, long-range transport from coal-burning regions, such as Ohio and Pennsylvania, has historically influenced air quality in the eastern US, but their contributions decreased by 68 % from 2005 to 2015 (Fig. S5.1).

At the national level, the US EPA NEI reports a 43 % reduction in total NO_x emissions from 2005 to 2015, with substantial declines in emissions from electric utilities (59 %), industrial fuel combustion (39 %), and the transportation sector (45 %; Fig. S5.2-S5.3). In particular, coal combustion was the largest source of electricity generation for several decades, but usage decreased by 28 % (from 1037 million short tons to 738 million short tons) as natural gas became a more cost-effective and lower-emission alternative(12). As a result of the transition from coal to natural gas for electricity generation, NO_x emissions decreased by 63% and 25 % for coal and natural gas, respectively, leading to significantly reduced health risks in the US(13). However,

despite large reductions in NO_x emissions, the responses in endpoints such as ozone, particulate matter, and deposition have not directly followed due to the complex non-linear chemistry feedback and potential uncertainties in emissions estimates(14–16).

Accurately assessing the impact of regulatory mitigation efforts requires reliable emission inventories, but previous studies have highlighted that emission estimates remain subject to significant uncertainties(7, 17–19). For example, conventional bottom-up approaches for estimating NO_x emissions could be affected by random sampling error, uncertainty in emission factors, and omission or underestimation of sources, all of which introduce substantial uncertainties, particularly for sectors with highly variable emissions such as transportation and industry(17, 20, 21). Similarly, top-down approaches from satellites or aircraft-based measurements to infer emissions have challenges related to measurement precision, chemical processing in the atmosphere, and the spatial and temporal resolution of data(22–24). These uncertainties limit the confidence of emission estimates, making it more challenging to optimize regulatory policies, assess health risks, and ensure that mitigation efforts are both effective and economically viable. Hence, accurate and updated emission inventories combined with observational constraints are needed to assess current pollution impacts on secondary chemistry and design effective control measures. The nitrogen stable isotope variation ($\delta^{15}N$) of particulate nitrate (pNO_3) has been identified as a powerful observational constraint for identifying atmospheric NO_x emission sources and understanding NO_x oxidation chemistry(25–29). In this study, we quantified $\delta^{15}N(pNO_3)$ collected in the northeastern US from 2005 to 2015–a critical period for emission reductions– to reconstruct NO_x emission sources and track the response of NO_x secondary products to emission regulations.

2. Materials and Methods

2.1 Filter Samples

Atmospheric PM_{10} samples were obtained from downtown Providence (41.82°N, -71.41°W) and West Greenwich (41.61°N, -71.72°W), Rhode Island, United States, from 2005 to 2015. Providence, as a state capital, is characterized by a mix of residential, commercial, industrial, and transportation-related activities, including major highways and business districts, which contribute to significant air pollution sources. In contrast, the West Greenwich site represents a suburban background air quality with abundant forest cover and minimal anthropogenic emission impact. Sample collections at both sites were conducted by the Rhode Island Department of Environmental Management (RI-DEM) and Rhode Island Department of Health (RI-DOH) via a high-volume sampler on a quartz-fiber filter. Sampling was performed every six days for 24 hours, following EPA protocols (USEPA-Method IO-2.1 1999). After collection, the filter samples were shipped to Brown University and separately extracted in ultra-high purity water (> 18 MΩ). The entire 10-year record was extracted for the Providence location, while a subset of samples was extracted for the endpoints of the West Greenwich record, including 2005–2006 and 2014–2015.

2.2 Stable nitrogen isotope analysis

Particulate nitrate (pNO_3) concentrations were determined using ion chromatography (Dionex Integrion HPIC). For quality control, working standards of two different concentrations were analyzed in every six samples. The average relative standard deviations (RSD) of replicate quality control standards were less than 3.4 %. For the West Greenwich samples, individual weekly samples were merged into monthly composites to ensure sufficient volume for further analysis. A detailed methodology for sampling and chemical analysis is described in Kim et al., 2025(33).

The water-soluble pNO_3 samples were analyzed for their stable nitrogen isotope utilizing the bacterial denitrifier method at Brown University(42). Nitrogen isotopic compositions are denoted using delta notation (δ), which is quantified as $\delta = (R_{sample}/R_{reference} - 1)$, where R is the ratio of the heavy isotope to the light isotope (e.g., $^{15}N/^{14}N$). Briefly, *Pseudomonas aureofaciens* bacteria, which lack the nitrous oxide (N_2O) reductase enzyme, were injected with the extracted NO_3^- samples to quantitatively reduce NO_3^- (and NO_2^-) to N_2O. The generated N_2O was extracted, purified, and concentrated using a customized GasBench interface and then continuously flowed into an Isotope Ratio Mass Spectrometer (IRMS) for *m/z* determination at 44, 45, and 46 for $\delta^{15}N$ determination. Samples were calibrated using internationally recognized nitrate salt reference materials that included IAEA-NO-3, USGS34, and USGS35 with $\delta^{15}N$ values of 4.7 ‰, -1.8 ‰, and 2.7 ‰, respectively(43, 44). Samples under a concentration of less than 3 μmol L^{-1}, were not analyzed due to the limited volume. The overall pooled standard deviations (σ) of isotopic reference materials were as follows: USGS34 ($\sigma(\delta^{15}N) = 0.5$ ‰); USGS35 ($\sigma(\delta^{15}N) = 0.4$ ‰), and IAEA-NO-3 ($\sigma(\delta^{15}N) = 0.3$ ‰). No significant spatial differences of observed $\delta^{15}N(pNO_3)$ between an urban (Providence, RI) and suburban (West Greenwich, RI) site were observed ($p > 0.05$) due to their close proximity (i.e., within 40 km); thus, we have prioritized the urban site in our analysis, which has a more frequent sampling record (every six days vs. monthly at the suburban site).

2.3 $\delta^{15}N(NO_x)$ estimation using the CMAQ simulations

To account for chemical influence on observed $\delta^{15}N(pNO_3)$, the US EPA CMAQ model (v5.4) was used to estimate NO_x, O_3, and pNO_3 concentrations, as well as NO_x oxidation and pNO_3 formation in Providence, RI. Briefly, the CMAQ model simulation was based on replicated runs from the US EPA's Air QUAlity TimE Series Project (EQUATES)(45, 46). The Carbon Bond 6

revision 3 gas-phase mechanisms and version 7 of the aerosol module chemical mechanism (cb6r3-ae07) with the addition of chlorine chemistry were used including the bidirectional ammonia (NH_3) exchange, the Surface Tiled Aerosol Gaseous Exchange (STAGE) dry deposition, and Weather Research and Forecasting (WRF) model (v.4.1.1)(47–55). Emissions were based on the 2017 NEI methods, with year-specific data used when available or scaled from 2017 levels(45). Model simulations were conducted for the northeastern US domain at a horizontal resolution of 12×12 km for 2005, 2010, and 2015. Daily averaged model outputs were aligned with observation dates for direct comparison.

Using model outputs with observed $\delta^{15}N(pNO_3)$, $\delta^{15}N(NO_x)$ values were calculated considering isotope effects during NO_x cycling and post-NO_x oxidation. We assumed here that our samples primarily represented the particulate phase of nitrate. The isotopic fractionation associated with HNO_3-to-pNO_3 gas-to-particle partitioning by thermodynamic equilibrium was considered to calculate $\delta^{15}N(HNO_3)$ as follows:

$$\delta^{15}N(HNO_3) = \delta^{15}N(pNO_3) - \varepsilon(pNO_3/HNO_3) \times (1-f(pNO_3)) \quad \text{(Eq.1)}$$

where $f(pNO_3)$ is the relative fraction of pNO_3 in total nitrate (pNO_3+HNO_3), which were determined using the modeled pNO_3 and HNO_3 outputs from CMAQ. $^{15}\varepsilon(pNO_3/HNO_3)$ is the isotope effects associated with HNO_3 conversion to pNO_3. We adopted 3‰ in this study for $^{15}\varepsilon(pNO_3/HNO_3)$ based on previous works(27, 29).

Considering $\delta^{15}N$ isotope fractionation that occurs during NO_x cycling and nitrate formation, $\delta^{15}N(HNO_3)$ values were used to infer $\delta^{15}N(NO_x)$ value (hereafter $\delta^{15}N(NO_x)_{calc}$) as follows:

$$\delta^{15}N(NO_x)_{calc} = \delta^{15}N(HNO_3) - {}^{15}\varepsilon(NO_2/NO) \times (1-f(NO_2)) - {}^{15}\varepsilon(NO_3/NO_2) \quad \text{(Eq.2)}$$

where ${}^{15}\varepsilon(NO_2/NO)$ and ${}^{15}\varepsilon(NO_3/NO_2)$ are the isotope effects associated with NO conversion to NO_2 (Eq. 3) and NO_2 conversion to NO_3 (Eq. 5), respectively. The fraction of NO_2 in NO_x, $f(NO_2)$, was calculated as $[NO_2]/[NO_x]$ using modeled NO and NO_2 concentrations. ${}^{15}\varepsilon(NO_2/NO)$ is assumed to be the combined isotope effects of the NO_x equilibrium isotope effect (EIE) and the Leighton cycle isotope effect (LCIE)(31) and can be calculated as

$${}^{15}\varepsilon(NO_2/NO) = EIE + LCIE = f_{EIE}({}^{15}\varepsilon_{EIE}) + (1-f_{EIE})({}^{15}\varepsilon_{LCIE}) \quad \text{(Eq.3)}$$

where ${}^{15}\varepsilon_{EIE}$ represents the NO_x equilibrium isotope effect between NO and NO_2. We used a value of 28.9±1.9‰, based on a previous experimental study conducted under ambient NO_x conditions. In addition, ${}^{15}\varepsilon_{LCIE}$ refers to the Leighton cycle isotope effects occurring during the NO_x photochemical cycle, including a combination of the kinetic isotope effect associated with NO oxidation mainly by O_3, and the isotope effect associated with NO_2 photolysis(27, 31, 56). The isotope fractionation associated with NO_2 photolysis is considered negligible(57), so we assume that the primary contributor to LCIE is the NO + O_3 isotope fractionation, which has been experimentally measured to be -10±5‰(27, 31). The relative contribution of EIE to NO oxidation (f_{EIE}) was calculated as:

$$f_{EIE} = \frac{k(NO_x\text{–EIE})\,[NO_2]}{k(NO+O_3)\,[O_3] + k(NO_x\text{–EIE})\,[NO_2]} \quad \text{(Eq.4)}$$

where $k(NO_x\text{–EIE})$ is the reaction rate of NO_x EIE with a reported value of 8.14×10^{-14} cm^3 s^{-1} and $k(NO+O_3)$ is the NO + O_3 reaction rate of 1.73×10^{-14} cm^3 s^{-1}(27). Modeled NO_2 and O_3 concentrations from the CMAQ model were used for the calculation.

For NO_2 oxidation to nitrate, we assumed based on a previous study that the two dominant pathways in polluted mid-latitude regions—NO_2 oxidation by OH radicals and N_2O_5 hydrolysis primarily contributed to nitrate formation in our study area(35):

$$^{15}\varepsilon(NO_3/NO_2) = f(NO_2 + OH) \times (^{15}\varepsilon(NO_2{+}OH)) + (1\text{-}f(NO_2 + OH)) \times (^{15}\varepsilon(N_2O_5)) \quad \text{(Eq.5)}$$

where $f(NO_2 + OH)$ indicates the fractional contribution of $NO_2 + OH$ pathway to NO_3 formation from CMAQ outputs. NO_2 oxidation by OH radical is known to have an isotope effect of -3 ‰ ($^{15}\varepsilon(NO_2{+}OH)$), while N_2O_5 hydrolysis has 28 ‰ of isotope effects ($^{15}\varepsilon(N_2O_5)$) at 284K during nitrate formation.

2.4 NO_x emission database and $\delta^{15}N(NO_x)_{emi}$ estimation

The $\delta^{15}N(pNO_3)$ can be a potential tracer of NO_x emission sources, as distinct $\delta^{15}N$ values from major NO_x emission sources and their chemical processing are preserved in $\delta^{15}N(pNO_3)$(25, 27, 58). In this study, we estimated $\delta^{15}N(NO_x)$ in the eastern US using the 2020 US EPA NO_x emission inventory from the midwest and northeastern US (hereafter, $\delta^{15}N(NO_x)_{emis}$). The NO_x emission inventory data were reported depending on fuel types and sectors for every year and state. Given the wide range of NO_x sources, we have simply divided them into five sectors by major source types for the calculation. Specifically, we have categorized NO_x emissions and defined their $\delta^{15}N(NO_x)$ values as follows: agriculture activity and soil NO_x emissions ($\delta^{15}N$ = -33.0±12.3 ‰(39)), transportation ($\delta^{15}N$ = -4.7±1.7 ‰(58, 59)), and biomass burning ($\delta^{15}N$ = 2.5±7.5 ‰). Energy production, industry, and combustion were grouped by fuel type as either combustion – coal & solid biofuel ($\delta^{15}N$ = 13.6±3.9 ‰(36)) or combustion – liquid fuel & process ($\delta^{15}N$ = -16.5±1.7 ‰(37)). Given NEI reports annual NO_x emission data, seasonal variations of these emissions sources were inferred using monthly NO_x emissions reported by the Emissions Database

for Global Atmospheric Research (EDGAR) (note that EDGAR data includes the whole US domain). Annual and seasonal $\delta^{15}N(NO_x)$ values from 2005 to 2015 were modeled based on isotope mass balance using the fraction of NO_x emissions by sector and fuel type and previously reported $\delta^{15}N(NO_x)$ emission signatures following a previously described method(27, 58):

$$\delta^{15}N(NO_x)_{emis} = \sum_{i=1}^{n} f_i \times \delta^{15}N_i(NO_x) \qquad \text{(Eq.6)}$$

where f_i represents fractions of each emission source compared to the whole NO_x emissions. $\delta^{15}N_i(NO_x)$ is the emission signature of sources. Details can be found in Bekker et al., 2023.

2.5 Stable isotope mixing model with Monte Carlo

A Bayesian isotope mixing model using Markov Chain Monte Carlo (MCMC) simulation was employed to quantify the relative contributions of different NO_x sources to $\delta^{15}N(NO_x)$, accounting for uncertainties in $\delta^{15}N$ source signatures. The goal was to identify the fractions of each source that best reproduce the target $\delta^{15}N$ value of NO_x, utilizing NEI estimates as an *a priori* constraint with an assumed uncertainty of ± 30 %. The model was run for 10,000 iterations, randomly sampling $\delta^{15}N$ source values from normal distributions based on literature-reported means and standard deviations. The modeled $\delta^{15}N(NO_x)$ values from each emission source were used for the mixing model to infer a detailed budget of NO_x emissions. Additionally, the MCMC method was applied to propagate uncertainties in the $\delta^{15}N$ source signatures and emission estimates, providing a rigorous error estimate characterized by the probability density function for the contributions of each NO_x source. This approach allowed for a more comprehensive assessment of the relative contributions of transportation, coal combustion, and natural gas/oil combustion with a basis on seasonal and temporal variations.

2.6 Back trajectory analysis

Air-mass back trajectories were traced to examine the frequency and origin of air masses based on the sampling site. The trajectory frequency analysis was conducted using the National Oceanic and Atmospheric Administration–Hybrid Single-Particle Lagrangian Integrated Trajectory (HYSPLIT) model with the archived Global Data Assimilation System (GDAS) meteorological data files via the HYSPLIT online interface. Backward trajectories were computed for 48 hours at 500 m for January and July 2005.

3. Result and Discussion

3.1 Quantifying chemical fractionation effect on $\delta^{15}N(pNO_3)$

The measured atmospheric nitrate $\delta^{15}N$ exhibited no significant spatial differences between the urban (Providence, RI) and suburban (West Greenwich, RI) datasets; thus, our primary analysis focuses on the urban record (Fig. 5.1a). At the urban site, observed $\delta^{15}N(pNO_3)$ values from 2005 to 2015 ranged from -3.8 ‰ to +21.7 ‰ with an average of +6.0($\pm$4.6) ‰ (n=534). A significant long-term decreasing trend in $\delta^{15}N(pNO_3)$ was observed from 2005 to 2015 (Fig. 5.1a; $p < 0.01$). The shift was more pronounced during the cold season (-0.6 ‰ yr^{-1}) compared to the warm season (-0.5 ‰ yr^{-1}; Fig. S5.4). Moreover, in the early years (2005–2010), the annual average rate of decrease in $\delta^{15}N(pNO_3)$ was more pronounced with a rate of -0.7 ‰ yr^{-1}, whereas in the most recent years (2011–2015), the decrease gradually slowed to a rate of -0.2 ‰ yr^{-1}. This slowdown in declining $\delta^{15}N(pNO_3)$ in recent years was similar to the observed trend of NO_x emissions and pNO_3 concentration in the eastern US(16, 30). Studies have suggested that the recent slowdown in NO_x reductions is due to shifts in dominant NO_x emission sources and the diminishing impact of emission controls, as major NO_x emissions have already been significantly reduced. Specifically,

the growing relative contributions of industrial areas and off-road mobile sources, along with slower-than-expected reductions from on-road diesel vehicles, have likely contributed to this slowdown(30). Therefore, we investigate the trends in $\delta^{15}N(pNO_3)$ and their reflection of NO_x emission changes and impact on NO_x oxidation chemistry.

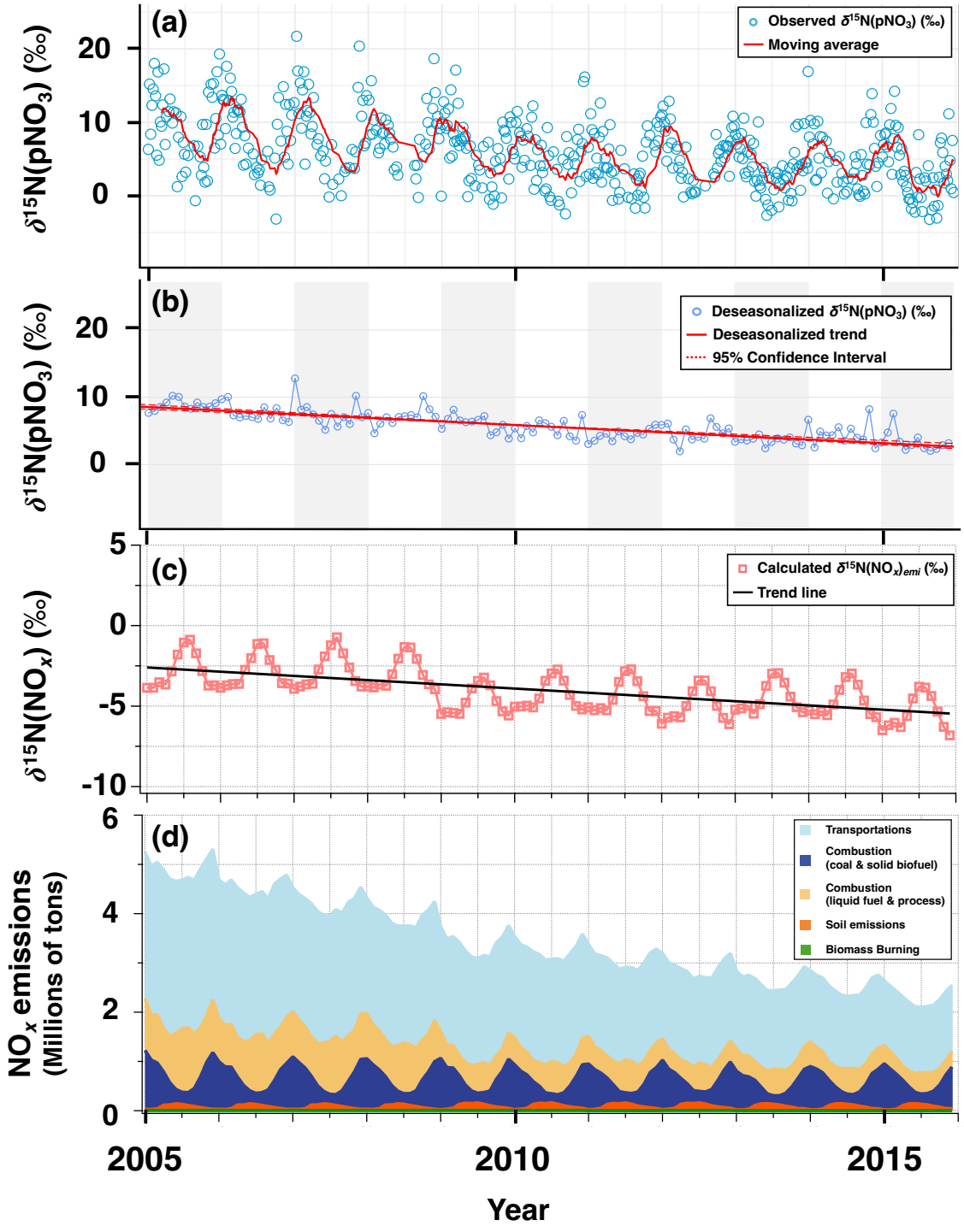

Figure 5.1. (a) observed $\delta^{15}N$ of pNO_3 in Providence (open circle) and West Greenwich (closed circle), RI, from 2005 to 2015 with moving average (red line). (b) deseasonalized monthly mean isotope values, with the solid red line indicating the trend estimate (–0.53/year; $p<0.01$) and the dashed red lines representing the 95% confidence intervals. (c) Calculated $\delta^{15}N(NO_x)_{emi}$ values using the EPA NEI estimates (d) total national NO_x emissions estimate in the eastern US from 2005 to 2015.

In addition to the long-term trend change, the observed $\delta^{15}N(pNO_3)$ exhibited a clear seasonality with relatively higher values in the cold season (Oct to Mar) and lower values in the warm season (Apr to Sep) throughout the years. As $\delta^{15}N(pNO_3)$ reflects both NO_x emission sources and/or isotopic effects during NO_x oxidation, its seasonality and long-term trend can be attributed to the variabilities of these factors by season. Previous studies in the northeastern US demonstrated that the seasonality of $\delta^{15}N(pNO_3)$ is largely driven by the isotope fractionation effect during NO_x oxidation chemistry compared to changes in NO_x emission sectors by fuel type(27). Once $\delta^{15}N(NO_x)$ values are imprinted by various emission sources, isotopic effects during the oxidation processes play a critical role in the final $\delta^{15}N(pNO_3)$ value(27, 29, 31). Key isotope effects associated with NO_x cycling include equilibrium isotope effects (EIEs), unidirectional kinetic isotope effects (KIEs), and photo-induced fractionation isotope effects (PHIEs). Theoretical calculation suggested that the KIE associated with the Leighton cycle (LCIE) by the $NO+O_3$ reaction is approximately -10±5 ‰ at room temperature, while the EIE between NO and NO_2 is approximately 28.9 ‰(27, 31). The relative contribution of EIE dominates under high NO_x concentrations relative to O_3 concentrations, leading to enriched ^{15}N in pNO_3, especially in the cold season. For post-NO_2 oxidation reactions, two major nitrate formation pathways are associated with the NO_2 + OH and N_2O_5 hydrolysis reactions in polluted areas of mid-latitude, and their fractionation factors are calculated as -3 ‰ and +28 ‰, respectively(26, 27, 32).

The US EPA Community Multiscale Air Quality (CMAQ) model was utilized to quantify the expected $\delta^{15}N$ fractionations associated with NO_x oxidation to pNO_3(33, 34). The CMAQ model has been shown to effectively capture oxidation chemistry changes in response to emission regulations in the northeastern US between 2005-2015 (33). Our previous work using oxygen isotopes of pNO_3 from the same filter records has demonstrated that an increase in ozone (O_3)

concentrations, driven by NO_x emission reductions over the past decade, has accelerated the conversion of nitric oxide (NO) to nitrogen dioxide (NO_2) and subsequently NO_2 to pNO_3. The production of pNO_3 occurs through enhanced dinitrogen pentoxide (N_2O_5) hydrolysis compared to the NO_2 + hydroxyl radical (OH) pathway in urban areas in the northeastern US(33).

Throughout the major cities in the northeastern US (e.g. Providence, Boston, New York City, and Washington D.C.), two primary NO_2 oxidation pathways–NO_2 + OH and N_2O_5 hydrolysis–are known to be dominant for nitrate formation(33, 35). Based on this information, we back-calculated $\delta^{15}N(NO_x)$ considering isotopic fractionation during the conversion of NO to NO_2 and NO_2 to NO_3 (Hereafter $\delta^{15}N(NO_x)_{calc}$; See method for details; Fig. 5.2). Predicted $\delta^{15}N(NO_x)_{calc}$ indicates that isotope effects significantly influence the $\delta^{15}N(pNO_3)$ seasonality. The EIE between NO and NO_2 (e.g., 28.9±2 ‰) dominates under the higher NO_x concentrations relative to O_3 concentrations, leading to enriched ^{15}N in pNO_3, especially in the cold season (Fig. S5.5). In addition, since N_2O_5 hydrolysis is the primary nitrate formation pathway during the cold season, its associated fractionation effect (e.g., +28 ‰) further enriches $\delta^{15}N$ in pNO_3. In contrast, during the warm season, the NO_2 + OH pathway dominates, with a much lower fractionation effect (e.g., -3 ‰), resulting in minor differences between $\delta^{15}N(NO_x)$ and $\delta^{15}N(pNO_3)$. These differences in isotope effects during the NO_x oxidation process drive a seasonal contrast between $\delta^{15}N(NO_x)$ and $\delta^{15}N(pNO_3)$, leading to higher values of $\delta^{15}N(pNO_3)$ in the cold season compared to the warm season, which results in an opposite trend to that of $\delta^{15}N(NO_x)$. In other words, the seasonality of $\delta^{15}N(pNO_3)$ is primarily driven by the fractionation effect, whereas the seasonality of $\delta^{15}N(NO_x)$ appears to be more strongly influenced by changes in NO_x emission sources than by isotope effects, as discussed further below.

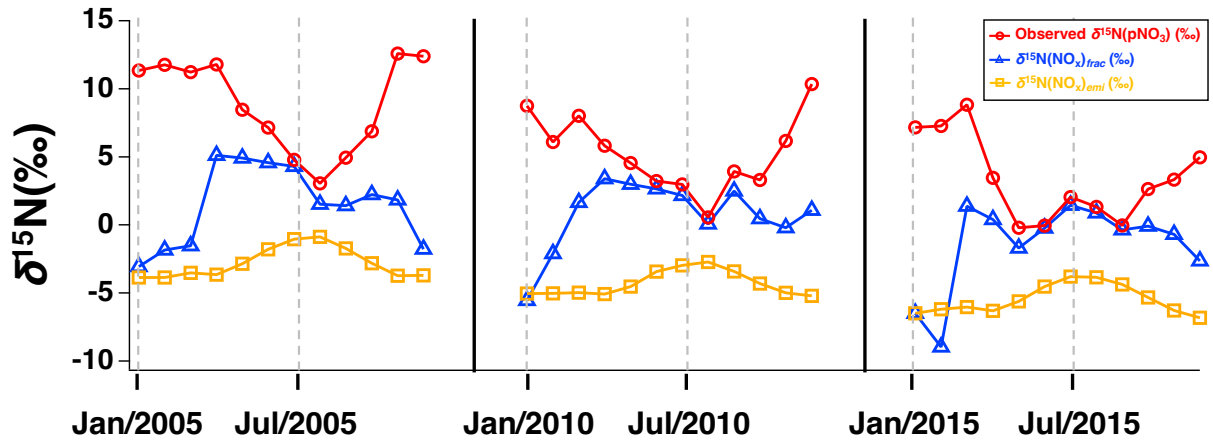

Figure 5.2. Monthly variations of observed $\delta^{15}N(pNO_3)$ with calculated $\delta^{15}N(NO_x)_{frac}$ and $\delta^{15}N(NO_x)_{emi}$ for 2005, 2010, and 2015.

Over the long-term, although the calculated $\delta^{15}N(NO_x)_{calc}$ values show a decreasing trend from 2005 to 2015 (Fig. 5.2), the decrease in isotope effect alone cannot explain the observed long-term decline in $\delta^{15}N(pNO_3)$. The predicted $\delta^{15}N(NO_x)_{calc}$ values suggest that the $\delta^{15}N$ kinetic isotopic effect (-10±5 ‰) has become increasingly important relative to the equilibrium isotope effect (+28±2‰), driven by the increase in O_3 concentrations, as NO_x emissions decreased over the past decade. Specifically, the increase in incomplete nighttime O_3 titration by NO, particularly for the cold season, enhanced the oxidation of NO to NO_2, contributing to a greater influence of the kinetic isotope effect under conditions of higher O_3 concentrations relative to NO_x concentrations in 2015. In this case, $^{14}NO_x$ reacts faster than $^{15}NO_x$, leading to a depletion of ^{15}N in pNO_3. However, the influence of the kinetic isotope effect on observed $\delta^{15}N(pNO_3)$ only explains approximately -1 to -2 ‰ change over 10 years compared to the observed $\delta^{15}N(pNO_3)$ depletion of -6 ‰ over the 10–year record. This highlights that the primary driver of the long-term decline in $\delta^{15}N(NO_x)$ was likely related to changes in NO_x emission sources.

3.2 Impact of emission changes on $\delta^{15}N(pNO_3)$

Using the US EPA NEI estimate and previous $\delta^{15}N(NO_x)$ source characterization studies, we modeled $\delta^{15}N(NO_x)$ values (hereafter, $\delta^{15}N(NO_x)_{emis}$) to see if changes in emission sources drive temporal variations in $\delta^{15}N(NO_x)$ and/or $\delta^{15}N(pNO_3)$ over the decade. Five major NO_x emission categories that have distinguishable isotopic signatures were considered(27): transportation (on-road, non-road, and shipping), combustion (residential, commercial, and industrial), soil emissions/agricultural activities, and biomass burning, accounting for roughly 95 % of all emitted NO_x in the eastern US. Combustion-related sources were further classified by fuel type into coal & solid biofuel versus liquid fuel & process combustion (see Methods for details). Predicted $\delta^{15}N(NO_x)_{emis}$ ranges from -6.8 ‰ to -0.7 ‰ (Fig. 5.1c) and exhibits clear seasonality with higher values in the warm season (on average -3.4±1.3 ‰ from Apr to Sep) than the cold season (on average -4.7±1.0 ‰ from Oct to Mar). This seasonal pattern reflects fuel-type variations as coal combustion with ^{15}N-enriched NO_x dominates in summer due to higher electricity demand from air conditioning, while natural gas with ^{15}N–depleted NO_x is heavily used for home heating in the winter season (27, 36, 37).

Over the past decade, the US has increasingly relied on natural gas for electric power production gradually taking old coal power plants offline (12, 38). This switch from coal to natural gas is reflected in $\delta^{15}N(NO_x)_{emis}$ as an increased portion of ^{15}N–depleted NO_x. Indeed, this energy transition contributed to the decadal decreasing trend of $\delta^{15}N(NO_x)_{emis}$ values at an average rate of -0.2(±0.01) ‰ year^{-1} for both cold and warm seasons (p<0.01; Fig. 5.1c). Coal-based electricity generation declined steadily across all seasons, decreasing from 22 % to 15 % of total NO_x emissions between 2005 and 2015. This reduction contributed to an overall change in $\delta^{15}N(NO_x)_{emis}$ at a consistent rate of approximately -0.8(±0.1) ‰ throughout all seasons from 2005

to 2015. At the same time, a significant increase in the usage of natural gas-based electricity generation was observed from 14 % to 22 % of total NO_x emissions playing an important role in the trend of $\delta^{15}N(NO_x)_{emis}$. The increase in natural gas use is especially pronounced during the cold seasons, driving a 1.8(±0.3) ‰ decrease of $\delta^{15}N(NO_x)_{emis}$ over the years. During the warm season there is also a decline in $\delta^{15}N(NO_x)_{emis}$, however this is more driven by an increase in the relative fraction of emissions from soils/agricultural activities as fossil fuel based sources have decreased. Additionally, soil/agriculatural emissions, containing ^{15}N-depleted NO_x, have gradually increased due to enhanced microbial activity and fertilizer application during the warm season (39, 40). Overall, the transition from coal to natural gas, combined with the increasing influence of soil-derived NO_x, has driven a long-term decline in $\delta^{15}N(NO_x)_{emis}$, reflecting broader changes in emission sources and regulatory efforts to reduce anthropogenic NO_x emissions.

3.3 $\delta^{15}N$ as a NO_x emission source constraints

The predicted $\delta^{15}N(NO_x)_{emis}$ values, based on NO_x emission estimates, effectively captured the seasonality of the predicted $\delta^{15}N(NO_x)_{calc}$ (Fig. 5.2). However, significant offset was observed between these predicted $\delta^{15}N(NO_x)_{emis}$ and the predicted $\delta^{15}N(NO_x)_{calc}$ values ($p<0.01$; Fig. 5.2), suggesting potential uncertainties in emission inventories, chemical mechanisms in the model, and/or isotope fractionation factors. While there might be some uncertainties in the chemical processes and/or isotope fractionation, we do not believe these factors significantly contribute to this discrepancy. This is because our previous study using oxygen isotopes has demonstrated that calculated oxygen isotope values using the chemical mechanisms in the CMAQ model matched well with observed values, indicating that the chemical mechanism in the model is likely accurately represented in our study region(33). Additionally, direct measurement of fractionation factors is unavailable and thus, we have used fractionation factors of theoretically calculated values or

experimentally determined values for the calculations in our study. While we acknowledge that uncertainties in isotope fractionation factors exist, we do not anticipate that they induce significant errors in our analysis. For example, the KIE associated with the NO to NO_2 conversion is experimentally estimated to be -10 ‰ with an uncertainty of ±5 ‰. However, this isotope effect contributes only partially to the final $\delta^{15}N(pNO_3)$. As a result, its propagated influence on the final $\delta^{15}N(pNO_3)$ value is expected to be limited, likely within ±1–2 ‰. Therefore, these uncertainties are insufficient to fully account for the offset between these predicted $\delta^{15}N(NO_x)_{emis}$ and $\delta^{15}N(NO_x)_{calc}$ values.

To better constrain NO_x sources, we treated the observation record as a predictor of sources and conducted a Bayesian framework-based isotope mixing model with a Markov Chain Monte Carlo (MCMC) method utilizing EPA emission estimates with an assumed uncertainty of ±30 % as an *a priori* constraint. Isotope-constrained model results indicated that transportation was the dominant NO_x source, contributing approximately 60±4 % of total year-round NO_x emissions, followed by coal and natural gas combustion (Fig. 5.1d). In both the EPA NEI and MCMC method results, coal combustion was more influential during the warm season, and natural gas and oil combustion were more dominant in the cold season in the early years (Figure 5.3). However, NO_x emissions from coal combustion turned out to be a more significant contributor to pNO_3 formation than reported by the EPA NEI, accounting for 22% and 29% for the cold and warm seasons, respectively. According to the U.S. Energy Information Administration (EIA), coal combustion typically increases during summer months due to higher electricity demand for air conditioning, resulting in elevated NO_x emissions(41). During the more recent years of the record, the atmospheric lifetime of NO_x has become shorter facilitating its rapid oxidation to pNO_3, which can be transported over long distances. This means that the influence of long-range transport of pNO_3

from coal-derived NO_x emitted in upwind regions, such as the Ohio River Valley, is a major source of coal combustion emissions in the eastern US. On the other hand, NO_x emissions from natural gas combustion for residential heating are more prominent during the cold season when the lower boundary layer height enhances the influence of local sources. Even though no significant seasonal differences in air masses were observed from back-trajectory analysis (Fig. S5.6), significant differences in their usage depending on the purpose led to seasonality of $\delta^{15}N(NO_x)$ in the eastern US regions. As coal has been replaced by liquid gas, coal's contribution to NO_x emissions has decreased by 7–9 %, with less seasonal contrast in recent years. Overall, model and isotope-based results suggest that NO_x emissions from coal combustion may have been less accounted for in conventional emission estimates than their actual contribution to the total NO_x budget in the eastern US. Therefore, despite the decreased portion in coal combustion, its contribution to pNO_3 formation appears to be still more significant, particularly during the warm season when long-range transport plays an important role.

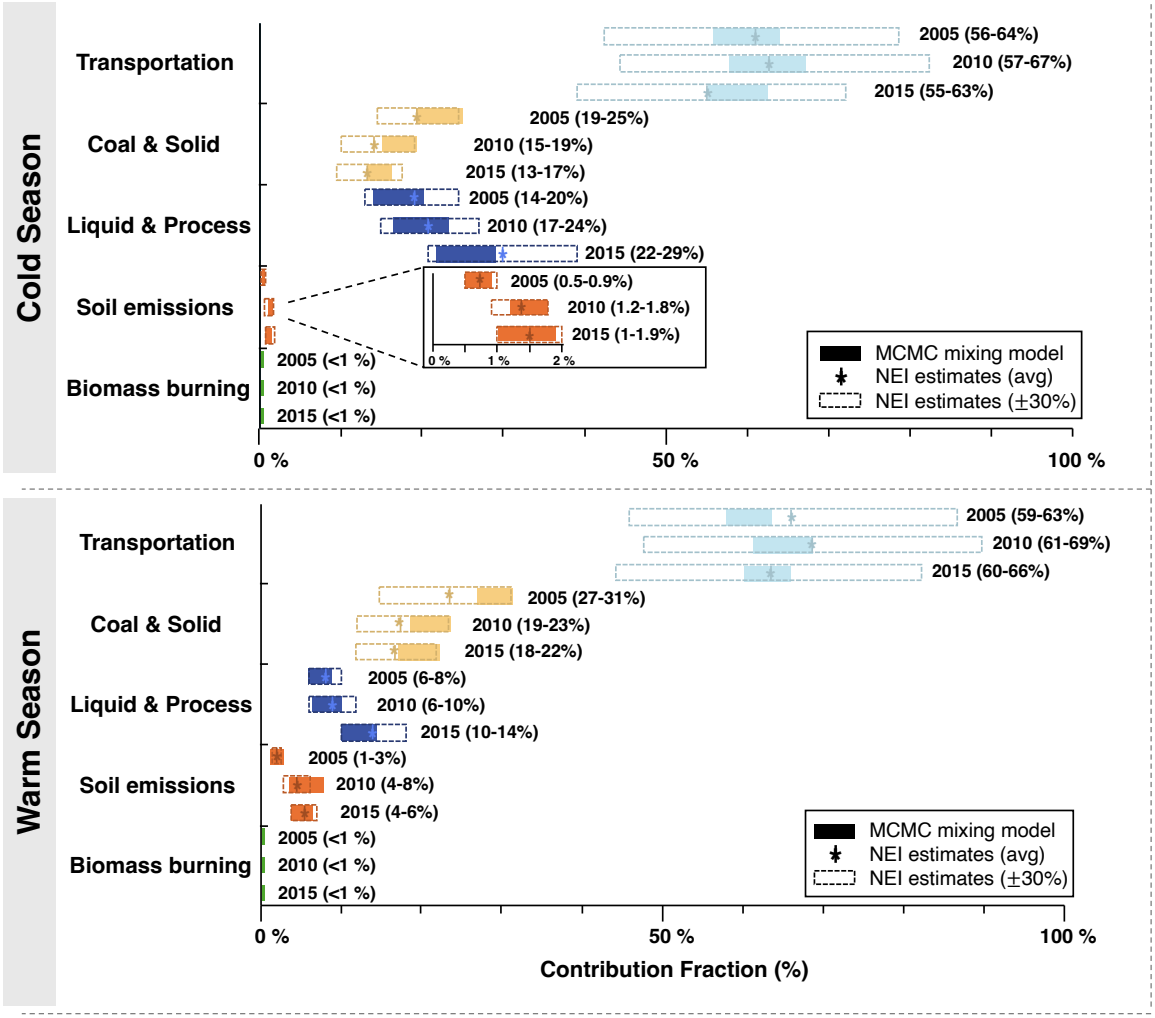

Figure 5. 3. Comparison of the relative fraction of NO_x emission sources from the EPA NEI versus MCMC isotope mixing model results.

A fundamental limitation in air quality regulation and emission assessments has been the inability to observationally connect primary emissions to secondary pollutants such as O_3, $PM_{2.5}$, and deposition. Our study addresses this gap by incorporating stable isotope measurements, which provide a powerful observational constraint on the sources and chemical processing of atmospheric nitrate. Our $\delta^{15}N(pNO_3)$ isotope records exhibit significant temporal shifts over the past decade, providing quantitative evidence of energy transition from coal to natural gas combustion of NO_x emissions in the eastern US. This highlights the effectiveness of coal combustion controls in

reducing NO_x emissions. As coal combustion has been phased out, the emergence of alternative energy sources brings new environmental trade-offs. For instance, while natural gas is cost-effective and produces lower emissions than coal, it still has challenges such as the potential risk of methane leakage and non-renewable sources. In addition, while anthropogenic NO_x emissions decline, the relative influence of natural sources, such as soil emissions and lightning, is expected to become more prominent in NO_x emissions. In our previous companion paper, oxygen isotopes of nitrate also revealed that emission regulation amendments have increased NO_x oxidation efficiency to inorganic and organic nitrate in heavily urbanized locations in the northeastern US. These unexpected consequences are further complicating future air quality management. Therefore, a comprehensive understanding of these trade-offs is essential for designing balanced energy policies that effectively mitigate air pollution while ensuring a reliable and sustainable energy transition.

4. Acknowledgments

We thank Ruby Ho for laboratory assistance. We thank the Rhode Island Department of Environmental Management (RI-DEM) and the Rhode Island Department of Health (RI-DOH) for filter collection.

5. References

1. J. N. Galloway, *et al.*, Nitrogen cycles: past, present, and future. *Biogeochemistry* **70**, 153–226 (2004).
2. R. W. Pinder, *et al.*, Climate change impacts of US reactive nitrogen. *Proc. Natl. Acad. Sci. U.S.A.* **109**, 7671–7675 (2012).
3. R. Van Dingenen, *et al.*, The global impact of ozone on agricultural crop yields under current and future air quality legislation. *Atmospheric Environment* **43**, 604–618 (2009).
4. C. T. Driscoll, *et al.*, Acidic Deposition in the Northeastern United States: Sources and Inputs, Ecosystem Effects, and Management Strategies: The effects of acidic deposition in the northeastern United States include the acidification of soil and water, which stresses terrestrial and aquatic biota. *BioScience* **51**, 180–198 (2001).
5. E. A. Holland, B. H. Braswell, J. Sulzman, J.-F. Lamarque, NITROGEN DEPOSITION ONTO THE UNITED STATES AND WESTERN EUROPE: SYNTHESIS OF OBSERVATIONS AND MODELS. *Ecological Applications* **15**, 38–57 (2005).

6. N. Z. Muller, R. Mendelsohn, W. Nordhaus, Environmental accounting for pollution in the United States economy. *American Economic Review* **101**, 1649–1675 (2011).
7. C. A. Miller, *et al.*, Air Emission Inventories in North America: A Critical Assessment. *Journal of the Air & Waste Management Association* **56**, 1115–1129 (2006).
8. A. P. Tai, M. V. Martin, C. L. Heald, Threat to future global food security from climate change and ozone air pollution. *Nature Climate Change* **4**, 817–821 (2014).
9. J. G. Lu, Air pollution: A systematic review of its psychological, economic, and social effects. *Current opinion in psychology* **32**, 52–65 (2020).
10. https://www.epa.gov/laws-regulations/summary-clean-air-act.
11. J. Fenger, Air pollution in the last 50 years–From local to global. *Atmospheric environment* **43**, 13–22 (2009).
12. https://www.eia.gov/coal/data/browser/.
13. L. Henneman, *et al.*, Mortality risk from United States coal electricity generation. *Science* **382**, 941–946 (2023).
14. V. Shah, *et al.*, Chemical feedbacks weaken the wintertime response of particulate sulfate and nitrate to emissions reductions over the eastern United States. *Proceedings of the National Academy of Sciences* **115**, 8110–8115 (2018).
15. L. Jaeglé, *et al.*, Nitrogen oxides emissions, chemistry, deposition, and export over the Northeast United States during the WINTER aircraft campaign. *Journal of Geophysical Research: Atmospheres* **123**, 12–368 (2018).
16. H. Kim, W. W. Walters, L. Kysela, M. G. Hastings, Long-term trends in inorganic aerosol chemical composition and chemistry at an urban and rural site in the northeastern US. *Science of The Total Environment* **904**, 166848 (2023).
17. H. C. Frey, Quantification of uncertainty in emission factors and inventories. *Unpublished manuscript, Department of Civil, Construction, and Environmental Engineering, North Carolina State University, Raleigh, NC Retrieved from https://www. researchgate. net/publication/228618100_Quantification_of_Uncertainty_in_Emission_ Factors_and_Inventories* (2007).
18. D. C. Anderson, *et al.*, Measured and modeled CO and NO_y in DISCOVER-AQ: An evaluation of emissions and chemistry over the eastern US. *Atmospheric Environment* **96**, 78–87 (2014).
19. B. C. McDonald, *et al.*, Modeling Ozone in the Eastern U.S. using a Fuel-Based Mobile Source Emissions Inventory. *Environ. Sci. Technol.* **52**, 7360–7370 (2018).
20. B. C. McDonald, D. R. Gentner, A. H. Goldstein, R. A. Harley, Long-Term Trends in Motor Vehicle Emissions in U.S. Urban Areas. *Environ. Sci. Technol.* **47**, 10022–10031 (2013).
21. D. D. Parrish, Critical evaluation of US on-road vehicle emission inventories. *Atmospheric Environment* **40**, 2288–2300 (2006).
22. A. H. Souri, *et al.*, Constraining NO_x emissions using satellite NO_2 measurements during 2013 DISCOVER-AQ Texas campaign. *Atmospheric environment* **131**, 371–381 (2016).
23. A. Lorente, *et al.*, Quantification of nitrogen oxides emissions from build-up of pollution over Paris with TROPOMI. *Scientific reports* **9**, 20033 (2019).
24. J. Peischl, *et al.*, A top-down analysis of emissions from selected Texas power plants during TexAQS 2000 and 2006. *J. Geophys. Res.* **115**, 2009JD013527 (2010).
25. E. M. Elliott, *et al.*, Nitrogen isotopes as indicators of NO_x source contributions to atmospheric nitrate deposition across the midwestern and northeastern United States. *Environmental Science & Technology* **41**, 7661–7667 (2007).
26. H. D. Freyer, Seasonal variation of $^{15}N/^{14}N$ ratios in atmospheric nitrate species. *Tellus B* **43**, 30–44 (1991).
27. C. Bekker, W. W. Walters, L. T. Murray, M. G. Hastings, Nitrate chemistry in the northeast US–Part 1: Nitrogen isotope seasonality tracks nitrate formation chemistry. *Atmospheric Chemistry and Physics* **23**, 4185–4201 (2023).
28. Z. Li, *et al.*, Nitrate Isotopic Composition in Precipitation at a Chinese Megacity: Seasonal Variations, Atmospheric Processes, and Implications for Sources. *Earth and Space Science* **6**, 2200–2213 (2019).
29. W. W. Walters, G. Michalski, Theoretical calculation of nitrogen isotope equilibrium exchange fractionation factors for various NO_y molecules. *Geochimica et Cosmochimica Acta* **164**, 284–297 (2015).
30. Z. Jiang, *et al.*, Unexpected slowdown of US pollutant emission reduction in the past decade. *Proc. Natl. Acad. Sci. U.S.A.* **115**, 5099–5104 (2018).
31. J. Li, X. Zhang, J. Orlando, G. Tyndall, G. Michalski, Quantifying the nitrogen isotope effects during photochemical equilibrium between NO and NO_2: implications for $\delta^{15}N$ in tropospheric reactive nitrogen. *Atmospheric Chemistry and Physics* **20**, 9805–9819 (2020).

32. W. W. Walters, G. Michalski, Theoretical calculation of oxygen equilibrium isotope fractionation factors involving various NO_y molecules, OH, and H_2O and its implications for isotope variations in atmospheric nitrate. *Geochimica et Cosmochimica Acta* **191**, 89–101 (2016).

33. H. Kim, W. W. Walters, H. O. T. Pye, K. M., Foley, & M. G. Hastings, Isotopes Constrain Nitrogen Oxides Chemistry Changes due to Emission Regulations in the Northeastern US, *Nature Geoscience, In review.*

34. W. W. Walters, H. O. T. Pye, H. Kim, M. G. Hastings, Modeling the Oxygen Isotope Anomaly ($\Delta^{17}O$) of Reactive Nitrogen in the Community Multiscale Air Quality Model: Insights into Nitrogen Oxide Chemistry in the Northeastern United States. *ACS EST Air* acsestair.3c00056 (2024). https://doi.org/10.1021/acsestair.3c00056.
35. H. Kim, W. W. Walters, C. Bekker, L. T. Murray, M. G. Hastings, Nitrate chemistry in the northeast US–Part 2: Oxygen isotopes reveal differences in particulate and gas-phase formation. *Atmospheric Chemistry and Physics* **23**, 4203–4219 (2023).
36. J. D. Felix, E. M. Elliott, S. L. Shaw, Nitrogen Isotopic Composition of Coal-Fired Power Plant NO_x : Influence of Emission Controls and Implications for Global Emission Inventories. *Environ. Sci. Technol.* **46**, 3528–3535 (2012).
37. W. W. Walters, B. D. Tharp, H. Fang, B. J. Kozak, G. Michalski, Nitrogen isotope composition of thermally produced NO_x from various fossil-fuel combustion sources. *Environmental science & technology* **49**, 11363–11371 (2015).
38. https://campd.epa.gov.
39. D. J. Miller, *et al.*, Isotopic Composition of In Situ Soil NO_x Emissions in Manure-Fertilized Cropland. *Geophysical Research Letters* **45** (2018).
40. Z. Yu, E. M. Elliott, Novel Method for Nitrogen Isotopic Analysis of Soil-Emitted Nitric Oxide. *Environ. Sci. Technol.* **51**, 6268–6278 (2017).
41. https://www.eia.gov/todayinenergy/detail.php?id=44976#:~:text=September%201%2C%202020-,As%20U.S.%20coal%2Dfired%20capacity%20and,decline%2C%20operators%20consider%20seasonal%20operation&text=Coal%2Dfired%20electricity%20generating%20capacity,fired%20power%20plants%20less%20economical.
42. D. M. Sigman, *et al.*, A bacterial method for the nitrogen isotopic analysis of nitrate in seawater and freshwater. *Analytical chemistry* **73**, 4145–4153 (2001).
43. J. K. Bohlke, C. J. Gwinn, T. B. Coplen, NEW REFERENCE MATERIALS FOR NITROGEN-ISOTOPE-RATIO MEASUREMENTS. *Geostandards Newsletter* **17**, 159–164 (1993).
44. J. K. Böhlke, S. J. Mroczkowski, T. B. Coplen, Oxygen isotopes in nitrate: new reference materials for ^{18}O: ^{17}O: ^{16}O measurements and observations on nitrate-water equilibration. *Rapid Comm Mass Spectrometry* **17**, 1835–1846 (2003).
45. K. M. Foley, *et al.*, 2002–2017 anthropogenic emissions data for air quality modeling over the United States. *Data in Brief* **47**, 109022 (2023).
46. S. E. Benish, *et al.*, Long-term regional trends of nitrogen and sulfur deposition in the United States from 2002 to 2017. *Atmospheric Chemistry and Physics* **22**, 12749–12767 (2022).
47. K. W. Appel, *et al.*, The Community Multiscale Air Quality (CMAQ) model versions 5.3 and 5.3. 1: system updates and evaluation. *Geoscientific model development* **14**, 2867–2897 (2021).
48. G. Sarwar, H. Simon, P. Bhave, G. Yarwood, Examining the impact of heterogeneous nitryl chloride production on air quality across the United States. *Atmospheric Chemistry and Physics* **12**, 6455–6473 (2012).
49. G. Yarwood, *et al.*, Updates to the Carbon Bond mechanism for version 6 (CB6) in *9th Annual CMAS Conference, Chapel Hill, NC*, (2010), pp. 11–13.
50. J. E. Pleim, L. Ran, W. Appel, M. W. Shephard, K. Cady-Pereira, New Bidirectional Ammonia Flux Model in an Air Quality Model Coupled With an Agricultural Model. *J Adv Model Earth Syst* **11**, 2934–2957 (2019).
51. J. O. Bash, E. J. Cooter, R. L. Dennis, J. T. Walker, J. E. Pleim, Evaluation of a regional air-quality model with bidirectional NH_3 exchange coupled to an agroecosystem model. *Biogeosciences* **10**, 1635–1645 (2013).
52. O. E. Clifton, *et al.*, A single-point modeling approach for the intercomparison and evaluation of ozone dry deposition across chemical transport models (Activity 2 of AQMEII4). *Atmospheric Chemistry and Physics* **23**, 9911–9961 (2023).
53. J. T. Walker, *et al.*, Atmospheric deposition of reactive nitrogen to a deciduous forest in the southern Appalachian Mountains. *Biogeosciences* **20**, 971–995 (2023).
54. Z. Wu, *et al.*, Estimating source-sink distributions and fluxes of reactive nitrogen and sulfur within a mixed forest canopy. *Agricultural and Forest Meteorology* **333**, 109386 (2023).

55. J. Beck, *et al.*, An evaluation of a hybrid, terrain-following vertical coordinate in the WRF-based RAP and HRRR models. *Weather and Forecasting* **35**, 1081–1096 (2020).
56. W. W. Walters, G. Michalski, Ab initio study of nitrogen and position-specific oxygen kinetic isotope effects in the NO+ O_3 reaction. *The Journal of chemical physics* **145** (2016).
57. H. Fang, W. W. Walters, D. Mase, G. Michalski, i_NRACM: incorporating ^{15}N into the Regional Atmospheric Chemistry Mechanism (RACM) for assessing the role photochemistry plays in controlling the isotopic composition of NO_x, NO_y, and atmospheric nitrate. *Geoscientific Model Development* **14**, 5001–5022 (2021).
58. W. W. Walters, S. R. Goodwin, G. Michalski, Nitrogen stable isotope composition ($\delta^{15}N$) of vehicle-emitted NO_x. *Environmental science & technology* **49**, 2278–2285 (2015).
59. D. J. Miller, P. K. Wojtal, S. C. Clark, M. G. Hastings, Vehicle NO_x emission plume isotopic signatures: Spatial variability across the eastern United States. *JGR Atmospheres* **122**, 4698–4717 (2017).

6. Supplementary

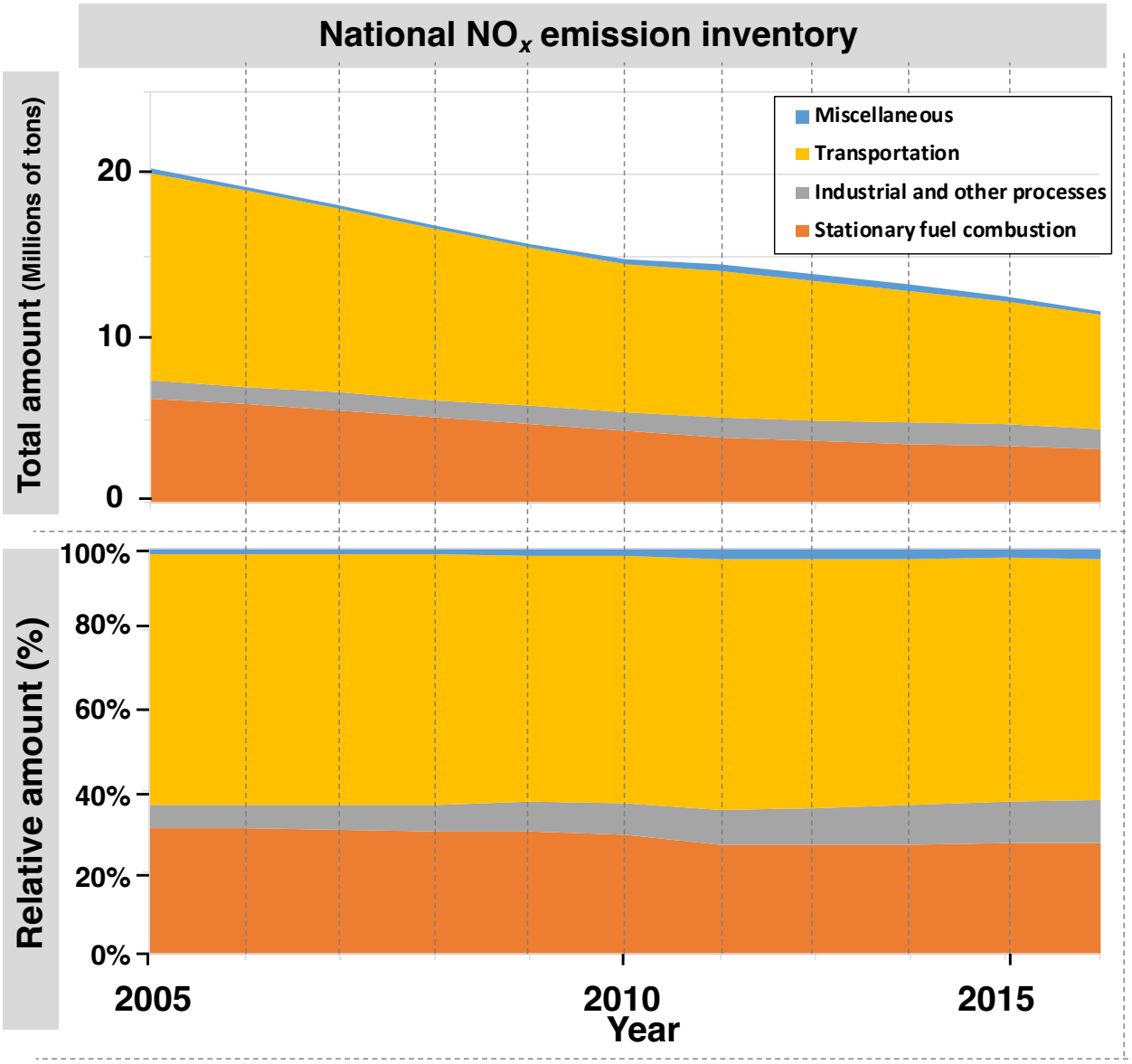

Figure S5.1. Total NO_x emission and their relative fraction for the whole United States from 2005 to 2015 from the Environmental Protection Agency (EPA) National Emission Inventory (NEI) estimates.

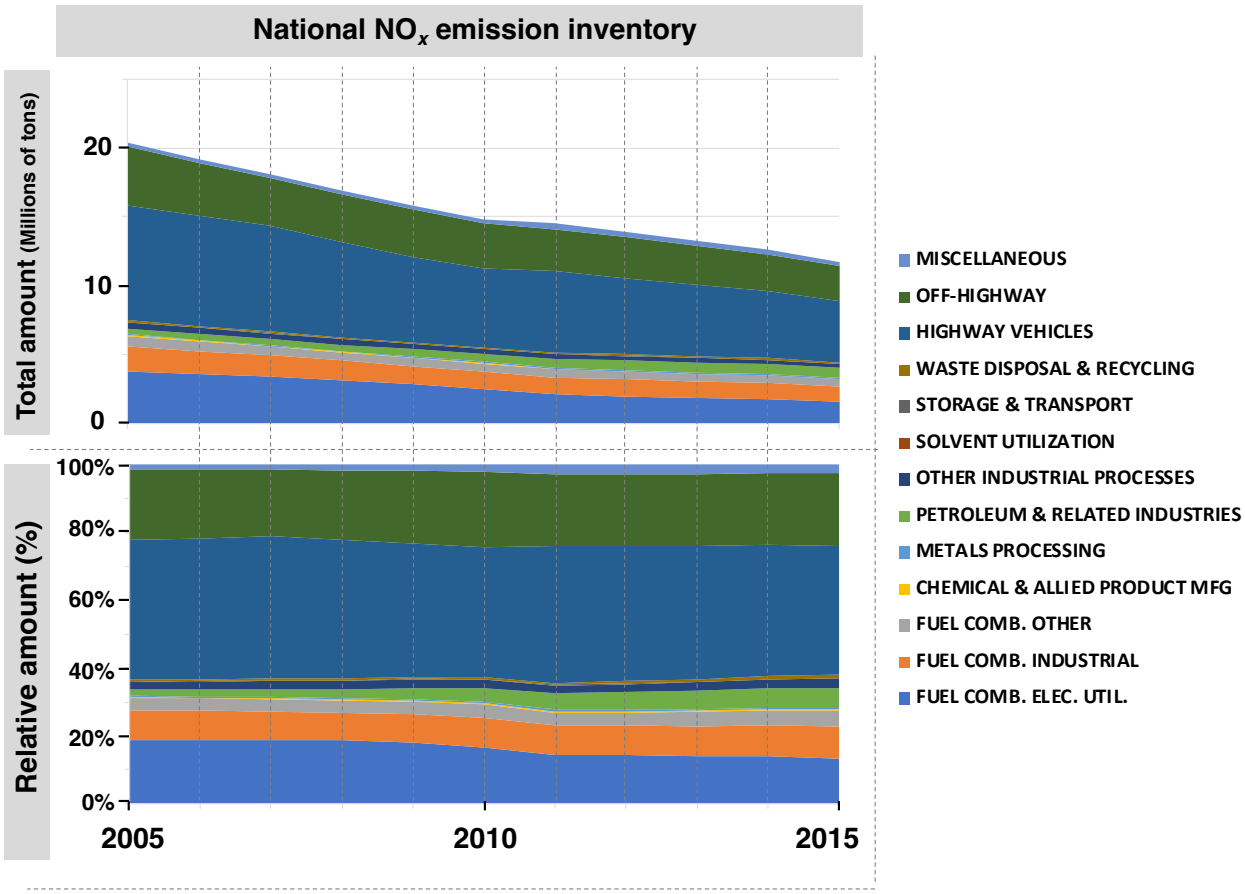

Figure S5.2. Total NO_x emission and their relative fraction by sectors for the whole United States from 2005 to 2015 from the EPA NEI estimates.

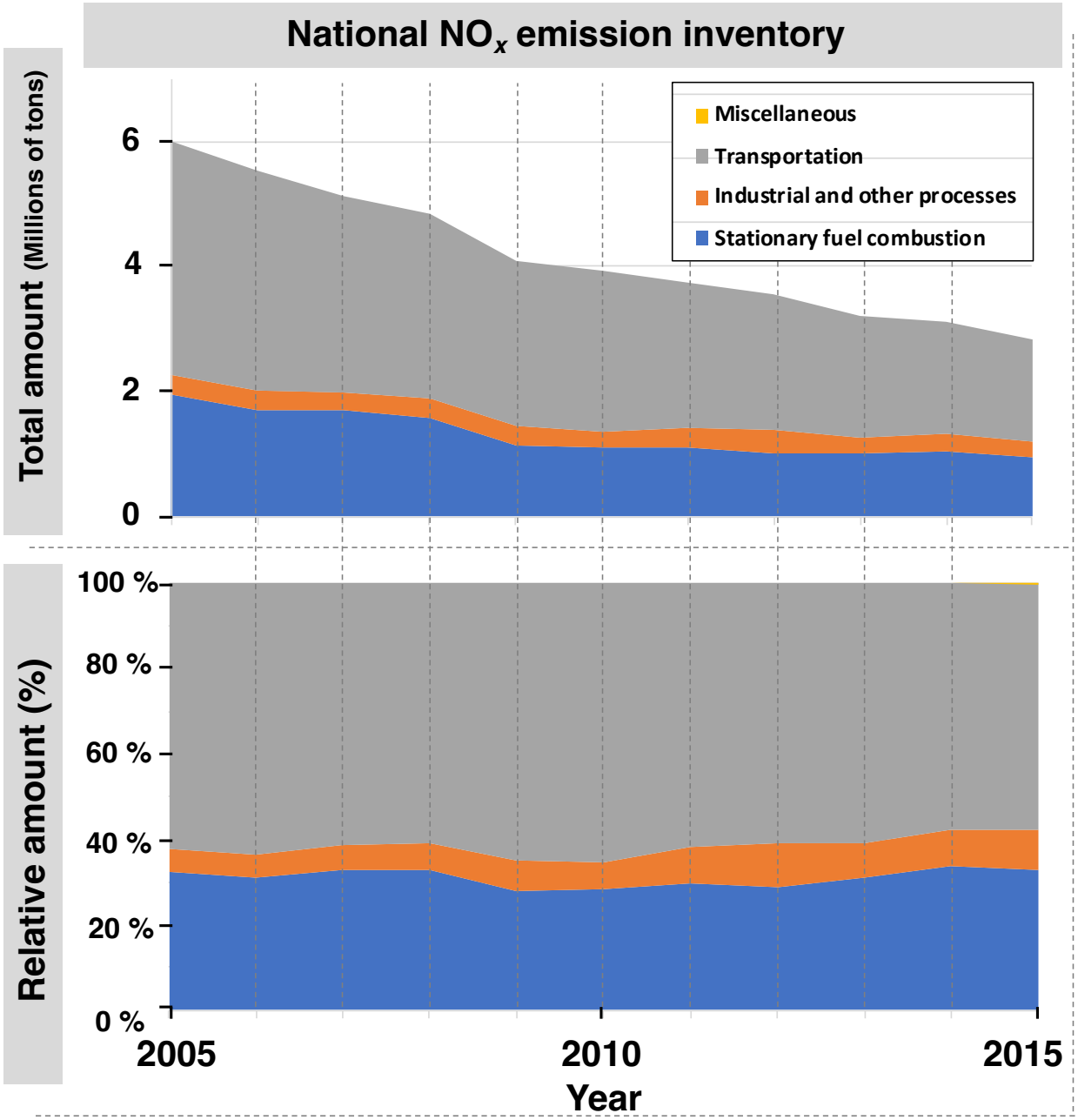

Figure S5 3. Total NO_x emission and their relative fraction for the eastern US from 2005 to 2015 from the EPA NEI estimates.

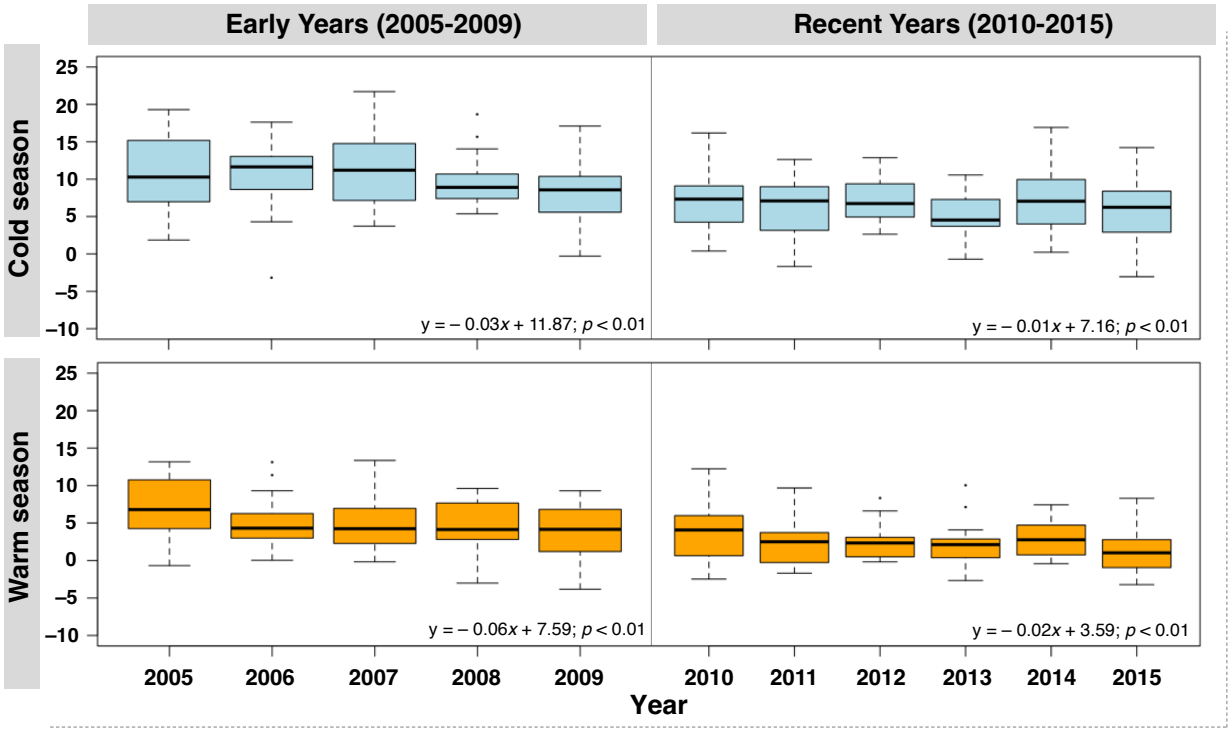

Figure S5.4. Box-and-whiskers plot describing the annual distribution of observed $\delta^{15}N$ of pNO_3 by early years (2005-2009) and recent years (2010-2015) by the cold (Oct-Mar) and the warm (Apr-Sep) season in Providence, RI.

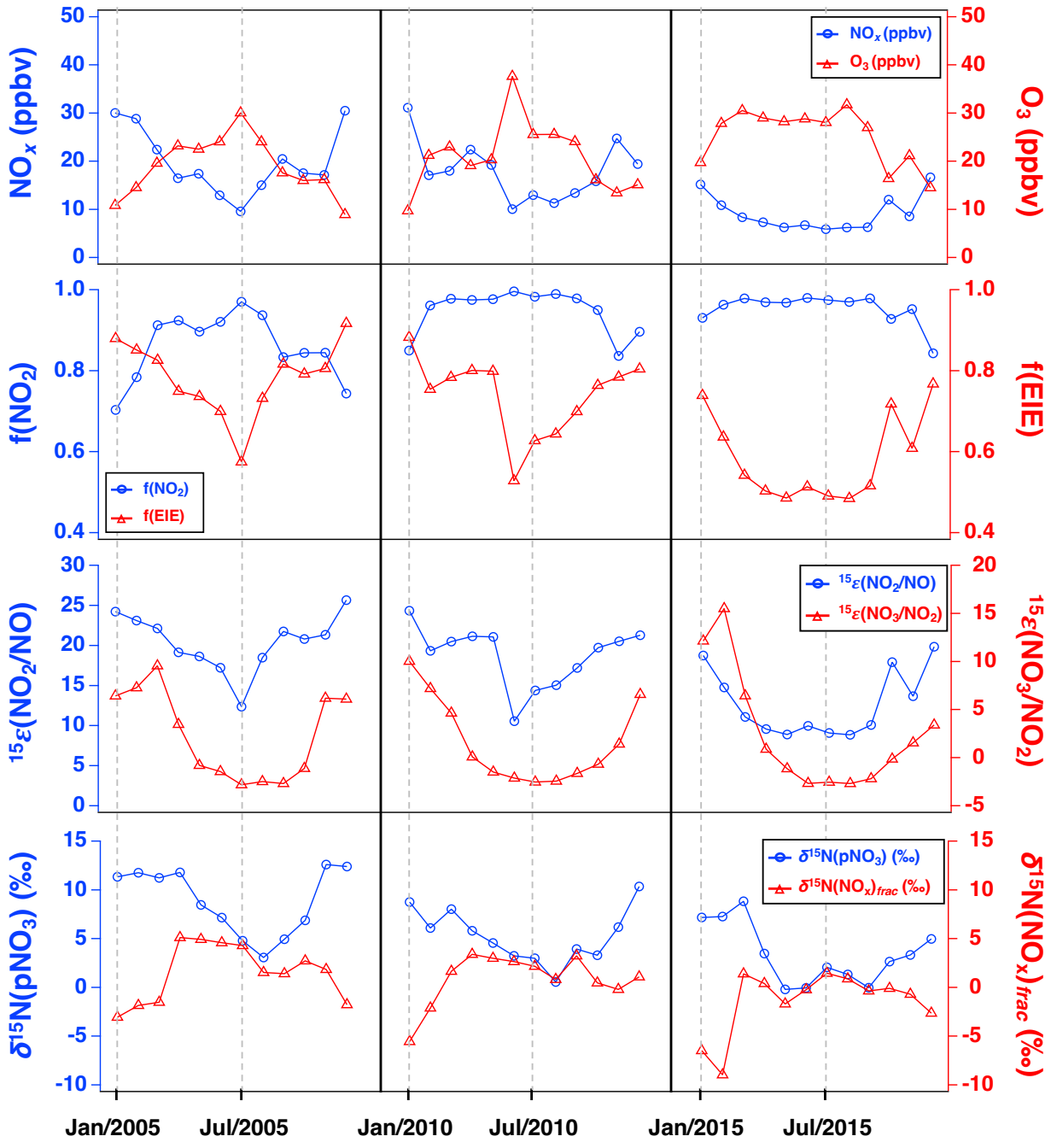

Figure S5.5. CMAQ output of O_3, NO_x, and $f(NO_2)$ and the calculated f(EIE), $^{15}\varepsilon(NO_2/NO)$, $^{15}\varepsilon(NO_3/NO_2)$, and predicted and observed $\delta^{15}N(pNO_3)$ for 2005, 2010, and 2015.

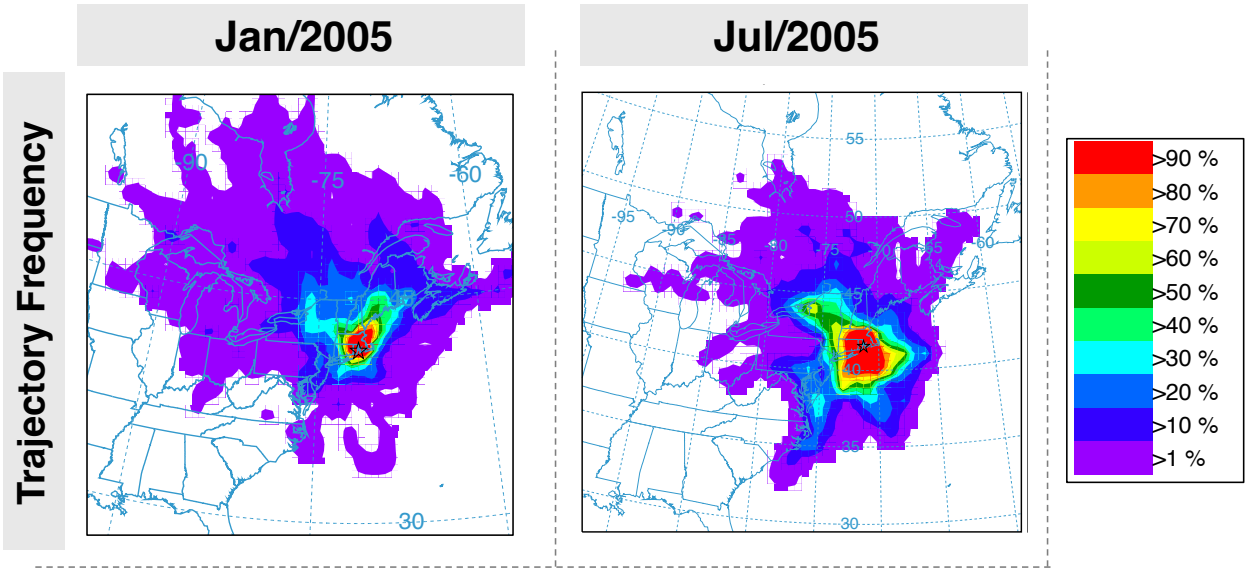

Figure S5.6. Backward trajectory frequency at 500 m for 48 hr using NOAA HYSPLIT model for January and July 2005.

CHAPTER 6

Tracking Atmospheric Nitrate Chemistry Change during COVID-19 Lockdown

Heejeong Kim[1,2], Wendell W. Walters[3], Meredith G. Hastings[1,2]

[1]Department of Earth, Environment, and Planetary Sciences, Brown University, Providence, RI 02912, USA.

[2]Institute at Brown for Environment and Society, Brown University, Providence, RI 02912, USA.

[3]Department of Chemistry and Biochemistry, University of South Carolina, Columbia, SC 29208, USA.

In preparation for submission to *Environmental Science & Technology (ES&T)*

Abstract

The outbreak of COVID-19 caused widespread restrictions on human activities, leading to unprecedented drops in emissions across the US. In this study, we utilized stable nitrogen ($\delta^{15}N$) and oxygen isotopes ($\delta^{18}O$ and $\Delta^{17}O$) of particulate nitrate to investigate atmospheric nitrate chemistry and its response to emissions reductions during the COVID-19 lockdown in the northeastern US. Precursor NO_x emission dramatically decreased in both urban and rural areas due to restrictions, but nitrate formation exhibited different sensitivity depending on the chemical regimes; in urban areas, reduced NO_x emissions enhanced ozone (O_3) levels, increasing the oxidizing capacity and leading to more efficient nitrogen oxidation process. On the other hand, a decrease in NO_x emission both reduced O_3 and nitrate formation during the COVID-19 lockdown in rural/suburban areas in the northeastern US. Isotope records suggest that shifts in NO_x oxidation chemistry, rather than changes in the type of emission sources, were the primary contributors to nitrate formation during the lockdown. These findings highlight the complex interactions between emission reductions, atmospheric oxidation chemistry, and secondary aerosol formation. Therefore, understanding these interactions is critical for making air quality policies to effectively mitigate air pollution.

1. Introduction

Reactive nitrogen species in the atmosphere (e.g., nitrogen oxides (NO_x = NO + NO_2) and nitrate (gas-phase nitric acid (HNO_3) and nitrate in particulate form (pNO_3))) play critical roles in air quality, climate, and human and ecosystem health[1,2]. NO_x influences the oxidative capacity of the atmosphere by controlling ozone (O_3) and hydroxyl radical (OH) levels, thereby affecting the lifetime of greenhouse gases such as methane (CH_4)[3,4]. Gaseous HNO_3 is a strong acid and highly water-soluble, which readily dissolves in cloud droplets, contributing to acid rain[5]. Gaseous HNO_3

is partitioned into the particle phase of NO_3, a major inorganic component of fine particulate matter ($PM_{2.5}$), with significant adverse effects on human health, visibility, and radiative forcing[5,6]. As a main sink of reactive nitrogen species, the wet and dry deposition of HNO_3 and pNO_3 contributes to acid deposition, damaging aquatic ecosystems, soil environments, and forest productivity[7,8].

Over the past several decades, the Clean Air Act Amendment in the US has been implemented in the US to mitigate major environmental threats such as acid rain, urban air pollution, and toxic air emissions. As a result, sulfur dioxide (SO_2) and NO_x emissions were successfully controlled with a total decrease of 73 % and 43 %, respectively, between 2005 and 2015 based on the US EPA National Emission Inventory (NEI)[9,10]. However, the response of changes in endpoints such as O_3, $PM_{2.5,}$ and deposition to emission regulations has not followed the expectation due to complex non-linear chemical feedbacks associated with NO_x chemistry[10,11]. For example, previous studies in the northeastern US have shown that wintertime pNO_3 concentrations have not changed over the decade, despite a significant decrease (~35 %) in NO_x emissions[10,11]. This is because increased O_3 concentrations enhanced atmospheric oxidizing capacity as NO_x emissions decreased, leading to more efficient pNO_3 formation in recent years[12]. In addition, the decrease in NO_x emissions has led to increased importance of organic nitrates ($RONO_2$) chemistry in many places in the US, significantly shifting the mechanisms of NO_x loss dominated by $RONO_2$ production[13,14]. These long-term emission reductions have driven substantial changes in air quality in the US for the past several decades, though the rate of emission reductions has recently slowed down due to the decreasing effectiveness of regulations[15,16].

However, in 2020, the outbreak of the COVID-19 pandemic led to an abrupt and unprecedented reduction in human activities worldwide, resulting in a significant decrease in air pollution and greenhouse gas emissions over a short time scale[17–19]. In the US, the COVID-19

lockdown began on March 15, 2020, imposing strict restrictions on various sectors, including transportation, industrial activities, travel, and economic operations. Consequently, these actions resulted in decreases in NO_x, SO_2, and carbon monoxide (CO) emissions by approximately -14(±2) %, -12(±10) %, and -11(±2) %, respectively[20,21]. This was a greater reduction than the average annual decline over the past decade. In contrast, SO_2 and $PM_{2.5}$ exhibited similar reduction rates to past trends, while ammonia (NH_3) emissions slightly increased during the COVID-19 lockdown[20]. The unprecedented drops in emissions during the COVID-19 lockdown similarly occurred across the countries in the world, but their response to air quality slightly varied by region. For example, in China, NO_2 concentrations considerably decreased by 60 %, similar to SO_2 and CO, but secondary pollutants such as O_3 and $PM_{2.5}$ concentrations are substantially enhanced, especially in heavily urbanized areas[22,23]. Additionally, despite the drop in various atmospheric aerosols and trace gases, $PM_{2.5}$ levels stayed unchanged or even increased in Europe due to an increase in NH_3 and the complicated gas-to-particle conversion process[24]. In contrast, South Korea experienced improved air quality, with significantly reduced concentrations of NO_2, CO, $PM_{2.5}$, and PM_{10} during the social distancing period for COVID-19[25,26]. Similarly, most of the areas in India also showed lower key pollutant levels such as $PM_{2.5}$ (-26 %), maximum daily 8 hr average O_3 (-11 %), NO_2 (-50 %), and SO_2 (-14 %) during the COVID-19 lockdown, though the scattered increases in O_3 (up to 21 %) in some urban locations were observed in the VOC-limited areas[27,28]. Overall, the COVID-19 lockdown globally provided a unique opportunity to experience the impact of restricted human activities on the local air quality over a short time scale.

Previous studies have demonstrated that stable nitrogen and oxygen isotopes (e.g., $\delta R_{sample} = [R_{sample}/R_{standard} - 1] \times 1000$ ($R = {}^{15}N/{}^{14}N$, ${}^{18}O/{}^{16}O$, and ${}^{17}O/{}^{16}O$)) of nitrate serve as powerful observational constraints for the understanding of atmospheric nitrate sources and/or chemical

processing[29–34]. Nitrogen isotope ($\delta^{15}N$) of nitrate has been proven to provide information about precursor NO_x emission sources such that each source, like transportation, fuel combustion, soil, and lightning, tends to have distinct $\delta^{15}N$ values[26,28–32]. Further, isotope fractionation during NO_x cycling and nitrate formation can affect $\delta^{15}N(pNO_3)$ values, reflecting variations in oxidation chemistry[33,40]. Oxygen isotopes ($\delta^{18}O$ and $\Delta^{17}O$ (= $\delta^{17}O - 0.52 \times \delta^{18}O$)) in nitrate have been proven to provide observational constraints on the oxidation pathways responsible for atmospheric nitrate formation[30,31,34]. Atmospheric oxidants such as O_3, $O_2/RO_2/HO_2$, H_2O, and OH possess distinct $\delta^{18}O$ and $\Delta^{17}O$ values and these unique signatures are incorporated into nitrate during NO_x oxidation chemistry. Atmospheric O_3 possesses an excess of ^{17}O, due to mass-independent fractionation during its formation. This ^{17}O excess is defined as $\Delta^{17}O$, which is the unique signature of O_3[41–43]. On the other hand, each atmospheric oxidant has distinct $\delta^{18}O$ values, allowing for further detailing of NO_x oxidation chemistry compared to $\Delta^{17}O$[34]. These unique characteristics thus enable us to quantify precursor emission sources and/or NO_x oxidation chemistry.

The northeastern US has historically experienced poor air quality due to emissions from highly populated and urbanized areas, as well as long-range transport from the Midwest, where coal-fired power plants, industrial facilities, and agricultural activities contribute to emissions. In this study, we analyzed nitrogen and oxygen isotopes of nitrate collected from the six Clean Air Status and Trends Network (CASTNET) sites in the northeastern US before and after the COVID-19 lockdown periods. This period provides a unique opportunity to assess the impacts of reduced human activity on air quality on a short time scale. Based on these isotope records, we aimed to quantitatively evaluate the spatiotemporal variabilities of atmospheric nitrate sources and/or chemical processing under the COVID-19 lockdown impact. Our study contributes to a better understanding of changes in atmospheric oxidation chemistry and chemical feedback to short-term

emission reductions, providing insights that can inform regulatory strategies for improving air quality in the future.

2. Methods

2.1 CASTNET filter

Atmospheric particulate matter ($PM_{2.5}$) samples were collected by the US EPA at several locations of the CASTNET sites in the northeastern US. Six CASTNET sites were selected (Fig. 6.1): Abington, CT (ABT147; 41.84°N, -72.01°W); Beltsville, MD (BEL116; 39.03°N, -76.82°W); Claryville, NY (CAT175; 41.94°N, -74.55°W); Connecticut Hill, NY (CTH110; 42.40°N, -76.65°W); Wash. Crossing (WSP144; 40.31°N, -74.87°W); Woodstock, NH (WST109; 43.94°N, -71.70°W). The samples were collected weekly from 01 January 2019 to 31 December 2020 using a three-stage filter pack system including Teflon, nylon, and cellulose filter. Based on EPA protocols, pNO_3, pSO_4, and pNH_4 were collected using a Teflon filter in the first stage of the filter pack, and gaseous HNO_3 was collected using a nylon filter. Filter pack flow rate is maintained at 1.50 L min^{-1} at standard conditions. The filters were extracted and analyzed for their concentrations following standardized protocols at the Wood Gainesville, FL, US laboratory[44]. Briefly, the filters were extracted using 25 mL of ultra-high purity water (> 18.2 MQ), and the filter extracts were measured using micromembrane-suppressed Ion Chromatography (IC) to determine HNO_3, pNO_3 and pSO_4 concentrations. For pNH_4 concentrations, the automated indophenol method with the Bran+Luebbe AutoAnalyzer 3 was used[45]. Mass concentrations in the air (μg m^{-3}) were calculated based on the volume of collected air. Following this analysis, the samples were stored in a laboratory at room temperature for up to 2 years until shipment to Brown University.

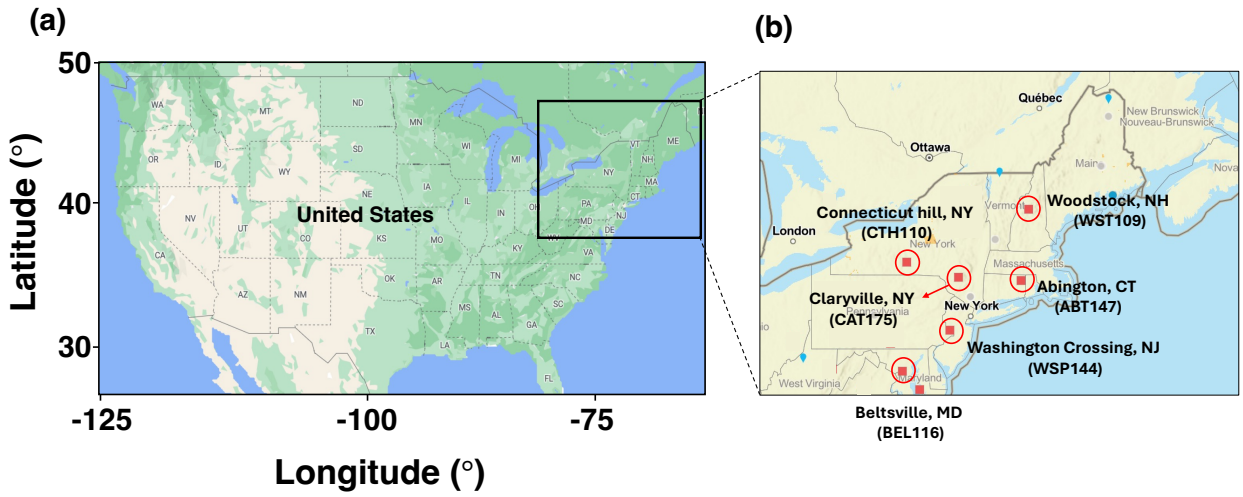

Figure 6.1. Map of United States (a) and selected CASTNET sites (b) for this study in the northeastern US. The image was created using Google Earth (© 2025 Google).

2.2 Concentration and Isotope Analysis

Extracted pNO_3 samples were shipped to Brown University. To secure enough volume for isotope analysis, samples were aggregated each month and remeasured their concentrations. Nitrate concentrations were measured for isotope analysis using ion chromatography (Dionex Integrion HPIC) employing suppressed conductivity detection. Nitrate concentrations were determined using a Dionex AS19-4 μm guard column (4×50 mm) and analytical column (4×250mm) with 20 mM KOH as eluent and a flow rate of 1 mL min^{-1}.

Nitrogen and oxygen isotopic compositions in pNO_3 were analyzed using the well-established bacterial denitrifier method at Brown University[46–48]. Briefly, samples were injected into a buffer solution containing *Pseudomonas aureofaciens*, which lacks the nitrous oxide (N_2O) reductase enzyme, and nitrate samples were quantitatively reduced to N_2O. For $\delta^{15}N$ and $\delta^{18}O$ analysis, the generated N_2O is injected into a Thermo-Finnigan Delta V Plus isotope ratio mass spectrometry (IRMS) with a modified GasBench system after flowing through an automated extraction and

purification system. N_2O was determined for their $\delta^{15}N$ and $\delta^{18}O$ compositions at an *m/z* of 44, 45, and 46 and corrected using internationally recognized isotopic reference materials that included IAEA-NO-3 ($\delta^{15}N$ = 4.7 ‰ and $\delta^{18}O$ = 25.6 ‰), USGS34 ($\delta^{15}N$ = –1.8 ‰ and $\delta^{18}O$ = −27.9 ‰), and USGS35 ($\delta^{15}N$ = 2.7 ‰ and $\delta^{18}O$ = 57.5 ‰). The $\Delta^{17}O$ was determined in a separate analysis. The bacteria-generated N_2O was decomposed to N_2 and O_2 in a gold furnace heated to 770°C and analyzed at m/z 32, 33, and 34 to determine $^{17}O/^{16}O$ and $^{18}O/^{16}O$ ratios of the evolved O_2. The 33/32 and 34/32 mass ratios were corrected using isotopic reference materials, USGS34 (−0.29 ‰) and USGS35 (21.6 ‰), and then $\Delta^{17}O$ was determined from $\Delta^{17}O = \delta^{17}O - 0.52 \times \delta^{18}O$. Due to sample mass limitations, some samples were only analyzed for $\delta^{18}O$. The overall pooled standard deviations of isotopic reference materials and sample numbers were as followed: USGS34 ($\sigma(\delta^{15}N)$=0.5 ‰ (n=137); $\sigma(\delta^{18}O)$=1 ‰ (n=137); $\sigma(\Delta^{17}O)$=2.9 ‰ (n=116)); USGS35 ($\sigma(\delta^{15}N)$=0.6 ‰ (n=137); $\sigma(\delta^{18}O)$=1.2 ‰ (n=137); $\sigma(\Delta^{17}O)$=2.5 ‰ (n=116)), and IAEA-NO-3 ($\sigma(\delta^{15}N)$=0.4 ‰ (n=137); $\sigma(\delta^{18}O)$ = 0.7 ‰ (n=137)).

2.3 NO_x emission database and $\delta^{15}N(NO_x)$ estimation

$\delta^{15}N(pNO_3)$ serves as a useful tracer of NO_x emission sources, as the distinct $\delta^{15}N$ signatures of NO_x from various emission sources are preserved in $\delta^{15}N(NO_x)$[33,37]. Here, we estimated the $\delta^{15}N(NO_x)$ value using the 2020 US EPA national NO_x emission inventory from the northeastern US. The NO_x emission inventory data were reported depending on fuel types and sectors for every year and state. Given the wide range of NO_x sources, we have simply divided them into five sectors by major source types for the calculation. Specifically, we have categorized emissions as follows[33,35–39,49]: agriculture activity and soil NO_x emissions ($\delta^{15}N$ = -33.0±12.3 ‰), transportation ($\delta^{15}N$ = -4.7±1.7 ‰), and biomass burning ($\delta^{15}N$ = 2.5±7.5 ‰). Energy production, industry, and combustion were grouped by fuel type as either combustion – coal & solid biofuel ($\delta^{15}N$ = 13.6±3.9

‰) or combustion – liquid fuel & process ($\delta^{15}N$ = -16.5±1.7 ‰). Given NEI reports annual NO_x emission data, seasonal variations of these emissions sources were inferred using monthly NO_x emissions reported by the Emissions Database for Global Atmospheric Research (EDGAR) (note that EDGAR data is the whole US domain). Annual and monthly $\delta^{15}N(NO_x)$ values from 2005 to 2015 were calculated based on isotope mass balance using the fraction of NO_x emissions by sector and fuel type and previously reported $\delta^{15}N(NO_x)$ emission signatures following a previously described method:

$$\delta^{15}N(NO_x) = \sum_{i=1}^{n} f_i \times \delta^{15}N_i(NO_x) \qquad \text{(Eq.1)}$$

where f_i represents fractions of each emission source compared to whole NO_x emissions. $\delta^{15}N_i(NO_x)$ is the emission signature of sources. Details can be found in Bekker et al., 2023[33].

2.4 Ancillary Near-Surface Observations

This study utilizes near-surface observations of gaseous pollutants, including O_3 and NO_x, from the Clean Air Status and Trends Network (CASTNET) and the Chemical Speciation Network (CSN), respectively. Hourly O_3 data from the CASTNET sites were used in this study. NO_x data were obtained from the nearest air quality monitoring station since the CASTNET sites are not measuring NO_x concentrations. In addition, gaseous NH_3 concentrations were used from the co-located Ammonia Monitoring Network (AMoN) sites, which were co-located with the CASTNET sites.

3. Results and discussions

3.1 Spatiotemporal variations of observation (overview)

Figure 6.2 shows the overview of the monthly averaged spatiotemporal variations of trace gases (O_3 and NO_x) and inorganic ion species (e.g., HNO_3, pNO_3, pSO_4, and pNH_4) for 2019 and 2020, and their statistics are summarized in Table S6.1. Throughout the two years, the observed species exhibit distinct spatial and temporal patterns. For example, CASTNET sites located near highly polluted urban areas, such as BEL116 and WSP144 (near Washington, D.C. and New York City, respectively), showed higher NO_x and inorganic ion concentrations than other locations due to their proximity to major emission sources. In contrast, remote sites like WST109, which are farther from urban centers, exhibited lower NO_x and inorganic ion concentrations due to the reduced influence of emissions. However, O_3 showed the opposite pattern, which is higher concentrations observed at sites farther from urban areas and lower concentrations near city centers, indicating that NO_x titration plays a significant role in O_3 levels.

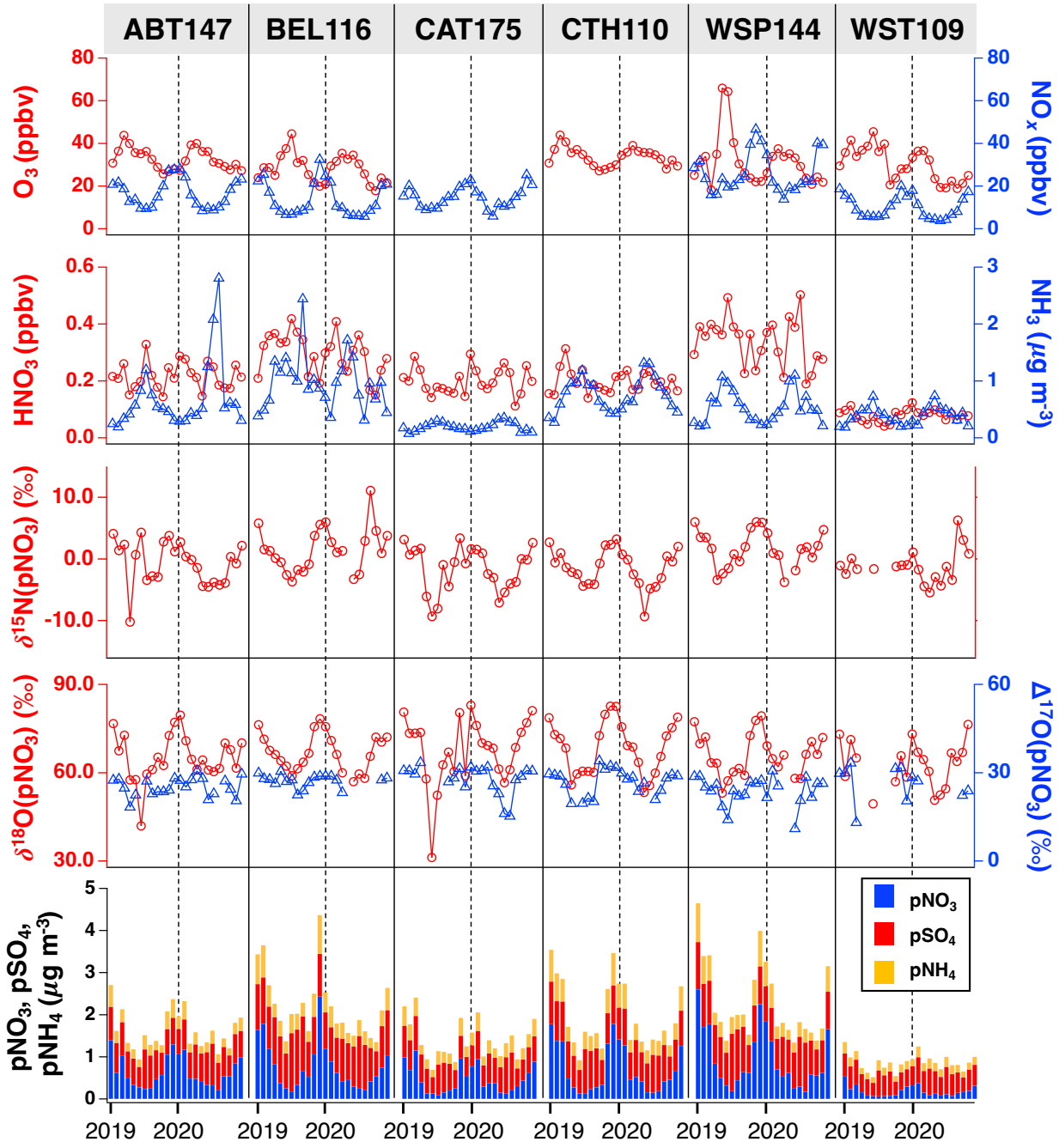

Figure 6.2. Overview of the monthly averaged spatiotemporal variations of trace gases (O_3 and NO_x), inorganic ion species (e.g., HNO_3, NH_3, pNO_3, pSO_4, and pNH_4), and isotopic compositions of pNO_3 ($\delta^{15}N$, $\delta^{18}O$, and $\Delta^{17}O$) from Jan 2019 to Dec 2020.

In terms of temporal variations, NO_x concentrations tend to be higher in winter due to a combination of reduced photochemical activity, increased lifetime, lower boundary layer height,

and seasonal emissions patterns. In contrast, O_3 concentrations peak in the warm season, driven by increased solar radiation and enhanced photochemical production under higher temperatures. A strong correlation between pNO_3 and pNH_4 exists for all periods ($R^2 = 0.88$; Fig. S6.1). This is likely driven by pNO_3 and pNH_4 concentrations being higher in the cold season compared to the warm season, primarily due to the increased formation of ammonium nitrate (NH_4NO_3) at lower temperatures. Temperature sensitivity has gradually increased as pH increases due to the low SO_2 concentration in the winter season. In colder temperatures, HNO_3 and NH_3 remain in the particle phase longer, resulting in a more pronounced wintertime seasonality for both pNO_3 and pNH_4. On the other hand, pSO_4 strongly correlated with HNO_3 ($R^2 = 0.75$; Fig. S6.1) over the measurement. pSO_4 concentrations are higher in the warm season compared to the cold season, as SO_2 oxidation was more efficient with higher oxidant availabilities driven by photochemical oxidation. SO_2 oxidation in winter was likely limited by oxidant availability, specifically in cloud water, due to reduced sunlight and high SO_2 concentrations relative to oxidant availability. However, the oxidants were sufficiently available to fully oxidize SO_2 to pSO_4 in the warm season due to the photochemical production of oxidants relevant to SO_2 oxidation, leading to an increase in pSO_4 concentrations. In addition, the presence of high pSO_4 content and elevated temperatures in summer led to more acidic aerosol pH[50], which in turn shifted HNO_3/pNO_3 partitioning toward the gaseous phase, increasing HNO_3 concentrations.

For isotope records, spatiotemporal variations of $\delta^{15}N$, $\delta^{18}O$, and $\Delta^{17}O$ in pNO_3 were observed from 2019 to 2020 (Fig. 6.2). The isotopic composition of pNO_3 provides insight into its precursor sources and formation pathways. Nitrogen isotope ($\delta^{15}N$) in pNO_3 serves as an indicator of NO_x emission sources and chemical processing in the atmosphere, and oxygen isotopes ($\delta^{18}O$ and $\Delta^{17}O$) reflect the oxidation chemistry during nitrate formation. Significantly higher $\delta^{15}N$ values

are observed for BEL and WSP sites compared to the other four sites. This is likely due to the dominant NO_x source in these areas, including vehicular traffic, industrial facilities, and power plants. In particular, the relative contribution of coal combustion emissions with ^{15}N-enriched NO_x dominates in these areas since major power plants are located in the Midwestern US area. Whereas no significant spatial differences were observed for the other four sites. In terms of oxygen isotope records, $\delta^{18}O$ and $\Delta^{17}O$ of pNO_3 did not exhibit strong spatial differences. It is expected that pNO_3 has a long atmospheric lifetime, and regional oxidation chemistry is similar; thus, regional influence is more important for NO_x oxidation chemistry compared to local influence.

For temporal variations, both nitrogen and oxygen isotopes show higher values in the winter season compared to the warm season (Fig. 6.2), which is consistent with previous studies in the northeastern US[33,34]. This seasonality can be attributed to changes in emission sources and oxidation chemistry by season. For example, fuel-type variations are reflected in $\delta^{15}N(NO_x)$ as coal combustion with ^{15}N-enriched NO_x dominates in summer due to higher electricity demand from air conditioning, while natural gas with ^{15}N-depleted NO_x is heavily used for home heating in the winter season. In addition, the isotope effect involved in NO_x cycling and atmospheric nitrate formation has an important role in determining $\delta^{15}N(pNO_3)$ values. Particularly, previous studies suggested that the fractionation effect during either NO to NO_2 oxidation or NO_2 to pNO_3 oxidation was significantly important in $\delta^{15}N(pNO_3)$ seasonality in the wintertime.

Oxygen isotopes of nitrate exhibit distinct seasonality, with higher $\delta^{18}O$ and $\Delta^{17}O$ values observed in the cold season and lower values in the warm season, which are driven by a shift in oxidation chemistry. During the cold season, the relative importance of N_2O_5 hydrolysis increased, resulting in more incorporation of O_3 into pNO_3 formation. This led to higher $\delta^{18}O$ and $\Delta^{17}O$ values

of pNO_3. In contrast, during the warm season, NO_2 oxidation by OH dominates compared to O_3. The contribution of O_3 is relatively diluted, leading to lower $\delta^{18}O$ and $\Delta^{17}O$ values.

3.2 Impact of COVID lockdown (2019 vs. 2020 March)

In the mid of March 2020, the COVID-19 lockdown was implemented across the US, leading to restrictions on travel, industrial activities, and economic operations. Most states issued stay-at-home orders, resulting in reduced transportation and industrial emissions. Consequently, the concentrations of primary pollutants such as NO_x, SO_2, and CO have dramatically decreased during the COVID-19 lockdown compared to pre-COVID-19 periods[20]. To assess the impact of the COVID-19 lockdown on air quality, we compared monthly datasets between 2019 and 2020. Since air pollutant concentrations are strongly influenced by meteorological factors such as temperature, relative humidity, boundary layer height, and sunlight, a month-to-month comparison minimizes those artifacts in our records. Our statistical analysis indicates that a significant decrease in NO_x, pNO_3, pSO_4, and pNH_4 concentrations due to the COVID-19 lockdown was observed in March exclusively ($p<0.05$). The concentrations of air pollutants rebounded after March and their changes were not significant in the following months. Therefore, our primary analysis in this section focused on the comparison between March 2019 and March 2020, when the most significant reductions were observed.

3.2.1 Changes in air pollutants

Figure 6.3 shows the relative changes of NO_x, O_3, HNO_3, NH_3, and inorganic ions (e.g., pNO_3, pSO_4, and pNH_4) concentrations as well as NO_x emissions between March 2019 and March 2020 in the northeastern US. In this region, the transportation sector, electric utilities, and industrial fuel combustion are known as the major NO_x sources[9,33]. According to the global emission estimates of the Emissions Database for Global Atmospheric Research (EDGAR), NO_x emissions

dramatically decreased by around -10 % in March across the US under the implementation of the COVID-19 lockdown. The reduction primarily occurred in the transportation and power generation sectors, yet their relative contributions remained unchanged (Fig. S6.2), indicating that all major NO_x sources were modeled to decline similarly. As a result of the NO_x emission reductions, atmospheric NO_x concentrations also decreased by approximately 14% in rural areas (i.e., ABT147, CAT175, CTH110, and WST109) and 20% in urban areas (i.e., BEL116 and WSP144). The impact on O_3 concentrations varied depending on the local chemical regime. In rural areas where O_3 production is a NO_x–limited regime, the decrease in NO_x concentration led to a 14% reduction in O_3 concentration. In contrast, in urban areas where O_3 concentration is sensitive to VOC level (i.e., VOC-limited regime), the decrease in NO_x emissions resulted in approximately a 5% increase in O_3 concentrations, particularly at nighttime due to reduced O_3 titration by NO.

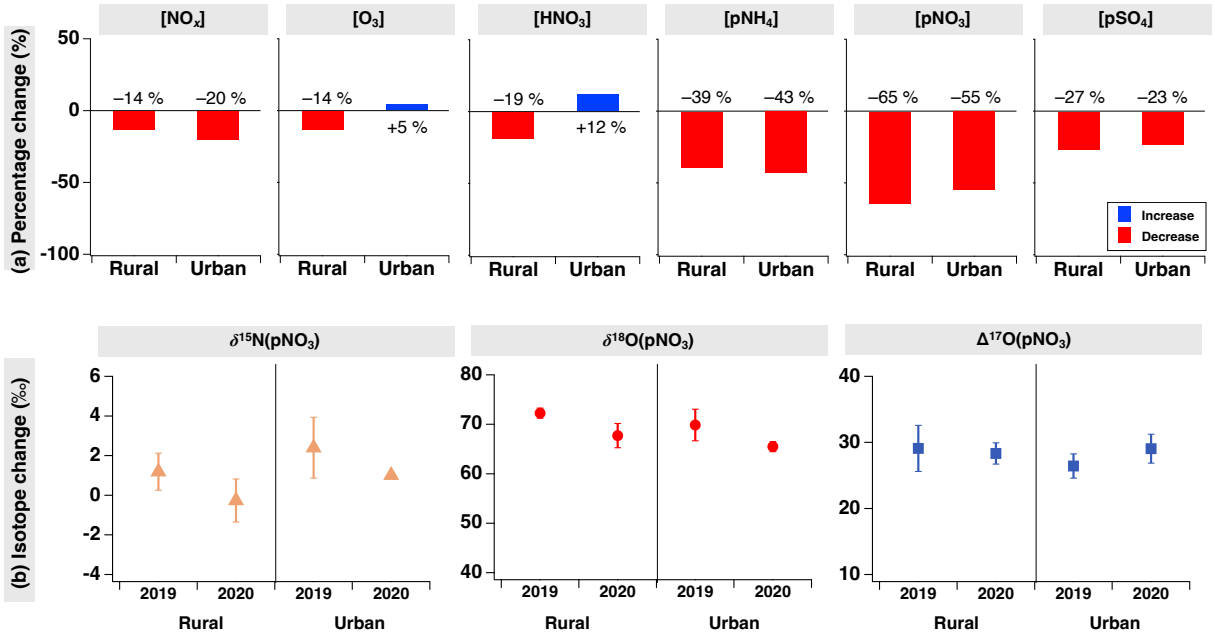

Figure 6.3. (a) Percentage change of NO_x, O_3, HNO_3, pNH_4, pNO_3, and pSO_4 concentrations between Mar 2019 and Mar 2020 for urban (BEL116 and WSP144) and rural areas (ABT147, CAT175, CTH110, and WST109). (b) Change in isotope value of $\delta^{15}N$, $\delta^{18}O$, and $\Delta^{17}O$ of pNO_3 between Mar 2019 and Mar 2020 for urban and rural areas.

The dramatic reductions in primary emissions during the COVID-19 lockdown also influenced secondary particulate matter formation. Overall, pNH_4 and pSO_4 concentrations decreased by 43 % and 23 % in urban areas and 39 % and 27 % in rural areas, respectively. pNO_3 concentrations have also decreased by 55 % and 65 % for urban and rural areas, respectively. However, in contrast to the overall reduction in inorganic chemical components in $PM_{2.5}$, gaseous HNO_3 concentrations have increased by 12 % in urban in the northeastern US. This different response is likely driven by shifts in gas-particle partitioning due to changes in primary emissions.

3.2.2 Changes in nitrogen and oxygen isotopes of pNO_3

To further understand the impact of these emission changes on nitrate formation, we analyze the nitrogen and oxygen isotopic composition of pNO_3. The $\delta^{15}N(pNO_3)$ provides a powerful tracer of observational constraints for identifying atmospheric NO_x emission sources and chemical processing during NO_x oxidation chemistry. During the COVID-19 lockdown period, observed $\delta^{15}N(pNO_3)$ significantly decreased from 2.4(±1.5) ‰ to 1.0(±0.1) ‰ and from 1.2(±0.9) ‰ to –0.3(±1.1) ‰ compared to March 2019 for both urban areas (BEL and WSP) and rural areas (ABT, CAT, CTH, and WST), respectively. Similarly, oxygen isotopes ($\delta^{18}O$ and $\Delta^{17}O$) in pNO_3 provide observational constraints on the oxidation pathways that are responsible for atmospheric nitrate formation. A notable decrease in $\delta^{18}O(pNO_3)$ was also observed during the COVID-19 lockdown period from 69.9(±3.2) ‰ to 65.5(±1.0) ‰ and from 72.3(±1.0) ‰ to 67.7(±2.5) ‰ for both urban areas (BEL and WSP) and rural areas (ABT, CAT, CTH, and WST), respectively. These are likely driven by changes in NO_x emissions and/or their impact on NO_x oxidation chemistry during the COVID-19 lockdown.

Previous spatiotemporal $\delta^{15}N$ differences in atmospheric nitrate in the midwestern and northeastern US had been concluded to reflect the importance of precursor emission sources [32,33,51].

By mass balance equation, we calculate the $\delta^{15}N(NO_x)$ value using the NO_x emission estimates with assumed emission source values to assess whether changes in emission sources significantly affect pNO_3 formation and thus they are responsible for the decrease in $\delta^{15}N(pNO_3)$ value during the COVID-19 lockdown. Five major NO_x emission categories that have distinguishable isotopic signatures were considered: transportation (on-road, non-road, and shipping), combustion (residential, commercial, and industrial), soil emissions/agricultural activities, and biomass burning, accounting for roughly 95 % of all emitted NO_x in the eastern US. Combustion-related sources were further classified by fuel type into coal & solid biofuel versus liquid fuel & process combustion (see Methods for details). Calculated $\delta^{15}N(NO_x)$ values using NO_x emission estimates were -2.9 ‰ and -3.0 ‰ for March 2019 and 2020, respectively, indicating that $\delta^{15}N(NO_x)$ values did not exhibit significant changes between 2019 and 2020. This modeled $\delta^{15}N(NO_x)$ suggests that changes in emission sources played an insignificant role in determining pNO_3 formation, while changes in NO_x oxidation chemistry due to the COVID-19 lockdown are likely more influential.

Assuming that the $\delta^{15}N(NO_x)$ value did not change during the COVID-19 lockdown period, we additionally investigated if NO_x oxidation chemistry changed in March 2020 using our observed $\delta^{15}N(pNO_3)$ and theoretically calculated fractionation factors in previous studies[33,40,52]. The influences of $\delta^{15}N$ fractionation associated with NO_x cycling (e.g., $^{15}\varepsilon(NO_2/NO)$) and NO_x to pNO_3 conversion (e.g., $^{15}\varepsilon(NO_3/NO_2)$) on $\delta^{15}N(HNO_3)$ were quantified based on a previous framework[33].

The impact of NO_x reductions varies by region due to differences in ozone production sensitivity and atmospheric conditions. In urban areas, NO_x emission reductions have led to an increase in O_3 concentrations. In this environment, the elevated O_3 levels enhance NO oxidation to NO_2, increasing the fraction of NO_2 to NO_x. Indeed, calculated $^{15}\varepsilon(NO_2/NO)$ indicated that

$^{15}\varepsilon(NO_2/NO)$ played an important role in a decrease in $\delta^{15}N(pNO_3)$ values compared to $^{15}\varepsilon(NO_3/NO_2)$ during the COVID-19 lockdown period. This is because the kinetic isotope effect, primarily associated with the $NO+O_3$ pathway, became more crucial relative to the equilibrium isotope effect (EIE), which is more important under lower $f(NO_2)$ conditions. Note that under conditions of higher O_3 concentrations relative to NO_x concentrations, the kinetic isotope effect dominates compared to the EIE, contributing to a depleted ^{15}N in pNO_3. Additionally, N_2O_5 hydrolysis still remains an important pathway for HNO_3 formation in an urban environment due to increased O_3 availability, leading to a higher nitrogen oxidation ratio (NOR) in March 2020. This indicates that as NO_x emission is reduced, nitrate formation becomes more efficient due to an increase in oxidizing capacity, contributing to an increase in HNO_3 concentration, not pNO_3 concentration during the COVID-19 lockdown. However, its impact on $\delta^{18}O(pNO_3)$ is counterbalanced by the $NO+O_3$ reaction, which yields lower $\delta^{18}O$ values because the oxygen atom in NO reflects the isotopic signature of its emission sources (e.g., O_2 in the case of combustion). This mechanism resulted in the observed decrease in $\delta^{18}O(pNO_3)$ value in March 2020, which is consistent with findings from a previous study[12].

On the other hand, in rural areas, reduction in NO_x emissions has led to a decrease in O_3 concentrations with an increase in $f(NO_2)$ such that O_3 formation is primarily constrained by the availability of NO_x. No significant change in $^{15}\varepsilon(NO_2/NO)$ was calculated, but $^{15}\varepsilon(NO_3/NO_2)$ value considerably decreased during the COVID-19 lockdown. We have assumed that two primary NO_2 oxidation pathways–NO_2+OH and N_2O_5 hydrolysis–were dominant in this area for nitrate formation as suggested in the previous study[53]. The calculated $^{15}\varepsilon(NO_3/NO_2)$ value indicates that the NO_2+OH pathway has been important for pNO_3 formation compared to N_2O_5 hydrolysis in March 2020, though total nitrate formation decreased. This is likely driven by insufficient NO_2

and O_3 levels for N_2O_5 hydrolysis, leading to a shift in the dominant pathway for HNO_3 formation toward the NO_2+OH reaction. The fractionation effect associated with the NO_2 + OH reaction is known to be -3 ‰, while fractionation during N_2O_5 hydrolysis is assumed to be approximately +28 ‰. This means that the shift in chemical processing toward NO_2+OH reaction resulted in lower $\delta^{15}N(pNO_3)$ values in March 2020 than in March 2019. As well as $\delta^{18}O(pNO_3)$ value decreased due to the diluted influence of O_3 into pNO_3. Overall, as NO_x and O_3 concentrations decreased, HNO_3 and pNO_3 concentrations decreased with decreased NOR, indicating that pNO_3 formation became less efficient during the COVID-19 lockdown in rural regions.

3.3 Sensitivity of nitrate formation to precursor emissions between urban and rural

As described in the previous section, during the COVID-19 lockdown, NO_x emissions notably decreased across all sites in the northeastern US, leading to a more than 50 % reduction in pNO_3 concentration. However, the response of HNO_3 concentration shows a significant contrast between urban and rural areas. This contrast might be because nitrate formation is sensitive not only to NO_x emissions, but also NH_3, SO_2, and VOC emissions and gas-to-particle partitioning rate, depending on local atmospheric conditions. Here, we further explored how the sensitivity of nitrate formation to precursor emissions differently affects urban and rural air quality.

In the presence of sufficient NH_3 to fully neutralize H_2SO_4, excess NH_3 can react with HNO_3, forming NH_4NO_3, shifting the equilibrium toward the particulate phase. In contrast, HNO_3 remains in the gas phase when NH_3 availability is limited. The partitioning process of HNO_3 between the gas and particle phase is influenced by ambient temperature (T), relative humidity (RH), and aerosol pH[5,50]. The pH value within a certain range plays an important role in the gas-particle partitioning of nitrate, which significantly impacts nitrate formation[10,50]. Interestingly, during the COVID-19 lockdown, surface NH_3 concentrations considerably increased by approximately 12–

49 % across nearly all sites, except for the WST site. This increase could be attributed to the reduction of SO_2 and NO_x–key precursors that react with NH_3–resulting in less chemical removal and a longer atmospheric lifetime than before. Additionally, it is likely driven by an increased relative portion of agricultural activities, a major source of NH_3 emissions, since they were not largely affected by the lockdown restrictions.

Under these abundant NH_3 conditions, as NO_x emission decreased, increased O_3 concentrations led to more NO oxidation to NO_2 in urban areas, contributing to more N_2O_5 hydrolysis reactions with efficient conversion of NO_x to nitrate in March 2020. Enhanced nitrate formation driven by increased O_3 levels led to elevated gas-phase HNO_3 concentrations during the COVID-19 lockdown. However, this did not directly result in an increase in pNO_3, suggesting that gas-to-particle partitioning was influenced by multiple factors, not only aerosol pH. For instance, meteorological conditions, including temperature and relative humidity, along with changes in pre-existing aerosol composition and atmospheric depositions, likely played a critical role in response to pNO_3 concentrations. This highlights the complexity of secondary aerosol formation under various chemical and physical conditions. On the other hand, the substantial decline in NO_x emissions directly leads to a decrease in O_3 concentration, which in turn reduction in HNO_3 production. Less efficiency in nitrate formation causes both HNO_3 and pNO_3 concentrations to decrease. Overall, due to the abrupt decrease in precursor emissions during the COVID-19 lockdown, different sensitivities of nitrate formation to emissions were observed between urban and rural.

4. Implications

This work presents a comprehensive understanding of nitrate formation sensitivity to precursor emissions restrictions during the COVID-19 lockdown across urban and rural environments. Isotope observations provide direct evidence that the shift in oxidation chemistry driven by emission restrictions during the COVID-19 lockdown played an important role in air quality and atmospheric chemistry. Prior to the lockdown, NO_x concentrations in urban areas were approximately 1.5 to 2 times higher than those observed at rural sites. However, during the COVID-19 lockdown, NO_x concentrations decreased substantially across both urban and rural sites, resulting in comparable NO_x levels between the two regions. Despite similar NO_x concentrations during the lockdown, the responses of secondary pollutant formation were clearly distinguished between the two regions due to differences in chemical regimes. Specifically, O_3 production sensitivity differed between urban and rural areas as NO_x emission was reduced. In urban regions, controls on NO_x emissions were not effective at reducing O_3 levels. Rather, this contributed to increased oxidizing capacity, boosting nitrate formation, while rural/suburban areas showed both decreases in O_3 and nitrate formation during the COVID-19 lockdown. These findings underscore that more stringent mitigation policies based on spatial variabilities are needed to achieve effective control of air pollution.

As anthropogenic NO_x emissions continue to decline with the transition to cleaner energy sources, NO_x emissions from natural sources, such as soil and lightning, are expected to be dominant, posing new challenges for air quality management. Understanding these future dynamics requires insight into how the atmosphere responds to substantial reductions in anthropogenic NO_x. The unprecedented drop in emissions during the COVID-19 lockdown

provided a unique and practical window that allowed us to project long-term regulatory impacts on air quality and atmospheric chemistry.

5. Acknowledgment

We thank Ruby Ho for sampling and lab- oratory assistance. We are grateful to the US EPA CASTNET pro- gram and staff for their cooperation in this study and their assistance with receiving archived samples for isotopic analysis.

6. Reference

(1) Galloway, J. N.; Dentener, F. J.; Capone, D. G.; Boyer, E. W.; Howarth, R. W.; Seitzinger, S. P.; Asner, G. P.; Cleveland, C. C.; Green, P. A.; Holland, E. A. Nitrogen Cycles: Past, Present, and Future. Biogeochemistry 2004, 70 (2), 153–226.

(2) Pinder, R. W.; Davidson, E. A.; Goodale, C. L.; Greaver, T. L.; Herrick, J. D.; Liu, L. Climate Change Impacts of US Reactive Nitrogen. Proc. Natl. Acad. Sci. U.S.A. 2012, 109 (20), 7671–7675. https://doi.org/10.1073/pnas.1114243109.

(3) Crutzen, P. J. The Role of NO and NO_2 in the Chemistry of the Troposphere and Stratosphere. Annual review of earth and planetary sciences 1979, 7, 443–472.

(4) Prinn, R. G. The Cleansing Capacity of the Atmosphere. Annu. Rev. Environ. Resour. 2003, 28 (1), 29–57. https://doi.org/10.1146/annurev.energy.28.011503.163425.

(5) Seinfeld, J. H.; Pandis, S. N. Atmospheric Chemistry and Physics: From Air Pollution to Climate Change; John Wiley & Sons, 2016.

(6) Andreae, M. O.; Jones, C. D.; Cox, P. M. Strong Present-Day Aerosol Cooling Implies a Hot Future. Nature 2005, 435 (7046), 1187–1190.

(7) Driscoll, C. T.; Lawrence, G. B.; Bulger, A. J.; Butler, T. J.; Cronan, C. S.; Eagar, C.; Lambert, K. F.; Likens, G. E.; Stoddard, J. L.; Weathers, K. C. Acidic Deposition in the Northeastern United States: Sources and Inputs, Ecosystem Effects, and Management Strategies: The Effects of Acidic Deposition in the Northeastern United States Include the Acidification of Soil and Water, Which Stresses Terrestrial and Aquatic Biota. BioScience 2001, 51 (3), 180–198.

(8) Holland, E. A.; Braswell, B. H.; Sulzman, J.; Lamarque, J.-F. NITROGEN DEPOSITION ONTO THE UNITED STATES AND WESTERN EUROPE: SYNTHESIS OF OBSERVATIONS AND MODELS. Ecological Applications 2005, 15 (1), 38–57. https://doi.org/10.1890/03-5162.

(9) Https://Www.Epa.Gov/Air-Emissions-Inventories/2020-National-Emissions-Inventory-Nei-Data.

(10) Shah, V.; Jaeglé, L.; Thornton, J. A.; Lopez-Hilfiker, F. D.; Lee, B. H.; Schroder, J. C.; Campuzano-Jost, P.; Jimenez, J. L.; Guo, H.; Sullivan, A. P. Chemical Feedbacks Weaken the Wintertime Response of Particulate Sulfate and Nitrate to Emissions Reductions over the Eastern United States. Proceedings of the National Academy of Sciences 2018, 115 (32), 8110–8115.

(11) Kim, H.; Walters, W. W.; Kysela, L.; Hastings, M. G. Long-Term Trends in Inorganic Aerosol Chemical Composition and Chemistry at an Urban and Rural Site in the Northeastern US. Science of The Total Environment 2023, 904, 166848.

(12) Kim, H., Walters, W. W., Pye, H.O.T., Foley, K. M., & Hastings, M. G. Isotopes Constrain Nitrogen Oxides Chemistry Changes due to Emission Regulations in the Northeastern US, Nature Geoscience, *In review*.

(13) Romer Present, P. S.; Zare, A.; Cohen, R. C. The Changing Role of Organic Nitrates in the Removal and Transport of NO_x. Atmospheric Chemistry and Physics 2020, 20 (1), 267–279.

(14) Perring, A. E.; Pusede, S. E.; Cohen, R. C. An Observational Perspective on the Atmospheric Impacts of Alkyl and Multifunctional Nitrates on Ozone and Secondary Organic Aerosol. Chem. Rev. 2013, 113 (8), 5848–5870. https://doi.org/10.1021/cr300520x.

(15) Kim, H., Walters, W. W., & Hastings, M. G. Regulation Impact on Particulate Nitrate Precursor Emissions in the Northeastern US, *In preparation*.

(16) Jiang, Z.; McDonald, B. C.; Worden, H.; Worden, J. R.; Miyazaki, K.; Qu, Z.; Henze, D. K.; Jones, D. B. A.; Arellano, A. F.; Fischer, E. V.; Zhu, L.; Boersma, K. F. Unexpected Slowdown of US Pollutant Emission Reduction in the Past Decade. Proc. Natl. Acad. Sci. U.S.A. 2018, 115 (20), 5099–5104. https://doi.org/10.1073/pnas.1801191115.

(17) Venter, Z. S.; Aunan, K.; Chowdhury, S.; Lelieveld, J. COVID-19 Lockdowns Cause Global Air Pollution Declines. Proc. Natl. Acad. Sci. U.S.A. 2020, 117 (32), 18984–18990. https://doi.org/10.1073/pnas.2006853117.

(18) Kroll, J. H.; Heald, C. L.; Cappa, C. D.; Farmer, D. K.; Fry, J. L.; Murphy, J. G.; Steiner, A. L. The Complex Chemical Effects of COVID-19 Shutdowns on Air Quality. Nature Chemistry 2020, 12 (9), 777–779.

(19) Liu, Z.; Ciais, P.; Deng, Z.; Lei, R.; Davis, S. J.; Feng, S.; Zheng, B.; Cui, D.; Dou, X.; Zhu, B. Near-Real-Time Monitoring of Global CO2 Emissions Reveals the Effects of the COVID-19 Pandemic. Nature communications 2020, 11 (1), 5172.

(20) He, J.; Harkins, C.; O'Dell, K.; Li, M.; Francoeur, C.; Aikin, K. C.; Anenberg, S.; Baker, B.; Brown, S. S.; Coggon, M. M. COVID-19 Perturbation on US Air Quality and Human Health Impact Assessment. PNAS nexus 2024, 3 (1), pgad483.

(21) Berman, J. D.; Ebisu, K. Changes in US Air Pollution during the COVID-19 Pandemic. Science of the total environment 2020, 739, 139864.

(22) Huang, X.; Ding, A.; Gao, J.; Zheng, B.; Zhou, D.; Qi, X.; Tang, R.; Wang, J.; Ren, C.; Nie, W. Enhanced Secondary Pollution Offset Reduction of Primary Emissions during COVID-19 Lockdown in China. National Science Review 2021, 8 (2), nwaa137.

(23) Zhang, Q.; Pan, Y.; He, Y.; Walters, W. W.; Ni, Q.; Liu, X.; Xu, G.; Shao, J.; Jiang, C. Substantial Nitrogen Oxides Emission Reduction from China Due to COVID-19 and Its Impact on Surface Ozone and Aerosol Pollution. Science of the Total Environment 2021, 753, 142238.

(24) Evangeliou, N.; Tichy, O.; Svendby Otervik, M.; Eckhardt, S.; Balkanski, Y.; Hauglustaine, D. Unchanged $PM_{2.5}$ Levels over Europe during COVID-19 Were Buffered by Ammonia. Aerosol Research Discussions 2024, 2024, 1–38.

(25) Ju, M. J.; Oh, J.; Choi, Y.-H. Changes in Air Pollution Levels after COVID-19 Outbreak in Korea. Science of the Total Environment 2021, 750, 141521.

(26) Koo, J.-H.; Kim, J.; Lee, Y. G.; Park, S. S.; Lee, S.; Chong, H.; Cho, Y.; Kim, J.; Choi, K.; Lee, T. The Implication of the Air Quality Pattern in South Korea after the COVID-19 Outbreak. Scientific reports 2020, 10 (1), 22462.

(27) Zhang, M.; Katiyar, A.; Zhu, S.; Shen, J.; Xia, M.; Ma, J.; Kota, S. H.; Wang, P.; Zhang, H. Impact of Reduced Anthropogenic Emissions during COVID-19 on Air Quality in India. Atmospheric Chemistry and Physics 2021, 21 (5), 4025–4037.

(28) Verma, R. L.; Kamyotra, J. S. Impacts of COVID-19 on Air Quality in India. Aerosol Air Qual. Res. 2021, 21 (4), 200482. https://doi.org/10.4209/aaqr.200482.

(29) Freyer, H. D.; Kley, D.; Volz-Thomas, A.; Kobel, K. On the Interaction of Isotopic Exchange Processes with Photochemical Reactions in Atmospheric Oxides of Nitrogen. Journal of Geophysical Research: Atmospheres 1993, 98 (D8), 14791–14796.

(30) Hastings, M. G.; Sigman, D. M.; Lipschultz, F. Isotopic Evidence for Source Changes of Nitrate in Rain at Bermuda. Journal of Geophysical Research: Atmospheres 2003, 108 (D24).

(31) Michalski, G.; Scott, Z.; Kabiling, M.; Thiemens, M. H. First Measurements and Modeling of $\Delta^{17}O$ in Atmospheric Nitrate. Geophysical Research Letters 2003, 30 (16).

(32) Elliott, E. M.; Kendall, C.; Boyer, E. W.; Burns, D. A.; Lear, G. G.; Golden, H. E.; Harlin, K.; Bytnerowicz, A.; Butler, T. J.; Glatz, R. Dual Nitrate Isotopes in Dry Deposition: Utility for Partitioning NO_x Source Contributions to Landscape Nitrogen Deposition. Journal of Geophysical Research: Biogeosciences 2009, 114 (G4).

(33) Bekker, C.; Walters, W. W.; Murray, L. T.; Hastings, M. G. Nitrate Chemistry in the Northeast US–Part 1: Nitrogen Isotope Seasonality Tracks Nitrate Formation Chemistry. Atmospheric Chemistry and Physics 2023, 23 (7), 4185–4201.

(34) Kim, H.; Walters, W. W.; Bekker, C.; Murray, L. T.; Hastings, M. G. Nitrate Chemistry in the Northeast US–Part 2: Oxygen Isotopes Reveal Differences in Particulate and Gas-Phase Formation. Atmospheric Chemistry and Physics 2023, 23 (7), 4203–4219.

(35) Miller, D. J.; Wojtal, P. K.; Clark, S. C.; Hastings, M. G. Vehicle NO_x Emission Plume Isotopic Signatures: Spatial Variability across the Eastern United States. JGR Atmospheres 2017, 122 (8), 4698–4717. https://doi.org/10.1002/2016JD025877.

(36) Miller, D. J.; Chai, J.; Guo, F.; Dell, C. J.; Karsten, H.; Hastings, M. G. Isotopic Composition of In Situ Soil NO_x Emissions in Manure-Fertilized Cropland. Geophysical Research Letters 2018, 45 (21). https://doi.org/10.1029/2018GL079619.

(37) Walters, W. W.; Tharp, B. D.; Fang, H.; Kozak, B. J.; Michalski, G. Nitrogen Isotope Composition of Thermally Produced NO_x from Various Fossil-Fuel Combustion Sources. Environmental science & technology 2015, 49 (19), 11363–11371.

(38) Felix, J. D.; Elliott, E. M.; Shaw, S. L. Nitrogen Isotopic Composition of Coal-Fired Power Plant NO_x: Influence of Emission Controls and Implications for Global Emission Inventories. Environ. Sci. Technol. 2012, 46 (6), 3528–3535. https://doi.org/10.1021/es203355v.

(39) Walters, W. W.; Goodwin, S. R.; Michalski, G. Nitrogen Stable Isotope Composition ($\delta^{15}N$) of Vehicle-Emitted NO_x Environmental science & technology 2015, 49 (4), 2278–2285.

(40) Walters, W. W.; Simonini, D. S.; Michalski, G. Nitrogen Isotope Exchange between NO and NO_2 and Its Implications for $\delta^{15}N$ Variations in Tropospheric NO_x and Atmospheric Nitrate. Geophysical Research Letters 2016, 43 (1), 440–448. https://doi.org/10.1002/2015GL066438.

(41) Thiemens, M. H. Mass-Independent Isotope Effects in Planetary Atmospheres and the Early Solar System. Science 1999, 283 (5400), 341–345. https://doi.org/10.1126/science.283.5400.341.

(42) Thiemens, M. H. History and Applications of Mass-Independent Isotope Effects. Annu. Rev. Earth Planet. Sci. 2006, 34, 217–262.

(43) Vicars, W. C.; Savarino, J. Quantitative Constraints on the ^{17}O-Excess ($\Delta^{17}O$) Signature of Surface Ozone: Ambient Measurements from 50°N to 50°S Using the Nitrite-Coated Filter Technique. Geochimica et Cosmochimica Acta 2014, 135, 270–287.

(44) Baumgardner, R. E.; Lavery, T. F.; Rogers, C. M.; Isil, S. S. Estimates of the Atmospheric Deposition of Sulfur and Nitrogen Species: Clean Air Status and Trends Network, 1990−2000. Environ. Sci. Technol. 2002, 36 (12), 2614–2629. https://doi.org/10.1021/es011146g.

(45) Https://Www3.Epa.Gov/Castnet/Docs/CASTNET_QAPP_v9-4_Main_Body_Final.Pdf.

(46) Sigman, D. M.; Casciotti, K. L.; Andreani, M.; Barford, C.; Galanter, M.; Böhlke, J. K. A Bacterial Method for the Nitrogen Isotopic Analysis of Nitrate in Seawater and Freshwater. Analytical chemistry 2001, 73 (17), 4145–4153.

(47) Casciotti, K. L.; Sigman, D. M.; Hastings, M. G.; Böhlke, J. K.; Hilkert, A. Measurement of the Oxygen Isotopic Composition of Nitrate in Seawater and Freshwater Using the Denitrifier Method. Analytical chemistry 2002, 74 (19), 4905–4912.

(48) Kaiser, J.; Hastings, M. G.; Houlton, B. Z.; Röckmann, T.; Sigman, D. M. Triple Oxygen Isotope Analysis of Nitrate Using the Denitrifier Method and Thermal Decomposition of N_2O. Analytical Chemistry 2007, 79 (2), 599–607.

(49) Fibiger, D. L.; Hastings, M. G. First Measurements of the Nitrogen Isotopic Composition of NO_x from Biomass Burning. Environ. Sci. Technol. 2016, 50 (21), 11569–11574. https://doi.org/10.1021/acs.est.6b03510.

(50) Pye, H. O.; Nenes, A.; Alexander, B.; Ault, A. P.; Barth, M. C.; Clegg, S. L.; Collett Jr, J. L.; Fahey, K. M.; Hennigan, C. J.; Herrmann, H. The Acidity of Atmospheric Particles and Clouds. Atmospheric chemistry and physics 2020, 20 (8), 4809–4888.

(51) Elliott, E. M.; Kendall, C.; Wankel, S. D.; Burns, D. A.; Boyer, E. W.; Harlin, K.; Bain, D. J.; Butler, T. J. Nitrogen Isotopes as Indicators of NO_x Source Contributions to Atmospheric Nitrate Deposition across the Midwestern and Northeastern United States. Environmental Science & Technology 2007, 41 (22), 7661–7667.

(52) Li, J.; Zhang, X.; Orlando, J.; Tyndall, G.; Michalski, G. Quantifying the Nitrogen Isotope Effects during Photochemical Equilibrium between NO and NO_2: Implications for $\delta^{15}N$ in Tropospheric Reactive Nitrogen. Atmospheric Chemistry and Physics 2020, 20 (16), 9805–9819.

(53) Walters, W. W.; Pye, H. O. T.; Kim, H.; Hastings, M. G. Modeling the Oxygen Isotope Anomaly ($\Delta^{17}O$) of Reactive Nitrogen in the Community Multiscale Air Quality Model: Insights into Nitrogen Oxide Chemistry in the Northeastern United States. ACS EST Air 2024, acsestair.3c00056. https://doi.org/10.1021/acsestair.3c00056.

7. Supplementary

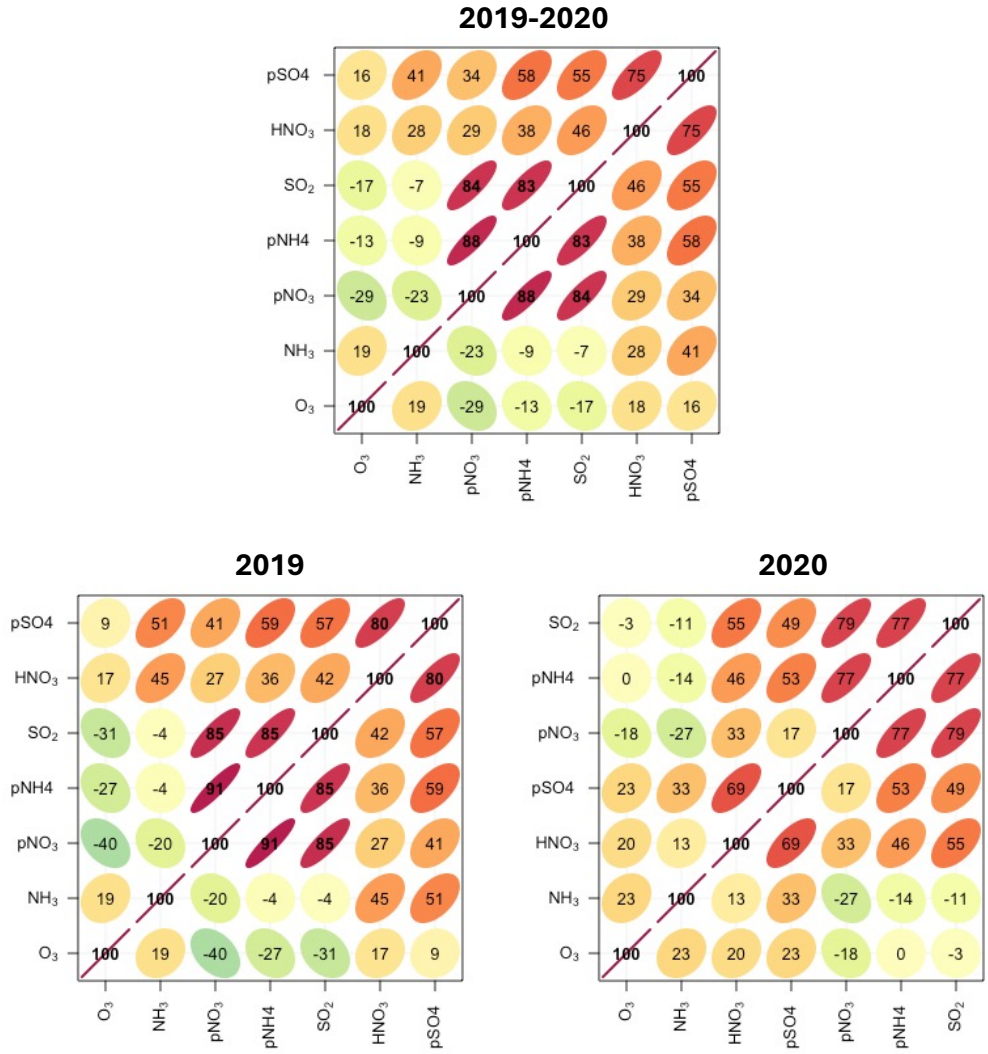

Figure S6.1. Correlation coefficients for O_3, NH_3, HNO_3, and PM_{10} inorganic ion compositions for entire periods, 2019 and 2020

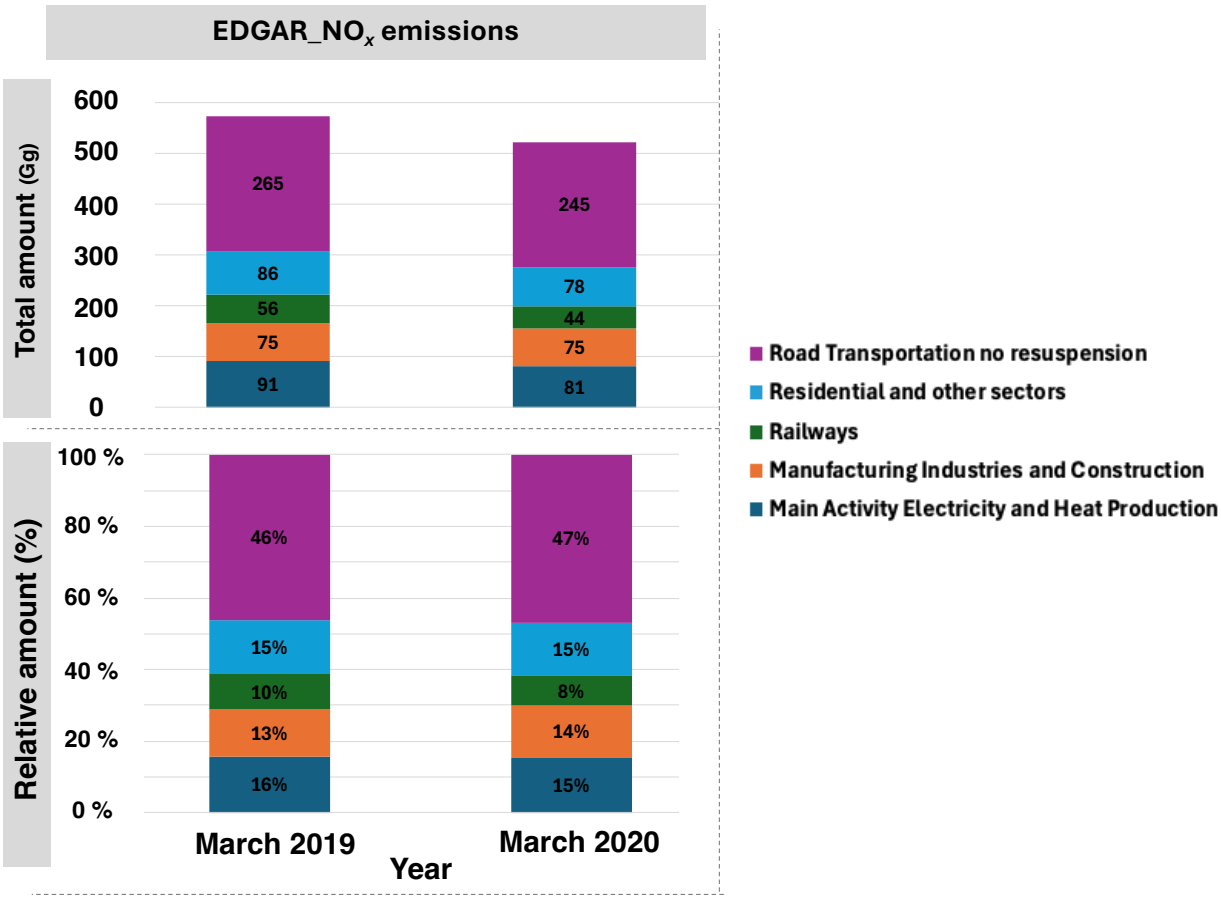

Figure S6.2. Emissions Database for Global Atmospheric Research (EDGAR)

Table S6.1. Statistics of yearly averaged values of trace gases (O_3 and NO_x) and inorganic ion species (e.g., HNO_3, pNO_3, pSO_4, and pNH_4).

Site	Year	NO_x (ppbv)	O_3 (ppbv)	HNO_3 (ppbv)	NH_3 ($\mu g\ m^{-3}$)	SO_2 (ppbv)	pNO_3 ($\mu g\ m^{-3}$)	NH_4 ($\mu g\ m^{-3}$)	SO_4 ($\mu g\ m^{-3}$)	$\delta^{15}N(pNO_3)$ (‰)	$\delta^{18}O(pNO_3)$ (‰)	$\Delta^{17}O(pNO_3)$ (‰)
ABT147	2019	17.20	33.35	0.21	0.53	0.12	0.67	0.30	0.68	0.11	64.34	24.55
	2020	16.07	32.28	0.22	0.84	0.11	0.62	0.26	0.70	-1.46	66.07	25.83
BEL116	2019	14.83	29.40	0.31	1.06	0.19	0.94	0.49	1.08	0.55	67.70	27.27
	2020	12.64	26.98	0.28	0.87	0.14	0.59	0.35	0.93	2.60	66.14	27.36
CAT175	2019	14.40	–	0.19	0.19	0.11	0.47	0.30	0.62	-1.65	64.33	29.50
	2020	15.01	–	0.21	0.20	0.10	0.45	0.31	0.63	-1.59	70.49	26.86
CTH110	2019	–	33.81	0.20	0.72	0.16	0.79	0.47	0.85	-0.97	68.61	26.51
	2020	–	33.67	0.20	0.79	0.14	0.61	0.39	0.78	-1.86	68.39	27.22
WSP144	2019	26.03	34.69	0.36	0.55	0.19	1.10	0.49	0.99	1.74	65.63	23.88
	2020	26.02	28.51	0.32	0.52	0.16	0.77	0.35	0.87	1.52	66.58	23.94
WST109	2019	10.90	34.19	0.07	0.37	0.08	0.18	0.19	0.47	-1.28	62.89	28.18
	2020	9.47	26.36	0.09	0.40	0.08	0.18	0.20	0.52	-1.10	62.93	24.44
Total		16.13	31.32	0.22	0.59	0.13	0.61	0.34	0.76	-0.15	64.59	25.48

CHAPTER 7

Conclusion

Heejeong Kim

Department of Earth, Environmental, and Planetary Sciences, Institute at Brown for Environment and Society, Brown University, Providence, RI 02912, USA

This thesis represents progress in our understanding of atmospheric chemistry and its responses to emission regulations in the United States. Specifically, this work focuses on understanding atmospheric nitrate chemistry in a densely populated region of the world that has often suffered from air quality degradation, while also seeing significant improvement in air quality in recent decades. Atmospheric nitrate is a key component of particulate matter and plays a crucial role in air quality and atmospheric chemistry, influencing human and ecosystem health and climate. The northeastern US has historically experienced poor air quality and serious acid deposition due to emissions from highly populated and urbanized areas. Utilizing long-term and short-term stable isotope measurements with atmospheric chemistry models, this work demonstrates the critical role of stable nitrogen and oxygen isotopes of nitrate as powerful observational constraints on atmospheric nitrate precursor sources and chemical processing. These isotopes have provided in-depth and quantitative insights about atmospheric nitrate chemistry that were not accessible using traditional tools.

This work began by focusing on recent atmospheric nitrate records in the northeastern US. Chapter 2 provides the spatiotemporal variabilities of atmospheric nitrate formation in the northeastern US during 2017–2018 using oxygen isotopes of nitrate ($\Delta^{17}O$ and $\delta^{18}O$) and output from a state-of-the-art atmospheric chemistry model. This study was the first quantitative evaluation of oxidation chemistry using the observed triple oxygen isotope compositions of both HNO_3 and pNO_3, employing the 3D global air quality model, GEOS-Chem, in this region. No significant spatial variabilities of oxygen isotopes, especially for pNO_3, were observed in our records, as nitrate formation is regionally influenced due to longer atmospheric nitrate. However, interestingly, significant differences between $\Delta^{17}O(pNO_3)$ and $\Delta^{17}O(HNO_3)$ were observed, indicating phase-dependent oxidation chemistry for atmospheric nitrate formation. Conventional

understanding would expect $\Delta^{17}O$ of HNO_3 and pNO_3 to be the same since HNO_3 is partitioned into the aerosol phase based on thermodynamic equilibrium (i.e., $NH_4NO_3(s) \rightleftharpoons HNO_3(g) + NH_3(g)$) or coarse uptake. However, our findings suggest that phase-dependent oxidation chemistry plays a more significant role in atmospheric nitrate formation. In addition, the GEOS-Chem model exhibited significant overestimations of HNO_3 and pNO_3 concentrations, largely due to an overprediction of a specific nitrate production pathway–N_2O_5 hydrolysis. Isotopic measurements ($\Delta^{17}O$ and $\delta^{18}O$) indicated a greater relative contribution of NO_2 + OH chemistry than previously expected, highlighting the need for improved model representation of nitrate-phase differences. Lastly, this study has shown that the use of $\delta^{18}O$ can further enhance our understanding of the oxidants contributing to nitrate formation, particularly for distinguishing oxidants that have similar $\Delta^{17}O$ values. Overall, this work provides important insight into the role of oxidation chemistry in reconciling a commonly observed positive bias for modeled atmospheric nitrate concentrations in the northeastern US.

In Chapters 3–5, we analyzed long-term aerosol records from 2005 to 2015, a critical period of emission regulations. This dataset allows us to assess the effectiveness of emission regulations on air quality over the decade. For Chapter 3, we examined a long-term trend (2005–2015) in inorganic aerosol composition at urban and rural sites in the northeastern US. This study addresses key uncertainties regarding the changes in production mechanisms of major anthropogenic inorganic ions such as nitrate, sulfate, and ammonium in response to emission regulation implementation with an emphasis on seasonal and spatial patterns. Our records reveal that in the northeastern US, the reduction in SO_2 emissions has resulted in a significant decrease in sulfate and ammonium aerosol concentrations. However, we observed an increase in nitrate concentration in the northeastern US during the same period. Our findings reveal that changes in

chemical mechanisms, specifically aerosol acidity due to the decrease in SO_2 emissions, are responsible for the observed increase in nitrate concentration in recent years. Furthermore, as anthropogenic emissions declined, natural sources, such as sea salt and crustal material, played an increasing role in aerosol chemistry. The reduction in SO_2 emissions has impacted the atmospheric lifetime and transport distance of ammonium, resulting in continued impacts on aerosol acidity and air quality. Overall, our study provides a valuable observational record and insights into the complex interaction between atmospheric aerosol chemistry and emissions reduction that have implications for atmospheric chemistry and air quality policy. Based on these findings, Chapters 4 and 5 further investigate the regulation impact on particulate nitrate precursor emissions and atmospheric oxidation chemistry on a process level using isotopic observations. In Chapter 4, the long-term record of oxygen isotopic compositions of nitrate ($\Delta^{17}O$ and $\delta^{18}O$) was analyzed to quantify the changes in NO_x oxidation pathways over time. Oxygen isotopes, especially $\delta^{18}O$, provided critical information for understanding NO_x oxidation chemistry. In this study, we used the US EPA Community Multiscale Air Quality (CMAQ) model, which accurately represents NO_x oxidation chemistry in the northeastern US. Our analysis demonstrates that as NO_x emissions have decreased, O_3 concentrations have increased in major cities in the northeastern US. The enhanced O_3 concentrations have strengthened atmospheric oxidation capacity, resulting in a shorter urban NO_x lifetime and increased aerosol formation. These processes have contributed to persistently high wintertime nitrate concentrations in the eastern US despite reductions in precursor emission. This study represents the first long-term quantitative assessment of NO_x oxidation chemistry and lifetime changes using field observations with an atmospheric chemistry model. In Chapter 5, we focus on the nitrogen isotope of pNO_3 to understand atmospheric NO_x emission sources and NO_x oxidation chemistry. Using the US EPA CMAQ air quality model, we quantify the isotope

fractionation impact on our observed $\delta^{15}N(pNO_3)$. Based on the framework developed in the previous chapters, the results reveal that isotope fractionations during NO_x oxidation chemistry can explain seasonal variations of $\delta^{15}N(pNO_3)$. In addition, long-term decreasing shifts in $\delta^{15}N(pNO_3)$ observed over the decade reflect a shift in the primary fuel for electric power generation in the US. Namely, coal combustion was replaced by natural gas, although coal emissions of NO_x over time may be underestimated in national emission inventories. This nitrogen isotope work provides critical observational constraints on the sources and chemical processing of atmospheric nitrate in response to policy-driven NO_x emission reductions. Overall, these long-term isotope records together with atmospheric chemistry models provide valuable insight to enable a more accurate evaluation of the effectiveness of emission control strategies.

In Chapter 6, we have investigated the impact of short-term emission disruptions on air quality. The outbreak of COVID-19 in 2020 caused widespread restrictions on human activities, leading to unprecedented drops in emissions across the US. This period provides a unique opportunity to assess the impacts of reduced human activity on air quality on a short time scale. In this case, the $\delta^{15}N$, $\delta^{18}O$, and $\Delta^{17}O$ of particulate nitrate were utilized to track atmospheric nitrate chemistry and its response to emissions changes during the COVID-19 lockdown in the northeastern US. The isotope observations reveal that shifts in oxidation capacity by the change in NO_x oxidation chemistry, rather than changes in emission sources, played a dominant role in determining nitrate formation efficiency during this period. Specifically, in urban areas, decreased NO_x emissions led to enhanced ozone, increasing the oxidizing capacity and more efficient N_r oxidation. In contrast, rural/suburban areas experienced decreases in NO_x, ozone, and nitrate formation. The unprecedented drop in emissions during the COVID-19 lockdown provided a unique and practical window that allowed us to project regulatory impacts on air quality and

atmospheric chemistry. These findings underscore that more stringent mitigation policies based on spatial variabilities are needed to achieve effective control of air pollution.

Overall, this dissertation provides a new framework for evaluating the effectiveness of precursor emission controls on key atmospheric secondary pollutants such as ozone, particulate matter, and deposition. Specifically, this study demonstrates that stable isotopes serve as a powerful tool for quantifying NO_x emission sources and their oxidation chemistry. One of the key takeaways from this work is the demonstrated utility of $\delta^{18}O$: we show that $\delta^{18}O$ is more sensitive than $\Delta^{17}O$ in detecting small, but significant changes in oxidation chemistry, providing more detailed information about the oxidants responsible for NO_x oxidation. This finding also suggests that future work should focus on better characterizing the $\delta^{18}O$ signatures of oxidants, as well as characterizing potential isotope effects during their transfer to NO_x to nitrate. In addition, stable isotopes contribute to refining the representation of nitrate formation in atmospheric chemistry models. By incorporating the oxygen isotope and atmospheric chemistry model, we were able to quantitatively assess the oxidation process and identify specific limitations in the model. These findings likely provide critical guidance for improving the model's performance for the atmospheric modeling community. By incorporating these quantitative diagnostic approaches employed in this study into regulatory assessments, policymakers can better prioritize control strategies that effectively reduce secondary pollutant levels, rather than relying solely on precursor mass reductions.

As precursor emission regulations have been implemented, shifts in atmospheric oxidation efficiency and pollutant lifetime suggest potential redistribution of acid and nutrient deposition, with broader environmental implications. This highlights the need for a more comprehensive approach to precursor emission regulation to more effectively mitigate air pollution and address

environmental challenges. Lastly, these findings are likely applicable to other regions where significant NO_x, SO_2, and NH_3 emissions deteriorate air quality, such as urban coastal areas in Western Europe, as well as Eastern China.